

From photons to cosmic rays: a multiwavelength pursuit of Galactic PeVatrons

Jooyun Woo

Submitted in partial fulfillment of the  
requirements for the degree of  
Doctor of Physics  
under the Executive Committee  
of the Graduate School of Arts and Sciences

COLUMBIA UNIVERSITY

2025

© 2025

Jooyun Woo

All Rights Reserved

## **Abstract**

From photons to cosmic rays: a multiwavelength pursuit of Galactic PeVatrons

Jooyun Woo

The origin of cosmic rays has been a century-long outstanding question. In particular, the accelerators of the most energetic cosmic rays in our galaxy, “Galactic PeVatrons”, have drawn great attention in the community for understanding an extreme cosmic-ray acceleration mechanism and other closely related processes such as diffusion and cooling. The most energetic cosmic rays emit TeV gamma rays and hard X-rays, whose spatial and energy distribution deliver crucial information about the cosmic rays and the astrophysical environment in which the cosmic rays are accelerated. Since different information is delivered in different energies of photons, one needs to observe a cosmic-ray source with multiwavelength instruments to obtain a complete view of physical processes in the cosmic-ray source. This work presents X-ray and gamma-ray observations of three Galactic PeVatron candidates – a young supernova remnant Cassiopeia A, a middle-aged pulsar wind nebula Dragonfly, and a halo around an old pulsar LHAASO J0621+3755. Each candidate is examined for its capability of cosmic-ray acceleration, and investigated for its unique insight into different cosmic-ray processes. Prospects for identifying Galactic PeVatrons are discussed.

## Table of Contents

Acknowledgments . . . . .	xv
Chapter 1: Introduction and Background . . . . .	1
1.1 Cosmic ray diffusion . . . . .	5
1.2 Cosmic ray acceleration . . . . .	10
1.2.1 Second-order Fermi acceleration . . . . .	10
1.2.2 Diffusive shock acceleration (First-order Fermi acceleration) . . . . .	12
1.2.3 Nonlinear diffusive shock acceleration . . . . .	16
1.2.4 Modified nonlinear diffusive shock acceleration . . . . .	16
1.3 CR cooling . . . . .	19
1.3.1 Pion deccay . . . . .	19
1.3.2 Nonthermal Bremsstrahlung . . . . .	22
1.3.3 Inverse Compton radiation . . . . .	23
1.3.4 Synchrotron radiation . . . . .	25
1.4 Cosmic ray source candidates . . . . .	30
1.4.1 Supernova remnants . . . . .	31
1.4.2 Pulsars and pulsar wind nebulae . . . . .	34
Chapter 2: Instruments . . . . .	39

2.1	NuSTAR: first focusing hard X-ray telescope . . . . .	40
2.1.1	Chandra and XMM-Newton: soft X-ray telescopes . . . . .	41
2.2	Fermi-LAT: space-based gamma-ray telescope . . . . .	42
2.3	VERITAS: imaging atmospheric Cherenkov telescope . . . . .	43
2.4	LHAASO: extensive air shower arrays . . . . .	48
Chapter 3: Cassiopeia A – young supernova remnant . . . . .		50
3.1	Introduction . . . . .	50
3.2	Multi-epoch X-ray analysis . . . . .	52
3.2.1	Observations and data reduction . . . . .	52
3.2.2	Background estimation . . . . .	53
3.2.3	Spectral analysis . . . . .	53
3.2.4	Image production . . . . .	55
3.3	Temporal synchrotron spectral energy distribution modeling . . . . .	55
3.3.1	SED model description . . . . .	57
3.3.2	SED modeling results . . . . .	59
3.4	Discussion . . . . .	60
3.4.1	Hard injection spectrum . . . . .	60
3.4.2	Modified nonlinear diffusive shock acceleration . . . . .	63
3.4.3	Proton acceleration at the hard X-ray knots? . . . . .	64
3.5	Summary and conclusion . . . . .	65
Chapter 4: Dragonfly – middle-aged pulsar wind nebula . . . . .		66
4.1	Introduction . . . . .	66

4.2	X-ray data analysis . . . . .	69
4.2.1	Timing analysis . . . . .	69
4.2.2	Imaging analysis . . . . .	70
4.2.3	Spectral analysis . . . . .	75
4.3	Fermi-LAT analysis . . . . .	79
4.4	Multiwavelength SED modeling . . . . .	80
4.4.1	Naima . . . . .	82
4.4.2	Dynamical model . . . . .	85
4.5	Discussion . . . . .	89
4.5.1	PeVatron pulsar wind nebulae . . . . .	89
4.5.2	Distance and proper motion . . . . .	91
4.5.3	Magnetic field . . . . .	92
4.6	Summary . . . . .	94
Chapter 5: LHAASO J0621+3755 – pulsar halo? . . . . .		95
5.1	Introduction . . . . .	96
5.2	VERITAS analysis . . . . .	97
5.2.1	3D acceptance map and FOV technique in Gammapy . . . . .	99
5.2.2	Generating a 3D acceptance map . . . . .	101
5.2.3	3D acceptance map validation and bias correction . . . . .	103
5.3	XMM-Newton analysis . . . . .	111
5.4	Discussion: LHAASO J0621+3755 as a pulsar halo . . . . .	112
5.5	Summary and conclusion . . . . .	116

Conclusion . . . . . 118

References . . . . . 120

## List of Figures

1.1	The CR spectrum measured by different experiments [2]. . . . .	2
1.2	<b>Top:</b> Galactic UHE sources detected by LHAASO [6]. <b>Bottom:</b> TeV–PeV neutrino emission along the Galactic Plane detected by IceCube [7]. . . . .	3
1.3	Galactic TeV sources (image credit: TeVCat ( <a href="http://tevcat2.uchicago.edu/">http://tevcat2.uchicago.edu/</a> )). . . . .	4
1.4	Schematic diagram of our galaxy [4] . . . . .	9
1.5	Schematic diagrams of the (second-order) Fermi acceleration ( <b>left</b> , image credit: Juan A. Aguilar) and the DSA (or the first-order Fermi acceleration) ( <b>right</b> , [13]). . . . .	11
1.6	<b>Left:</b> schematic diagram of the formation of a precursor (image credit: Stefano Gabici). <b>Right:</b> Comparison between the NLDSA (precursor (region 1) only) and mNLDSA (precursor and postcursor (region 2))) [21] . . . . .	15
1.7	Schematic diagram of synchrotron radiation and relativistic aberration [31]. . . . .	26
1.8	Synchrotron radiation pulses and its power spectrum [35]. . . . .	26
1.9	The SEDs of various radiative processes for protons and electrons [33]. See text for details. . . . .	29
1.10	Schematic diagram of the evolution of an SNR and PWN system [44]. . . . .	30
1.11	Schematic diagram of a PWN [54]. . . . .	34
1.12	Schematic diagram of the striped pulsar wind [61]. . . . .	35
1.13	<b>Left:</b> plasma velocity and number density profile in a young SNR Cassiopeia A [63]. <b>Right:</b> A simulated evolution of the radii of an SNR forward shock (blast wave), reverse shock, and a PWN [64]. . . . .	37

2.1	X-ray and gamma-ray instruments placed on the corresponding energy bands with different colors. A typical two-hump SED of a CR source is overlaid (black solid line). Ground-based gamma-ray observatories are labeled with the hemisphere of their location. . . . .	39
2.2	NuSTAR instrument [10] . . . . .	40
2.3	Fermi-LAT instrument [73] . . . . .	43
2.4	Comparison of a gamma-ray-induced electromagnetic shower ( <i>left</i> ) and CR-induced hadronic shower ( <i>right</i> ): schematic diagrams of the showers ( <b>top row</b> , [78]), shower particle trajectories ( <b>middle row</b> ) and Cherenkov photon distributions on the ground ( <b>bottom row</b> ). The images in the middle and bottom rows are from simulations ([79]). . . . .	45
2.5	An illustration of the stereoscopic imaging technique of IACTs [80]. . . . .	46
2.6	VERITAS (photo credit: Center for Astrophysics   Harvard & Smithsonian) . . . .	47
2.7	<b>Top:</b> the LHAASO site (photo credit: Chinese Academy of Sciences.) <b>Bottom:</b> a schematic diagram of different detector types [86]. . . . .	49
3.1	<b>Historical X-ray flux of Cas A in the 15-50 keV band.</b> The flux was calculated from the best-fit spectral model for each telescope data. The errors for the spectral model parameters were propagated to calculate the error for the flux. For HEAO 1 A-2, a power law model was fitted to the spectral data reported in [96]. Previously reported best-fit spectral parameters were used for CGRO [97], RXTE [98], BeppoSAX [99], and Suzaku [100]. For NuSTAR, the error bars are smaller than the markers. The dashed black line shows the flux decrease rate ( $1.6 \pm 0.1$ )% yr <sup>-1</sup> found from a linear regression of all the data points accounting for the error bars. . . . .	54
3.2	<b>15-50 keV flux maps of Cas A in 2013 (a) and 2023 (b), and a difference map between 2013 and 2023 (c).</b> For (a) and (b), background-subtracted counts maps were divided by vignetting-corrected exposure maps, then iteratively deconvolved using the on-axis NuSTAR point spread function (PSF, see §3.2.4). The two images were scaled equally to ensure direct comparison. (c) was generated by subtracting (b) from (a). All three images were smoothed with a Gaussian kernel ( $\sigma = 3.5'' = 1.5$ pixel). The L-band radio contour [110] is overlaid in black. A circle with diameter 14'' is overlaid at the right bottom corner of each image to indicate the size of the NuSTAR PSF (14'' FWHM). Fading over the entire remnant is clearly noticeable. Most prominently, the brightest knots inside the remnant (in the middle and on the west) dimmed significantly. . . . .	56

3.3	<p><b>Top: Synchrotron (left) and inverse Compton (right) spectrum from the best-fit electron distribution for <math>B_0 = 6 \mu\text{G}</math>.</b> With this magnetic field, the predicted gamma-ray flux significantly exceeds the observed gamma-ray flux. <b>Bottom: Synchrotron and inverse Compton spectrum in 2013 (left), and the synchrotron spectrum in 2013 and 2023 (right) from the best-fit electron distribution for the lower-limit magnetic field <math>B_0 = 123 \pm 3 \mu\text{G}</math>.</b> The lower-limit magnetic field predicts over 50% decrease in the 15-50 keV flux, much faster than the observed decrease (<math>15 \pm 1\%</math>). The Fermi-LAT and VERITAS spectra were taken from 4FGL-DR4 [76, 77] and [53], respectively. . . . .</p>	61
3.4	<p><b>Synchrotron spectrum in 2013 and 2023 calculated with the temporal synchrotron cooling and injection model.</b> The black (red) solid line is the synchrotron spectrum calculated using the best-fit parameters in Table 3.2 for 2013 (2023). The red dashed line is the synchrotron spectrum of the preexisting electrons in 2023, and the red dotted line shows the contribution of the injected electrons to the synchrotron spectrum in 2023. The NuSTAR spectrum from this work and the radio spectrum from [116] are overlaid. The error bars of the data points are for <math>1\sigma</math> uncertainties in this figure and all the figures hereafter. . . . .</p>	62
4.1	<p>Merged (observation IDs 8502 and 7603) and exposure-corrected Chandra images of the Dragonfly in 2 – 6 keV. The scales were adjusted for better legibility. PSR J2021+3651 is marked as a cross (X) in both images. <b>Left:</b> <math>1' \times 1'</math> image after Gaussian smoothing with <math>\sigma = 1.5 \text{ pixel} = 0.7''</math>. The <math>20'' \times 10''</math> inner nebula and the pulsar jet stretching out to <math>\sim 30''</math> from the pulsar are marked with dashed lines. <b>Right:</b> <math>21' \times 11'</math> image after Gaussian smoothing with <math>\sigma = 3 \text{ pixel} = 3.0''</math>. The arc in length <math>\sim 7.7'</math> is traced with a dotted line. The extent of the outer nebula seen by XMM is marked as a dashed line. . . . .</p>	70
4.2	<p>Merged (FPMA and FPMB), exposure- and vignetting-corrected, and smoothed (Gaussian kernel with <math>\sigma = 1.5 \text{ pixels} = 4.7''</math>) NuSTAR images. The scales were adjusted for better legibility. <b>Left:</b> <math>21' \times 11'</math> image containing PSR J2021+3651 and WR 141 marked with a cross (X) and a plus (+), respectively. The extent of the outer nebula seen by XMM is marked with a dashed line. <b>Right:</b> <math>4' \times 4'</math> image of the inner nebula. PSR J2021+3651 is marked with a cross (X). A dashed circle of radius <math>1'</math> is shown as a reference. . . . .</p>	72
4.3	<p><b>Left:</b> Merged (MOS1 and MOS2), QPB-subtracted, exposure-corrected, and smoothed XMM image in 2 – 6 keV. PSR J2021+3651 and WR 141 are marked with a cross (X) and a plus (+) sign, respectively. The extent of the outer nebula <math>\sim 10'</math> is marked with dashed lines. A “ring” is marked with a dotted line. <b>Right:</b> VLA 20cm image from [161]. The radio nebula extends out to <math>&gt; 20'</math> from PSR J2021+3651. The XMM contours are overlaid in blue. The permission for the use of the image was acquired from AIP Publishing via RightsLink®. . . . .</p>	74

- 4.4 **Left:** Chandra ObsID 8502 and 7603 (black and red crosses, respectively) spectra of PSR J2021+3651. The background is dominant outside of 0.5 – 7 keV. The source spectra were extracted from a circular region with radius 2'' centered at the pulsar. The background spectra were extracted from an annulus region with radii 2 – 4'' centered at the pulsar. **Middle:** Chandra ObsID 8502 (black) and 7603 (red), XMM MOS1 (green) and MOS2 (blue), NuSTAR FPMA (magenta) and FPMB (cyan) spectra of the inner nebula. The background is dominant outside of 0.5 – 7 keV for Chandra, 0.5 – 8 keV for XMM, and 3 – 20 keV for NuSTAR. The source spectra were extracted from an annulus region with radii 2 – 20'' for Chandra, a circular region with radius 40'' for XMM, and a circular region with radius 1' for NuSTAR, all centered at PSR J2021+3651. The background spectra were extracted from a 2' × 2' box in a source-free region. For XMM and NuSTAR, the pulsar spectra were subtracted. The best-fit models are displayed as solid lines in both plots. **Right:** XMM MOS1 and MOS2 (green and blue, respectively) spectra of the outer nebula. The source spectra were extracted from the dashed polygon in the Figure 4.3 *left* panel. The Line and continuum backgrounds are dominant below 2 keV and above 6 keV, respectively. The best-fit models are displayed as solid lines. 76
- 4.5 HAWC significance map (2° × 2°) centered at the centroid of eHWC J2019+368. The eHWC J2019+368 flux extraction region is marked with a dashed circle (radius 0.5°). PSR J2021+3651 and Sh 2-104 are marked with a star and a triangle, respectively. The shaded region is the XMM spectrum extraction region of the outer nebula. The dotted line shows the extent of the outer nebula seen by VLA. The angular resolution of HAWC varies depending on the energy and zenith angle. The approximate size of the 68% containment region at 56 TeV (radius 0.2°) is marked with a solid white circle at the top left corner. The HAWC image was obtained from the 3HWC survey public data (<https://data.hawc-observatory.org/datasets/3hwc-survey/fitsmaps.php>), and the VLA nebular extent was estimated from [161]. . . . . 81
- 4.6 The best-fit SED model from Naima. The model parameters are given in Table 2. Synchrotron flux (Sync), inverse Compton flux from the CMB (CMB), infrared emission from the interstellar dust grains (IR), synchrotron self-Compton component (SSC), and total flux are plotted. The SSC flux level is very low and located below the lower bound of the y-axis. Radio, X-ray, and TeV flux data points, and GeV upper limits are overlaid. The residuals are plotted in terms of significance ((data–model) / (1σ uncertainty of data)). . . . . 84

4.7 *Top left:* The SED model for the Dragonfly from the dynamical model. The model parameters are given in Table 3. Radio, X-ray, and TeV flux data points are overlaid. The residuals are plotted in terms of significance  $((\text{data}-\text{model})/(1\sigma \text{ uncertainty of data}))$ . *Top right:* Time evolution of the PWN radius ( $R_{pwn}$ , blue solid line), SNR reverse shock radius ( $R_{RS}$ , orange dashed line), and magnetic field inside the PWN (B field, green dotted line) over the true age from our model (16 kyr). The PWN collided with the SNR reverse shock at  $t_{RS} = 12$  kyr. *Bottom:* Time evolution of the radiation (*left*) and particle (*right*) spectrum of the Dragonfly. 87

5.1 *Left:* A significance map ( $3.5^\circ \times 3.5^\circ$ ) of the region around LHAASO J0621+3755 in 0.3–10 TeV. The source region (86% containment region of 1LHAASO J0622+3754, a circular region with a radius of  $1^\circ$  centered at the centroid of LHAASO J0621+3755) is overlaid with a black solid line. The pixel size is  $0.05^\circ \times 0.05^\circ$ , and the image was smoothed using a Gaussian kernel ( $\sigma = 1$  pixel). *Right:* TeV gamma-ray SED of LHAASO J0621+3755. The 95% VERITAS flux upper limits for a circular region with a radius of  $1^\circ$  from this work (black), LHAASO KM2A flux points and 95% flux upper limit from [148] (blue), LHAASO WCDA and KM2A best-fit power-law spectral models (yellow and red solid lines, respectively) and statistical uncertainties (grey shaded area) for 1LHAASO J0622+3754 are overlaid. The LHAASO flux points, upper limits, spectral models and uncertainties were scaled to the same region size as the VERITAS source region size for comparability. . . . 100

5.2 Observing conditions of the on runs (top row, labeled “on” ) and off runs for the 3D acceptance map (bottom row, labeled “off”). On each row, from the left, the **first plot** is a histogram of elevations (blue bar) and an exposure-weighted Gaussian fit to the histogram (black curve). The mean ( $\mu$ ) and standard deviation ( $\text{std}$ ) of the fit are provided in the figure title. The **second plot** is a scatter plot of elevations (blue dot). The mean and  $(\text{mean} \pm 1\sigma)$  are marked as a red line and a red-shaded region. The **third plot** is a scatter plot of azimuths (blue dot) and the exposure-weighted mean of azimuths (red line). The **last plot** is a histogram of a night sky background (NSB) averaged over a run duration (blue bar). An exposure-weighted Gaussian fit to the histogram is overlaid as a black curve, and the mean ( $\mu$ ) and the standard deviation ( $\sigma$ ) of the fit are provided in the figure title. . . . . 102

5.3	<p>Demonstration of excising a point-like gamma-ray source and filling the excised region with the events from a reflected region. All the sky maps are <math>3.5^\circ \times 3.5^\circ</math>, and the bin size is <math>0.05^\circ \times 0.05^\circ</math>. (c) is a mask map (black is zero, white and orange are one), and all the other maps are count maps whose color bars show the number of counts in each bin. For the counts map, all the gamma-like events were plotted (lowest energy 0.1 TeV, highest energy 9.8 TeV). (a) The bright gamma-ray source in the FoV is Markarian 421. The observation was taken at the <math>0.5^\circ</math> south wobble. (b) Events from a circle with radius <math>0.4^\circ</math> centered at the position of Markarian 421 are excised. (c) The white circle is the excised region, and the orange circles are the reflected regions. All three regions are <math>0.5^\circ</math> offset from the center of the FoV. (d) Events from one of the reflected regions are plotted. (e) The events plotted in (d) are copied, and their coordinates are rotated around the center of the FoV such that the events are located at the excised region. (f) The events from (b) and (e) are added to create a blank sky map. . . . .</p>	104
5.4	<p>3D acceptance map in the unit of <math>\text{TeV}^{-1} \text{s}^{-1} \text{sr}^{-1}</math>. Each image is a 2D (detector X and detector Y) acceptance map in each energy bin, as labeled in the figure titles. . . . .</p>	105
5.5	<p>The same plots as Figure 5.2 for the off runs for three mimic datasets (“mimic0–2”). . . . .</p>	106
5.6	<p>The same plots as Figure 5.2 for the off runs for three mimic datasets (“mimic3–5”). . . . .</p>	107
5.7	<p>Mimic datasets 0–2 on each row: the <b>first plot</b> is the distribution of FoV norms of each off run (blue bar) and a Gaussian fit to the distribution (black curve). The numbers on the top right corner are the mean <math>\pm</math> standard deviation of the fit. The <b>second plot</b> is the significance map, and the <b>third plot</b> is the significance distribution from all (FoV) and on (source extraction region) regions as well as a Gaussian fit to the significances from the on region. The mean (<math>\mu</math>) and standard deviation (std) of the fit are labeled on the left top corner of the plot. . . . .</p>	108
5.8	<p>The same plots as Figure 5.7 for mimic datasets 3–5. Note that the significance map and distribution of mimic dataset 5 are after bias correction. . . . .</p>	109
5.9	<p>Bias maps for the six energy bins as labeled in the figure titles. . . . .</p>	110
5.10	<p>The same <b>first</b> and <b>second</b> plots as Figure 5.7 for on runs. The <b>third</b> plot is the significance distribution from all (Fov) and off (FoV minus source extraction region) regions as well as a Gaussian fit to the significances from the off region. Note that the significance map and distribution are after bias correction. . . . .</p>	110

5.11 *Left:* Mosaiced, background-subtracted, and exposure-corrected image of the XMM-Newton FoV in 2–7 keV. The white circle (radius 10' centered at PSR J0622+3749) marks the source region from which the flux upper limit for a putative halo was calculated. The location of PSR J0622+3749 and the centroid of LHAASO J0621+3755 are marked with a white star and a white cross, respectively. *Right:* Observation ID 923400101 MOS2 counts map in 0.2–3 keV around PSR J0622+3749 ( $0.2^\circ \times 0.2^\circ$ ). The source and background regions for the pulsar spectrum presented in [210] are marked with solid circle and dashed box, respectively. . . . . 113

5.12 Multiwavelength SED model for LHAASO J0621+3755 as a pulsar halo [210]. . . 113

5.13 The sensitivity curves for different gamma-ray experiments ( $5\sigma$  detection of a point-like source). . . . . 119

## List of Tables

3.1	List of archival and new observations . . . . .	52
3.2	Best-fit parameters for the synchrotron cooling and injection model . . . . .	60
4.1	Summary of X-ray spectral analysis results . . . . .	78
2	Best-fit SED model parameters using Naima . . . . .	83
3	SED model parameters using the dynamical model . . . . .	85
4.4	Comparison between PeVatron pulsar wind nebulae . . . . .	88
5.1	PSR J0622+3749, Geminga, and Monogem pulsar properties. . . . .	98

## Acronyms

- CMB** Cosmic microwave background. 23
- CR** Cosmic ray. 1
- CTAO** Cherenkov Telescope Observatory. 91
- CXB** Cosmic X-ray background. 41
- DSA** Diffusive shock acceleration. 2
- EASA** Extensive Air Shower Array. 48
- EPIC** European Photon Imaging Camera. 41
- FOV** Field of view. 40
- FWHM** Full width half maximum. 41
- GBO** Green Bank Observatory. 57
- H.E.S.S.** High Energy Stereoscopic System. 48
- HAWC** High-Altitude Water Cherenkov. 48
- HPD** Half power diameter. 41
- IACT** Imaging atmospheric Cherenkov telescope. 44
- IR** Infrared. 23
- ISM** Interstellar medium. 19
- IXPE** Imaging X-ray Polarimetry Explorer. 57
- KM2A** Kilometer Square Array. 48
- LAT** Large Area Telescope. 42
- LHAASO** Large High-Altitude Air Shower Observatory. 3

**MAGIC** Major Atmospheric Gamma Imaging Cherenkov Telescopes. 48

**mNLDSA** Modified nonlinear diffusive shock acceleration. 17

**NLDSA** Nonlinear diffusive shock acceleration. 16

**NuSTAR** Nuclear Spectroscopic Telescope Array. 4

**NuSTARDAS** NuSTAR Data Analysis Software. 52

**PMT** Photomultiplier tube. 48

**PWN** Pulsar wind nebula. 4

**QPB** Quiescent particle background. 73

**SED** Spectral energy distribution. 28

**SNR** Supernova remnant. 4

**SP** Soft proton. 69

**SWCX** Solar wind charge exchange. 73

**SWG0** Southern Wide-field Gamma-ray Observatory. 91

**UHE** Ultra-high-energy (photon energy  $> 100$  TeV). 3

**UV** Ultraviolet. 23

**VERITAS** Very Energetic Radiation Imaging Telescope Array System. 4

**VHE** Very-high-energy (photon energy  $> 100$  GeV). 3

**WCDA** Water Cherenkov Detector Array. 48

**WFCTA** Wide Field of View Cherenkov Telescope Array. 48

**XMM-ESAS** XMM-Newton Extended Source Analysis Software. 69

## Acknowledgements

I was privileged to be advised by the three best mentors during my PhD: Professor Chuck Hailey, Professor Reshmi Mukherjee, and Dr. Kaya Mori.

Chuck has become my academic father – my harshest critic, but also my fiercest supporter.

Despite being one of the busiest men in the world, he always made his students his top priority.

He questioned every aspect of my work to ensure I understood the science down to its most fundamental level. Whenever I had a presentation, he gave feedback on every detail, from the title of each slide to the tone of my voice. Striving to surpass his high expectations pushed me to grow beyond what I thought I was capable of, not to mention that his hard-earned approval was the most rewarding part of all. A pioneer in his field, he leads by example – always present, always working, never watching from a throne. His words are a torch I will carry throughout my career: "There will always be people who say that your idea won't work. Don't be discouraged by them. If you believe in it, then keep pushing. And I think your idea is fantastic."

Reshmi has become my academic mother, who fostered a thriving scientific ecosystem that I was fortunate to be part of. Whenever I faced difficulties, she would check in thoughtfully, provide what she could, and connect me with those who could offer what she could not. She is always eager to learn from anyone and to share her passion for science with everyone. An enthusiastic advocate for undergraduate research, she trained her graduate students to become good mentors of undergraduates and encouraged us to grow alongside our mentees. She has built – and continues to expand – a warm and healthy community around her, within and beyond Columbia:

a safe place where people support each other and collaborate for bigger and better science. Her genuine care and love for both science and people taught me a lifelong lesson: we are humans before scientists, and we can go farther if we go together.

Kaya has become my academic uncle, who rolled up his sleeves and raised me as a researcher. Of all my mentors, he saw me at the closest distance, witnessing every step of my growth. His door (just one away from mine) was always open; we often spent hours discussing the scientific and technical details of my project, the progress of our papers, the past, present, and future of our field, or astro-politics. By assisting this master writer in numerous observing proposals, I learned how an ambitious idea is shaped into a compelling proposal. He actively introduced me to opportunities that helped me become more visible, connect with fellow scientists, and expand my perspective. Watching him mentor undergraduates with patience, trust, and personalized guidance taught me how to become a better mentor myself. The energy he radiates through his limitless curiosity and vigorous pursuit of science has left a permanent mark on me – a reminder to keep asking questions and pushing boundaries.

Chuck, Reshmi, and Kaya not only provided exceptional mentorship but also gifted me an academic family – lifelong friends and collaborators who make me feel grounded in academia. I couldn't have completed the gamma-ray part of my dissertation without Ruo-Yu Shang, a rigorous and fearless scientist and truly the best postdoc I could have asked for. He always offered technical guidance and emotional encouragement whenever I needed it, setting a model I hope to follow as a postdoc myself. I am also grateful to Colin Adams and Svanik Tandon, my academic siblings on the gamma-ray side and dear friends. Colin was a generous mentor, an outstanding teacher, and a genuinely good person whose care for others and commitment to doing the right thing deeply inspired me. Svanik, a kind and driven scientist and a great mentor to undergraduates, brought tireless positive energy into the group. The time the four of us spent together – discussing science or grabbing lunch and debating politics, history, and culture – remains among the most precious moments of my graduate life. I also thank Massimo Capasso and Deivid Ribeiro, who were once kind mentors and are now good friends. Gabriel Bridges and

Shifra Mandel, my academic siblings on the X-ray side, are two other passionate and fierce scientists. They motivated me to learn faster and think harder, and provided scientific and emotional support that meant the world to me. Undergraduate students were a crucial part of my PhD. I was lucky to work with many brilliant, bright, and passionate students. Among them, I thank my direct mentees – Sarah Silverman, Claudia Tang, Lela Spira-Savett, Lain Brewer, and Jon Kwong – for their hard work and for giving me the chance to improve as a mentor.

I extend my gratitude to my close collaborators – Yosi Gelfand, Samar Safi-Harb, Hongjun An, Brian Grefenstette, Silvia Manconi, and many others – and to members of the VERITAS collaboration, particularly Brian Humensky, Jamie Holder, Manel Errando, Sajan Kumar, Matthew Lundy, and Anne Duerr, for their guidance and collaboration. I am grateful for the friendships with Moaz Abdelmaguid, Jaegeun Park, Chanho Kim, and Isabel Sander, which began through co-authorship. It has been a joy to witness each of us grow from students into independent researchers.

I was able to run at full speed in my professional life only because of the love and care I received in my personal life. I thank Ilia Komissarov for running the race of graduate school with me, and for always being right by my side to double the joy and lighten the load. I am also grateful to Taehee Jeong and Seon-mi Ahn for their unwavering support and friendship across continents and time zones. The camaraderie among my cohort and friends in the Columbia Physics PhD program – the drinks we shared and Friendsgivings we celebrated – was an oasis in my busy days, and something I am deeply thankful for.

I cannot think of who I am now without the unending love and support of my family. I moved to the U.S. nine years ago, leaving them behind in my hometown, Seoul. Since then, I have only been able to visit every two to three years, and we speak on the phone once a week or two. I am not usually homesick, but whenever life hands me a lemon, I miss them terribly. My family has lived in Korea their entire lives, and their world is far from science or academia. Now, I understand the confusion and worry they must have felt when I left my home, my family, and my career to move to a foreign country and pursue a dream in an unfamiliar field. Yet they embraced

me, tried to understand my work, and supported me in every way they could. They have always been my biggest fans, and their pride in me is more rewarding than any other achievement. My parents, Kwang-sik Woo and Jeongwon Lee, raised me to be honest and responsible, to do my best no matter what, to care for those around me, and to be grateful always. Those values have been the anchor I have held onto – the source of strength that allowed me to build a new home in a new country and a new field. It is the greatest gift I could have been given, and I am endlessly thankful to them for it. My sister, Seo-yeon, and my brother, Hee-young, are the reason I can be far from our parents without constant worry. I am deeply grateful to them for supporting our parents up close while managing their own lives, and for always cheering me on from afar. My journey in physics began at Indiana University in Bloomington, where I audited classes in the physics and math departments. Professor Emilie Passemar, Mike Snow, Scott Wissink, Sima Setayeshgar, and many others went out of their way to help me follow my passion. I cannot thank them enough for their extraordinary support, which made it possible for me to pursue this new career. I also thank Dr. Yunchang Shin, Professor Yannis Semertzidis, Dr. Dong-ok Kim, and Dr. Younggeun Kim for their guidance during my time at the Center for Axion and Precision Physics Research, Institute for Basic Science.

I close this long statement of gratitude with Patty and John Kelley, who became my second parents and made me feel at home when I first came to the U.S., and Michael Hartwell – the best English tutor, writer, jack-of-all-trades, and a warm-hearted friend.

Completing my PhD holds a special meaning for me – far beyond the degree itself. I now look forward to running my own race as an independent researcher, carrying forward the mentorship, friendship, and spirit of collaboration that shaped me, and continuing to contribute to physics and the academic community.

## Chapter 1: Introduction and Background

Cosmic rays (CRs) are relativistic charged particles traveling the universe. Since Viktor Hess discovered CRs in 1912 [1], numerous CR experiments led to the discovery of new subatomic particle species such as the positron, muon, pion, and kaon. This aspect of the CR experiment evolved into collider experiments that control particles with up to TeV energies, eventually becoming a foundation of the empire of particle physics. On the other hand, spectral measurements of local CRs show the ample presence of CRs with energies much greater than that achievable in colliders. Given that it was already highly challenging to accelerate particles to TeV energies in colliders, the evidence of much more powerful particle accelerators in the universe directed scientists' attention to outer space for physics that cannot be studied on Earth. Where are CRs coming from? What is the mechanism behind the particle acceleration to such high energies? How do such energetic particles behave in extreme cosmic environments? Does it change our knowledge of fundamental physics? While the field of astroparticle physics has grown to answer those questions using the CRs detected on or near Earth, high-energy (X-ray and gamma-ray) astrophysics emerged as a unique window to the CR sources inside and outside of our galaxy, bringing the findings from the local and farther side of the universe.

Many experiments have measured the CR composition and spectrum with unprecedented precision (see Figure 1.1). CRs consist of 90% protons, 9% helium nuclei, 1% electrons, and even smaller amounts of heavier nuclei, antiprotons, and positrons. The all-particle CR energy spectrum is well described as a smooth power-law of energy ( $dN/dE \propto E^{-\Gamma}$ ) with features where the spectral index  $\Gamma$  changes. Up to the “knee” at  $\sim 3$  PeV,  $\Gamma \sim 2.7$ . CRs with energies below the knee are believed to originate in our galaxy. Above the “ankle” at  $\sim 1$  EeV,  $\Gamma \sim 2.7$ . CRs with energies above the ankle are believed to originate outside our galaxy. The spectrum is steeper between the knee and ankle with  $\Gamma \sim 3-3.3$ . CRs with energies in this range are believed to be a mixture of

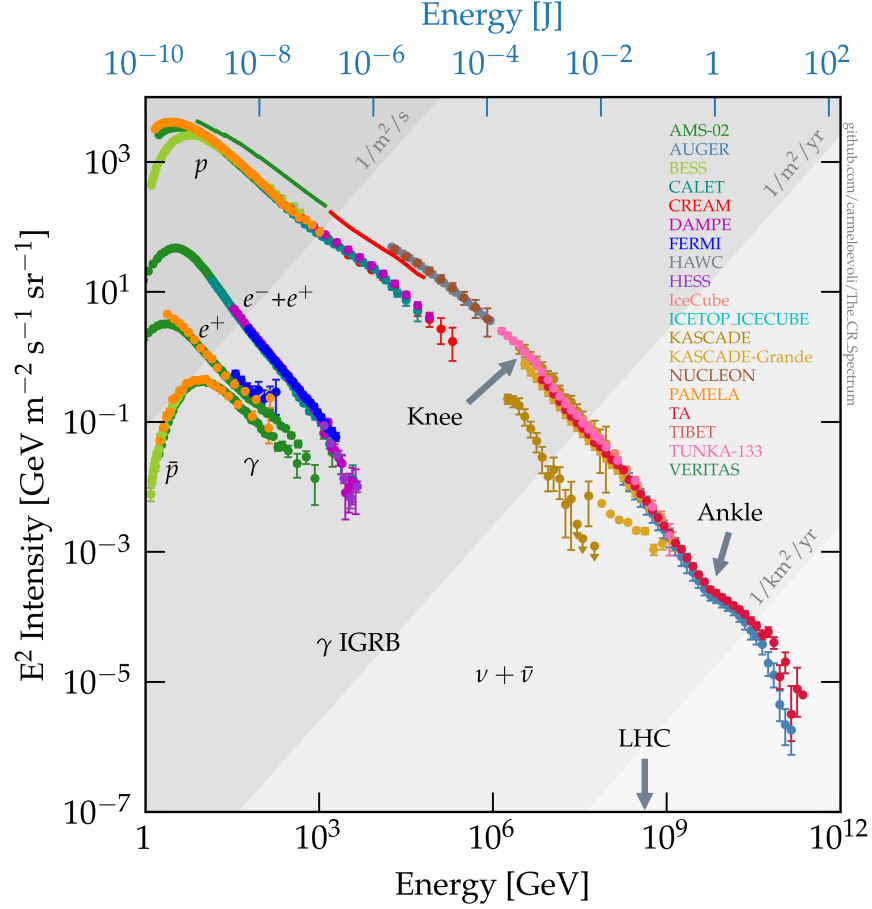


Figure 1.1: The CR spectrum measured by different experiments [2].

Galactic and extragalactic origin.

One can write down a simplified transport equation for CRs [3, 4, 5]:

$$\frac{\partial f}{\partial t} = \vec{\nabla} \cdot (D \vec{\nabla} f) + Q - \frac{f}{\tau_{loss}}, \quad (1.1)$$

where  $f = f(\vec{p}, \vec{x}, t)$  is the CR density in phase space, and each term on the right-hand side represents the three essential CR processes: diffusion, acceleration (§1.2), and cooling (§1.3).

CRs are deflected by diffusion, i.e., scattering with universal magnetic irregularities. The strength of diffusion is characterized by the diffusion coefficient  $D$ . Diffusion plays a crucial role in CR acceleration, among the most famous mechanisms of which is diffusive shock acceleration (DSA). Accelerated CRs have power-law spectra in energy  $Q \propto E^{-\Gamma}$  whose index  $\Gamma$  depends on

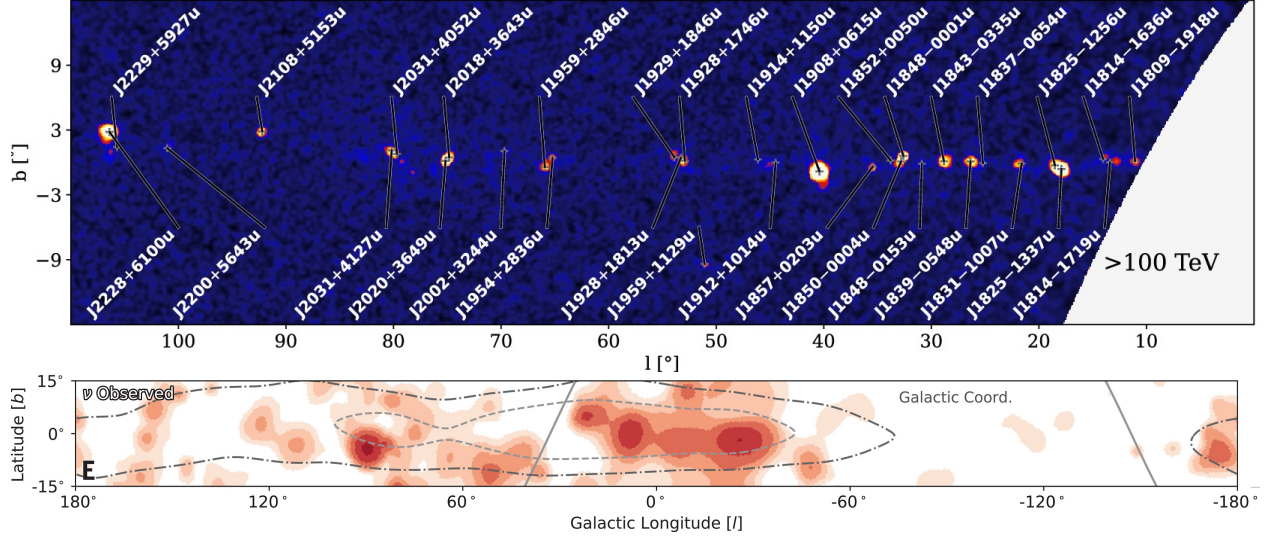


Figure 1.2: **Top**: Galactic UHE sources detected by LHAASO [6]. **Bottom**: TeV–PeV neutrino emission along the Galactic Plane detected by IceCube [7].

the acceleration mechanism and environment. CRs not only gain but also lose energy by interacting with their surroundings. The energy loss is often characterized by  $\tau_{loss}$ , the time it takes for a CR to lose a significant part of its energy. Part of the lost energy is converted into neutral particles such as photons and neutrinos. Since diffusion erases the directional information of CRs, these neutral byproducts that travel along the straight line are the only way to locate the CR accelerators. In addition, the spectra of these neutral particles bear information about their parent CR spectra and the surroundings in which they were produced.

The most energetic Galactic CR protons and electrons with PeV energies emit ultra-high-energy (UHE,  $> 100$  TeV) gamma rays by pion decay and inverse Compton scattering, respectively. The same pion decay process also produces neutrinos with energies about half the gamma-ray energies. Large High-Altitude Air Shower Observatory (LHAASO [8]), a UHE observatory with unprecedented sensitivity up to PeV energies, recently reported the detection of 43 UHE sources in our galaxy [6] (*top* panel of Figure 1.2). A recent detection of TeV–PeV neutrino emission from the Galactic Plane by a neutrino observatory IceCube [7] (*bottom* panel of Figure 1.2) further confirms the presence of the most energetic accelerators of PeV CRs in our galaxy, the Galactic PeVatrons. Very-high-energy (VHE,  $> 100$  GeV) observatories, such as Very Energetic Radiation

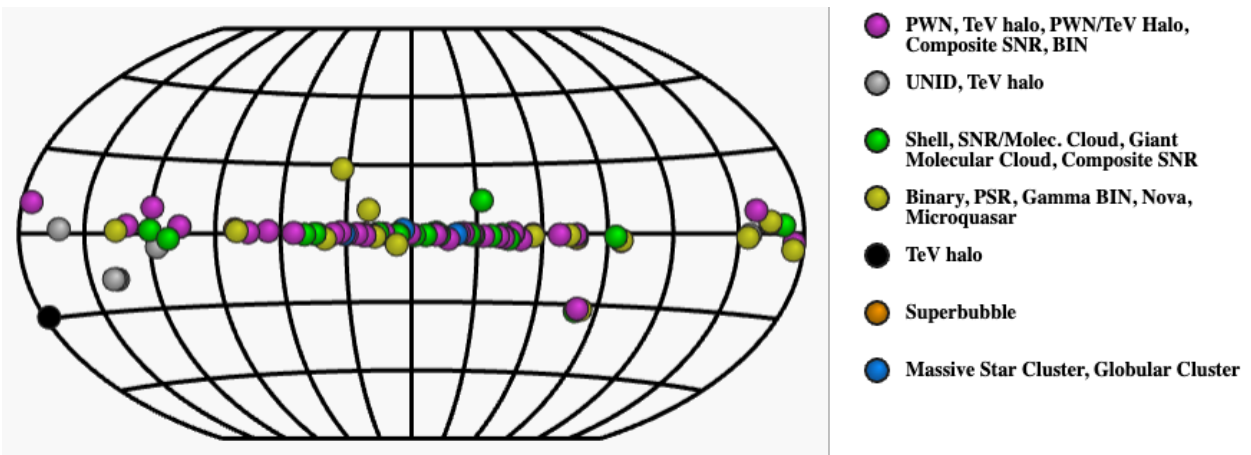


Figure 1.3: Galactic TeV sources (image credit: TeVCat (<http://tevcat2.uchicago.edu/>)).

Imaging Telescope Array System (VERITAS [9]), complement UHE observatories in measuring broadband gamma-ray spectra of Galactic PeVatrons as well as resolve their morphology with superior angular resolution. However, one cannot disentangle the information about CR species (electron or proton), CR spectra, and environmental parameters such as ambient photon and matter density from gamma-ray spectra alone. To do so requires a multiwavelength approach. In particular, the CR electrons probed by the VHE and UHE observatories emit synchrotron radiation in the hard X-ray band above  $\sim 10$  keV. As the only focusing broadband hard X-ray telescope, the Nuclear Spectroscopic Telescope Array (NuSTAR [10]) provides the missing puzzle piece for a complete picture of Galactic PeVatrons.

Nearly a hundred galactic gamma-ray sources have been detected in the TeV range (Figure 1.3). The only identified Galactic PeVatron is the Crab nebula, a pulsar wind nebula (PWN) around a young pulsar. About half of the TeV sources are likely associated with energetic pulsars and their PWNe, the most promising Galactic leptonic (CR electron) PeVatrons. Supernova remnants (SNRs) are historically and theoretically believed to be the Galactic hadronic (CR proton) PeVatrons; yet SNRs have not been observed in the UHE range.

In this dissertation, I aim to find the origin of the most energetic Galactic CRs by observing Galactic PeVatron candidates with X-ray and gamma-ray instruments. The dissertation is struc-

tured as follows. In the rest of this chapter, the theoretical background of CR diffusion (§1.1), acceleration (§1.2), and cooling (§1.3) as well as the Galactic PeVatron candidates (§1.4) is laid out. In Chapter 2, the instruments used for this work are introduced. Chapters 3–5 present the observation and interpretation of the Galactic PeVatron candidates in three different evolutionary stages: a young SNR (Cassiopeia A; Chapter 3), a middle-aged PWN (the Dragonfly PWN; Chapter 4), and a halo around an old pulsar (LHAASO J0621+3755; Chapter 5). The dissertation concludes in Chapter 6 with remarks on the future prospects of the Galactic PeVatron search.

## 1.1 Cosmic ray diffusion

Our galaxy is filled with irregular magnetic fields. The electromagnetic interaction between these magnetic irregularities and CRs causes diffusion, i.e., deviation from the initial CR momentum. Such deviation averages to zero, but its mean square is nonzero, having a macroscopic impact on CR transport.

In an ordered magnetic field, a charged particle simply gyrates along the magnetic field line. For a magnetic field  $\vec{B} = (0, 0, B_0)$  and a charged particle with the charge  $q$ , mass  $m$  and velocity  $\vec{v} = (v_x, v_y, v_z)$ , Lorentz’s force law  $d\vec{p}/dt = q\vec{v} \times \vec{B}$  gives

$$\begin{aligned} \frac{dv_z}{dt} &= 0 \Rightarrow v_z(t) = v_z(0) = v_{\parallel} = v \cos \theta = v\mu \\ \frac{d^2 v_{x,y}}{dt^2} &= -\left(\frac{qB_0}{\gamma m}\right)^2 v_{x,y} = -\Omega^2 v_{x,y} \Rightarrow v_x(t) = v_{\perp} \cos(\phi - \Omega t), \\ v_y(t) &= v_{\perp} \sin(\phi - \Omega t), \end{aligned} \tag{1.2}$$

where  $\theta$  is the “pitch angle”, the angle between  $\vec{B}$  and  $\vec{v}$ ,  $\Omega = qB_0/\gamma m$  is the gyrofrequency,  $v_{\perp} = v \sin \theta = v\sqrt{1 - \mu^2}$  is the particle velocity perpendicular to the magnetic field, and  $\phi$  defines the initial condition such that  $v_x(0) = v_{\perp} \cos \phi$  and  $v_y(0) = v_{\perp} \sin \phi$ . Note that the pitch angle, as well as the particle’s motion parallel to the magnetic field, do not change. Diffusion does not occur in an ordered magnetic field.

Let us consider a small perturbation in the magnetic field perpendicular to the ordered magnetic

field:  $\vec{B} = \vec{B}_0 + \delta\vec{B}$ , where  $\vec{B}_0 = (0, 0, B_0)$ ,  $\delta\vec{B} = (\delta B_x, \delta B_y, 0)$ , and  $B_0 \gg \delta B$ , as in Alfvén waves.

In the wave frame, where there are no electric fields, Lorentz's force law reads

$$\begin{aligned}\gamma m \frac{dv_x}{dt} &= q(v_y B_0 - v_z \delta B_y), \\ \gamma m \frac{dv_y}{dt} &= q(v_z \delta B_x - v_x B_0), \\ \gamma m \frac{dv_z}{dt} &= q(v_x \delta B_y - v_y \delta B_x).\end{aligned}\tag{1.3}$$

$v_{x,y}$  is weakly perturbed  $\sim O(\delta B)$ . Now,  $dv_z/dt$  is nonzero, while  $\gamma$  is conserved, so  $d\mu/dt$  should be nonzero. Keeping only the terms  $\sim O(\delta B)$  for  $dv_z/dt$ , i.e., taking the unperturbed solutions for  $v_{x,y}$ ,

$$\gamma m v \frac{dv_z}{dt} = \gamma m v \frac{d\mu}{dt} = q v_{\perp} [\delta B_y \cos(\phi - \Omega t) - \delta B_x \sin(\phi - \Omega t)].\tag{1.4}$$

Assuming a circularly polarized wave,

$$\begin{aligned}\delta B_y &= \delta B \cos(kz + \psi), \quad \delta B_x = \pm \delta B \sin(kz + \psi) \\ \Rightarrow \gamma m v \frac{d\mu}{dt} &= q v_{\perp} \delta B [\cos(kz + \psi) \cos(\phi - \Omega t) \pm \sin(kz + \psi) \sin(\phi - \Omega t)] \\ &= q v_{\perp} \delta B \cos(\phi - \Omega t \pm kz \pm \psi).\end{aligned}\tag{1.5}$$

Approximating  $z \approx v_{\parallel} t = v \mu t$  for the unperturbed travel distance,

$$\frac{d\mu}{dt} = \frac{q B_0}{\gamma m} \frac{\delta B}{B_0} \sqrt{1 - \mu^2} \cos[\phi \pm \psi \pm (k v \mu \mp \Omega) t].\tag{1.6}$$

As anticipated, the pitch angle diffusion averages to zero:  $\langle \Delta\mu \rangle = \lim_{T \rightarrow \infty} \int_0^T (d\mu/dt) dt = 0$ .

However, the mean square of the pitch angle does not vanish:

$$\begin{aligned}
\langle \Delta\mu\Delta\mu \rangle &= \Omega^2 \left( \frac{\delta B}{B_0} \right)^2 (1 - \mu^2) \lim_{T \rightarrow \infty} \int_0^{2\pi} \frac{d\phi}{2\pi} \int_0^T dt \times \\
&\quad \int_0^T dt' \cos [\phi \pm \psi \pm (kv\mu \mp \Omega)t] \cos [\phi \pm \psi \pm (kv\mu \mp \Omega)t'] \\
&= \Omega^2 \left( \frac{\delta B}{B_0} \right)^2 (1 - \mu^2) \frac{1}{2} \lim_{T \rightarrow \infty} \int_0^T dt \int_0^T dt' \cos [(kv\mu \mp \Omega)(t - t')] \\
&= \pi \Omega^2 \left( \frac{\delta B}{B_0} \right)^2 (1 - \mu^2) T \delta(kv\mu \mp \Omega).
\end{aligned} \tag{1.7}$$

Finally, the pitch angle diffusion coefficient is defined as [4]

$$D_{\mu\mu} = \frac{1}{2} \langle \frac{\Delta\mu\Delta\mu}{T} \rangle = \frac{\pi}{2} \left( \frac{\delta B}{B_0} \right)^2 (1 - \mu^2) \Omega |k_{res}| \delta(k - k_{res}). \tag{1.8}$$

The pitch angle diffusion is resonant for the perturbation wavenumber  $k_{res} = \pm \Omega/v\mu$  due to the Dirac delta function. For  $\mu = 1$ , this resonance condition becomes  $k_{res}^{-1} = r_L$ , where  $r_L$  is the Larmor radius of the charged particle. If the perturbation has a much smaller length scale than the particle Larmor radius,  $k^{-1} \ll r_L$ , the perturbation will average to zero over a gyration cycle, and so will the pitch angle diffusion. If the perturbation has a much larger length scale than the particle Larmor radius,  $k^{-1} \gg r_L$ , the particle will glide along the perturbation without a significant change in the pitch angle.

Intuitively, efficient pitch angle diffusion indicates inhibited propagation and, hence, suppressed spatial diffusion. For a spectrum of perturbation, and noting that  $\Delta\mu = \Delta(\cos \theta) = \sin \theta \Delta\theta = \sqrt{1 - \mu^2} \Delta\theta$ , the diffusion coefficient for  $\theta$  is

$$D_{\theta\theta} = \frac{1}{2} \langle \frac{\Delta\theta\Delta\theta}{T} \rangle = \frac{D_{\mu\mu}}{1 - \mu^2} = \frac{\pi}{2} \Omega \int dk \left( \frac{\delta B(k)}{B_0} \right)^2 |k_{res}| \delta(k - k_{res}) = \frac{\pi}{2} \Omega \mathcal{F}(k_{res}), \tag{1.9}$$

where  $\mathcal{F}(k_{res})$  is a dimensionless power spectrum evaluated at  $k = k_{res}$ , which represents the power of pitch angle diffusion. One can approximate the time it takes for the particle pitch angle to change by one radian  $\tau_{rev} \sim D_{\theta\theta}^{-1}$ . Then spatial diffusion can be defined in terms of the distance

traveled during  $\tau_{rev}$ , assuming isotropy such that  $3D_{zz}\tau_{rev} = (v\tau_{rev})^2$  [4],

$$D_{zz}(p) = \frac{1}{3}v^2\tau_{rev} = \frac{2}{3\pi} \frac{v^2}{\Omega(p)\mathcal{F}(k_{res})} = \frac{2}{3\pi} \frac{vr_L(p)}{\mathcal{F}(k_{res})}. \quad (1.10)$$

As expected, spatial diffusion is inversely proportional to the power of pitch angle diffusion. Phenomenologically, a power-law form of the particle momentum  $p$  is adopted for  $\mathcal{F}$ . This results in the particle energy dependence of spatial diffusion coefficient,  $D \propto E^\delta$ , where some of the widely used values for  $\delta$  are  $\delta = 1$  (Bohm regime),  $1/3$  (Kolmogorov regime),  $1/2$  (Kraichnan regime).

Clear evidence of CR diffusion in our galaxy is the ratio of secondary to primary CRs. Light elements such as Li, Be, and B (“secondary” CRs) can be formed only through the spallation of heavier elements such as C and O (“primary” CRs). The production rate of secondary CRs is  $q_s(E) \sim n_p(E)n_{ISM}\sigma c$ , where  $n_p(E)$  and  $n_{ISM} \sim 1 \text{ cm}^{-3}$  are the primary CR and ISM number density, respectively,  $\sigma$  is the spallation cross-section, and  $c$  is the speed of light. Then the number density of secondary CRs is  $n_s(E) = q_s(E)\tau_{res}$  where  $\tau_{res}$  is the CR residence time in the Galactic disc. The secondary-to-primary ratio  $n_s/n_p \sim \tau_{res}n_{ISM}\sigma c$ , when compared with the measurements such as the B/C ratio, yields  $\tau_{res} \sim$  a few Myr [11]. The distance traveled by CRs during this time,  $\tau_{res}c \sim$  a few Mpc, far exceeds the size of our galaxy of a few tens kpc, indicating that the motion of CRs is diffusive rather than ballistic.

Let us consider the conventional picture of CRs in our galaxy. Figure 1.4 shows a schematic diagram of our galaxy comprising a thin galactic disc and a galactic halo above and beneath the disc. It is a cylinder where the disc lies at  $z = 0$ , and the halo extends out to  $z = \pm H$ . The disc has a surface area  $2\pi R_d^2$  over which CR sources are uniformly distributed. CRs diffuse uniformly within the halo. For the steady state, Equation 1.1 becomes

$$-\frac{\partial}{\partial z}D(p)\frac{\partial f(p,z)}{\partial z} = Q(p,z) - \frac{f(p,z)}{\tau_{loss}(p)}. \quad (1.11)$$

Let us assume the CR sources are impulsive events, each of which produces a CR spectrum

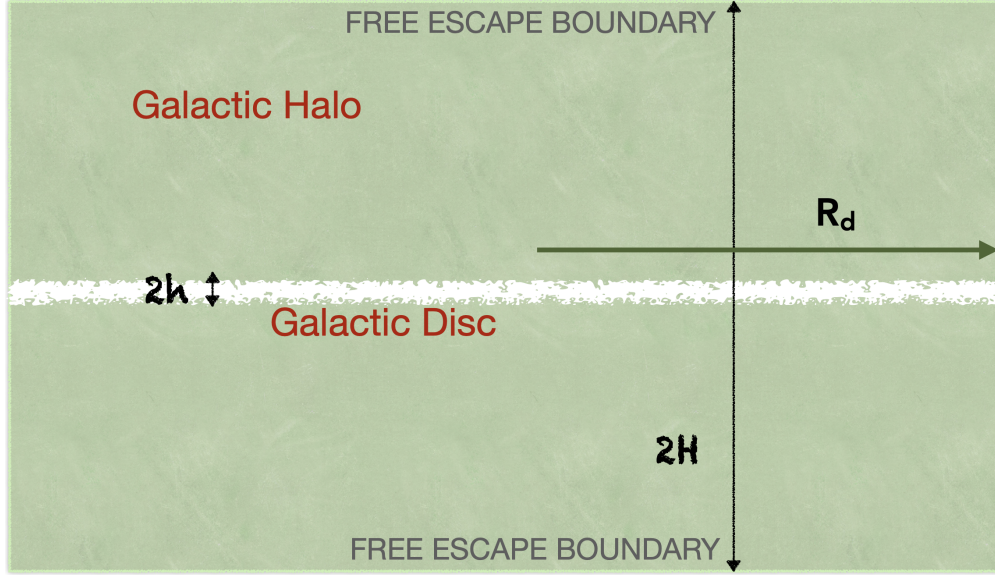


Figure 1.4: Schematic diagram of our galaxy [4]

$N(p)$  and occurs at a rate  $R$ , such that  $Q(p, z) = N(p)R\delta(z)/2\pi R_d^2$ . CRs are allowed to escape at the edge of the halo freely, i.e.,  $f(p, z = |H|) = 0$ . For  $z > 0$ ,

$$\frac{\partial^2 f(p, z)}{\partial z^2} = \frac{f(p, z)}{D(p)\tau_{loss}(p)} \Rightarrow$$

$$f(p, z) = f_+(p, 0) \exp\left(\frac{z}{\sqrt{D(p)\tau_{loss}(p)}}\right) + f_-(p, 0) \exp\left(\frac{-z}{\sqrt{D(p)\tau_{loss}(p)}}\right). \quad (1.12)$$

Imposing the free-escape boundary condition,

$$f(p, H) = 0 \Rightarrow f_+(p, 0) = -f_-(p, 0) \exp\left(\frac{-2H}{\sqrt{D(p)\tau_{loss}(p)}}\right). \quad (1.13)$$

Integrating Equation 1.11 over a narrow region around  $z = 0$  and utilizing the symmetry along the  $z$  axis,

$$\begin{aligned}
-2D(p) \frac{\partial f(p, z)}{\partial z} \Big|_{z=+0} &= \frac{2D(p)}{\sqrt{D(p)\tau_{loss}(p)}} f_-(p, 0) \left[ 1 + \exp\left(\frac{-2H}{\sqrt{D(p)\tau_{loss}(p)}}\right) \right] = \frac{N(p)R}{2\pi R_d^2} \\
\Rightarrow f_-(p, 0) &= \frac{N(p)R}{2\pi R_d^2} \frac{\tau_{loss}(p)}{2\sqrt{D(p)\tau_{loss}(p)}} \left[ 1 + \exp\left(\frac{-2H}{\sqrt{D(p)\tau_{loss}(p)}}\right) \right]^{-1}.
\end{aligned} \tag{1.14}$$

Then, the CR density on the disc is

$$f(p, 0) = f_+(p, 0) + f_-(p, 0) = f_-(p, 0) \left[ 1 - \exp\left(\frac{-2H}{\sqrt{D(p)\tau_{loss}(p)}}\right) \right] = \frac{N(p)R}{2\pi R_d^2} \frac{\tau_{loss}(p)}{2\sqrt{D(p)\tau_{loss}(p)}}, \tag{1.15}$$

where, in the last step,  $H/\sqrt{D\tau_{loss}} = \sqrt{\tau_{esc}/\tau_{loss}} \gg 1$  was assumed to account for the case where CRs experience significant energy loss before escaping our galaxy (energy loss timescale  $\tau_{loss} \ll$  escape timescale  $\tau_{esc}$ ). Replacing momentum  $p$  with energy  $E$  for ultrarelativistic CRs ( $p \simeq E$ ), and adopting  $D(E) \propto E^\delta$ ,  $N(E) \propto E^{-\Gamma}$  (see §1.2), and  $\tau_{loss} \propto E^{-\xi}$  (see §1.3),  $f(E) \propto E^{-\Gamma-(\delta+\xi)/2}$ . Therefore, the observed CR spectrum is softer than the injected CR spectrum.

## 1.2 Cosmic ray acceleration

### 1.2.1 Second-order Fermi acceleration

Diffusion of charged particles due to magnetic irregularities, or equivalently, scattering of charged particles with a perturbative electromagnetic wave, was introduced by Hannes Alfvén in the context of Alfvén waves. Based on this concept, Enrico Fermi proposed a CR acceleration mechanism [12], now known as the (second-order) Fermi acceleration. This simple but powerful idea is the first and, after 75 years, still the only well-established CR acceleration mechanism, along with numerous variations of its original format that account for more realistic physical conditions and adopt the findings from numerical simulations.

Magnetic fields do not do work, and hence, particle energy is preserved. To increase the energy

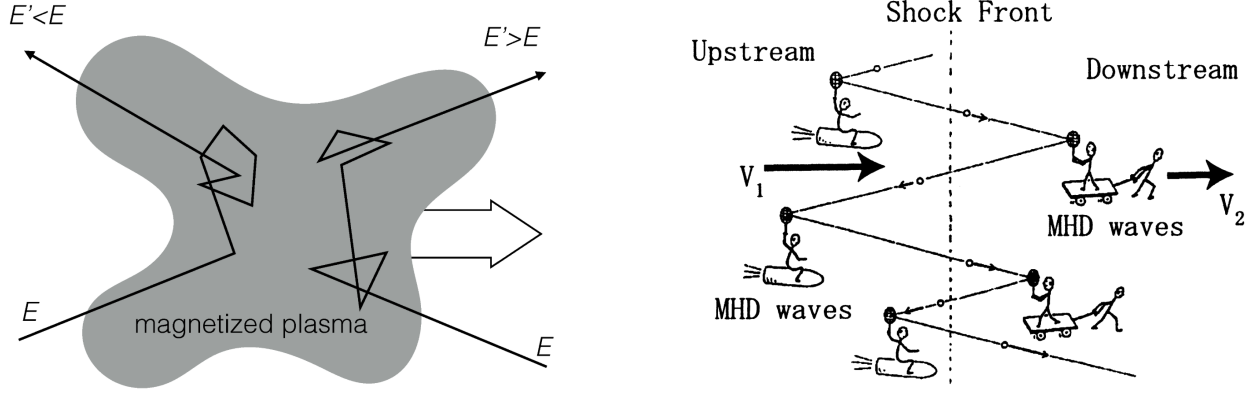


Figure 1.5: Schematic diagrams of the (second-order) Fermi acceleration (*left*, image credit: Juan A. Aguilar) and the DSA (or the first-order Fermi acceleration) (*right*, [13]).

of a particle requires the presence of electric fields. The astrophysical environment is mostly plasma, which does not sustain large-scale electric fields. However, moving magnetic irregularities can induce small-scale electric fields. While, in §1.1, we resided in the wave frame where electric fields vanish, moving back to the lab frame brings electric fields into the picture. This is the ground of the Fermi acceleration mechanism. In the case of Alfvén waves, this induced electric field changes the particle momentum by  $\Delta p/p \sim v_A/c$ , where  $v_A = B_0/\sqrt{\rho\mu_0}$  is the Alfvén velocity in a medium with the density  $\rho$ . If we define a diffusion coefficient for momentum change as  $D_{pp} = \langle \Delta p \Delta p / T \rangle \sim p^2 (v_A/c)^2 / T$ , then the time scale for momentum change  $\tau_{acc} \sim p^2 / D_{pp} \sim T (v_A/c)^{-2}$  ( $\gg T$  in most cases since  $v_A \ll c$ ) indicates that it is a second-order process [4].

As shown in §1.1, changes in the pitch angle could eventually turn the particle around, in which case the magnetic irregularity responsible for such changes is working as a “mirror”. A particle hitting this moving mirror head-on will gain energy, whereas it will lose energy by a tail-on scattering. Let us consider such a magnetic mirror moving at the velocity  $\vec{V} = V\hat{x}$  ( $V \ll c$ ) and a particle moving at the velocity  $\vec{v} = -v\mu\hat{x} - v\sqrt{1-\mu^2}\hat{y}$ , where  $\mu = \cos\theta$  and  $\theta$  is the angle between  $\vec{V}$  and  $\vec{v}$ . The initial particle energy  $E_i$  and momentum  $p_i = E_i v/c^2$  in the lab frame are transformed into the mirror frame as  $E'_i = \gamma(E_i + V p_i \mu)$  and  $p'_{i,x} = \gamma(p_i \mu + E_i V/c^2)$ , where  $\gamma = 1/\sqrt{1 - (V/c)^2}$ . Assuming an elastic scattering with a very massive magnetic mirror compared with the particle, the particle energy and momentum in the mirror frame after the scattering are simply  $E'_f = E'_i$  and

$p'_{f,x} = -p'_{i,x}$ . Back in the lab frame after the scattering,

$$\begin{aligned}
E_f &= \gamma(E'_f - Vp'_{f,x}) = \gamma^2 \left( E_i + 2Vp_i\mu + E_i \frac{V^2}{c^2} \right) = \gamma^2 E_i \left( 1 + \frac{V^2}{c^2} + \frac{2Vv\mu}{c^2} \right) \\
\implies \frac{\Delta E}{E} &= \frac{E_f - E_i}{E_i} \approx 2 \frac{V}{c} \left( \frac{V}{c} + \frac{v\mu}{c} \right) \quad (\gamma \rightarrow 1).
\end{aligned} \tag{1.16}$$

The probability for the pitch angle  $P(\mu)$  is proportional to the relative velocity [14]:

$$\begin{aligned}
P(\mu) &= A \frac{V\mu + v}{1 + vV\mu/c^2} \approx A(V\mu + c) \quad (V \ll c, v \rightarrow c) \\
\int_{-1}^1 P(\mu) d\mu &= 1 \implies A = \frac{1}{2c} \\
\left\langle \frac{\Delta E}{E} \right\rangle &= \int_{-1}^1 P(\mu) \frac{\Delta E}{E} d\mu = \int_{-1}^1 \frac{V\mu + c}{2c} \frac{2V}{c} \left( \frac{V}{c} + \frac{v\mu}{c} \right) d\mu = \frac{8}{3} \left( \frac{V}{c} \right)^2.
\end{aligned} \tag{1.17}$$

As found for  $\tau_{acc}$ , the average energy gain is in the second order of  $V/c$ , so the name ‘‘second-order’’ Fermi acceleration. As mentioned for  $\tau_{acc}$ ,  $v_A \ll c$  in most cases, such as interstellar magnetic turbulence. Therefore, energy gain by the second-order Fermi acceleration is very inefficient. This is because the scattering is not always head-on. If all scatterings are head-on, energy gain will be much more efficient.

### 1.2.2 Diffusive shock acceleration (First-order Fermi acceleration)

Purely head-on scattering is made possible across a shock, an extreme phenomenon yet commonly found in the universe. The Fermi acceleration mechanism applied to astrophysical shocks, such as those in SNRs, is referred to as DSA [15, 16, 17, 18, 19]. A shock is a discontinuity in physical properties due to the supersonic motion of a fluid in a medium. In the frame of a 1D shock, one can write down the continuity equations for mass, momentum, and energy that hold in the shock’s upstream (unshocked) and downstream (shocked) separately:

$$\frac{\partial}{\partial x}(\rho u) = 0, \quad \frac{\partial}{\partial x}(\rho u^2 + P) = 0, \quad \frac{\partial}{\partial x} \left( \frac{1}{2} \rho u^3 + \frac{\gamma}{\gamma - 1} P u \right), \tag{1.18}$$

where  $\rho$ ,  $u$ ,  $P$ , and  $\gamma$  are the mass density, velocity, pressure, and the adiabatic index of the fluid. With the upstream and downstream quantities denoted by the subscripts 1 and 2, respectively, the discontinuity of these quantities at the shock is described by the Rankine-Hugoniot jump conditions:

$$\begin{aligned}
R \equiv \frac{\rho_2}{\rho_1} = \frac{u_1}{u_2} &= \frac{(\gamma + 1)\mathcal{M}_1^2}{(\gamma - 1)\mathcal{M}_1^2 + 2} \rightarrow \frac{\gamma + 1}{\gamma - 1}, \\
\frac{P_2}{P_1} &= \frac{2\gamma\mathcal{M}_1^2}{\gamma + 1} - \frac{\gamma - 1}{\gamma + 1} \rightarrow \frac{2\gamma\mathcal{M}_1^2}{\gamma + 1}, \\
\frac{T_2}{T_1} &= \frac{[2\gamma\mathcal{M}_1^2 - (\gamma - 1)][(\gamma - 1)\mathcal{M}_1^2 + 2]}{(\gamma + 1)^2\mathcal{M}_1^2} \rightarrow \frac{2\gamma\mathcal{M}_1^2(\gamma - 1)}{(\gamma + 1)^2},
\end{aligned} \tag{1.19}$$

where  $\mathcal{M} = u/c_s$  is the sonic Mach number,  $c_s = \sqrt{\gamma P/\rho}$  is the sound speed,  $T$  is the temperature, and the equations on the right-hand side of the arrows are for the case of a strong shock ( $\mathcal{M}_1 \gg 1$ ) such as SNR forward shocks. For a monoatomic ideal gas ( $\gamma = 5/3$ ), the compression ratio  $R \rightarrow 4$ .

Let us consider a 1D shock at  $x = 0$  with the upstream (downstream) at  $x < 0$  ( $x > 0$ ). In the shock frame, the upstream (downstream) plasma moves at the velocity  $u_1$  ( $u_2$ ) in the positive  $x$  direction. A particle with the velocity  $v_i \gg u_1$ , energy  $E_i$ , and the pitch angle  $\mu_i = \cos \theta_i$  is in the downstream of this shock. If the particle crosses the shock ( $-1 \leq \mu_i \leq 0$ ) to the upstream, its energy in the upstream frame is  $E'_i = \gamma E_i (1 - V v_i \mu_i / c^2)$ , where  $V = u_1 - u_2$  is the relative velocity between the upstream and downstream plasma, and  $\gamma = 1/\sqrt{1 - (V/c)^2}$ . The particle may be scattered back to the downstream with the velocity  $v'_f$  and pitch angle  $0 \leq \mu'_f \leq 1$  by magnetic irregularities in the upstream. Then, a DSA cycle is completed, and the particle energy in the downstream is

$$E_f = \gamma^2 E_i \left(1 - \frac{V v_i \mu_i}{c^2}\right) \left(1 + \frac{V v'_f \mu'_f}{c^2}\right) \approx \gamma^2 E_i \left(1 - \frac{V \mu_i}{c}\right) \left(1 + \frac{V \mu'_f}{c}\right) \quad (v_i, v_f \rightarrow c). \tag{1.20}$$

Assuming both the upstream and downstream plasma are isotropized, the probabilities for the pitch angles  $P(\mu_i)$  and  $P(\mu'_f)$  are proportional to the particle flux  $Nv\mu$  [14]:

$$\begin{aligned}
P(\mu_i) &= ANv_i\mu_i, & -\int_{-1}^0 P(\mu_i)d\mu_i &= 1 \quad \Rightarrow \quad A = \frac{2}{Nv_i}, & P(\mu_i) &= 2\mu_i \\
P(\mu'_f) &= ANv'_f\mu'_f, & \int_0^1 P(\mu'_f)d\mu'_f &= 1 \quad \Rightarrow \quad A = \frac{2}{Nv'_f}, & P(\mu'_f) &= 2\mu'_f \\
\left\langle \frac{\Delta E}{E} \right\rangle &= -\int_{-1}^0 d\mu_i \int_0^1 d\mu'_f P(\mu_i)P(\mu'_f) \frac{E_f - E_i}{E_i} \\
&= -\int_{-1}^0 d\mu_i \int_0^1 d\mu'_f 4\mu_i\mu'_f \left[ \gamma^2 \left( 1 - \frac{V}{c}\mu_i \right) \left( 1 + \frac{V}{c}\mu'_f \right) - 1 \right] \\
&\approx \frac{4V}{3c} = \frac{4u_1 - u_2}{3c} \quad (\gamma \rightarrow 1).
\end{aligned} \tag{1.21}$$

Since the energy gain of the DSA is of the first order of  $V/c$ , the DSA is also known as the first-order Fermi acceleration. It is an efficient particle acceleration mechanism for nonrelativistic shocks; for relativistic shocks, particles downstream would have difficulties returning to the shock upstream.

To derive the resultant particle spectrum, let  $N_0$  be the initial number of particles with the energy  $E_0$ . In each cycle of the DSA, the particles gain energy by  $G = 1 + \Delta E/E$ . Some particles may leave the accelerator after each cycle, and the fraction  $P$  of the particles will move on to the next cycle. After  $k$  cycles, the number of particles  $N_k = P^k N_0$ , and the particle energy  $E_k = G^k E_0$ .  $G$  is given in Equation 1.21. To estimate  $P$ , let  $n$  be the isotropized particle number density. The particle flux that crosses the shock from downstream and comes back from upstream is  $nv/4$ , where  $v$  is the particle velocity. Once back in the downstream, the flux that advects downstream without going on to the next DSA cycle is  $nu_2$ . Then  $P = 1 - nu_2/(nv/4) \approx 1 - 4u_2/c$  for  $v \rightarrow c$ . Using  $k = \ln(N_k/N_0)/\ln P = \ln(E_k/E_0)/\ln G$  [18],

$$\begin{aligned}
\ln \frac{N_k}{N_0} &= \frac{\ln P}{\ln G} \ln \frac{E_k}{E_0} = -Q \ln \frac{E_k}{E_0} \quad \Rightarrow \quad N_k = N_0 \left( \frac{E_k}{E_0} \right)^{-Q} \\
Q &= -\frac{\ln(1 - 4u_2/c)}{\ln[1 + 4(u_1 - u_2)/3c]} \approx \frac{3u_2}{u_1 - u_2} = \frac{3}{R - 1} \quad (u_1, u_2 \ll c) \\
&\Rightarrow \frac{dN}{dE} \propto E^{-(Q+1)} = E^{-\Gamma}, \quad \Gamma = \frac{R + 2}{R - 1}.
\end{aligned} \tag{1.22}$$

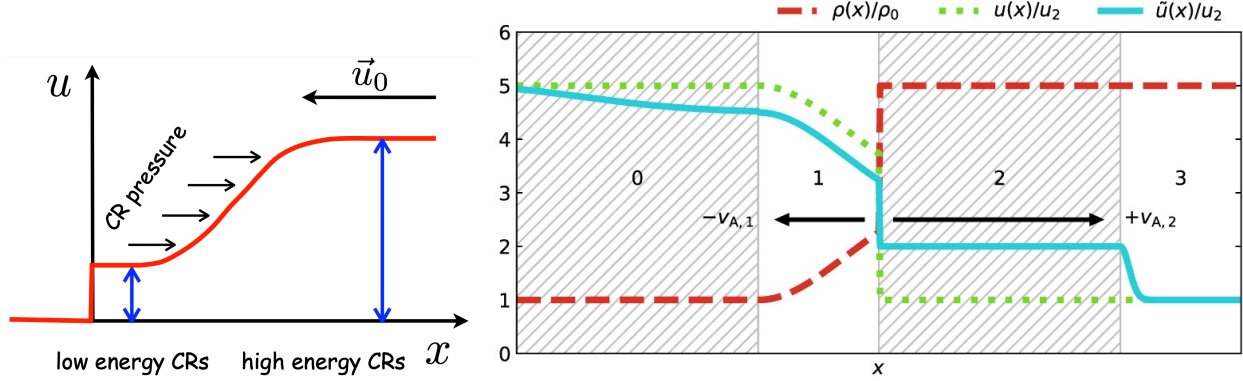


Figure 1.6: **Left:** schematic diagram of the formation of a precursor (image credit: Stefano Gabici). **Right:** Comparison between the NLDSA (precursor (region 1) only) and mNLDSA (precursor and postcursor (region 2))) [21]

Therefore, the DSA produces a power-law spectrum of relativistic particles with an index that depends on nothing but the shock compression ratio  $R$ . For a strong shock with  $R \rightarrow 4$ , the universal particle spectrum is a power law with index 2.

Since the total particle energy calculated from this spectrum is divergent ( $\int_{E_{th}}^{\infty} E(dN/dE)dE$  where  $E_{th}$  is the threshold particle energy for injection into the DSA cycle), the maximum particle energy is required to keep the total particle energy finite. The maximum energy can be estimated as the energy a particle can achieve within the time  $T = \min(t_{age}, t_{loss})$ , where  $t_{age}$  is the age of the accelerator and  $t_{loss}$  is the particle cooling time scale (see §1.3). For protons whose  $t_{loss}$  is in general much longer than  $t_{age}$ , the maximum energy  $E_{max}$  is found by equating the acceleration time  $t_{acc} \sim D(E)/v_{sh}$  and  $t_{age}$ , where  $D(E)$  is the energy-dependent spatial diffusion coefficient, and  $v_{sh}$  is the shock velocity. The Galactic average diffusion coefficient estimated from the primary-to-secondary CR ratio measurement is  $D \sim 7 \times 10^{28} (E/4 \text{ GeV})^{0.4} \text{ cm}^2 \text{ s}^{-1}$  [20]. Adopting this value and the typical age of an SNR  $\sim$  a kyr with a strong shock  $v_{sh} \sim$  a few 1000  $\text{km s}^{-1}$ ,  $t_{acc}(E_{max}) = t_{age}$  gives  $E_{max} \sim \text{GeV}$ , far from the knee of the CR spectrum  $\sim \text{PeV}$ . To explain the CRs with energies much higher than GeV, the diffusion coefficient at the accelerator should be much smaller than that of the Galactic average so that particles can spend a longer time around the shock and gain more energy.

### 1.2.3 Nonlinear diffusive shock acceleration

Suppressed diffusion can be achieved by strong magnetic instabilities driven by the particles themselves. The enhanced magnetic turbulence will increase the total magnetic field at the accelerator by 10-100 times the ISM magnetic field. Such amplified magnetic fields are often observed in young SNRs (see §1.4). Treating CRs as active participants of an accelerator system, instead of passive test particles, causes highly nonlinear effects on the accelerator. Understanding these nonlinearities requires numerical simulations, the first of which adopted the two-fluid approach where CR ions and electrons are treated as two fluids of relativistic particles. Such simulations provided the foundation of the revised DSA theory, so-called nonlinear DSA (NLDSA; e.g., [22, 23] for review). The key difference between the DSA and NLDSA lies in the compression ratio. Firstly, the contribution of relativistic particles is taken into account as the relativistic adiabatic index  $\gamma = 4/3$ , and hence,  $R \rightarrow 7$  for a strong shock. Secondly, CR pressure slows down the upstream plasma, forming a region called “precursor” (Figure 1.6 *left*). Low-energy ( $\sim$  GeV) CRs confined in the vicinity of the shock experience a decrease in the upstream velocity  $u_1$  within the precursor, and hence, a reduced compression ratio  $R_{sub} = u_1/u_2 \lesssim 4$ . High-energy CRs still experience the total compression ratio  $R_{tot} = u_0/u_2 \rightarrow 7$ , where  $u_0$  is the plasma velocity in the far upstream (region 0 in Figure 1.6 *right*). Then, the resulting particle spectrum is such that the low-energy spectrum is softer than the DSA spectrum ( $\Gamma > 2$ ), and the high-energy spectrum is harder than the DSA spectrum ( $\Gamma < 2$ ). Such a concave CR spectrum, however, does not agree with observation. As demonstrated at the end of §1.1, the measured CR spectral index  $\sim 2.7$  and the Galactic diffusion spectral index  $\sim 0.4$  require a much softer spectrum with  $\Gamma = 2.7 - 0.4 = 2.3$  up to the knee for protons whose energy loss is negligible. Gamma-ray observations of SNRs also indicate CR spectra softer than the DSA spectrum (see §1.3).

### 1.2.4 Modified nonlinear diffusive shock acceleration

The two-fluid simulations provide insight into the shock dynamics modified by the fluid of relativistic CRs. However, treating the CRs as a fluid inherently prohibits the knowledge of the en-

energetics of CRs modified by the shock-CR interaction, which in turn modifies the shock dynamics, which affects the CR energetics, and so on. To self-consistently model the CR-shock interactions and extract the resulting CR spectra requires the kinetic approach that treats CRs as particles. Recent hybrid simulations of kinetic ions and fluid electrons [24, 25] found the formation of a “postcursor” downstream a shock, an equivalent of a “precursor” in the upstream, that changes the shock dynamics and CR spectrum to an even greater extent than the precursor does. This so-called modified NLDSA (mNLDSA) made an important step toward a better understanding of CR acceleration at shocks. In a precursor (region 1 in Figure 1.6), CRs are drifted away from the shock front relative to the background fluid by CR-driven magnetic turbulence at the local Alfvén speed  $-v_{A,1}$ . In a postcursor (region 2 in Figure 1.6), the same drift happens at speed  $v_{A,2}$ . For high-energy CRs that probe the upstream infinity and the downstream, the compression ratio experienced by the CRs is [25]

$$\tilde{R}_{tot} \simeq \frac{u_0}{u_2 + v_{A,2}} \simeq \frac{R_{tot}}{1 + \alpha_2}; \quad \alpha_2 \equiv \frac{v_{A,2}}{u_2}, \quad (1.23)$$

where  $v_0$  is the fluid velocity in the far upstream, and  $R_{tot}$  is the compression ratio experienced by the background fluid, that of the NLDSA. The parameter  $\alpha_2$  characterizes the postcursor effect on the CR spectrum. Since  $\alpha_2 > 0$ ,  $\tilde{R}_{tot}$  is always smaller than  $R_{tot}$ . For low-energy CRs that probe both the precursor and postcursor, the compression ratio experienced by the CRs is [25]

$$\tilde{R}_{sub} \simeq \frac{u_1 - v_{A,1}}{u_2 + v_{A,2}} \simeq R_{sub} \frac{1 - \alpha_1}{1 + \alpha_2}; \quad \alpha_1 \equiv \frac{v_{A,1}}{u_1}. \quad (1.24)$$

If magnetic fields are compressed at the shock such that  $B_2 \approx R_{sub} B_1$ ,

$$\alpha_2 = \frac{B_2}{u_2 \sqrt{\mu_0 \rho_2}} \simeq \frac{R_{sub} B_1}{(u_1 / R_{sub}) \sqrt{\mu_0 R_{sub} \rho_1}} = R_{sub}^{3/2} \frac{B_1}{u_1 \sqrt{\mu_0 \rho_1}} = R_{sub}^{3/2} \alpha_1 \lesssim 8 \alpha_1, \quad (1.25)$$

therefore, the postcursor effect dominates over the precursor effect. For the majority of the CR

population  $> \text{GeV}$ , the mNLDSA prediction for the particle spectrum is (see Equation 1.22)

$$\tilde{\Gamma} \equiv \frac{\tilde{R}_{tot} + 2}{\tilde{R}_{tot} - 1} = \frac{(R_{tot} + 2) + 2\alpha_2}{(R_{tot} - 1) - \alpha_2} \quad (1.26)$$

is softer than the DSA spectrum. One can view the same result with respect to the balance between energy gain and particle escape as in Equation 1.22:

$$\tilde{\Gamma} \simeq 1 + \frac{P - 1}{G - 1} \simeq 1 + \frac{3\tilde{u}_2}{\tilde{u}_1 - \tilde{u}_2} = 1 + \frac{3u_2 + 3v_{A,2}}{u_1 - u_2 - v_{A,1} - v_{A,2}}. \quad (1.27)$$

This is a demonstration that the postcursor effect softens the CR spectrum by increasing the particle escape probability (numerator) more than it decreases the energy gain (denominator) by a factor of 3. Overall, the CR current weakens the shock, then the DSA becomes less efficient, which in turn decreases the CR current, self-regulating the CR spectrum [25].

While the hybrid approach provided significant findings on CR spectra at shocks, it still treats electrons as a fluid and hence fails to dissect their kinematics. A full kinematic approach, realized by particle-in-cell simulations, will be the ultimate resolution, yet it is computationally exceptionally expensive given the current technology.

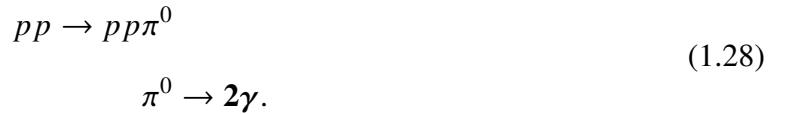
An important caveat is that all the shock acceleration theories assume that CRs are already ultrarelativistic. In reality, it is not a trivial question as to how a fraction of CRs in a thermal pool downstream of the shock gains enough energy to travel against the fluid and cross the shock. One of the proposed solutions to this “injection problem” is the “thermal leakage” model (e.g., [26, 27, 28, 29]). Most astrophysical shocks are collisionless, i.e., the mean free path of binary Coulomb collision is far greater than the size of the shock. The isotropization occurs via waves such as scattering off moving magnetic turbulence. Unlike collisional shocks, where particles quickly establish the Maxwellian distribution by collisions, it takes a longer time for collisionless shocks to thermalize particles and may leave some suprathermal particles in the high-energy tail of the Maxwellian. These particles, whose gyroradius may be large enough to make a DSA cycle across the shock in a single orbit, could become the seeds of CRs.

### 1.3 CR cooling

CRs constantly interact with the surroundings, i.e., the interstellar medium (ISM) and the interstellar electromagnetic fields. Such interactions directly or indirectly produce photons over a broad energy range. The spectrum of this continuum emission contains information about the primary CR spectrum and the surroundings with which the CRs interact. These photons also preserve directional information, guiding us to CR acceleration sites. This chapter has been adapted from [30, 31, 32, 33, 34, 35].

#### 1.3.1 Pion decay

The dominant energy loss mechanism of CR protons is pion production from inelastic scattering with the ISM (mainly hydrogen). Above the threshold kinetic energy of CR proton  $\sim 290$  MeV, neutral pions are produced, which in turn decay into gamma rays after only  $8.4 \times 10^{-17}$  s.



A CR proton loses 50% of its energy after one interaction. Well above the threshold energy, the cross-section of this interaction,  $\sigma_{pp} \sim 40$  mb, is only very mildly energy-dependent. The lifetime of a CR proton then can be approximated to

$$t_{pp} \equiv \frac{E_p}{-dE_p/dt} \simeq \frac{E_p}{0.5E_p c \sigma_{pp} n_p} \simeq 5.3 \times 10^7 \left( \frac{n_p}{\text{cm}^{-3}} \right)^{-1} \text{ yr}, \tag{1.29}$$

where  $E_p$  is the CR proton energy,  $c$  is the speed of light, and  $n_p$  is the hydrogen number density. Since the lifetime of CR protons is nearly energy-independent, this interaction preserves the initial spectral shape of the CR protons.

The photons are emitted back-to-back in the pion rest frame, each with an equal share of the pion energy  $E_\gamma = m_\pi c^2/2 \simeq 67.5$  MeV, where  $m_\pi$  is the pion mass and  $c$  is the speed of light.

In the lab frame, where the pion energy is  $E_\pi = \gamma m_\pi c^2 = m_\pi c^2 / \sqrt{1 - \beta^2}$ , the photon energy is  $E_\gamma = \gamma_\pi (1 + \beta_\pi \cos \theta) m_\pi c^2 / 2$ , where  $\gamma_\pi$  is the pion Lorentz factor,  $\beta_\pi$  is the ratio of the pion velocity and  $c$ , and  $\theta$  is the angle between the pion and photon trajectories. Since the photons are emitted isotropically ( $dN_\gamma/d\Omega = 1/4\pi \Rightarrow dN_\gamma = 1/2 d \cos \theta$ ), the photon energy distribution is

$$\frac{dN_\gamma}{dE_\gamma} = \frac{1/2 d \cos \theta}{\gamma_\pi \beta_\pi m_\pi c^2 / 2 d \cos \theta} = \frac{1}{\gamma_\pi \beta_\pi m_\pi c^2} = \frac{1}{E_\pi \beta_\pi} = \frac{1}{\sqrt{E_\pi^2 - m_\pi^2 c^4}}. \quad (1.30)$$

Therefore, for a single pion, the photon energy distribution is constant within the range  $[E_\gamma^{min}, E_\gamma^{max}] = [\gamma_\pi (1 - \beta_\pi) m_\pi c^2 / 2, \gamma_\pi (1 + \beta_\pi) m_\pi c^2 / 2]$ . In particular, in log-energy space, this range is centered at

$$\frac{1}{2} (\log E_\gamma^{min} + \log E_\gamma^{max}) = \log \sqrt{E_\gamma^{min} E_\gamma^{max}} = \log \frac{m_\pi c^2}{2} \simeq \log 67.5 \text{ MeV}. \quad (1.31)$$

Then the photon energy distribution for a distribution of pions is a superposition of the constant distributions within different photon energy ranges, depending on the pion energy, but all centered at 67.5 MeV in log-energy space. This means the photon log-energy distribution peaks at 67.5 MeV, the so-called ‘‘pion bump’’. The pion bump is considered the signature of the CR protons. Multiple works have reported a hint of the pion bump in the gamma-ray spectra of SNRs (e.g., [36, 37])<sup>1</sup>.

The photon emissivity,

$$\begin{aligned} q_\gamma(E_\gamma) &= \frac{dN_\gamma}{dE_\gamma dt}(E_\gamma) \\ &= 2 \int_{E_\pi^{min}(E_\gamma)}^{\infty} \frac{dN_\gamma}{dE_\gamma} q_\pi(E_\pi) dE_\pi = 2 \int_{E_\gamma + m_\pi^2 c^4 / 4E_\gamma}^{\infty} \frac{q_\pi(E_\pi)}{\sqrt{E_\pi^2 - m_\pi^2 c^4}} dE_\pi, \end{aligned} \quad (1.32)$$

has a similar spectral shape to the CR proton energy distribution but with a more gradual cutoff in the highest-energy regime. Here,  $q_\pi$  is the pion emissivity, and  $E_\pi^{min} - E_\gamma^{max} = E_\gamma^{min} =$

---

<sup>1</sup>In fact, the pion bump is outside of the sensitivity limit of the current-generation gamma-ray instruments, and hence this spectral feature cannot be directly observed. For more discussion on the detection of the pion bump, see [38, 11].

$m_\pi^2 c^4 / 4E_\gamma^{max} \Rightarrow E_\pi^{min}(E_\gamma) = E_\gamma + m_\pi^2 c^4 / 4E_\gamma$ . The gamma-ray spectrum of a monoenergetic CR proton with energy  $E_p$  peaks at  $E_\gamma = 0.1E_p$ .

Above  $\sim 100$  GeV, charged pions are produced with a nearly equal probability to that of neutral pions.  $\sim 50\%$  of the CR proton energy is nearly equally shared by  $\pi_0, \pi^+$  and  $\pi^-$ , and hence  $E_{\pi_0, \pi^\pm} \simeq (1/6)E_p$ . Charged pions decay into a muon or antimuon. The timescale of the decay,  $\approx 2.6 \times 10^{-8}$  s, is much longer than that of a neutral pion.

$$\begin{aligned}
pp &\rightarrow pp\pi^+ \\
\pi^+ &\rightarrow \mu^+ \nu_\mu \\
\mu^+ &\rightarrow e^+ \nu_e \bar{\nu}_\mu
\end{aligned} \tag{1.33}$$

$$\begin{aligned}
pp &\rightarrow pp\pi^- \\
\pi^- &\rightarrow \mu^- \bar{\nu}_\mu \\
\mu^- &\rightarrow e^- \bar{\nu}_e \nu_\mu
\end{aligned} \tag{1.34}$$

Since these interactions uniquely produce neutrinos<sup>2</sup>, neutrinos are considered another signature of CR protons. The secondary neutrinos, electrons, and positrons have similar spectral shapes to that of gamma rays from neutron pions. The energy of a pion,  $E_{\pi^\pm} \simeq 1/6E_p$ , is shared between three neutrinos and one electron (positron) such that  $E_{\nu, e^\pm} \simeq (1/24)E_p$ , whereas for two gamma rays from a neutral pion,  $E_\gamma \simeq (1/12)E_p$ . Due to a longer lifetime of charged pions than neutral

---

<sup>2</sup>An interaction between a CR proton and a photon can also produce pions,

$$p\gamma \rightarrow \Delta^+ \rightarrow \pi^+ n \text{ or } \pi^0 p, \tag{1.35}$$

that decay into gamma rays and neutrinos as shown in Equation 1.28 and 1.33. The cross-section of this interaction is two orders of magnitude smaller than the proton-proton interaction. However, the proton-photon interaction becomes important in an environment with extremely dense radiation, such as the jet of an active galactic nucleus, or for any extragalactic cosmic rays traveling a Mpc to Gpc distance in the cosmic microwave background (CMB) field. The threshold proton energy for this interaction with a CMB photon,  $E_p \sim 10^{20}$  eV, is known as the Greisen-Zatsepin-Kuzmin (GZK) limit [39, 40] above which the measured local CR proton flux is highly suppressed.

pions, the energy loss of charged pions through different interactions prior to the decay can result in smaller fluxes of secondary neutrinos, electrons, and positrons at very high energies.

Interaction between an energetic CR proton and a hydrogen in the ISM may also produce antimatter:

$$pp \rightarrow pp \bar{p}p \bar{n}n, \quad (1.36)$$

where  $\bar{p}$  and  $\bar{n}$  are antiproton and antineutron, respectively. Then, the antiproton and antineutron can fuse to form an antideuteron  $\bar{d}$ . Given a much higher proton energy threshold for this process ( $17m_p c^2$ ) than pion production, antideuteron production by CR protons is extremely rare, especially in low energies (below a few GeV where the flux ratio of  $\bar{d}/p \ll 10^{-10}$ ) [41]. On the other hand, multiple theories predict antideuteron production from dark matter annihilation or decay (e.g., [42]), making low-energy antideuterons great targets for indirect dark matter search such as the General AntiParticle Spectrometer (GAPS) experiment [43].

### 1.3.2 Nonthermal Bremsstrahlung

CR electrons (and secondary electrons produced by CR protons) also undergo inelastic scattering with the ISM. When the electron energy exceeds the critical energy (344.8 MeV for hydrogen), the main energy loss mechanism of the electron switches from ionization to bremsstrahlung – braking radiation of electrons in the electric fields of nuclei. Bremsstrahlung photons with sufficiently high energies ( $E_\gamma \geq 2m_e c^2$ , where  $m_e$  is the electron mass) subsequently undergo pair production, initiating an electromagnetic cascade (see §2.3). The radiation length  $X_0$  is a characteristic length scale of these interactions over which an electron has traveled before losing all but  $1/e$  of its energy:

$$\frac{1}{X_0} = 4\alpha r_e^2 Z(Z+1) \frac{N_A}{A} \frac{\ln(183Z^{-1/3})}{1 + 0.12(Z/82)^2}, \quad (1.37)$$

where  $\alpha$  is the fine-structure constant,  $r_e$  is the classical electron radius,  $Z$  is the atomic number,  $N_A$  is the Avogadro's number, and  $A$  is the atomic molar mass. The radiation length of hydrogen

is  $63.04 \text{ g cm}^{-2}$ . Then, the lifetime of a CR electron can be approximated to

$$t_{br} \equiv \frac{E_e}{-dE_e/dt} \simeq \frac{E_e}{(cm_p n_p / X_0) E_e} \simeq 4 \times 10^7 \left( \frac{n_p}{\text{cm}^{-3}} \right)^{-1} \text{ yr.} \quad (1.38)$$

As was the case for pion decay, the lifetime of CR electrons is energy-independent, and hence, bremsstrahlung preserves the initial spectral shape of the CR electrons. The bremsstrahlung photon energy distribution from a power-law CR electron energy distribution ( $dN_e/dE_e \propto E_e^\Gamma$ ) has the same spectral shape as that of the CR electrons ( $dN_\gamma/dE_\gamma \propto E_\gamma^\Gamma$ ).

### 1.3.3 Inverse Compton radiation

Electromagnetic fields are ubiquitous in the universe. Interactions of CRs with interstellar electromagnetic fields provide another important energy loss mechanism. Since the cross-sections of electromagnetic interactions are inversely proportional to the quartic mass, such interactions are important for CR electrons to a far greater extent than for CR protons. Therefore, the discussion in this and the next section focuses on the electromagnetic energy loss of CR electrons.

Our galaxy is filled with homogeneous and isotropic cosmic microwave background (CMB) photons as well as localized dust and stellar lights in the infrared (IR) to ultraviolet (UV) band. CR electrons interact with those photons by inverse Compton scattering in which the electron energy greatly exceeds the target photon's energy. This interaction ( $e\gamma \rightarrow e'\gamma'$ ) can be described using four-momenta of the photon ( $k, k'$ ) and the electron ( $p, p'$ ).

$$\begin{aligned} k_\mu + p_\mu &= k'_\mu + p'_\mu, & m_e^2 c^4 &= p^2 = p'^2, & 0 &= k^2 = k'^2, \\ m_e^2 c^4 &= (p + k - k')_\mu (p + k - k')^\mu = m_e^2 c^4 + 2p \cdot (k - k') - 2k \cdot k' \implies p \cdot (k - k') = k \cdot k'. \end{aligned} \quad (1.39)$$

In the electron rest,  $p = (m_e c^2, 0, 0, 0)$ ,  $k = (\tilde{E}_\gamma, \tilde{E}_\gamma, 0, 0)$ , and  $k' = (\tilde{E}'_\gamma, \tilde{E}'_\gamma \cos \tilde{\theta}, \tilde{E}'_\gamma \sin \tilde{\theta}, 0)$ , where  $\tilde{\theta}$  is the angle between the incoming and outgoing directions of the photon in the electron rest frame. Then Equation 1.39 becomes

$$m_e c^2 (\tilde{E}_\gamma - \tilde{E}'_\gamma) = \tilde{E}_\gamma \tilde{E}'_\gamma (1 - \cos \tilde{\theta}) \implies \tilde{E}'_\gamma = \frac{\tilde{E}_\gamma}{1 + (\tilde{E}_\gamma/m_e c^2)(1 - \cos \tilde{\theta})}. \quad (1.40)$$

In the lab frame where the electron is moving with the velocity  $\beta$  (Lorentz factor  $\gamma$ ),

$$\begin{aligned} \tilde{E}_\gamma &= E_\gamma \gamma (1 - \beta \cos \theta), & E'_\gamma &= \gamma (1 + \beta \cos(\pi - \tilde{\theta})) \tilde{E}'_\gamma \\ \implies E'_\gamma &= \gamma (1 - \beta \cos \tilde{\theta}) \frac{\tilde{E}_\gamma}{1 + (\tilde{E}_\gamma/m_e c^2)(1 - \cos \tilde{\theta})} = \gamma^2 E_\gamma \frac{(1 - \beta \cos \tilde{\theta})(1 - \beta \cos \theta)}{1 + (E_\gamma E_e/m_e^2 c^4)(1 - \beta \cos \theta)(1 - \cos \tilde{\theta})}. \end{aligned} \quad (1.41)$$

In the non-relativistic (Thomson) regime ( $E_\gamma E_e \ll m_e^2 c^4$ ), using  $\cos \theta = (\cos \tilde{\theta} - \beta)/(1 - \beta \cos \tilde{\theta})$  and the isotropic photon distribution in the electron rest frame,

$$E'_\gamma = \gamma^2 E_\gamma (1 - \beta \cos \tilde{\theta})^2 \implies \langle E'_\gamma \rangle = \frac{4}{3} \gamma^2 E_\gamma \approx 5 \frac{E_\gamma}{\text{eV}} \left( \frac{E_e}{\text{GeV}} \right)^2 \text{ MeV}. \quad (1.42)$$

In the ultra-relativistic (Klein-Nishina) regime ( $E_\gamma E_e \gg m_e^2 c^4$ ),

$$E'_\gamma \approx \gamma m_e c^2 \sim E_e. \quad (1.43)$$

The angle-averaged total cross-section of inverse Compton scattering can be approximated to

$$\sigma_{IC} = \frac{3\sigma_T}{8\kappa_0} \left[ \left( 1 - \frac{2}{\kappa_0} - \frac{2}{\kappa_0^2} \right) \ln(1 + 2\kappa_0) + \frac{1}{2} + \frac{4}{\kappa_0} - \frac{1}{2(1 + 2\kappa_0)^2} \right], \quad (1.44)$$

where  $\sigma_T$  is the Thomson cross-section, and  $\kappa_0 = E_\gamma E_e/m_e^2 c^4$  is the only parameter of  $\sigma_{IC}$ . In the non-relativistic (Thomson) regime with  $\kappa_0 \ll 1$ ,  $\sigma_{IC} \approx \sigma_T(1 - 2\kappa_0)$ , while in the ultra-relativistic (Klein-Nishina) regime with  $\kappa_0 \gg 1$ ,  $\sigma_{IC} \approx (3/8)\sigma_T \kappa_0^{-1} \ln(2\kappa_0)$ . Then, the energy loss rate of CR electrons by these monoenergetic photons is ( $\beta \rightarrow 1$ )

$$\begin{aligned} dE_e/dt &= \frac{4}{3} \sigma_T c E_\gamma n_\gamma \left( \frac{E_e}{m_e c^2} \right)^2 && \text{in the Thomson regime,} \\ dE_e/dt &= \frac{3}{8} \frac{\sigma_T c n_\gamma}{E_\gamma/m_e c^2} \left( \ln 4\kappa_0 - \frac{11}{6} \right) && \text{in the Klein-Nishina regime,} \end{aligned} \quad (1.45)$$

where  $n_\gamma$  is the photon number density.

Therefore, in the Thomson regime, photons get frequently upscattered to energies proportional to  $E_e^2$  while electrons lose only a fraction of their energy ( $E'_\gamma/E_e \ll 1$ ) every time. Consequently, for a power-law CR electron distribution ( $dN_e/dE_e \propto E_e^{\Gamma_e}$ ), the upscattered photons form a harder power-law distribution  $dN'_\gamma/E'_\gamma \propto E'_\gamma^{\Gamma_\gamma}$  with  $\Gamma_\gamma = (\Gamma_e + 1)/2$ . On the other hand, in the Klein-Nishina regime, the interaction is suppressed, the upscattered photon energy is nearly independent of the electron energy, and electrons lose a significant amount of energy after only a single interaction. This leads to a very sharp cutoff in the upscattered photon energy distribution with  $\Gamma_\gamma = \Gamma_e + 1$  for a power-law CR electron distribution.

When photons are distributed over an energy range, the electron energy loss rate integrated over the photon energy distribution depends only on the total photon energy density  $U_\gamma$ . As a result, the lifetime of a CR electron  $t_{IC}$  is

$$t_{IC} \approx 3 \times 10^8 (U_\gamma/\text{eV}/\text{cm}^3)^{-1} (E_e/\text{GeV})^{-1} \text{ yr.} \quad (1.46)$$

Since  $t_{IC}$  is inversely proportional to the electron energy, inverse Compton scattering makes the CR electron spectrum softer.

#### 1.3.4 Synchrotron radiation

Interstellar magnetic fields<sup>3</sup> of  $B = 1\text{--}10 \mu\text{G}$  as well as locally enhanced magnetic fields of 10s  $\mu\text{G}$  to over  $10^{12}$  G at astrophysical sources are universal in our galaxy. Similar to the parameter  $\kappa_0 = E_\gamma E_e/m_e^2 c^4$  in inverse Compton scattering, interactions of CR electrons with magnetic fields can be treated classically as long as  $BE_e/B_{cr} m_e c^2 \ll 1$ , where  $B_{cr} = m_c^2 c^3/e\hbar \approx 4.4 \times 10^{13}$  G is the Schwinger limit of a magnetic field over which electron-positron pairs can be produced by vacuum polarization. Such high magnetic fields are achieved, for example, at the magnetic pole of a pulsar and, hence, pulsar winds of electrons and positrons (see §1.4.2). Other than these extreme cases, magnetic field strengths in most astrophysical environments are well below  $B_{cr}$ .

<sup>3</sup>Assuming equipartition with the CMB photons,  $U_\gamma = 0.26 \text{ eV cm}^{-3} = U_B = B^2/2\mu_0$ ,  $B \sim 3 \mu\text{G}$ .

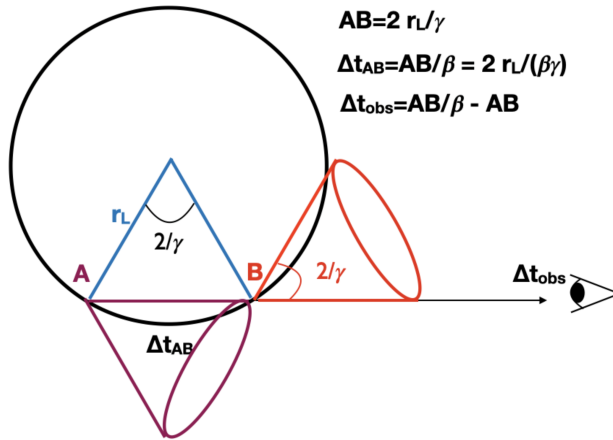
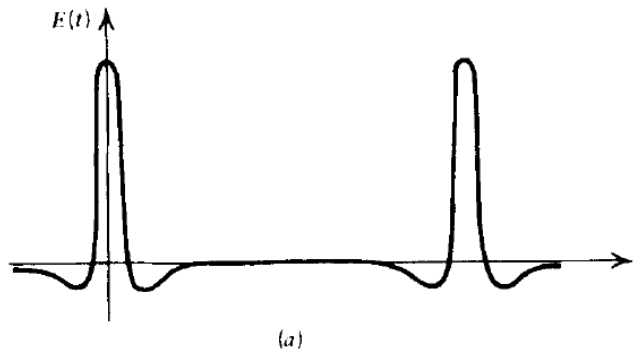
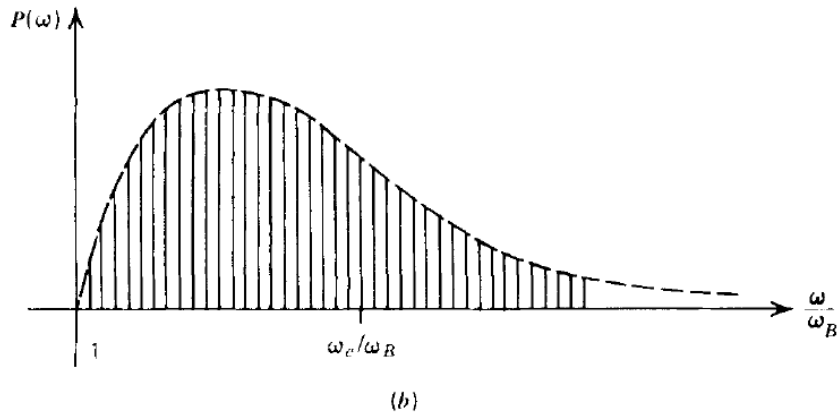


Figure 1.7: Schematic diagram of synchrotron radiation and relativistic aberration [31].



**Figure 6.10a** Time dependence of electric field from a rapidly moving particle in a magnetic field (synchrotron radiation).



**Figure 6.10b** Power spectrum for a.

Figure 1.8: Synchrotron radiation pulses and its power spectrum [35].

Similar to bremsstrahlung radiation in a nuclear electric field, an electron accelerated in a magnetic field produces synchrotron radiation, also known as magneto-bremsstrahlung. An electron moving with the velocity  $\beta$  (Lorentz factor  $\gamma$ ) in a magnetic field  $B$  experiences acceleration in the direction perpendicular to its velocity,  $a_{\perp} = evB \sin \theta / \gamma m_e$ , where  $\theta$  is the angle between the electron velocity and the magnetic field. The relativistic Larmor formula states that the (Lorentz-invariant) power radiated by this electron is

$$dE_e/dt = \frac{2}{3} \frac{\gamma^4 e^2 a_{\perp}^2}{4\pi\epsilon_0 c^3} = \frac{2}{3} \frac{\gamma^2 e^4 v^2 B^2 \sin^2 \theta}{4\pi\epsilon_0 m_e^2 c^3} = 2\sigma_T \beta^2 \gamma^2 c U_B \sin^2 \theta, \quad (1.47)$$

where  $\epsilon_0$  is the vacuum permittivity, and  $U_B = B^2/2\mu_0$  is the magnetic field energy density. The angle-averaged power,

$$\langle dE_e/dt \rangle = \frac{4}{3} \sigma_T c U_B \left( \frac{E_e}{m_e c^2} \right)^2, \quad (1.48)$$

is in the exact same form as Equation 1.45 with the photon energy density  $U_{\gamma} = E_{\gamma} n_{\gamma}$  replaced with the magnetic energy density  $U_B$ . Therefore, the ratio of synchrotron and inverse Compton flux provides an estimate of the ratio of magnetic and photon energy density. The lifetime of a CR electron  $t_{syn}$  depends on the electron energy, and hence, synchrotron radiation softens the CR electron spectrum.

$$t_{syn} \approx 1 \times 10^{10} (B/\mu\text{G})^{-2} (E_e/\text{GeV})^{-1} \text{ yr}. \quad (1.49)$$

Due to the relativistic aberration, in the lab frame, synchrotron radiation of a CR electron (Lorentz factor  $\gamma$ ) becomes a narrow beam along the electron's velocity with a width of  $2/\gamma$ . Therefore, a CR electron gyrating along a magnetic field line with the Larmor radius  $r_L = \gamma m_e v_{\perp} / eB$  creates light pulses observable only during a very short time period (see Figure 1.7

$$\Delta t_{obs} = \frac{\overline{AB}}{v_{\perp}} - \frac{\overline{AB}}{c} = \frac{2r_L}{\gamma v_{\perp}} \left( 1 - \frac{1}{\beta} \right) \approx \frac{2r_L}{\gamma v_{\perp}} \frac{1}{2\gamma^2} = \frac{1}{\omega_B \gamma^3 \sin \theta} \quad (1.50)$$

out of the period  $2\pi/\omega_L$ , where  $\omega_B$  is the larmor frequency. The synchrotron radiation spectrum

of this electron is a superposition of harmonics of  $\omega_B$  that peaks around the critical frequency  $\omega_c = (3/2)\gamma^3\omega_B \sin \theta$  (see Figure 1.8). The synchrotron spectrum of distribution of electrons is a superposition of the synchrotron spectra of individual electrons – a power-law distribution of CR electrons ( $dN_e/dE_e \propto E_e^{\Gamma_e}$ ) produces a power-law distribution of synchrotron photons ( $dN_\gamma/dE_\gamma \propto E_\gamma^{\Gamma_\gamma}$ ) where  $\Gamma_\gamma = (\Gamma + 1)/2$ , same as that of inverse Compton scattering.

Figure 1.9 [33] shows the spectral energy distributions (SEDs) of the radiative processes introduced in this chapter. Panels (a) and (b) are monoenergetic electrons and protons, respectively, with energies of 1 TeV (red) and 100 TeV (blue). Panels (c) and (d) are a distribution of electrons and protons, respectively, with an exponential cutoff power-law spectrum  $dN/dE \propto E^{-2} \exp(-E/E_c)$ , where  $E_c = 1$  (red), 100 (blue) TeV is the cutoff energy. Therefore, the panels (c) and (d) are a superposition of the SEDs in (a) and (b) for a spectrum of energy, respectively. As a result, panels (c) and (d) show the typical SEDs of CR sources consisting of two humps, one in the radio to X-ray band and the other in the gamma-ray band. For electrons, the solid lines are synchrotron (the humps in the lower energies,  $B = 3 \mu\text{G}$ ) and inverse Compton (the humps in the higher energies) spectra. Different inverse Compton humps are for different seed photon fields (CMB, far IR dust emission, starlight). The dashed lines are bremsstrahlung spectra. For protons, the solid lines are secondary electrons' synchrotron emission (the humps in the lower energies,  $B = 30 \mu\text{G}$ ) and primary protons' pionic gamma-ray spectra (the humps in the higher energies). Continuous injection and cooling of secondary electrons for  $10^4$  yr (solid lines) and  $10^5$  yr (dashed lines) were assumed. It is clear that the most energetic CRs with energies above 100 TeV are best probed in the hard X-ray ( $> 10$  keV) and VHE–UHE band. While CR protons and electrons can have similar gamma-ray spectra in the VHE–UHE band, they exhibit very different hard X-ray spectra. GeV gamma-ray observation can provide further information on the CR species and spectra. Therefore, multiwavelength observation in the X-ray to gamma-ray band is a powerful tool for studying the most energetic galactic CRs.

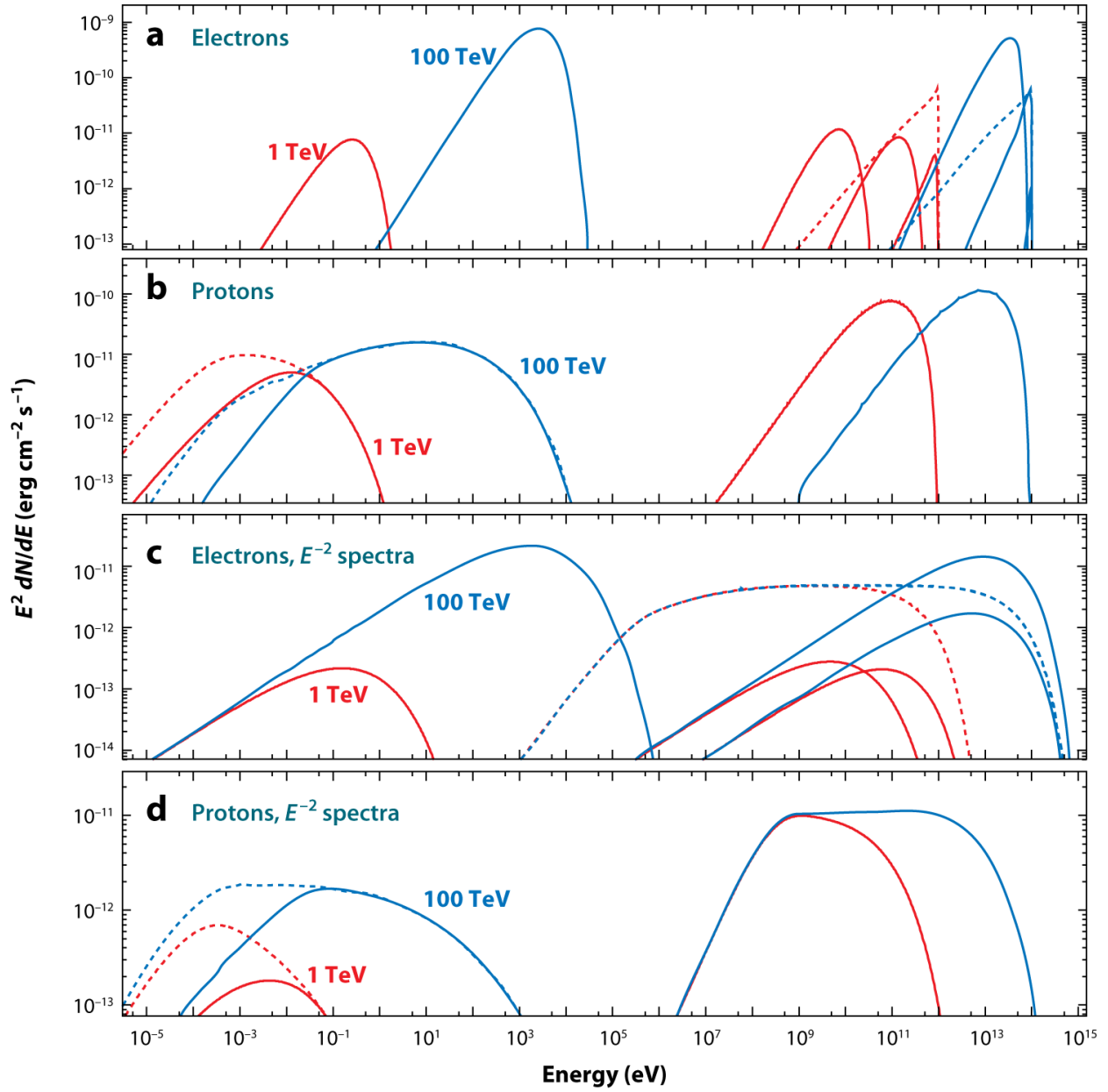


Figure 1.9: The SEDs of various radiative processes for protons and electrons [33]. See text for details.

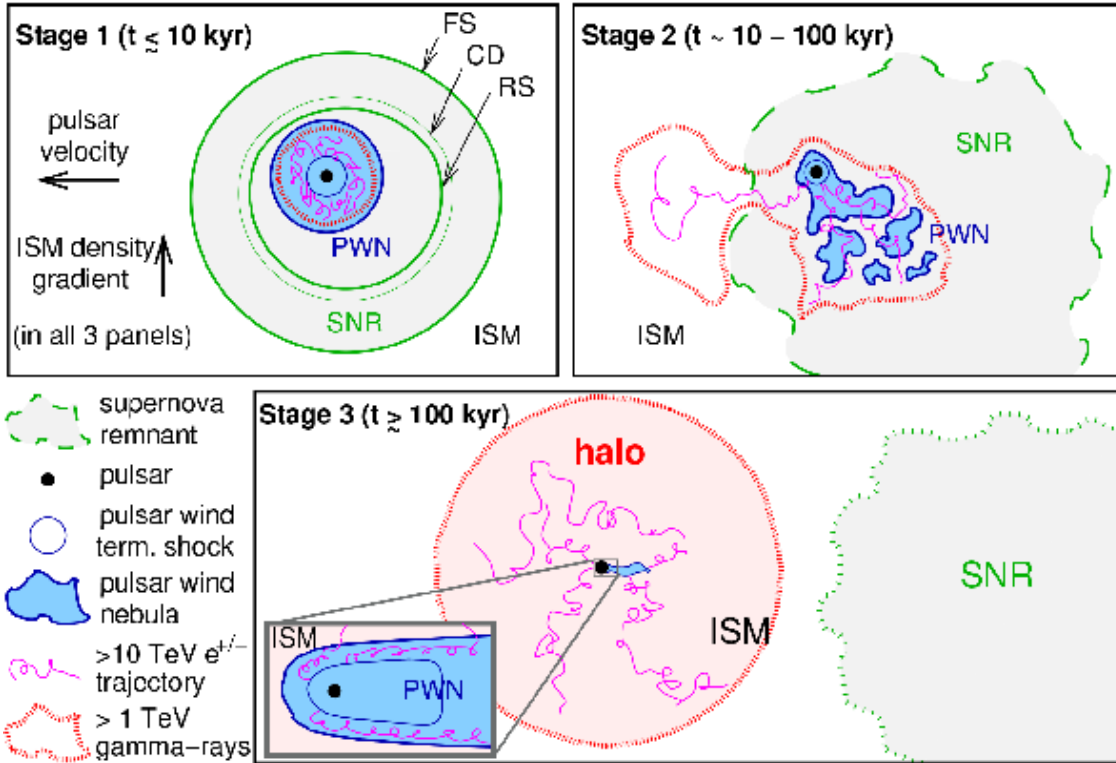


Figure 1.10: Schematic diagram of the evolution of an SNR and PWN system [44].

#### 1.4 Cosmic ray source candidates

In their seminal paper in 1934 [45], Walter Baade and Fritz Zwicky proposed two of the most important things in the history of astroparticle physics and high-energy astrophysics: (1) supernovae as the origin of CRs, and (2) formation of neutron stars from supernovae. For supernovae, even though the initial proposal was made for extragalactic CRs, Galactic supernovae, and their remnants (SNRs) have been considered the most promising candidates for Galactic CR accelerators. For neutron stars, discovered as a pulsar (pulsating radio source; [46]), the nebulae powered by pulsar wind (PWNe) were found to be the most common origin of gamma rays, and hence, another promising Galactic CR accelerator candidate. While an SNR and PWN are born together, they involve different physical processes and are responsible for different CR populations. Figure 1.10 summarizes the three evolutionary stages of a system of an SNR and PWN. The details of their evolution, relevant CR processes and properties, and observational findings are summarized

below.

#### 1.4.1 Supernova remnants

The steady-state CR luminosity estimated from the proton flux measurement is  $\sim 10^{40}$  erg  $s^{-1}$  [5]. Considering the Galactic core-collapse supernova rate  $\sim 2$  per century and the typical supernova explosion energy  $\sim 10^{51}$  erg  $s^{-1}$ , the necessary CR luminosity is fulfilled by supernovae if only a few percent of their explosion energy is converted into CRs. Combined with the DSA theories, SNRs make ideal Galactic CR accelerators for protons (the main constituents of the ISM being shocked).

When a massive ( $\gtrsim 8 M_{\odot}$ ) star explodes,  $M_{ej} = 1 - 10 M_{\odot}$  of the ejecta is released into the cold ISM with the kinetic energy of  $E_{SN} = 10^{51}$  erg. This explosion forms a strong shock (“forward shock”, FS in the first diagram of Figure 1.10) propagating into the ISM with tens thousands of km  $s^{-1}$  and sweeping up the ISM. When the swept-up ISM mass  $M_{sw}$  is much smaller than the ejecta mass, the swept-up mass has negligible impact on the SNR evolution. The ejecta freely expands with a constant velocity  $v_s = \sqrt{2E_{SN}/M_{ej}} = 10^4 (E_{SN}/10^{51} \text{ erg})^{1/2} (M_{ej}/M_{\odot})^{1/2}$  km  $s^{-1}$ . This “free-expansion phase” lasts until  $M_{ej} \approx M_{sw} = (4\pi/3)R_s^3 \rho_{ISM}$ , where  $\rho_{ISM} \approx 1.7 \times 10^{-24}$  g  $cm^{-3}$  is the average ISM mass density, and  $R_s = v_s t_s \approx 2(M_{ej}/M_{\odot})^{1/3}$  pc is the SNR radius at the end of the free-expansion phase. The age of the SNR  $t_{age}$  at that moment is  $t_s \approx 200(M_{ej}/M_{\odot})^{1/6}$  yr.

At this point, the shock starts slowing down, and the SNR parameters are described by the well-known Sedov-Taylor self-similar solution [47], thereby the name “Sedov-Taylor phase”. The shock-heated swept-up mass reaches the temperature  $kT_2 = (3/16)m_p v_s^2 \gtrsim 1$  keV and radiates thermal X-rays. The radiative cooling time scale  $\tau_c \propto T_2^{1/2} \gtrsim 10^6$  yr is much greater than  $t_{age}$ , and hence, the radiative loss is negligible, and the energy is conserved (therefore, another name

“adiabatic phase”). The shock radius  $R_s$  and velocity  $v_s$  are [48]

$$\begin{aligned} R_s &\approx \left(\frac{E_{SN}}{\rho_{ISM}}\right)^{1/5} t^{2/5} \approx 4.5 \left(\frac{E_{SN}}{10^{51} \text{ erg}}\right)^{1/5} \left(\frac{t}{1000 \text{ yr}}\right)^{2/5} \text{ pc}, \\ v_s = \frac{dR_s}{dt} &\approx \frac{2}{5} \left(\frac{E_{SN}}{\rho_{ISM}}\right)^{1/5} t^{-3/5} \approx 1800 \left(\frac{E_{SN}}{10^{51} \text{ erg}}\right)^{1/5} \left(\frac{t}{1000 \text{ yr}}\right)^{-3/5} \text{ km s}^{-1}. \end{aligned} \quad (1.51)$$

The Sedov-Taylor phase lasts until  $t_{age} \sim \tau_c$ . Since  $\tau_c \propto v_s \propto t^{-3/5}$ , the “radiative phase” starts when  $t_{age} \sim 50$  kyr. The shock radius and velocity at this point are  $R_s \approx 20$  pc and  $v_s \approx 200$  km s<sup>-1</sup>, respectively.

CR acceleration in SNRs is most active during the free-expansion and adiabatic phase when the shock and magnetic field are strong. Considering the CR luminosity  $L_{CR}$  as a fraction  $\eta$  (acceleration efficiency) of the swept-up mass energy flux,

$$\begin{aligned} L_{CR} &= \eta 4\pi R_s^2 \rho_{ISM} \frac{v_s^2}{2} \propto R_s^2 v_s^3 \\ \implies L_{CR} &\propto t^2 \text{ (Free-expansion phase), } t^{-1} \text{ (Sedov-Taylor phase),} \end{aligned} \quad (1.52)$$

assuming a constant acceleration efficiency. Therefore, the CR luminosity should peak at the transition between the free-expansion and Sedov-Taylor phase.

The maximum CR energy of each phase can be estimated in a similar way to that in §1.1 ( $t_{acc} = D(E_{max})/v_s^2 = t_{age}$ ) but with an added constraint from the diffusion length  $\lambda_D = D(E_{max})/v_s = R_s$ . Assuming the Bohm regime where diffusion is highly effective such that CRs suffer scattering every Larmor radius  $r_L$ , the diffusion coefficient  $D(E) = r_L c/3 = c^2 E/3eB \propto E/B$ . For the free-expansion phase, the two constraints are equal:

$$D(E_{max}) = t_{age} v_s^2 = R_s v_s \quad \implies \quad E_{max} \propto B t_{age}. \quad (1.53)$$

For the Sedov-Taylor phase, the diffusion length constraint  $\lambda_D = R_s \propto t_{age}^{2/5}$  is met sooner than the

acceleration time constraint  $t_{acc} = t_{age}$ :

$$D(E_{max}) = R_s v_s \quad \Rightarrow \quad E_{max} \propto B t_{age}^{-1/5}. \quad (1.54)$$

Therefore,  $E_{max}$  continues increasing in the free-expansion phase, then starts decreasing as the Sedov-Taylor phase starts. Here,  $B$  is not constant; as the CR flux increases and decreases, the CR-driven magnetic instabilities and the total magnetic field will also increase and decrease. The maximum CR energy throughout the lifetime of an SNR will then be achieved at the transition between the free-expansion and Sedov-Taylor phase:

$$D(E_{max}) = t_{ST} v_{free}^2 \quad \Rightarrow \quad E_{max} \approx 20 \left( \frac{B}{100 \mu\text{G}} \right) \left( \frac{v_{free}}{10^4 \text{ km s}^{-1}} \right) \left( \frac{t_{ST}}{200 \text{ yr}} \right) \text{ PeV}. \quad (1.55)$$

Indeed, SNRs are capable of accelerating CRs up to the “knee”  $\sim 3$  PeV, but such an energetic phase will last only for a very short time. Once the maximum energy is achieved and the shock starts slowing down, the highest-energy CRs whose Larmor radii are larger than the shock radius will escape the SNR, as we imposed the diffusion length constraints when calculating the maximum energy.

The first observational evidence of CR acceleration in SNRs was found in the radio band. Nonthermal radio spectra of SNRs were attributed to synchrotron emission from CR electrons [49]. High-resolution X-ray imaging resolved bright nonthermal filaments and knots in SNRs where CR electrons are actively accelerated and cooled in a highly amplified ( $\gtrsim 100 \mu\text{G}$ ) magnetic field (e.g., [50]). Even though SNRs are believed to be the source of CR protons, observational confirmation of proton acceleration is nontrivial. Since the pion decay rate depends on the number of target nuclei, detecting pionic gamma rays from an SNR requires the presence of dense material nearby, such as molecular clouds (e.g., [51, 52]). In the TeV band, pionic gamma rays and leptonic gamma rays (from inverse Compton scattering) are indistinguishable. Currently, observations indicate proton acceleration in SNRs up to only a few TeV (e.g., [53]), challenging the status of SNRs as Galactic PeVatrons.

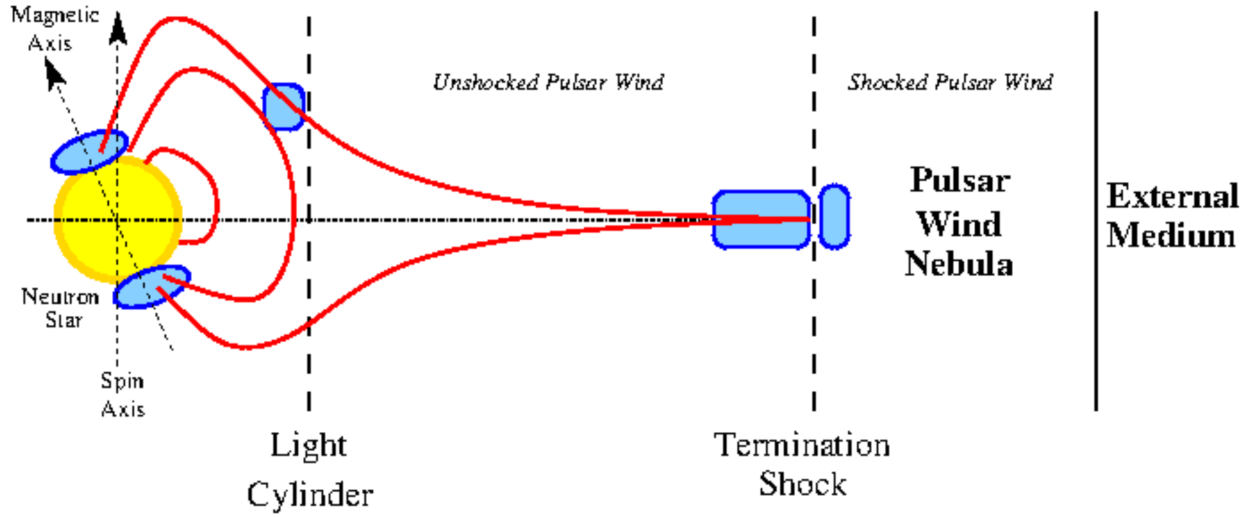


Figure 1.11: Schematic diagram of a PWN [54].

#### 1.4.2 Pulsars and pulsar wind nebulae

The Crab nebula, a PWN of a young ( $t_{age} \approx 970$  yr) pulsar PSR B0531+21, is the first and only astrophysical source identified as a Galactic PeVatron where CR electrons are accelerated to energies above 1 PeV. While the Crab is an exceptionally powerful accelerator, two decades of VHE gamma-ray observation revealed nearly half of the bright Galactic TeV sources are spatially coincident with energetic pulsars and their PWNe (e.g., [55]).

A neutron star is born from the same supernova explosion that creates an SNR – a compact object supported by neutron degeneracy. The angular momentum and magnetic flux of a giant progenitor star are inherited by a neutron star with a typical radius  $R_{\star} \sim 10$  km and mass  $M_{\star} \sim 2 - 3M_{\odot}$  [56, 57]. Therefore, a neutron star is spinning very fast (period  $P \sim 10$ s to 100s of ms) and highly magnetized (surface magnetic field  $B \sim 10^{12}$  G). Just like a Faraday disk, induced electric fields strip off electrons and nuclei from the neutron star’s surface, which fill the neutron star magnetosphere. These charged particles are supposed to screen the electric fields and bring the magnetosphere to a steady state. However, there can be some regions where the available charge density is below that required to screen the electric fields completely (“Goldreich and Julian charge density”  $\rho_{GJ} = -\vec{\Omega} \cdot \vec{B} / 2\pi c$  [58], where  $\Omega = 2\pi/P$ ). In these regions (polar cap, slot gap, and outer

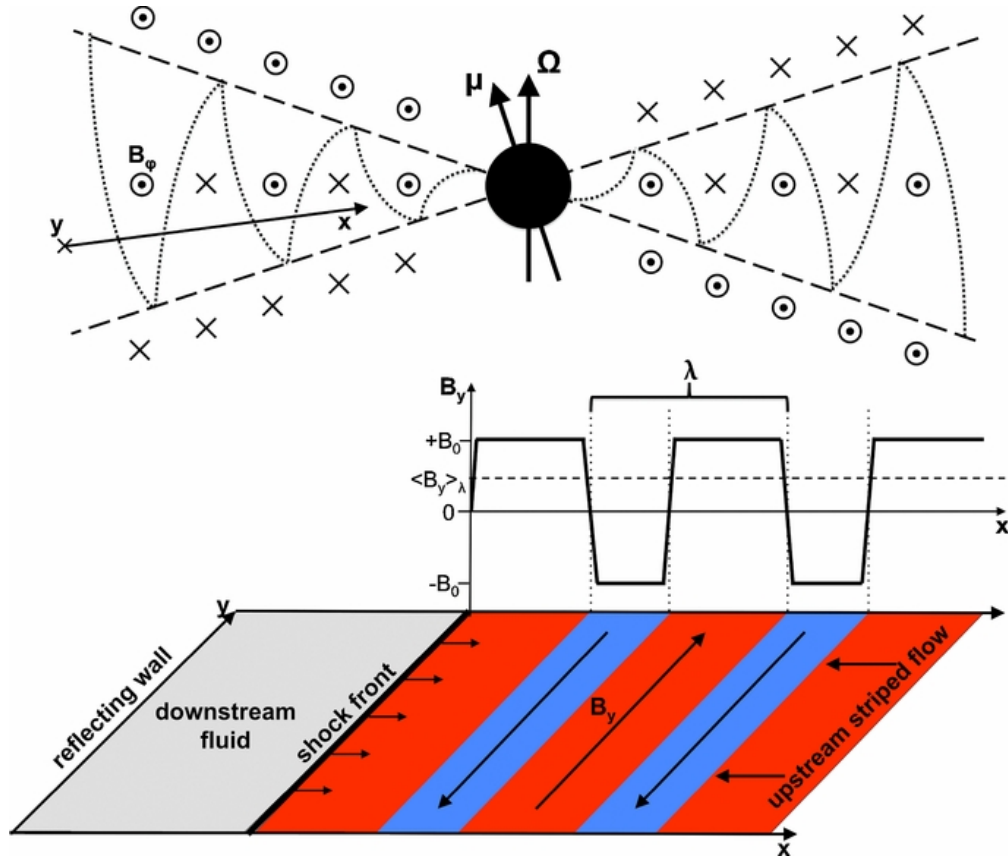


Figure 1.12: Schematic diagram of the striped pulsar wind [61].

gap; marked as blue-shaded regions inside the light cylinder in Figure 1.11), the stripped electrons and nuclei are accelerated to a Lorentz factor  $\gamma_0 \sim 10^7$  [59] by the electric field parallel to the magnetic field. In particular, relativistic electrons emit gamma rays by synchrotron or curvature radiation, and these gamma rays are converted into a pair of an electron and positron in a strong magnetic field (see §1.3.4). This cascade produces electrons and positrons  $\kappa = 10^3 - 10^5$  times the number of primary electrons stripped from the neutron star surface [60]. This pair production reduces the particle energy to  $\gamma_w = \gamma_0/\kappa \sim 10^3$ . Since nuclei do not initiate such a cascade, pulsar winds are predominantly leptonic.

Magnetic field lines can corotate with the neutron star and remain closed if their velocity does not exceed the speed of light. This condition is met up to the “light cylinder” where the tangential velocity equals the speed of light:  $2\pi R_L/P = R_L\Omega = c \rightarrow R_L = c/\Omega$ . Beyond this point are open field lines from the polar cap region on the neutron star surface – a region around the

magnetic pole out to  $\theta_{pc} = \arcsin \sqrt{R_\star/R_L}$ . The open field lines are in opposite directions in each hemisphere, forming the striped pulsar wind (Figure 1.12). The accelerated particles travel along these open field lines as an ultrarelativistic (bulk Lorentz factor  $\Gamma_w = 10^3 - 10^7$ ) wind. The absence of synchrotron radiation from this wind indicates that the wind is cold. When this wind encounters the external medium, that is, supernova ejecta, an ultrarelativistic shock (“termination shock”) is formed. Pulsar wind particles are (re)accelerated at the termination shock to even higher energies and create a PWN. The location of the termination shock  $R_{TS}$  is where the pulsar wind ram pressure equals the nebular pressure. The particle acceleration mechanism at the termination shock is unknown; as mentioned in §1.2, DSA may be difficult at relativistic shocks. Toroidal magnetic fields also make diffusion across the shock difficult. Another possibility is magnetic reconnection driven by the compressed striped alternating magnetic fields at the termination shock [61].

When a neutron star is approximated as an inclined rotating magnetic dipole, the electromagnetic power can be calculated using the Larmor formula [62]:

$$\dot{E} = \frac{B^2 R_\star^6 \Omega^4 \sin^2 \chi}{6c^3} = 10^{40} \left( \frac{B}{10^{12} \text{ G}} \right)^2 \left( \frac{P}{1 \text{ ms}} \right)^{-4} \sin^2 \chi \text{ erg s}^{-1}, \quad (1.56)$$

where  $\chi$  is the inclination angle. This power is converted into particle (relativistic electron and ion) and magnetic energies:

$$\dot{E} = \kappa \dot{N}_{GJ} m_e \Gamma_w c^2 \left( 1 + \frac{m_i}{\kappa m_e} + \sigma \right), \quad (1.57)$$

where  $\kappa$  is the multiplicity of pair production,  $\dot{N}_{GJ} = B\Omega^2 R_\star^3 / 2ec$  is the primary particle flux ( $c\rho_{GJ}/e$ ) integrated over the polar cap,  $m_{e,i}$  are electron and ion mass, and  $\sigma = B^2 / 4\pi\kappa\dot{N}_{GJ}m_e\Gamma_w c^2$  is the wind magnetization. The wind is Poynting-flux-dominated at the light cylinder ( $\sigma \sim 10^4$ ). However, it becomes kinetic-energy-dominated at the termination shock ( $\sigma \ll 1$ ). This drastic change of  $\sigma$  is not understood and is known as the “ $\sigma$  problem” [32].

The maximum energy achievable at the termination shock due to the potential drop can be estimated as  $E_{max} = Ze\eta_E B_{TS} R_{TS}$ , where  $Z$  is the atomic number of a pulsar wind particle,  $\eta_E =$

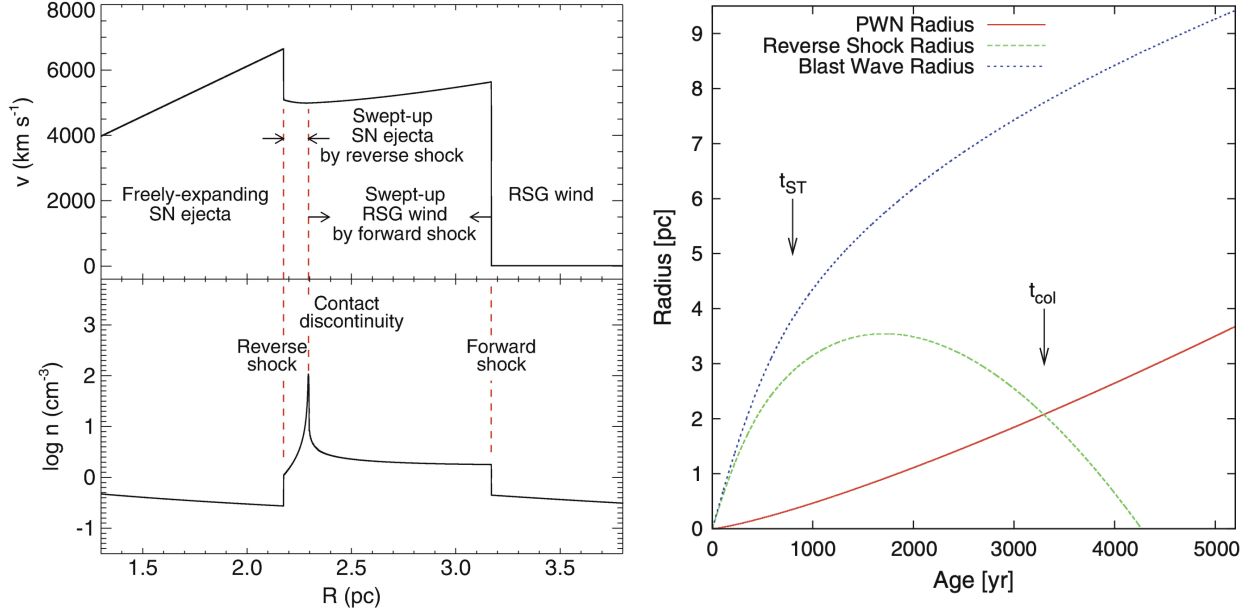


Figure 1.13: **Left:** plasma velocity and number density profile in a young SNR Cassiopeia A [63]. **Right:** A simulated evolution of the radii of an SNR forward shock (blast wave), reverse shock, and a PWN [64].

$E/B$  is the ratio of the electric field to the magnetic field, and  $B_{TS}$  is the magnetic field at the termination shock. Taking a fraction  $\eta_B$  of the pulsar wind ram pressure as the magnetic pressure,

$$\frac{B_{TS}^2}{4\pi} = \frac{\eta_B \dot{E}}{4\pi c R_{TS}^2} \Rightarrow E_{max} = Z e \eta_E \eta_B^{1/2} \dot{E}^{1/2} c^{-1/2} = 2 Z \eta_E \eta_B^{1/2} \left( \frac{\dot{E}}{10^{36} \text{ erg s}^{-1}} \right)^{1/2} \text{ PeV}, \quad (1.58)$$

where  $\eta_E \approx v_w/c \approx 1$  with the wind particle velocity  $v_w \sim c$ , and  $\eta_B < 1$ . Therefore, only the pulsars with  $\dot{E} > 10^{36} \text{ erg s}^{-1}$  have a chance to be leptonic PeVatrons.

As a PWN evolves from stage 1 to stage 2, the PWN encounters the reverse shock of its host SNR. A reverse shock is a shock developed behind the forward shock of an SNR by the high-pressure swept-up material (*left* panel of Figure 1.13). A reverse shock travels backward, i.e., toward the neutron star in the frame of the forward shock, sweeping up the supernova ejecta. In the lab frame, it initially travels forward, then slows down and starts traveling backward (*right* panel of Figure 1.13). The reverse shock can compress the PWN and raise the pressure inside the PWN. Once the PWN pressure exceeds the reverse shock pressure, the PWN can re-expand. While compression and re-expansion continue, the pulsar with a kick velocity  $v_{psr}$  may escape the

PWN. The relic PWN left behind the pulsar keeps radiating by synchrotron and inverse Compton emission and loses energy without any further injection, while the pulsar forms a new PWN around it with freshly accelerated energetic particles. As the largest group of VHE sources, PWNe in this stage often exhibit extended and irregular morphology [55].

The pulsar will eventually escape the host SNR and supersonically travel in the ISM, forming a bow-shock PWN. The time of the pulsar's escape  $t_{esc}$  can be estimated by equating the pulsar's travel distance and the SNR forward shock radius during the Sedov-Taylor phase [62]:

$$t_{esc} \approx 30 \left( \frac{E_{SN}}{10^{51} \text{ erg}} \right)^{1/3} \left( \frac{n_{ISM}}{1 \text{ cm}^{-3}} \right)^{-1/3} \left( \frac{v_{psr}}{400 \text{ km s}^{-1}} \right)^{-5/3} \text{ kyr.} \quad (1.59)$$

Pulsar wind particles can escape the bow-shock PWN and form a large (10s of pc) halo around the still-energetic ( $> 10^{34} \text{ erg s}^{-1}$ ) pulsar, emitting VHE gamma rays by inverse Compton scattering (e.g., [65]). Such halos serve as ideal astrophysical sources for studying suppressed diffusion around CR accelerators as well as positron excess in the case of nearby pulsars.

## Chapter 2: Instruments

Since Earth's atmosphere is opaque to gamma rays and X-rays, observing in this energy band, in principle, must be performed above the Earth's upper atmosphere. Such high-energy photons are most likely to interact with matter inelastically; therefore, a traditional way of focusing photons using mirrors and lenses onto a focal plane is not applicable. Moreover, a power-law spectrum of CRs means exponentially fewer photons in higher energies and, hence, a larger collection area, which is highly limited for space instruments. In this chapter, I introduce X-ray and gamma-ray telescopes designed to tackle those challenges and provide a high-energy view of our universe.

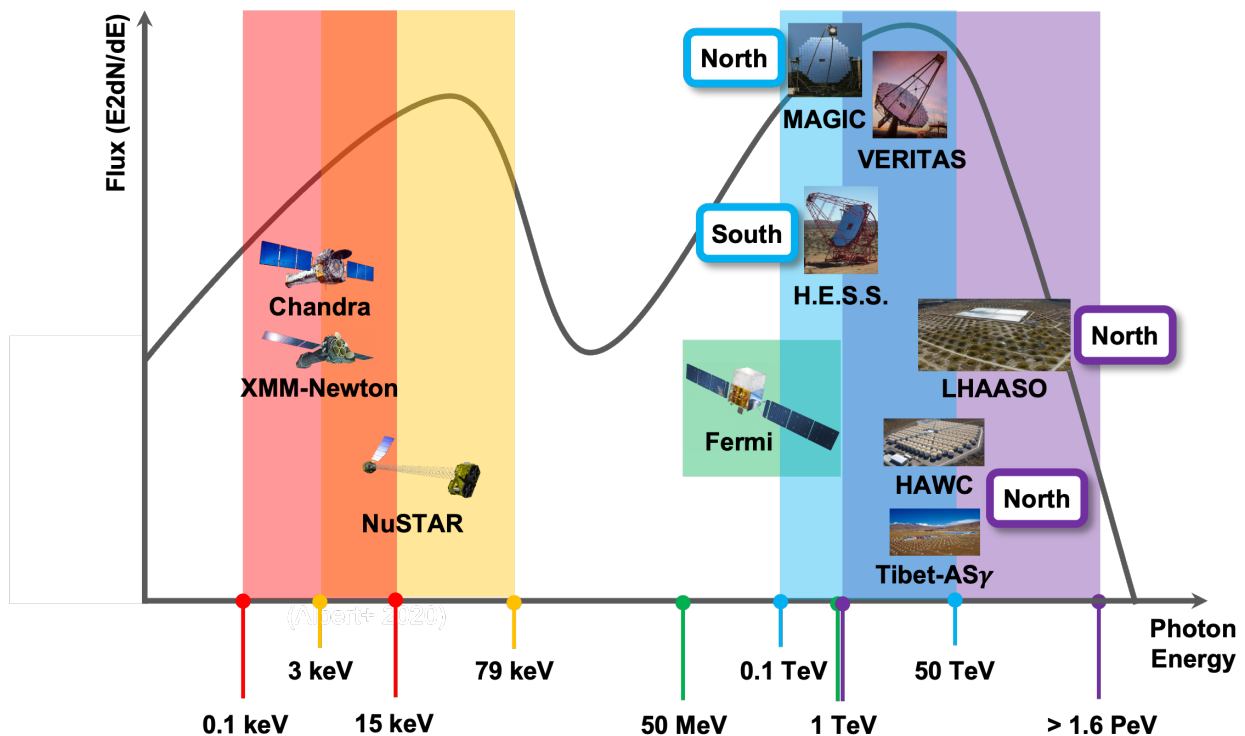


Figure 2.1: X-ray and gamma-ray instruments placed on the corresponding energy bands with different colors. A typical two-hump SED of a CR source is overlaid (black solid line). Ground-based gamma-ray observatories are labeled with the hemisphere of their location.

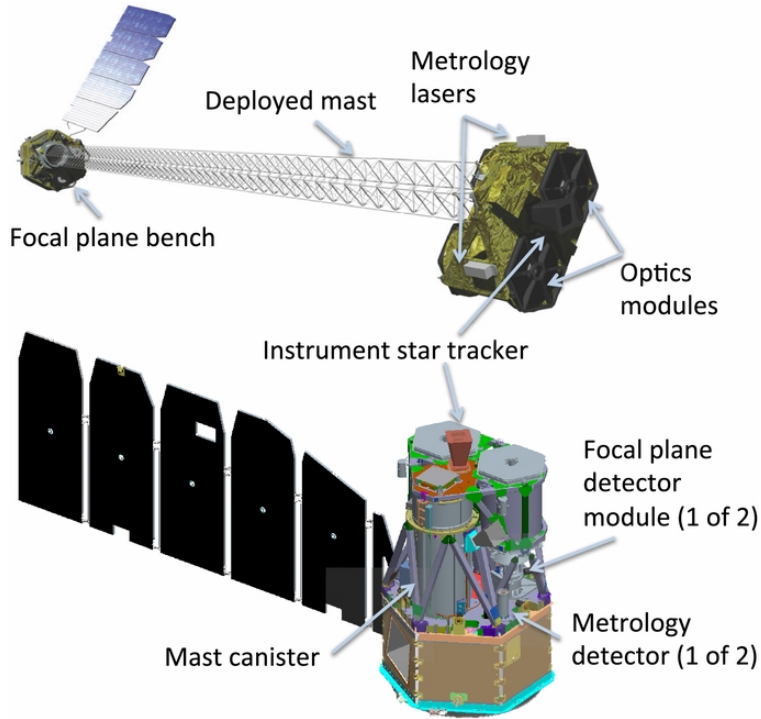


Figure 2.2: NuSTAR instrument [10]

## 2.1 NuSTAR: first focusing hard X-ray telescope

NuSTAR is a space-based X-ray telescope operating in the 3–78.4 keV range. Focusing hard X-ray photons requires a near-90° incidence angle (“grazing incidence”) to a smooth and highly reflective surface. Grazing incidence poses another challenge of a highly limited collection area. NuSTAR’s optics module comprises 133 concentric shells of conical-approximation Wolter type I mirrors coated with 200 alternating pairs of a low and high-density material layer (W/Si and Pt/SiC) [66]. Such an innovative optics design allows the focusing of hard X-ray photons with increased collection area, enabling imaging above 15 keV for the first time. An optics module is paired with a detector module carrying a  $2 \times 2$  array of state-of-the-art room-temperature CdZnTe photon counting detectors that provide a 12’ field of view (FOV). The detectors are surrounded by an anti-coincidence CsI shield that vetos signals from CRs or gamma rays [67]. NuSTAR carries two co-aligned hard X-ray telescopes, each consisting of an optics module and a focal plane module separated by a 10.14m (focal length) mast. NuSTAR’s angular resolution is 14’’ in

full width half maximum (FWHM) (58'' in half power diameter (HPD)), timing resolution is 2  $\mu$ s, and energy resolution is 400 eV at 10 keV (900 eV at 68 keV) [10].

NuSTAR's open geometry introduces unfocused X-rays from the cosmic X-ray background (CXB) and nearby astrophysical X-ray sources within 1°–4° as the dominant background components below  $\sim$  20 keV [68]. The background above  $\sim$  20 keV is mainly of instrumental origin (Compton-scattered gamma-rays, activation, and fluorescence lines). In particular, NuSTAR's low-inclination orbit keeps its CR-induced background level low [69]. Other background components include reflected solar X-rays, focused CXB, and partially focused X-rays (zero, one, or back bounce photons, also called ghost rays, in contrast to completely focused double front bounce photons). The NuSTAR background components are spatially and spectrally well characterized and can be modeled especially for extended source analysis [70].

#### 2.1.1 Chandra and XMM-Newton: soft X-ray telescopes

Even though the soft X-ray ( $< 10$  keV) band is often dominated by thermal continuum and line emission, it can still complement hard X-ray observation of nonthermal CR sources. For example, choosing the narrow band (i.e., 4–6 keV) without strong line emission can extend the X-ray spectrum of CR sources to lower energies with a possible contribution of a thermal continuum. Soft X-ray telescopes also utilize grazing incidence but do not adopt multilayer coating. Chandra [71] is sensitive in 0.1–10 keV. With an unbeatable subarcsecond angular resolution, Chandra provides a detailed view of the central engines of CR sources and substructures around them. XMM-Newton [72] carries three coaligned X-ray telescopes and the European Photon Imaging Camera (EPIC) sensitive in 0.1–15 keV. The EPIC consists of three CCD cameras (MOS1, MOS2, PN). With a moderate angular resolution (FWHM 6'') and outstanding FOV (0.5° in diameter), XMM-Newton provides a comprehensive view of diffuse extended CR sources.

## 2.2 Fermi-LAT: space-based gamma-ray telescope

Gamma rays with energies above 10 MeV interact with matter mainly through pair production. The Large Area Telescope (LAT) onboard the Fermi gamma-ray space telescope (Fermi-LAT; [73]) is a pair conversion detector that observes gamma-rays in the energy range of 50 MeV to 1 TeV. The LAT carries 16 tracker modules and 16 calorimeter modules. Each tracker module consists of multiple layers of tungsten foils and silicon-strip tracking detectors. Gamma rays entering a tracker module are converted into electron-positron pairs in one of the tungsten foils. The following detectors track the paths of the pairs to reconstruct the direction of the incident gamma rays until the pairs are deposited into a calorimeter module for energy reconstruction of the incident gamma rays. Scattering of the pairs in the conversion foils limits LAT's angular resolution. Therefore, LAT's angular resolution is highly energy-dependent; 68% containment angle is  $\sim 3.5^\circ$  at 100 MeV and  $\sim 0.1^\circ$  above 10 GeV. CRs incident on the LAT outnumber gamma rays by a factor of  $10^2$  to  $10^5$ . While minimal CR rejection is provided by the anti-coincident detectors surrounding the LAT, the data acquisition system onboard the LAT filters out remaining CR events according to the energy deposited in the calorimeters, signal registered by the anti-coincidence detector, and the track detected by the trackers [74].

The gamma-ray background of the LAT consists of the Galactic and isotropic (extragalactic) diffuse emissions. The Galactic gamma rays mainly originate from decays of pions produced by interactions between hadronic CRs, nonthermal Bremsstrahlung emission from leptonic-hadronic CR interactions, and ICS of interstellar photons off of leptonic CRs. These Galactic background components can be modeled using the matter and photon distributions derived from observations in other wavelengths and relevant theoretical models. The residual Galactic background and all of the isotropic background are attributed to unresolved Galactic and extragalactic astrophysical gamma-ray sources, respectively [75].

With its large FOV of 2.4 sr (19% of the sky), the LAT has been operating as a survey telescope since its launch in June 2008. The LAT's sensitivity has been ever-increasing thanks to the

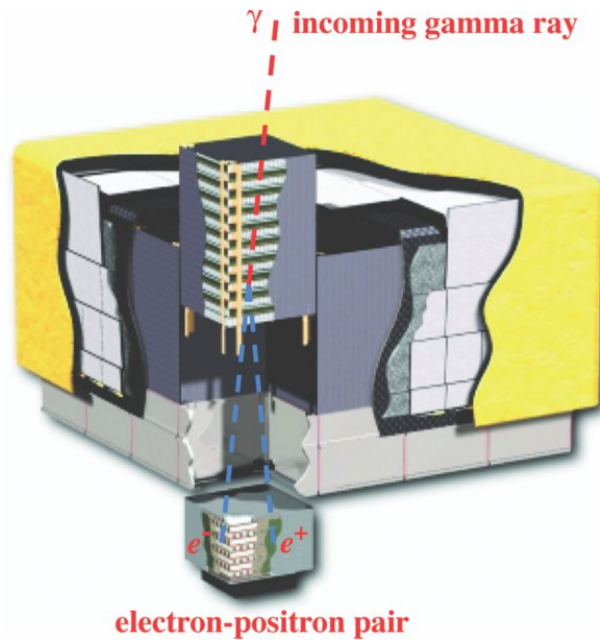


Figure 2.3: Fermi-LAT instrument [73]

cumulated photon statistics and improvement in the event filtering and reconstruction software. The latest LAT source catalog (4FGL-DR4 based on the first 14 years of data; [76, 77]) includes 7194 gamma-ray sources.

### 2.3 VERITAS: imaging atmospheric Cherenkov telescope

Detecting gamma rays with even higher energies requires more conversion material and a larger collection area. Due to the mass limit of a satellite, space-based pair conversion detectors are unsuitable for gamma-ray observation above the LAT's energy range. On the other hand, Earth's atmosphere can practically work as a giant conversion material for higher-energy gamma rays; the vertical atmospheric depth at the sea level,  $1030 \text{ g cm}^{-2}$ , is roughly 28 radiation lengths (one radiation length is  $37.1 \text{ g cm}^{-2}$ ). Moreover, the atmosphere acts as an amplifier in which the pairs created by a gamma ray radiate bremsstrahlung gamma rays, which create more pairs, and so on. These pairs travel along nearly the same trajectory as the original gamma ray. This chain reaction of pair conversion and bremsstrahlung emission, so-called electromagnetic shower, continues until the shower particle (electrons and positrons) energies reach the critical energy  $\approx 87 \text{ MeV}$  at which

the main energy loss mechanism of the shower particles changes from bremsstrahlung radiation to ionization. The shower starts after one radiation length at an altitude of  $\sim 20$  km, reaches its maximum (i.e., the maximum number of shower particles) when the shower particle energy equals the critical energy, then slowly dies out. The number of shower particles at the shower maximum ( $N_{max}$ ) and the altitude of the shower maximum ( $h_{max}$ ) depend on the gamma-ray energy – ( $N_{max} = 1.3 \times 10^2$ ,  $h_{max} = 10.3$  km) for 100 GeV gamma rays, and ( $N_{max} = 9.3 \times 10^4$ ,  $h_{max} = 5.5$  km) for 100 TeV gamma rays. [78]

The atmosphere also serves as a calorimeter for the pairs from the shower. All shower particles move faster than the speed of light in the atmosphere for the wavelengths to which the atmosphere is transparent; that is, the velocity  $v$  of electrons and positrons in a cascade at any altitude  $h$  is always greater than the speed of light in the atmosphere  $c(\omega, h)$  for all frequencies  $\omega$  within the visible window on Earth. Such motion of electrons and positrons produces Cherenkov radiation with an intensity proportional to photon frequency, and hence, brightest in the blue to near-UV band for the visible window on Earth. Since all shower particles emit Cherenkov photons, the energy and other properties of an initial gamma ray can be deduced from those photons.

A Cherenkov photon is emitted at an angle  $\theta = \cos^{-1}[c(\omega, h)/v] = \cos^{-1}[1/\beta n(\omega, h)]$  with respect to the direction of motion for the electron, where  $\beta = c_0/v$ ,  $c_0$  is the speed of light in vacuum, and  $n(\omega, h) = c/c(\omega, h)$  is the refraction index of the atmosphere as a function of photon frequency and altitude. Due to the altitude dependency of  $c(\omega, h)$  and  $\theta$ , Cherenkov photons, mainly from around the shower maximum, reach the ground within only a few nanosecond windows and form a ring at  $\sim 130$ -170 m centered at the gamma-ray impact position. This means that a telescope equipped with an optical reflector and a camera with a  $\sim 10$  nanoseconds integration time can capture the image of the Cherenkov photons from anywhere within the ring. This image (“shower image”; in particular, the shape and intensity of the image), combined with highly convoluted simulations of particle interactions and atmospheric effects, can be reconstructed into a gamma ray with energy and sky coordinates, enabling imaging of astrophysical gamma-ray sources. Such telescopes, called imaging atmospheric Cherenkov telescopes (IACTs), opened the era of VHE

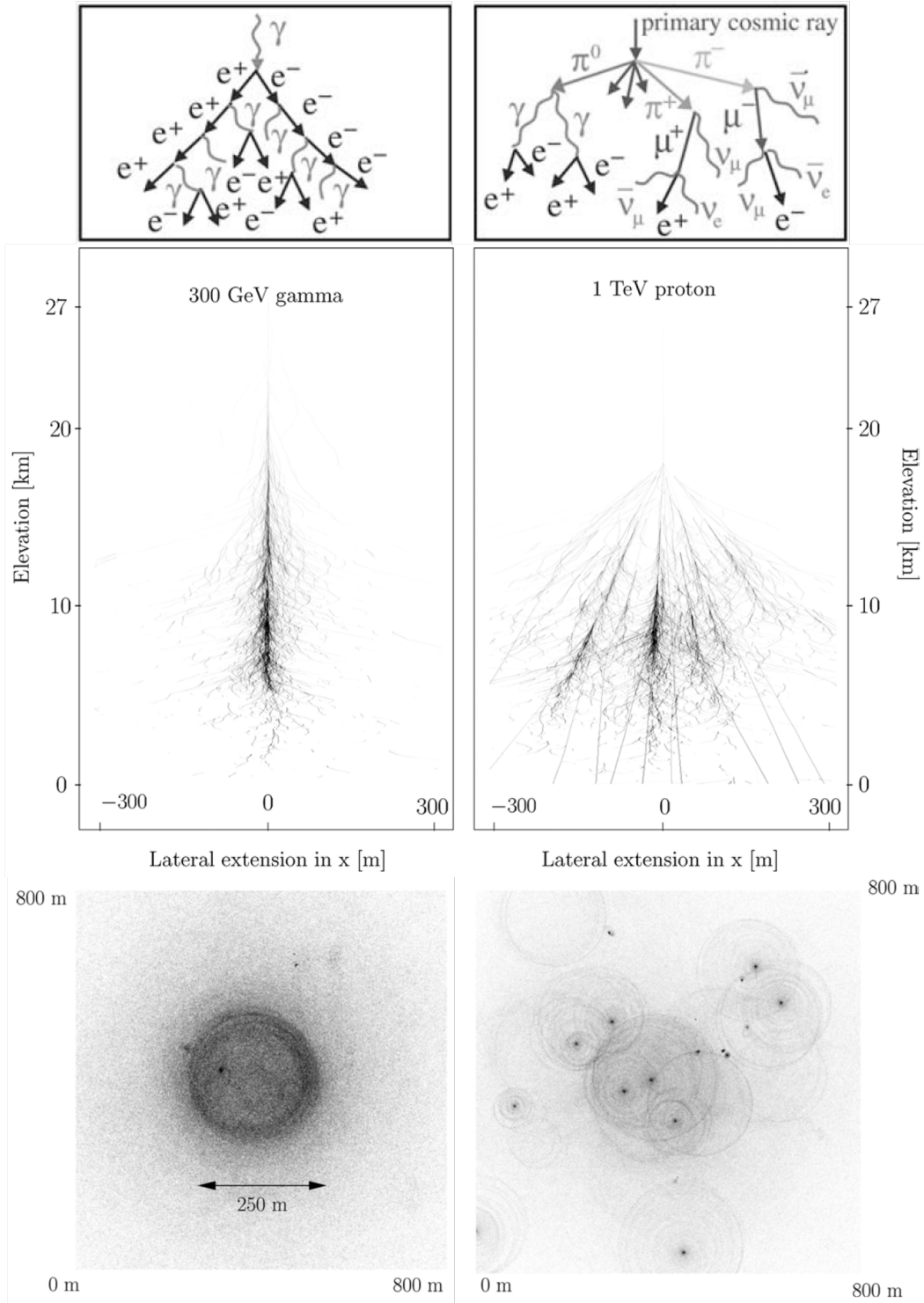


Figure 2.4: Comparison of a gamma-ray-induced electromagnetic shower (*left*) and CR-induced hadronic shower (*right*): schematic diagrams of the showers (**top row**, [78]), shower particle trajectories (**middle row**) and Cherenkov photon distributions on the ground (**bottom row**). The images in the middle and bottom rows are from simulations ([79]).

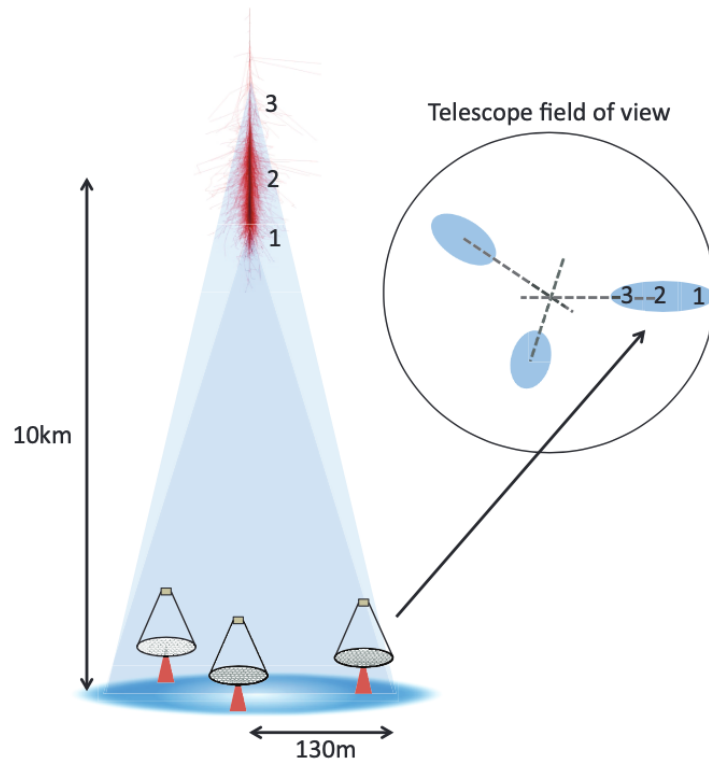


Figure 2.5: An illustration of the stereoscopic imaging technique of IACTs [80].

gamma-ray astronomy. Multiple IACTs can be configured into an array to capture images of the same shower at different locations (“stereoscopic imaging technique”), enhancing the geometrical shower reconstructions.

Unfortunately, gamma-ray-induced electromagnetic shower particles are not the only sources of Cherenkov photons in the atmosphere. As shown in §1.3.1, CR protons interact with atmospheric nuclei to produce pions, which decay into gamma rays and muons. The secondary gamma rays produce the same electromagnetic showers as those induced by gamma rays, while the secondary muons may survive until near the ground (“local muons”), producing Cherenkov photons or decay into electrons and positrons, which also produce Cherenkov photons. These hadronic showers overwhelm gamma-ray-induced showers in numbers by a factor of  $10^3$  to  $10^4$ , making them the major background component of gamma-ray observation. However, hadronic shower particles inherit only  $\sim 1/3$  of the primary proton energy and have larger transverse momenta than gamma-ray-induced shower particles. This results in the weaker and more irregular Cherenkov radiation



Figure 2.6: VERITAS (photo credit: Center for Astrophysics | Harvard & Smithsonian)

of a CR-induced hadronic shower compared with well-defined bright Cherenkov rings of a shower induced by a gamma ray with the same energy as the CR. Such differences in the shower images allow one way to discriminate between CR and gamma-ray events. High-energy local muons may still produce Cherenkov rings, similar to that seen in gamma-ray showers, but near the ground. In the case of an array of IACTs, these local events will be detected only by a single IACT, while Cherenkov rings of gamma-ray showers at a much higher altitude will be detected by more than one IACT. This different multiplicity of telescopes for different events provides another discrimination power.

VERITAS, located in Amado, Arizona, is an array of four IACTs sensitive in 85 GeV to  $>30$  TeV. Each telescope is equipped with a 12m optical reflector and 499-pixel photomultiplier tube

(PMT) cameras, providing a FOV of  $3.5^\circ$  in diameter and angular resolution of  $0.08^\circ$  (68% containment radius) at 1 TeV [9]. Other operating IACTs are Major Atmospheric Gamma Imaging Cherenkov Telescopes (MAGIC) in La Palma [81] and High Energy Stereoscopic System (H.E.S.S.) in Namibia [82]. Unlike space-based observatories, observing time of IACTs on the ground is limited to dark times, i.e., nighttime without a bright Moon (10-20% duty cycle).

## 2.4 LHAASO: extensive air shower arrays

Gamma rays with energies even greater than the IACT energy range produce showers that reach the ground level. One can use scintillators to directly detect the shower particles or use giant water tanks to induce water Cherenkov radiation that PMT cameras can detect. Arrays of those scintillators or water Cherenkov detectors, called extensive air shower arrays (EASAs), are located on the mountains to be as close to the shower maximum of TeV-PeV gamma rays as possible. EASAs offer large FOVs ( $\sim 2$  sr) and  $\sim 100\%$  duty cycle [83]. LHAASO [8] is an EASA in China comprising three sub-arrays: Water Cherenkov Detector Array (WCDA, sensitive in 1-25 TeV), Kilometer Square Array (KM2A, a scintillation detector array sensitive in 10 TeV - 1.6 PeV), and Wide Field of View Cherenkov Telescope Array (WFCTA, an IACT array). While the WCDA discriminates CR background events using the shower image properties, similar to IACTs, the KM2A utilizes the penetrating capability of muons to detect them with underground water Cherenkov detectors and provide an accurate measurement of the background. Moreover, the KM2A is the first gamma-ray observatory sensitive above 1 PeV, pioneering UHE gamma-ray astronomy and bringing us closer to the mystery of PeVatrons. Other operating EASAs include High-Altitude Water Cherenkov (HAWC) in Mexico [84] and Tibet AS-Gamma in Tibet, China [85]. LHAASO was not used for this work.

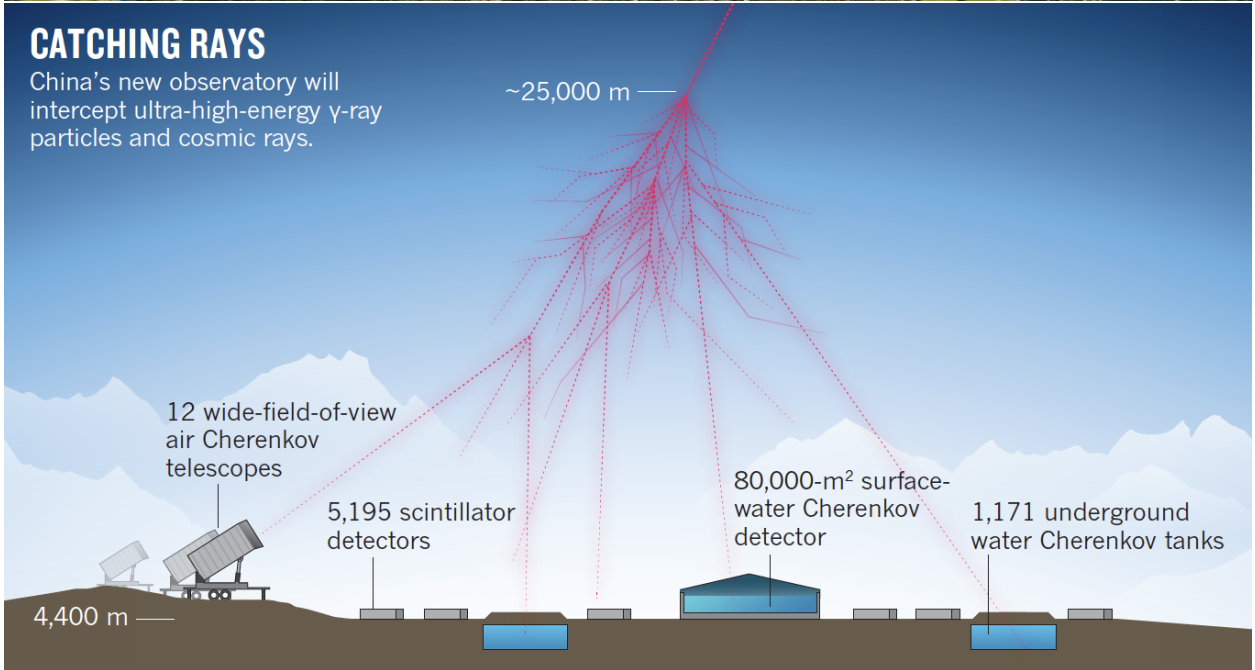


Figure 2.7: **Top**: the LHAASO site (photo credit: Chinese Academy of Sciences.) **Bottom**: a schematic diagram of different detector types [86].

## Chapter 3: Cassiopeia A – young supernova remnant

The contents of this chapter have been peer-reviewed and published [87]. The summary and key findings of this chapter are as follows.

- We observe the synchrotron radiation (§1.3.4) of Cassiopeia A in the hard X-ray band using NuSTAR (§2.1) to deduce the spectrum and location of ongoing CR electron acceleration. The spectrum and location of CR acceleration are used to elucidate the CR acceleration mechanism in this young SNR (§1.4.1, “Stage 1” in Figure 1.10).
- The deduced CR electron spectrum indicates Cas A is not a leptonic PeVatron. VHE observations of Cas A indicate CR protons are accelerated and produce gamma rays by pion decay (§1.3.1), but Cas A is not a hadronic PeVatron (e.g., [53]).
- While the forward shock of a young SNR is often considered the main CR acceleration site (§1.4.1), the reverse shock appears to be powering the most energetic CR acceleration in Cas A.
- The spectral index of CR electrons from this work matches the prediction of mNLDSA (§1.2.4). It also agrees with the CR proton spectral index deduced from VHE observations [53], indicating the same acceleration mechanism and location for CR electrons and protons, namely mNLDSA and the reverse shock, respectively.

### 3.1 Introduction

SNRs have been considered excellent candidates for Galactic CR accelerators due to the large energy of supernova explosions ( $E_{SN} \gtrsim 10^{51}$  erg) and formation of a strong shock (Mach number  $\mathcal{M} \gg 1$ ). In particular, at the early stage of their evolution ( $< 1$  kyr), their fast shock velocities

( $v_{sh} \sim$  several thousand  $\text{km s}^{-1}$ ) and amplified magnetic fields ( $B \sim$  a few hundred  $\mu\text{G}$ ) make SNRs ideal CR accelerators. The resultant CR spectrum bears crucial information about the shock acceleration mechanism operating in SNRs and about their acceleration environments, such as shock velocity, magnetic field, and ambient matter density. The spectrum of the most energetic CR electrons with teraelectronvolt (TeV,  $10^{12}$  eV) energies can be probed via the X-rays they emit by gyrating around magnetic fields (synchrotron radiation). Long-term monitoring with Chandra revealed that some young SNRs exhibited localized year-scale increases and decreases of soft X-ray flux in the 4-6 kiloelectronvolt (keV,  $10^3$  eV) band by  $\sim 50\%$ . This rapid and extreme variability was attributed to fast electron acceleration and synchrotron cooling in a high magnetic field,  $B \geq 100 \mu\text{G}$  [88, 89, 90]. However, the energetics and spectrum of CR electrons cannot be inferred from such narrow-band observations. A further complication arises due to the contamination of their soft X-ray spectrum by significant bremsstrahlung radiation of thermal electrons ( $kT \sim$  a few keV).

A direct measurement of CR electrons comes from hard X-ray observations above  $\sim 15$  keV where the contamination by thermal electrons is minimal. The spatial distribution of the most energetic CR electrons in Cas A, a young ( $\sim 350$  years old [91]) nearby (3.4 kpc away [92]) SNR, was first resolved by NuSTAR. Cas A is a bright X-ray source whose synchrotron emission from ultra-relativistic CR electrons extends up to  $\sim 50$  keV. The 2.4 Ms of data collected in 2012-2013 showed that X-rays above 15 keV are predominantly emitted from knots [93] coincident with the regions that showed fast variability in the soft X-ray observations with Chandra [89, 94, 95]. In addition, these regions are located at the reverse shock rather than the forward shock, where the strongest particle acceleration is expected (Figure 3.2 (a)).

NuSTAR observed Cas A again in 2023 for 188 ks. Combined with archival observations (Table 3.1), the multi-epoch NuSTAR data above 15 keV obtained over a 10-yr baseline allowed us a unique opportunity to track the most extreme particle acceleration and cooling process operating in Cas A.

Table 3.1: List of archival and new observations

Observation ID	Date	Position angle (deg)	Offset <sup>†</sup> (arcmin)	Exposure (ks)
40001019002	2012-08-18	84	0.9	291
40021001002	2012-08-27	76	2.0	170
40021001005	2012-10-07	33	1.5	183
40021002002	2012-11-23	338	0.3	271
40021002006*	2013-03-02	249	3.9	136
40021002008*	2013-03-05	249	4.0	189
40021003003	2013-05-28	151	3.5	198
40021011002	2013-10-30	7	1.8	236
40021012002	2013-11-27	335	1.1	206
40021015003	2013-12-23	312	1.6	137
Total exposure (archival data)				2,017
40801003002	2023-03-24	229	2.2	92
40801013002	2023-04-04	217	2.5	95
Total exposure (new data)				188

The exposure has been corrected for deadtime and SAA passages. For the archival data, only the observations with exposures over 100 ks are listed.

\*Only these two observations (total exposure 325 ks) were used in this work to represent the archival data to minimize the systematic uncertainties.

<sup>†</sup>Offsets were calculated as an angular separation between the pointing coordinates and the center of a circular region with a radius of 30'' encompassing the two bright kongs on the west (see Figure 3.2).

## 3.2 Multi-epoch X-ray analysis

### 3.2.1 Observations and data reduction

Cas A was observed by NuSTAR in August 2012 - December 2013 for a net exposure of 2.2 Ms in total, and in March - April 2023 for a net exposure of 188 ks in total (Table 3.1). We reduced the data using NuSTAR Data Analysis Software (NuSTARDAS) version 2.1.2 and CALDB version 20240325. The NuSTARDAS pipeline produces cleaned event files with good time intervals after screening the South Atlantic Anomaly (SAA) passages and applying data quality cuts. We applied the most conservative criteria for filtering the SAA passages to ensure the most stable and accurate flux measurement.

### 3.2.2 Background estimation

Since Cas A is a bright extended ( $\sim 6'$  across) source, no region in the NuSTAR field of view ( $13' \times 13'$ ) is truly source-free to be used for background estimation. Instead, we modeled the background of each observation using `nuskybgd`, a code for simulating NuSTAR’s background [70]. NuSTAR’s background is comprised of three components: (1) focused cosmic X-ray background (CXB), (2) non-focused (“stray light”) CXB, and (3) internal background composed of a continuum and multiple lines. (3) is predominant above 10 keV, while (2) is strongest below 10 keV [93]. `nuskybgd` generates a model for each component and normalizes it utilizing regions outside of the source where no additional emission to the background components is expected. To account for the smearing of Cas A’s emission into the regions outside of the remnant due to the finite size of the PSF (14'' FWHM), we added a phenomenological source model to the `nuskybgd` background model. After normalizing, the source model was removed, and the background model was used to simulate the background spectrum in the source region (radius 3' circle) with the `fakeit` command in Xspec for an exposure of 10 Ms. Background images were also generated using the normalized background-only model.

### 3.2.3 Spectral analysis

We analyzed the data in the 15-50 keV band. This choice of energy range ensures negligible contribution of thermal X-rays ( $kT < 4$  keV [101, 102, 103, 104, 105]) and source emission above the background level. In addition, the uncertainty of background estimation is minimized in this energy range since the predominant background component (internal background) is well understood, and the smearing of the source counts is minimal. While combining multiple archival observations may reduce statistical uncertainty in spectral shape and flux measurement, it can introduce even greater systematic uncertainties caused by instrumental (different telescope pointing) and physical (source variability) effects. To minimize these systematic uncertainties, we selected two representative archival observations (observation ID 40021002006 and 40021002008, total exposure 324 ks) to compare with the new observations, given their similar position angles to the

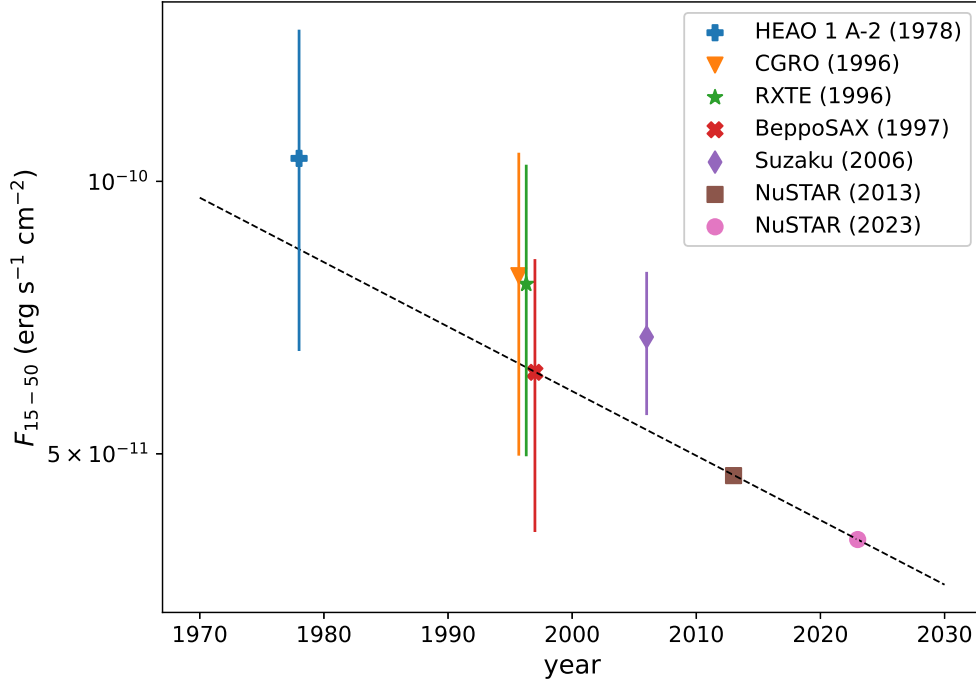


Figure 3.1: **Historical X-ray flux of Cas A in the 15-50 keV band.** The flux was calculated from the best-fit spectral model for each telescope data. The errors for the spectral model parameters were propagated to calculate the error for the flux. For HEAO 1 A-2, a power law model was fitted to the spectral data reported in [96]. Previously reported best-fit spectral parameters were used for CGRO [97], RXTE [98], BeppoSAX [99], and Suzaku [100]. For NuSTAR, the error bars are smaller than the markers. The dashed black line shows the flux decrease rate ( $1.6 \pm 0.1$ )% yr $^{-1}$  found from a linear regression of all the data points accounting for the error bars.

new observations and the minimal time gap (3 days) between them. The two selected archival observations are referred to as the archival observations hereafter.

We extracted the source spectra for the entire remnant (radius 6' circle). We modeled the spectra with an absorbed power law where the hydrogen column density was fixed to  $N_H = 2.14 \times 10^{22}$  cm $^{-2}$  [106]. The abundance table from [107] was used. The spectral parameters were linked among the observations within each epoch. A cross-normalization term was multiplied to each spectra with respect to the FPMA spectra of the earliest observations in each epoch. The average cross-normalizations are  $1.019 \pm 0.005$  for the archival data, and  $1.011 \pm 0.007$  for the new data. The model fits the data well (reduced  $\chi^2 \sim 1$ ). The best-fit power-law photon index for the archival observations is  $3.42 \pm 0.02$ , and the 15-50 keV flux is  $(4.73 \pm 0.04) \times 10^{-11}$  erg s $^{-1}$  cm $^{-2}$ . The

new observations after 10 years show that the spectral shape remains unchanged within statistical uncertainties (power-law index  $3.37 \pm 0.02$ ), and the 15-50 keV flux ( $(4.02 \pm 0.04) \times 10^{-11}$  erg s $^{-1}$  cm $^{-2}$ ) decreased by  $(15 \pm 1)\%$  (Figure 3.1). If the flux decreased simply by electrons' synchrotron cooling, the spectrum should have become softer due to the inverse relation between synchrotron loss and electron energy. The null-detection of X-ray spectral softening, therefore, indicates that additional physical processes are operating in addition to synchrotron cooling.

### 3.2.4 Image production

We produced a counts map, background image, and exposure map for each observation and focal plane module in the 15-50 keV range. Vignetting was corrected in the exposure maps for the mean energy (32.5 keV). Flux maps were calculated by subtracting a background image from a count map and dividing it by an exposure map. Individual flux maps were combined within each epoch to generate a flux map for 2013 and 2023. We applied the Lucy-Richardson deconvolution algorithm [108, 109] to the flux maps for 50 iterations using the on-axis NuSTAR PSF for the 20-79 keV range (Figure 3.2 (a) and (b)).

## 3.3 Temporal synchrotron spectral energy distribution modeling

For the sub-petaelectronvolt (PeV,  $10^{15}$  eV) electrons emitting synchrotron X-rays with photon energy  $E_\gamma$  in a highly amplified magnetic field  $B$  (0.1-1 mG), [111, 112, 113, 50, 114, 89, 94], the synchrotron cooling time [115]

$$t_{1/2} = 12 \left( \frac{E_\gamma}{10 \text{ keV}} \right)^{-1/2} \left( \frac{B}{100 \mu\text{G}} \right)^{-3/2} \text{ yr} \quad (3.1)$$

is much shorter than the length of our baseline. Without ongoing electron acceleration, the hard X-ray flux of Cas A would have decreased by more than 90%. Instead, we observe a  $(15 \pm 1)\%$  decrease in the 15-50 keV flux from the whole remnant over the past 10 years (Figure 3.1, uncertainties are  $1-\sigma$  hereafter). The largest flux decrease is observed at the bright knots on the western

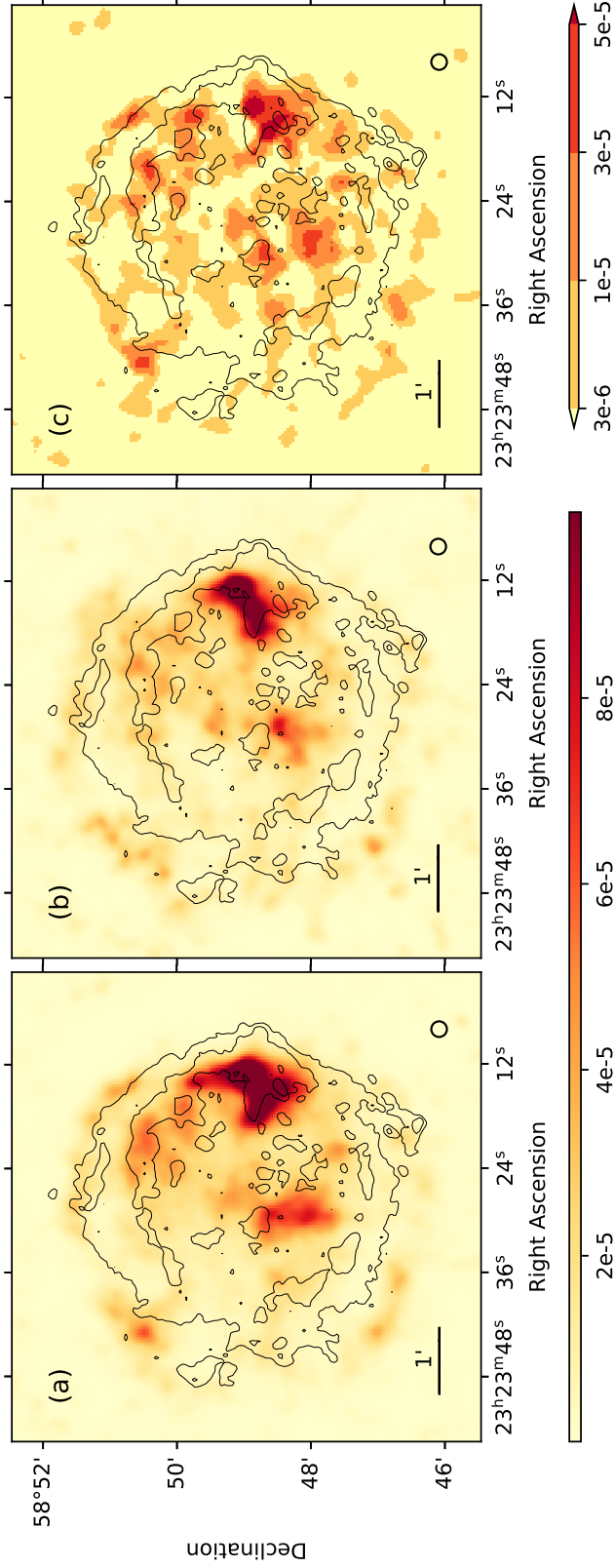


Figure 3.2: **15-50 keV flux maps of Cas A in 2013 (a) and 2023 (b), and a difference map between 2013 and 2023 (c).** For (a) and (b), background-subtracted counts maps were divided by vignetting-corrected exposure maps, then iteratively deconvolved using the on-axis NuSTAR point spread function (PSF, see §3.2.4). The two images were scaled equally to ensure direct comparison. (c) was generated by subtracting (b) from (a). All three images were smoothed with a Gaussian kernel ( $\sigma = 3.5'' = 1.5$  pixel). The L-band radio contour [110] is overlaid in black. A circle with diameter  $14''$  is overlaid at the right bottom corner of each image to indicate the size of the NuSTAR PSF ( $14''$  FWHM). Fading over the entire remnant is clearly noticeable. Most prominently, the brightest knots inside the remnant (in the middle and on the west) dimmed significantly.

rim of the reverse shock (Figure 3.2 (c)). Moreover, the synchrotron cooling mechanism naturally softens the radiation spectrum (producing a larger photon index  $\Gamma$  when  $dN_\gamma/dE_\gamma \propto E_\gamma^{-\Gamma}$ ), whereas our spectral analysis does not find a statistically significant spectral softening in the 15-50 keV band ( $\Gamma = 3.42 \pm 0.02$  in 2013 and  $\Gamma = 3.37 \pm 0.02$  in 2023). Extreme electron acceleration must be operative in Cas A injecting freshly accelerated electrons. The X-ray spectrum of the injected electrons, when combined with the X-ray spectrum of the rapidly cooling preexisting electrons, leads to an essentially constant photon index with time.

To constrain the spectrum of ongoing electron acceleration in Cas A, we modeled a multi-wavelength SED of Cas A. We first constructed the multiwavelength SED of the whole remnant using the NuSTAR spectrum from this work and the radio spectrum from [116] for each epoch. The radio spectrum was calculated for each epoch in the L (1395 MHz) and X (9000 MHz) band using the temporal spectral model in [116] (eq. 14, Table 5). This radio spectral model provides the best fit to the 20-yr (1995–2014) Green Bank Observatory (GBO) 40-foot L-band data and the 3-yr (2014-2017) GBO 20-m L-band and X-band data. A Gaussian quadrature sum of the  $1-\sigma$  uncertainty of each model parameter was used as a  $1-\sigma$  uncertainty of the radio spectrum (eq. 15, Table 5). The radio flux variability calculated from this model is 8% and 6% decrease in the L and X bands, respectively.

### 3.3.1 SED model description

The SED was modeled with a synchrotron radiation spectrum in a Gaussian turbulent magnetic field [117]. A recent X-ray polarization measurement by the Imaging X-ray Polarimetry Explorer (IXPE) [118] suggests magnetic turbulence in Cas A on a scale smaller than  $\sim 0.4$  pc (IXPE angular resolution  $24''$  at the source distance 3.4 kpc). A Gaussian distribution of the magnetic field strength in an SNR is theoretically motivated (e.g., [119]). The magnetic field distribution is assumed unchanged between 2013 and 2023. Nonthermal electrons present in 2013 (“preexisting

electrons”) are modeled with an exponential cutoff power law distribution:

$$\frac{dN}{dE} = N_0 \left( \frac{E}{1 \text{ TeV}} \right)^{-q} \exp \left( -\frac{E}{E_{cut}} \right)^\beta. \quad (3.2)$$

The minimum and maximum energy bound for the electron distribution were set to  $E_{min} = 100$  MeV and  $E_{max} = 3$  PeV, respectively. The electrons lose energy by adiabatic and synchrotron cooling every time step.

An injected electron spectrum follows an exponential cutoff power law distribution with a distinct set of parameters from preexisting electrons.  $N_0$  is determined by normalizing the distribution to (constant injection rate)  $\times$  (time step) between the same  $E_{min}$  and  $E_{max}$  as preexisting electrons.  $\beta = 2$  is held fixed to reflect the synchrotron-loss-limited electron acceleration at the Bohm limit [120]. These electrons are injected and lose energy every time step by adiabatic and synchrotron cooling.

The same adiabatic and synchrotron loss formulae are used for both preexisting and injected electrons. Adiabatic energy loss is

$$\dot{E}_{ad} = \frac{\langle \dot{R}_{sh} \rangle}{\langle R_{sh} \rangle} E, \quad (3.3)$$

where  $E$  is an electron energy,  $\langle \dot{R}_{sh} \rangle / \langle R_{sh} \rangle$  is an average expansion rate of all electrons. Pitch-angle-averaged synchrotron energy loss is [117]

$$\langle \dot{E}_{syn} \rangle = \frac{4}{3} \sigma_T \left( 1 - \frac{1}{\gamma^2} \right) \gamma^2 c \frac{B_0^2}{8\pi}, \quad (3.4)$$

where  $\sigma_T$  is the Thomson cross-section,  $\gamma$  is an electron Lorentz factor, and  $B_0$  is a standard deviation of a Gaussian distribution of magnetic field strength. Synchrotron loss of radio-emitting electrons is negligible ( $\ll 1\%$ ) over the 10-year period of our consideration for any reasonable magnetic field strength  $<$  a few mG. The adiabatic loss rate  $\sim 0.3\% \text{ yr}^{-1}$  is necessary to reproduce the observed radio spectral variability. This rate is comparable to the average expansion rate of Cas A’s forward shock ( $0.218 \pm 0.029\%$ )  $\text{yr}^{-1}$  measured with multi-epoch Chandra observation [121].

On the other hand, for X-ray-emitting electrons, synchrotron loss ( $\gg 50\%$ ) overpowers adiabatic loss in any reasonable magnetic field strength  $>$  a few tens of  $\mu\text{G}$ .

We first find a preexisting electron spectrum that reproduces the NuSTAR and radio spectrum in 2013. Then an injected electron spectrum is added every time step on top of the best-fit preexisting electron spectrum, and both electron populations are cooled every time step to reproduce the NuSTAR and radio spectrum in 2023. The size of the time step is  $\min(0.1 \text{ yr}, E_{max}/\dot{E}_{syn})$ .

### 3.3.2 SED modeling results

Setting the injection rate to zero, magnetic field  $B_0 \sim 6 \mu\text{G}$  is required for the observed 15% flux decrease in the 15-50 keV band (Figure 3.3 *top left*). This magnetic field is at least an order of magnitude smaller than the previous estimations [111, 112, 113, 50, 114, 89, 94]. Inverse Compton scattering [122] of the cosmic microwave background and infrared (temperature  $\sim 100$  K, energy density  $2 \text{ eV cm}^{-3}$  [123]) photons off the electron distribution found with this magnetic field produces significantly more gamma rays than those observed by VERITAS [53] and Fermi-LAT [76, 77] (Figure 3.3 *top right*), or MAGIC [124].

Assuming that the observed TeV gamma rays are produced entirely by inverse Compton Scattering of electrons, the lower limit on the magnetic field is found to be  $B_0 = 123 \pm 8 \mu\text{G}$  (Figure 3.3 *bottom left*). This is comparable to the lower limit placed by [53] ( $\sim 150 \mu\text{G}$ ) using a similar approach. The best-fit electron distribution found with this magnetic field, however, reproduces the radio and X-ray spectrum only in 2013. Due to a much faster synchrotron cooling than when  $B_0 = 6 \mu\text{G}$ , the predicted X-ray flux in 2023 is  $\sim 10$  times lower, and the spectrum is much softer than the observed X-ray flux. This discrepancy between the prediction and observation leaves no possibility other than electron injection into Cas A compensating extremely rapid energy loss of preexisting electrons.

We constrain the characteristics of the preexisting and injected electron spectra using the lower-limit magnetic field found in this work ( $123 \pm 8 \mu\text{G}$ ) and the upper-limit magnetic field established in the previous works ( $B \sim 1 \text{ mG}$ , [111, 112, 113, 50, 114, 89, 94]). The best-fit model parameters

Table 3.2: Best-fit parameters for the synchrotron cooling and injection model

Electron population	Preexisting electrons <sup>†</sup>	Injected electrons		
$B_0$ ( $\mu\text{G}$ )	$123 \pm 8$	$123 \pm 8$	400*	1000*
$q$	$2.44 \pm 0.03$	2.2	2.0	1.9
$E_{cut}$ (TeV)	$4 \pm 1$	36	19	12
$\beta$	$0.74 \pm 0.05$	2*	2*	2*
Total electron energy (fraction) <sup>‡</sup>	$(1.09 \pm 0.02) \times 10^{49}$ erg	0.4%	0.9%	2.1%
Injection rate ( $10^{37}$ erg s <sup>-1</sup> )	–	14	4	2

\*Parameters were held fixed.

<sup>†</sup>The parameters for preexisting electrons are given only for the lower-limit magnetic field  $B_0 = 123 \pm 8 \mu\text{G}$ . For higher magnetic fields,  $q$  and  $\beta$  do not change, while  $E_{cut}$  and total electron energy decrease.

<sup>‡</sup>Total electron energy is reported for preexisting electrons. The fraction of the total energy of the preexisting electrons that were injected between 2012-2013 is reported for injected electrons.

for preexisting and injected electrons for magnetic fields  $B_0 = (123, 400, 1000) \mu\text{G}$  are listed in Table 3.2.

### 3.4 Discussion

#### 3.4.1 Hard injection spectrum

For the lower-limit magnetic field of  $B = 123 \mu\text{G}$ , 0.4% of the total energy of the preexisting electrons needs to be injected over 10 years. The corresponding electron spectrum ( $dN/dE \propto E^{-q} \exp[(-E/E_{cut})^\beta]$ ) is significantly harder for the injected electrons ( $q = 2.15$ ) than that of the preexisting electrons ( $q = 2.44 \pm 0.03$ ). The cutoff energy of the spectrum is much higher for the injected electrons ( $E_{cut} = 36$  TeV) than the preexisting electrons ( $E_{cut} = 4 \pm 1$  TeV) (Figure 3.4).

For the upper-limit magnetic field of  $B \sim 1$  mG, 2.1% of the preexisting electron energy needs to be injected with an even harder electron spectrum ( $q = 1.86$ ), and cutoff energy is still higher than the preexisting electrons ( $E_{cut} = 12$  TeV). The higher magnetic field produces faster synchrotron cooling, and that requires more electron injection, while the electron spectral index  $q$  and the cutoff energy  $E_{cut}$  are self-consistently regulated by the radio and NuSTAR data in 2023, respectively.

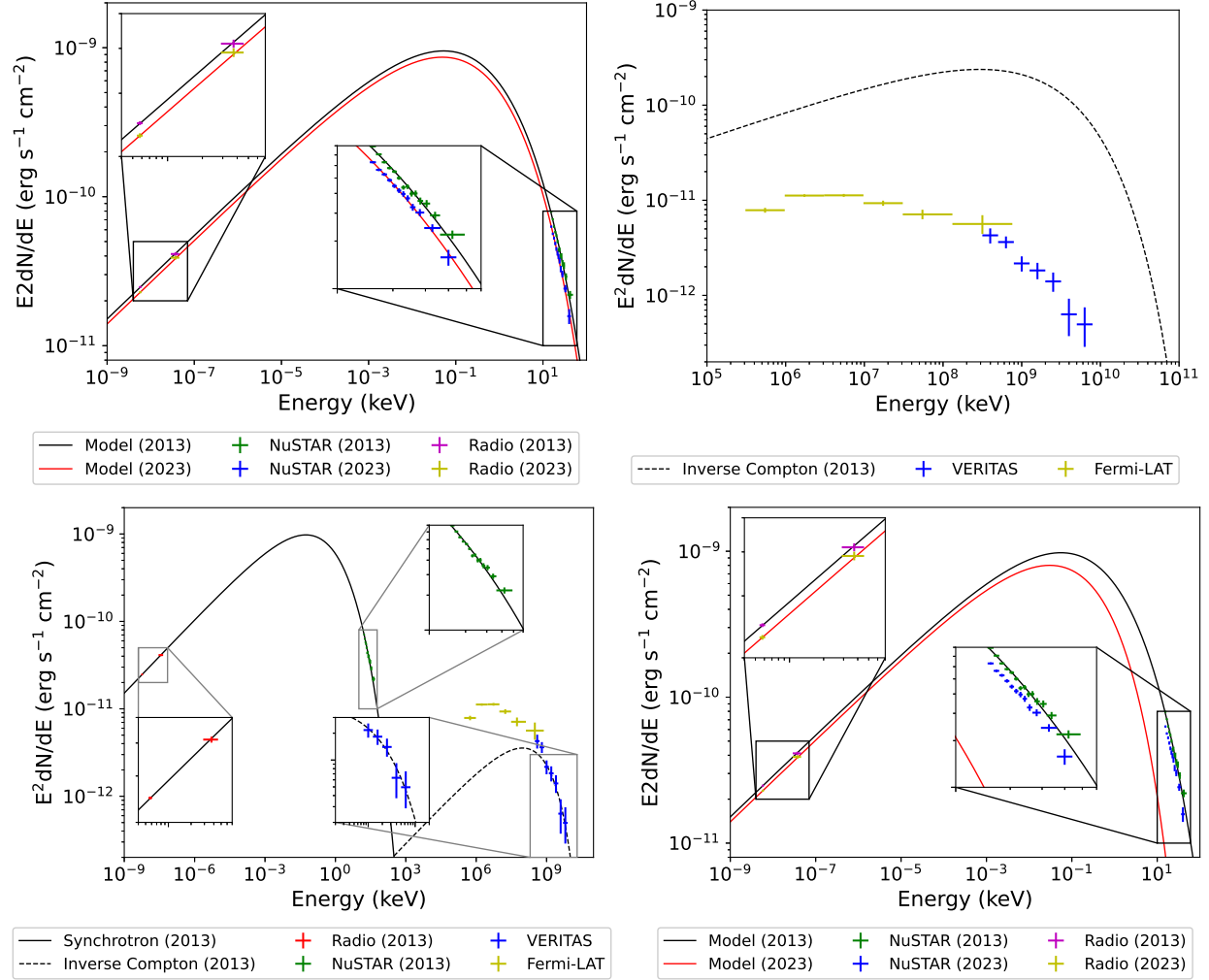


Figure 3.3: *Top: Synchrotron (left) and inverse Compton (right) spectrum from the best-fit electron distribution for  $B_0 = 6 \mu\text{G}$ . With this magnetic field, the predicted gamma-ray flux significantly exceeds the observed gamma-ray flux. Bottom: Synchrotron and inverse Compton spectrum in 2013 (left), and the synchrotron spectrum in 2013 and 2023 (right) from the best-fit electron distribution for the lower-limit magnetic field  $B_0 = 123 \pm 3 \mu\text{G}$ . The lower-limit magnetic field predicts over 50% decrease in the 15-50 keV flux, much faster than the observed decrease ( $15 \pm 1\%$ ). The Fermi-LAT and VERITAS spectra were taken from 4FGL-DR4 [76, 77] and [53], respectively.*

Further evidence that such hard-spectrum injection has been operating in Cas A comes from radio and infrared observations. Spectral hardening in the radio band has been observed since 1949 [125, 126, 116, 127]. Spectral hardening continues in the infrared band as the infrared synchrotron flux was measured to exceed the power-law extrapolation of the radio flux [128, 129]. The radio-infrared spectral hardening is most significant at the bright X-ray knots where the hard-spectrum

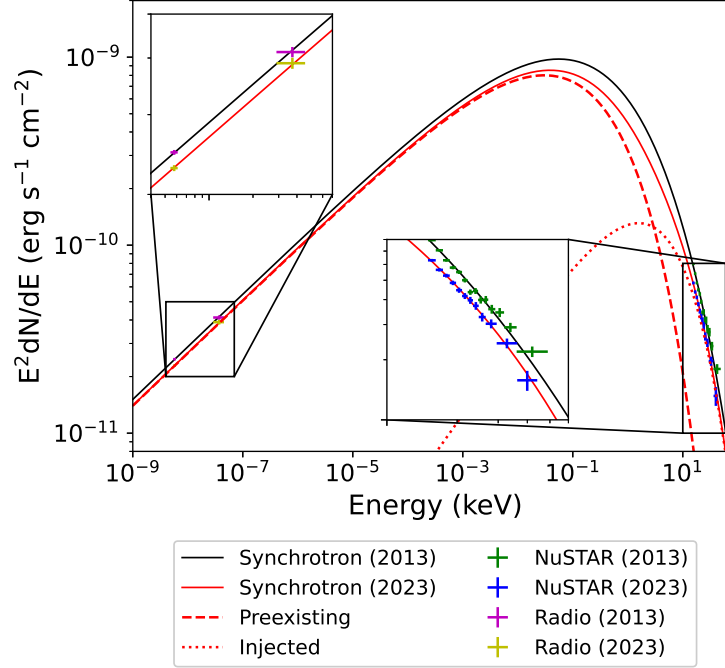


Figure 3.4: **Synchrotron spectrum in 2013 and 2023 calculated with the temporal synchrotron cooling and injection model.** The black (red) solid line is the synchrotron spectrum calculated using the best-fit parameters in Table 3.2 for 2013 (2023). The red dashed line is the synchrotron spectrum of the preexisting electrons in 2023, and the red dotted line shows the contribution of the injected electrons to the synchrotron spectrum in 2023. The NuSTAR spectrum from this work and the radio spectrum from [116] are overlaid. The error bars of the data points are for  $1\sigma$  uncertainties in this figure and all the figures hereafter.

injection is expected to operate [110].

The preexisting electron spectrum reflects the entire history of electron acceleration in Cas A up to 2013. Since low-energy electrons have a cooling time scale much longer than the age of Cas A, the spectral index of the preexisting electrons is governed by the synchrotron radio spectrum of low-energy electrons. On the other hand, the injected electron spectrum reflects only the electron acceleration operating in Cas A at the current time. This is mainly determined by the fast-cooling high-energy electrons and their synchrotron hard X-ray variability.

Equivalently, the hard X-ray morphology locates only the current CR acceleration site (injected electrons), whereas the radio morphology also reveals the location of CRs accelerated in the past (preexisting electrons). The hard X-ray morphology of Cas A shows a high concentration of emission on the knots. On the other hand, the radio morphology is more isotropic with enhancement at

the same knots and along the reverse shock (e.g. [110]). The brightening in both wavelengths locates the knots as the current most active particle acceleration sites (e.g. [130]), while the globally isotropic radio emission traces the electrons that were accelerated at an earlier time, most likely at the forward shock, and diffused out.

The soft-spectrum electrons that were accelerated earlier dominate the radio-emitting electron population, whereas the hard-spectrum electrons that were accelerated recently dominate the X-ray-emitting electron population. The combination of these two distinct electron populations creates a slower cutoff in the overall electron spectrum (best-fit cutoff index  $\beta = 0.74 \pm 0.05$ ), compared with analytic solutions for synchrotron-loss-limited diffusive shock acceleration in the case of Bohm diffusion ( $\beta = 2$  [120]). This slow cutoff in the electron spectrum propagates to the synchrotron spectrum creating a harder X-ray spectrum than the aforementioned synchrotron-loss-limited case. There were efforts to explain this spectral behavior of Cas A by hard-spectrum ( $q = 2.1$ ) electrons accelerated at the fast-moving jet-like structure [131] or the jitter radiation (magnetobremstrahlung emission of electrons in magnetic turbulence with a scale much smaller than the electron gyroradii) [132, 133, 134, 135]. The former overpredicts the upper limits placed by LHAASO in 10 TeV - 1 PeV [136], and the latter requires a magnetic turbulence scale  $< 100$  km, much smaller than an observable scale (e.g., IXPE angular resolution  $24''$  is equivalent to  $0.4$  pc =  $3 \times 10^{13}$  km at the distance 3.4 kpc). Our work provides the most natural explanation for the observed spatial-dependent spectral behavior of Cas A.

### 3.4.2 Modified nonlinear diffusive shock acceleration

One can examine if the derived CR spectra are consistent with recent theoretical expectations. NLDSA theories address CR-driven modification to the standard DSA by introducing a region upstream of a shock with an enhanced density due to CR pressure (“precursor”, e.g. [137, 138, 22, 23]) that leads to an increased shock compression ratio ( $R > 4$ ). Recent hybrid (kinetic ion-fluid electron) simulations [24, 25] discovered that the equivalent of a precursor is formed downstream of a shock (“postcursor”) whose contribution to the increased compression ratio dominates that

of a precursor. On the other hand, the compression ratio experienced by CRs is decreased since magnetic fluctuations and CRs drift away from the shock in a postcursor. This postcursor effect on the “effective” compression ratio is parameterized by a factor  $\alpha$ , which depends on shock velocity, upstream density, and downstream magnetic field. In mNLDSA, the correction factor  $\alpha$  for shock compression ratio can be deduced from observables as [25]

$$\alpha \simeq 5 \frac{B}{1 \text{ mG}} \frac{1000 \text{ km s}^{-1}}{v_{sh}} \left( \frac{R \text{ cm}^{-3}}{5 n} \right)^{1/2}, \quad (3.5)$$

where  $B$  is a post-shock magnetic field,  $v_{sh}$  is a shock speed,  $R$  is a shock compression ratio, and  $n$  is a pre-shock plasma number density. Measuring  $R$  is nontrivial. Adopting a nominal  $R = 5$  (e.g.  $R \sim 4 - 7$ , [139]) and observed  $v_{sh} \sim 6000 \text{ km s}^{-1}$  [95, 121],  $n \sim 1 \text{ cm}^{-3}$  [140], and  $B = 0.7 \text{ mG}$  ( $0.1 \text{ mG} \lesssim B \lesssim 1 \text{ mG}$ ), eq. 3.5 gives  $\alpha \sim 0.6$ .

Within this framework (mNLDSA), the CR spectral index is given by  $q = 3R/(R - 1 - \alpha) - 2$ . Typical values of  $R \sim 5$  and  $\alpha \sim 0.6$  [25] predict  $q \sim 2.4$  as we found for the preexisting electron population. At the reverse shock, our inferred spectrum of  $q \sim 2.2$  is consistent with the theoretical prediction if the postcursor is not present (in which case  $\alpha \rightarrow 0$  and  $R \rightarrow 4$ ). This is plausible since, at the reverse shock, the postcursor may not form due to the presence of contact discontinuity in the downstream region.

### 3.4.3 Proton acceleration at the hard X-ray knots?

The injected electron spectrum ( $q \sim 2.2$ ) agrees with the proton spectrum found from gamma-ray observations ( $q \sim 2.2$ , [53]), indicating that the same acceleration mechanism is operating for both electrons and protons at the same acceleration site. The hard X-ray knots at the reverse shock are observed to move inward at a much higher speed than the forward shock ( $v_{sh} \sim 8000 \text{ km s}^{-1}$  in the ejecta frame, [95, 121]) while the rest of the reverse shock is still moving outward. As it has been proposed, this requires the presence of an overdense region on the western rim of the reverse shock, such as molecular clouds [141, 142] or an asymmetric circumstellar shell [143]. CR protons

accelerated at the reverse shock can inelastically scatter with the overdensity and produce copious gamma rays by pion production and decay.

### **3.5 Summary and conclusion**

Our multi-epoch hard X-ray observations enabled the isolation of a pure synchrotron radiation component of Cas A. Such radiation is associated with energetic, nonthermal CR electrons. By temporal modeling of this emission, we were able to establish the existence of two distinct populations of CR electrons. One population is more energetic and associated with a powerful, active accelerator, and the second population is less energetic and associated with an accelerator that was more active in the past. The X-ray morphology of Cas A allowed us to identify the sites of both accelerators. These observations and associated modeling provide the first self-consistent analysis of a young SNR that connects the CR spectrum and acceleration location to the broadband multiwavelength spectrum from radio to gamma-ray energies with interpretation through the most recent work on the mNLDSA theory. Our observational and theoretical approach can be applied to other young SNRs to elucidate the acceleration mechanism and environment of CRs below the “knee” of their spectrum at  $\sim 3$  PeV.

## Chapter 4: Dragonfly – middle-aged pulsar wind nebula

The contents of this chapter have been peer-reviewed and published [144]. The summary and key findings of this chapter are as follows.

- We observe the synchrotron radiation (§1.3.4) of the Dragonfly PWN in the hard X-ray band using NuSTAR (§2.1) and soft X-ray band using Chandra and XMM-Newton (§2.1.1). We also observe the gamma rays from inverse Compton scattering (§1.3.3) in the GeV band using Fermi-LAT (§2.2).
- We construct a multiwavelength SED utilizing the X-ray and GeV spectra from this work as well as the published radio and VHE spectra. We model this SED as the synchrotron and inverse Compton radiation of CR electrons accelerated by a middle-aged pulsar PSR J2021+3651 from its birth to now (§1.4.2, “Stage 2” in Figure 1.10).
- The CR electron spectrum that produces the multiwavelength SED has a maximum energy greater than 1 PeV, that is, the Dragonfly PWN is a leptonic PeVatron.

### 4.1 Introduction

PWNe of energetic (spin-down luminosity  $\dot{E} > 10^{36}$  erg/s) middle-aged (characteristic age  $\tau = 10 - 100$  kyr) pulsars are often associated with VHE sources (e.g., [55]). Many of them are luminous above a hundred TeV without a hint of a spectral cutoff (e.g., [145] and [146]). Recently, the higher energy regime of their spectra was unveiled by LHAASO, the first gamma-ray observatory sensitive to PeV-energy gamma rays, and their detection of 14 Galactic UHE sources [147], [148], and [149]. The highest photon energies detected from these sources range from several hundred TeV to above 1 PeV: irrefutable evidence of particle acceleration above 1 PeV in

both hadronic (neutral pion decay) and leptonic (inverse Compton scattering) cases. Identifying these Galactic “PeVatrons” is the key to the origin of the highest-energy Galactic CRs observed on the Earth (in hadronic case) as well as a better understanding of the particle acceleration, radiation, and transportation mechanism (in both hadronic and leptonic case).

The majority of the LHAASO sources are spatially coincident with middle-aged energetic PWNe, well-known leptonic particle accelerators. Our NuSTAR observational campaign of energetic PWNe aims to explore the extreme nature of such PWNe [150]. Broadband hard X-ray observations with NuSTAR provide a unique window to the highest end of their parent particle spectra by resolving their synchrotron radiation without contamination from thermal radiation. Combined with modeling the multiwavelength SED of the PWNe over 20 decades of energy range, it allows deducing the key physical parameters that define the systems, such as the maximum particle energy and magnetic field. Our NuSTAR observation and multiwavelength SED modeling have functioned as powerful probes of PWNe as energetic leptonic CR accelerators in our Galaxy (e.g., [151], [152], and [153]).

G75.2+0.1 (“Dragonfly”) is one of the eight target PWNe of our NuSTAR observational campaign and is likely associated with LHAASO J2018+3651. The Dragonfly is powered by PSR J2021+3651 (RA = 20:21:05.40, Dec = +36:51:04.5) first discovered by [154] as a radio pulsar with a rotation period  $P \cong 104$  ms. The radio observation of the pulsar was motivated by the detection of an unidentified X-ray source AX J2021.1+3651 [155], which was a follow-up observation of an unidentified gamma-ray source GeV J2020+3658 [156]. As a middle-aged pulsar whose characteristic age  $\tau \equiv P/2\dot{P} \sim 17$  kyr, PSR J2021+3651 is still energetic, with  $\dot{E} \sim 3.4 \times 10^{36}$  erg s<sup>-1</sup>. PSR J2021+3651 is detected in X-ray as a soft (mostly) thermal ( $kT_{BB} = 0.16 \pm 0.02$  keV) point source by Chandra [157] and [158]. The authors of both works reported the detection of X-ray pulsations to be insignificant. The PWN G75.2+0.1 of PSR J2021+3651 was first observed in X-ray by [157] and was named the “Dragonfly” by [158] for its double-torus structure. Fermi-LAT observation by [159] detected GeV pulsations from PSR J2021+3651, yet its spectrum sharply cuts off below 10 GeV with no evidence of higher energy emission from the PWN.

PSR J2021+3651 and the Dragonfly are located in the Cygnus region, an active star-forming region. The first TeV gamma-ray source detected in spatial coincidence with PSR J2021+3651 and the Dragonfly was MGRO J2019+37 [160]. MGRO J2019+37 is the second brightest TeV source in the northern hemisphere after the Crab Nebula and largely extended (circular 2D Gaussian with  $\sigma = 0.32^\circ \pm 0.12^\circ$ ). Since its detection, numerous observations in different wavebands have been carried out as attempts to identify the origin of such high energy emissions. [161] observed the region with the VLA in radio (20 cm) and the XMM-Newton (XMM) in soft X-rays. Both observations revealed a more comprehensive picture of G75.2+0.1 beyond the substructures seen by Chandra – a conical diffuse nebula pivoted at PSR J2021+3651 that extends out to  $\sim 20'$  (radio) and  $\sim 10'$  (soft X-ray) on the west with decreasing surface brightness. In this work, the entire structure of the PWN is referred to as the Dragonfly.

VERITAS resolved MGRO J2019+37 into two separate sources [162]: VER J2019+368 and VER J2016+371. While VER J2016+371 is dominated by low-energy (below 1 TeV) emission near an SNR CTB 87, VER J2019+368 (RA = 20:19:25, Dec = 36:48:14, elliptical 2D Gaussian with major-axis  $\sigma_{maj} = 0.34^\circ \pm 0.03^\circ$  and minor-axis  $\sigma_{min} = 0.13^\circ \pm 0.02^\circ$ ) is bright above 1 TeV. With additional 120 hours of data, [163] reported that VER J2019+368 may be resolved into two source candidates, VER J2020+368\* and VER J2018+367\*. HAWC found the high-energy emission from VER J2019+368 to be significant even above 56 TeV and named the source eHWC J2019+368 [145]. Its significant detection above 100 TeV by LHAASO with the maximum photon energy  $0.27 \pm 0.02$  PeV [147] confirms that one or more PeVatrons of Galactic origin are present in this region. This extreme Galactic source, namely LHAASO J2018+3651, is spatially coincident with multiple possible CR accelerators, including a Wolf-Rayet (WR) star WR 141, H II region Sh 2-104, PSR J2021+3651 and the Dragonfly.

In this work, we aim to evaluate the Dragonfly's potential as a leptonic PeVatron. We report the first hard X-ray observation of the Dragonfly using NuSTAR. We analyze the archival Chandra and XMM data and 13 years of Fermi-LAT data on the Dragonfly. We combine the spectra of the Dragonfly extracted from our analyses with the radio and TeV spectra from the previous works to

model the multiwavelength SED of the Dragonfly. We discuss the common features of PeVatron PWNe, source distance, and magnetic field.

## 4.2 X-ray data analysis

We analyzed two sets of archival Chandra data (observation ID 8502, 34 ks, 2006 Dec 25, and observation ID 7603, 60 ks, 2006 Dec 29), one set of archival XMM data (observation ID 0674050101, 135 ks, 2012 Apr 17), one set of new NuSTAR data (observation ID 40660004002, 61 ks, 2021 May 19). We processed the Chandra data using the `chandra_repro` task in CIAO 4.13 [164] and the calibration database CALDB 4.9.5. We processed NuSTAR data using the `nuproducts` task in NuSTARDAS v2.0.0 contained within HEASOFT 6.28 and the NuSTAR calibration database (CALDB version 20210315). We processed the XMM EPIC MOS data using the `emchain` and `emfilter` tasks in the XMM-Newton Extended Source Analysis Software (XMM-ESAS) package contained within the XMM-Newton Science Analysis System (SAS v20.0.0). The net exposure after removing soft proton (SP) flares is 85 ks. The XMM EPIC pn data was not used since it was obtained in small window mode (one single CCD) and, hence, is inappropriate for observing a large diffuse nebula that extends over multiple CCDs.

### 4.2.1 Timing analysis

A marginal ( $3.7\sigma$ ) detection of X-ray pulsations in 0.5 – 3 keV from PSR J2021+3651 was reported in [157] using Chandra data in continuous-clocking mode and contemporaneous radio ephemeris. The same authors reported significant timing noise and a possibility of large glitches in PSR J2021+3651. We attempted to search for hard X-ray pulsations from PSR J2021+3651 using the NuSTAR data. We applied an astrometric correction on the pulsar position to the cleaned event files using the Chandra data analyzed in this work. We applied a barycentric correction to these event files for the corrected pulsar position using the `barycorr` task in NuSTARDAS. We used `extractor` to select position- and timing-corrected events within the  $r = 30''$  circular region around PSR J2021+3651 corresponding to the HPD of NuSTAR. We generated binned light curves

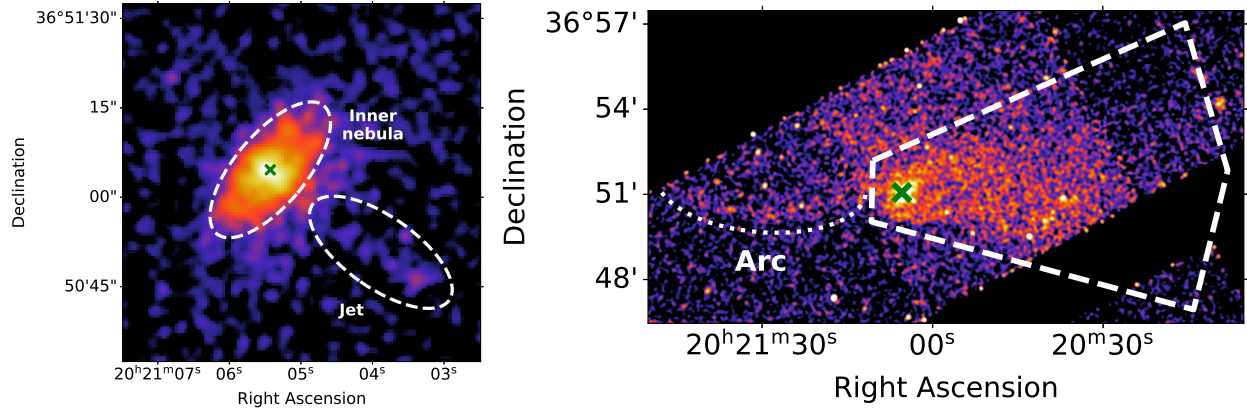


Figure 4.1: Merged (observation IDs 8502 and 7603) and exposure-corrected Chandra images of the Dragonfly in 2 – 6 keV. The scales were adjusted for better legibility. PSR J2021+3651 is marked as a cross (X) in both images. **Left:**  $1' \times 1'$  image after Gaussian smoothing with  $\sigma = 1.5$  pixel =  $0.7''$ . The  $20'' \times 10''$  inner nebula and the pulsar jet stretching out to  $\sim 30''$  from the pulsar are marked with dashed lines. **Right:**  $21' \times 11'$  image after Gaussian smoothing with  $\sigma = 3$  pixel =  $3.0''$ . The arc in length  $\sim 7.7'$  is traced with a dotted line. The extent of the outer nebula seen by XMM is marked as a dashed line.

from the selected events in 3 – 6, 6 – 20, and 3 – 20 keV bands (bin size = 1 ms) using the timing analysis software `HENDRICS 7.0` [165]. We used the light curves to create power spectra with the timing analysis software `Stingray v1.1` [166]. No significant frequency features were found. Given the lack of contemporaneous pulsar ephemeris, we performed  $Z_n^2$  ( $n = 2$ ) searches around the radio pulsar frequency and frequency derivative found by [154]. This search did not yield a significant detection of pulsations.

#### 4.2.2 Imaging analysis

Chandra resolved the substructures of the PSR J2021+3651 and the Dragonfly [158]. Such substructures include pulsar jets,  $20'' \times 10''$  double-torus inner nebula, a bow shock standoff, and a peculiar “arc” stretching toward the east of the pulsar (dotted line in the bottom figure of Figure 4.1). An outer nebula with a size much larger than the inner nebula seen by Chandra was discovered by [161] using XMM. [167] used XMM observations covering the region further west to that of [161] and constrained the size of the outer nebula to 10 – 15' to the west of PSR J2021+3651. [168] not only confirmed the western extent of the outer nebula measured by [167] using Suzaku

but also claimed the emission seen by XMM on the east of PSR J2021+3651 including the “arc” is part of the outer nebula.

In this section, we discuss the X-ray morphology of the Dragonfly seen by Chandra, XMM, and NuSTAR. We investigate a change in the morphology of the hard X-ray nebula in two different energy ranges: soft band (3 – 6 keV) and hard band (6 – 20 keV). We present the XMM image of the Dragonfly to study the morphology of the outer nebula and briefly discuss the nature of the “arc.” Chandra images in 2 – 6 keV are compared to the NuSTAR and XMM images in similar energy ranges (3 – 6 keV and 2 – 6 keV, respectively). A detailed description of the Chandra image can be found in [158].

### **Chandra image**

We merged the two Chandra observations (observation IDs 8502 and 7603) using the `merge_obs` task in CIAO to create an exposure-corrected image in 2 – 6 keV.

Figure 4.1 shows smaller (inner nebula and jet) and larger (outer nebula and arc) structures of the Dragonfly. The inner nebula is centered at PSR J2021+3651 and axis-symmetric along the jet. Its size is 20'' along the major axis and 10'' along the minor axis in diameter. The jet is measured to extend out to 30'' from the pulsar. The observations covered only part of the outer nebula seen by XMM (dashed line in the bottom panel of Figure 4.1), yet it is clearly visible. The arc continues to the edge of the FOV, measuring 7.7' in length.

### **NuSTAR image**

We created images for both focal plane modules (FPMA and FPMB) in the soft band (3 – 6 keV) and the hard band (6 – 20 keV) using `extractor`. The corresponding exposure maps after vignetting correction were created using `nuexpomap` task in NuSTARDAS. We combined the FPMA and FPMB images and corrected the exposure using `XIMAGE` to create Figure 4.2.

A bright emission is detected in both energy bands at the location of PSR J2021+3651 (marked with a cross (X) in the figure) and the surrounding region (inner nebula). The west of PSR

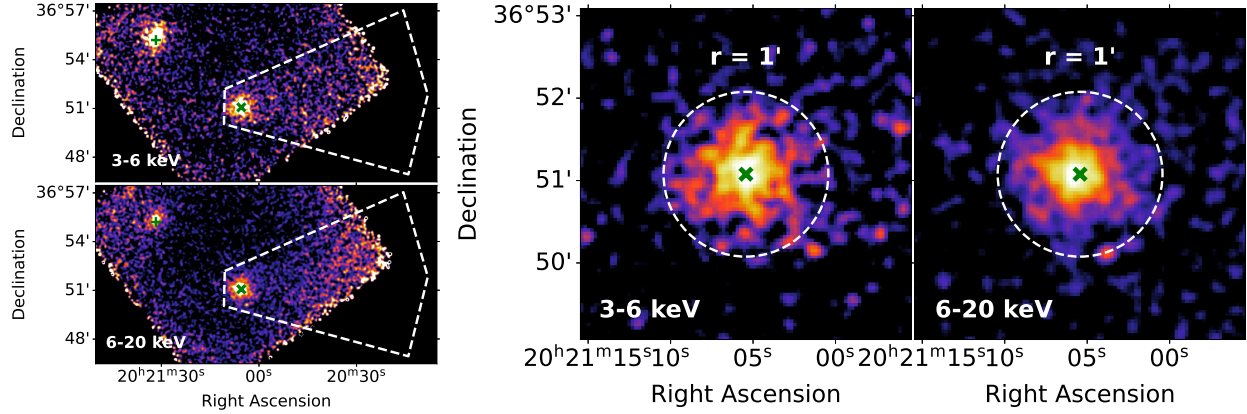


Figure 4.2: Merged (FPMA and FPMB), exposure- and vignetting-corrected, and smoothed (Gaussian kernel with  $\sigma = 1.5$  pixels =  $4.7''$ ) NuSTAR images. The scales were adjusted for better legibility. **Left:**  $21' \times 11'$  image containing PSR J2021+3651 and WR 141 marked with a cross (X) and a plus (+), respectively. The extent of the outer nebula seen by XMM is marked with a dashed line. **Right:**  $4' \times 4'$  image of the inner nebula. PSR J2021+3651 is marked with a cross (X). A dashed circle of radius  $1'$  is shown as a reference.

J2021+3651 is contaminated by a stray light background, so it is difficult to estimate the emission from the faint outer nebula. WR 141 (marked with a plus sign (+) in the figure) becomes significantly dimmer in the hard band. To examine the detailed morphology of the inner nebula, we created zoomed-in images (Figure 4.2 right panel). The emission is roughly symmetric about the pulsar in both energy bands. The nebula fits well in a radius  $1'$  circle, while it shows an apparent decrease in size in the hard band ( $6 - 20$  keV). We fitted PSF-convolved models to the images using *Sherpa* [169], a fitting and modeling application in CIAO. Both images are fitted with a constant background and a single 2D Gaussian. The FWHM of the Gaussian is  $26.5'' \pm 3.2''$  for the soft band and  $15.2'' \pm 2.0''$  for the hard band.

### XMM image

XMM is the only instrument whose image captures the entirety of the outer nebula in the X-ray band. To study this large diffuse emission, we first removed the contamination of the outer nebula by bright point sources in the FOV, such as PSR J2021+3651, WR 141, and a star USNO-B1.0 1268-0448692. We created Swiss cheese masks for MOS1 and MOS2 images that reduce the surface brightness of point sources to 20% of the surrounding background using the *cheese* task.

These masks were applied to the cleaned event files using the `mos-spectra` task to create MOS1 and MOS2 images of the entire FOV in 2 – 6 keV. The quiescent particle background (QPB) image was generated for the entire FOV in the same energy range using the `mos_back` task. Residual SP contamination was found to be negligible (see §4.2.3). No significant instrumental or solar wind charge exchange (SWCX) background is present in the energy range of our analysis, and no significant stray light background was observed in the image. Therefore, after combining the MOS1 and MOS2 images (`comb` task), we subtracted only the QPB image, corrected the exposure, and adaptively smoothed it using the `adapt` task to create the Figure 4.3 *left* panel.

Significant emissions are present on the east and west of PSR J2021+3651 (marked with X). The emission on the east of PSR J2021+3651 (“ring”-like structure, marked with dotted line) shows no low-energy counterpart in the radio (VLA L band) observation by [161]. [168] claimed this ring-like structure to be part of the Dragonfly. On the other hand, [158] and [170] detected a bow-shock structure from the inner nebula of the Dragonfly in the X-ray (Chandra) and radio (VLA C and L band) observations, respectively. Such detections indicate a supersonic motion of PSR J2021+3651 toward the east, in which case it is unlikely to expect PWN emission ahead of the bow shock formed by the pulsar. Possible origins of the emission on the west of the pulsar are discussed in the last paragraph of this section.

The emission on the west of PSR J2021+3651 (“outer nebula”, marked with dashed line) extends out to  $\sim 10'$  with decreasing surface brightness. This X-ray nebula is spatially coincident with the first half of the radio nebula, as shown in the Figure 4.3 *right* panel. The radio nebula extends further out to  $> 20'$  [161], whose flux was used for modeling the SED of the Dragonfly (see §4.4). For consistency, we analyze the X-ray counterpart of the radio nebula, namely the outer nebula, and use its spectrum for SED modeling.

A ring-like structure is centered at WR 141 and has radius  $\sim 5'$ . The “arc” seen by Chandra comprises the lower part of this ring. [168] claimed that the “ring” is part of the PWN based on the similar spectral index between the “ring” and the “outer nebula.” [171] explained the “arc” as a “kinetic jet”: pulsar wind particles that escaped into the ISM due to magnetic reconnection

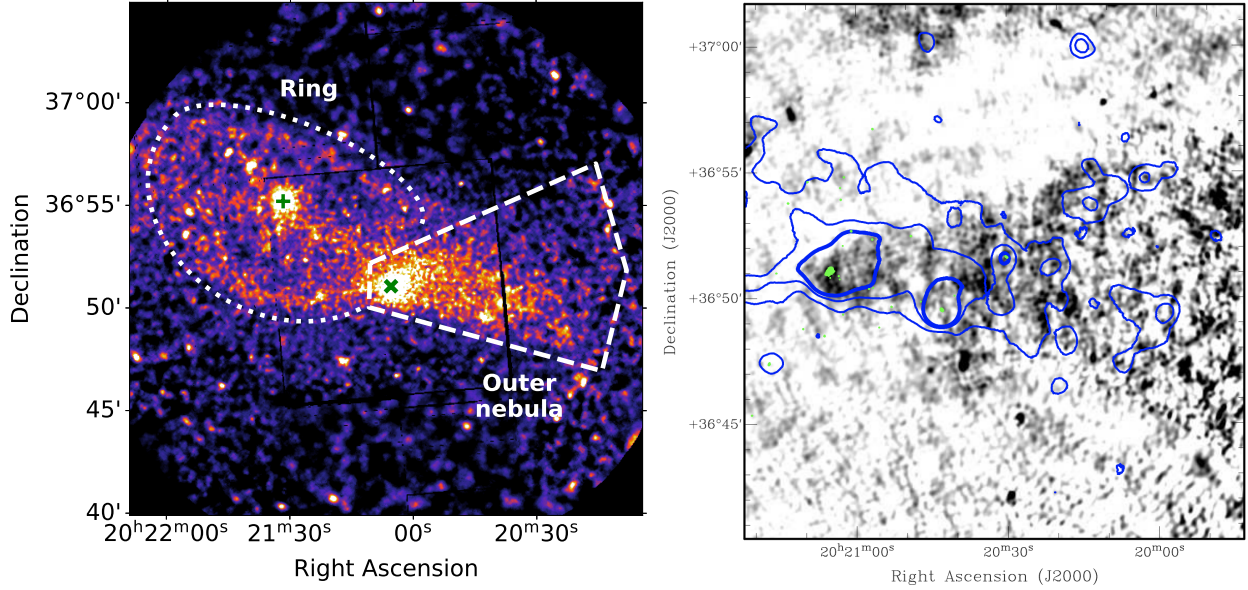


Figure 4.3: **Left:** Merged (MOS1 and MOS2), QPB-subtracted, exposure-corrected, and smoothed XMM image in 2 – 6 keV. PSR J2021+3651 and WR 141 are marked with a cross (X) and a plus (+) sign, respectively. The extent of the outer nebula  $\sim 10'$  is marked with dashed lines. A “ring” is marked with a dotted line. **Right:** VLA 20cm image from [161]. The radio nebula extends out to  $> 20'$  from PSR J2021+3651. The XMM contours are overlaid in blue. The permission for the use of the image was acquired from AIP Publishing via RightsLink<sup>®</sup>.

between the PWN and the ISM and became visible in a high  $> 10 \mu\text{G}$  ISM magnetic field. A similar filamentary emission ahead of the main body of the PWN (“outer nebula”) was observed in the “Snail” PWN, whose “prongs” may be the result of the interaction between the PWN and the reverse shock of its host SNR [172]. We propose that the “ring” in our XMM image is possibly associated with WR 141. WR stars are known to have strong stellar winds that can create a bubble of several parsecs in radius [173]. This bubble is often observed as a ring-shaped nebula and can be visible in X-ray (e.g., [174]). The parallax of 0.5024 mas in Gaia DR3 [175] implies a 2.0 kpc distance to WR 141. This yields the radius of the bubble = 2.9 pc. Part of the “ring” was also seen in  $\text{H}\alpha$  photometry by [176], which the authors postulated to be part of the ring nebula photoionized by WR 141.

### 4.2.3 Spectral analysis

We present a spectral analysis of PSR J2021+3651 and its PWN using Chandra, XMM, and NuSTAR data. We first characterize the pulsar spectrum with Chandra taking advantage of its fine angular resolution (HPD  $< 0.5''$ ). We analyze the spectrum of the inner nebula taking into account the contribution of the pulsar by individually and jointly fitting the Chandra, XMM, and NuSTAR spectra. We use the XMM data to study the spectrum of the outer nebula. All the spectral models for X-ray analysis presented in this work were multiplied by a cross-normalization factor (`const`) to adjust relative normalization between different detectors and instruments.

#### **Pulsar spectrum**

We used Chandra data to analyze the spectrum of PSR J2021+3651. We extracted the source spectra from a circular region with radius  $2''$  centered at PSR J2021+3651, and the background spectra from an annulus around PSR J2021+3651 with radii  $2 - 4''$  using the `specextract` command in `CIAO`. The source spectra were binned to have at least  $3\sigma$  significance over the background in each bin. We began by fitting an absorbed power law (`const*tbabs*pow`) to the spectra in  $0.5 - 7$  keV where the source emission dominates over the background. The abundance table was set to `wilm` [107] for all the X-ray spectral analyses presented in this work. This model gives a reasonable fit ( $\chi^2/d.o.f = 130/152$ ) with the best-fit  $\Gamma = 1.73^{+0.13}_{-0.12}$  and  $N_H = (0.26 \pm 0.05) \times 10^{22} \text{ cm}^{-2}$ . However, this best-fit  $N_H$  is 3 times smaller than the  $N_H$  found from the Chandra spectra of the inner nebula. When the  $N_H$  was fixed to the best-fit value found from the Chandra inner nebula spectra ( $0.76 \times 10^{22} \text{ cm}^{-2}$ , see §4.2.3), the fit quality became worse ( $\chi^2/d.o.f = 190/152$ ) with much softer  $\Gamma = 2.87 \pm 0.15$ . This is because the pulsar has significant emission in both below and above 3 keV. Initially, a small  $N_H$  was favored to explain the emission below 3 keV. Later, the  $\Gamma$  was significantly softened to compensate for the larger  $N_H$ , leaving the emission above 3 keV poorly fitted. We added a black body component to fit the emission below 3 keV while the power law component explains the emission above 3 keV (`const*tbabs*(bbod+pow)`).  $N_H$  is highly degenerate with the black body temperature and the power law index, so we fixed

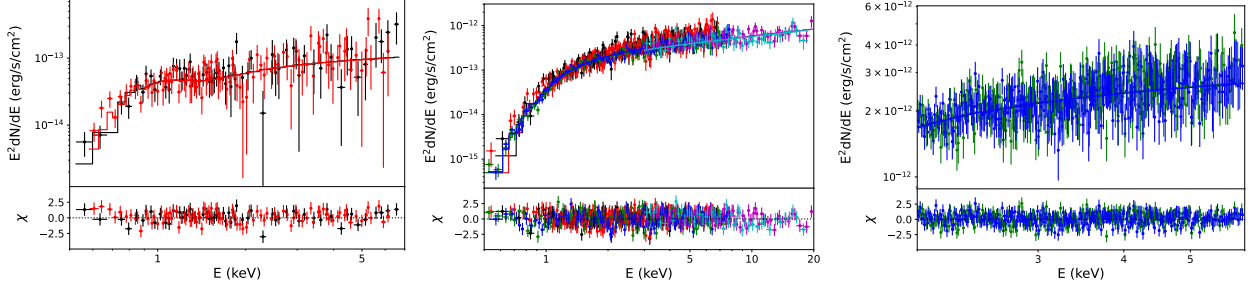


Figure 4.4: **Left:** Chandra ObsID 8502 and 7603 (black and red crosses, respectively) spectra of PSR J2021+3651. The background is dominant outside of 0.5 – 7 keV. The source spectra were extracted from a circular region with radius  $2''$  centered at the pulsar. The background spectra were extracted from an annulus region with radii  $2 - 4''$  centered at the pulsar. **Middle:** Chandra ObsID 8502 (black) and 7603 (red), XMM MOS1 (green) and MOS2 (blue), NuSTAR FPMA (magenta) and FPMB (cyan) spectra of the inner nebula. The background is dominant outside of 0.5 – 7 keV for Chandra, 0.5 – 8 keV for XMM, and 3 – 20 keV for NuSTAR. The source spectra were extracted from an annulus region with radii  $2 - 20''$  for Chandra, a circular region with radius  $40''$  for XMM, and a circular region with radius  $1'$  for NuSTAR, all centered at PSR J2021+3651. The background spectra were extracted from a  $2' \times 2'$  box in a source-free region. For XMM and NuSTAR, the pulsar spectra were subtracted. The best-fit models are displayed as solid lines in both plots. **Right:** XMM MOS1 and MOS2 (green and blue, respectively) spectra of the outer nebula. The source spectra were extracted from the dashed polygon in the Figure 4.3 *left* panel. The Line and continuum backgrounds are dominant below 2 keV and above 6 keV, respectively. The best-fit models are displayed as solid lines.

$N_H$  to the Chandra value of the inner nebula. This gives the best-fit  $kT = 0.13 \pm 0.01$  keV and  $\Gamma = 1.63 \pm 0.17$  with  $\chi^2/d.o.f = 123/151$ . We used this model as the initial pulsar component when jointly fitting the Chandra spectra of the inner nebula and the XMM and NuSTAR spectra of the pulsar and the inner nebula (see §4.2.3). We iteratively fit the Chandra pulsar spectra by changing the  $N_H$  to the best-fit value found from the joint fit of the Chandra, XMM, and NuSTAR spectra. The pulsar model converged to  $kT = 0.11 \pm 0.01$  keV and  $\Gamma = 1.77 \pm 0.17$  with  $\chi^2/d.o.f = 123/151$ . The best-fit parameters are comparable to [158] ( $\Gamma = 1.73^{+1.15}_{-1.02}$ ,  $kT = 0.16 \pm 0.02$  keV, and  $N_H = 0.67 \times 10^{22}$  cm $^{-2}$ ) considering the degeneracy between  $kT$  and  $N_H$ . The unabsorbed flux of PSR J2021+3651 in 3 – 10 keV is  $F_{3-10} = (1.20^{+0.18}_{-0.17}) \times 10^{-13}$  erg/s/cm $^2$ .

## Inner nebula spectrum

We individually and jointly fitted the Chandra, XMM, and NuSTAR spectra of the inner nebula. The Chandra spectra were extracted from an annulus region with radii  $2 - 20''$  centered at PSR J2021+3651. The XMM spectra were extracted from circular regions with radius  $40''$  using the `xmmselect` task in `SAS`. Response files were generated using `rmfgen` and `arfgen` tasks. NuSTAR spectra were extracted from circular regions with radius  $1'$  using `nuproducts` task in `NuSTARDAS`. The sizes of the source region for different instruments were determined considering the PSF sizes of the instruments (HPD  $1''$  for Chandra,  $34''$  for XMM, and  $58''$  for NuSTAR) and the cross-normalization term between the source spectra. The background spectra for all three instruments were taken from a  $2' \times 2'$  box in a nearby source-free region. Fitting was performed in the energy range where the source emission dominates over the background ( $0.5 - 7$  keV for Chandra,  $0.5 - 8$  keV for XMM,  $3 - 20$  keV for NuSTAR). All spectra were binned such that the source counts have at least  $3\sigma$  significance above the background counts in each bin.

We first modeled the Chandra spectra of the inner nebula using an absorbed power law (`const*tbabs*pow`) to find the best-fit  $N_H = (0.76 \pm 0.06) \times 10^{22} \text{ cm}^{-2}$ . Using this  $N_H$ , the best-fit model for the pulsar was found ( $kT = 0.13 \pm 0.01$  keV,  $\Gamma = 1.63 \pm 0.17$ , see §4.2.3). This pulsar component was included and held fixed in the model for the XMM and NuSTAR spectra of the inner nebula. The  $N_H$  for both instruments were held fixed to the value found from the Chandra-only fit. The best-fit  $\Gamma$  for Chandra and XMM are in good agreement ( $1.25 \pm 0.06$  and  $1.35 \pm 0.03$ , respectively), while the NuSTAR spectra give much softer  $\Gamma = 1.73 \pm 0.07$ . We jointly fitted the Chandra, XMM, and NuSTAR spectra to constrain the model for the inner nebula more tightly and to test the presence of a spectral break. The iterative fitting of the pulsar spectrum was performed in parallel (see §4.2.3). An absorbed power law model with  $N_H = (0.96 \pm 0.04) \times 10^{22} \text{ cm}^{-2}$  and  $\Gamma = 1.49 \pm 0.03$  explains the spectra well ( $\chi^2/d.o.f = 710/705$ ). Adding a break to the power law does improve the fit (F test probability = 0.002); however, the break energy  $E_{break} = 6.02_{-1.19}^{+0.75}$  keV near the borderline between the Chandra and XMM vs. NuSTAR energy ranges is suspect. We concluded that the hint of spectral break might originate from the imperfect cross-calibration between the different

Table 4.1: Summary of X-ray spectral analysis results

Region	Instrument <sup>†</sup>	Energy (keV)	$N_H$ ( $10^{22}$ cm $^{-2}$ )	$kT$ (keV)	$\Gamma$	$F_{3-10}$ ( $10^{-13}$ erg/s/cm $^2$ )	$\chi^2/d.o.f$
Pulsar	C	0.5 – 7	0.96 <sup>‡</sup>	0.11 ± 0.01	1.77 ± 0.17	1.20 <sup>+0.18</sup> <sub>-0.17</sub>	128/151
	C	0.5 – 7	0.76 ± 0.06	–	1.26 ± 0.06	6.80 <sup>+0.32</sup> <sub>-0.31</sub>	345/349
Inner nebula	X	0.5 – 8	0.76 <sup>‡</sup>	–	1.35 ± 0.03	5.58 <sup>+0.18</sup> <sub>-0.17</sub>	246/240
	N	3 – 20	0.76 <sup>‡</sup>	–	1.73 ± 0.07	5.50 ± 0.22	106/114
	C+X+N	0.5 – 20	0.96 ± 0.04	–	1.49 ± 0.03	5.31 ± 0.21	710/705
Outer nebula	X	2 – 6	0.96 <sup>‡</sup>	–	1.82 ± 0.03	32.53 ± 0.69	509/541

<sup>†</sup> C = Chandra, X = XMM, N = NuSTAR. <sup>‡</sup> held fixed.

instruments. The unabsorbed flux of the inner nebula is  $F_{3-10} = (5.31 \pm 0.21) \times 10^{-13}$  erg/s/cm $^2$ .

The best-fit  $\Gamma$  for the inner nebula from the joint fit is comparable with [158] ( $1.45 \pm 0.09$ ).

### Outer nebula spectrum

We used the XMM data to analyze the outer nebula spectrum. The cleaned event files and the Swiss cheese masks (see §4.2.2) were processed with the `mos-spectra` task to extract the source spectra from the dashed polygon in the Figure 4.3 *left* panel. We followed the procedures described in the manual for the use of XMM-ESAS<sup>1</sup> to carefully estimate the background in such a large source region ( $\sim 10'$ ). First, the QPB spectra were generated for the same region using the `mos_back` task. Second, the background spectrum below 2 keV contains multiple instrumental and SWCX lines. We chose 2 – 6 keV for the energy range of our analysis to avoid modeling too many background components. The continuum background dominates over 6 keV. Third, we attempted to model the remaining background components on `Xspec`: SP residuals and the CXB. The QPB spectra were loaded as background spectra. The source spectra were binned to have at least  $3\sigma$  significance over the QPB spectra in each bin. The background from SP residuals was modeled with a power law using unitary response matrices, but none of the model parameters were constrained. Therefore we assumed that the contribution from residual SP is insignificant and excluded it from the model. The CXB was modeled with an absorbed power law (`const*tbabs*pow`). All of its model parameters were fixed to the canonical values ( $\Gamma = 1.41$ ,

<sup>1</sup><https://heasarc.gsfc.nasa.gov/FTP/xmm/software/xmm-esas/xmm-esas-v13.pdf>

normalization=11.6 photons/keV/s/cm<sup>2</sup>/sr at 1 keV, [177]) to circumvent the degeneracy between the two power-law components (CXB and the outer nebula). We used the Galactic hydrogen column density<sup>2</sup> at the center of the source extraction region (1.13 cm<sup>-2</sup>) as the  $N_H$  for the CXB.

The outer nebula was modeled with an absorbed power law (`const*tbabs*pow`). The  $N_H$  is not constrained in the energy range of this analysis (2 – 6 keV). We fixed the  $N_H$  to the best-fit value found from the Chandra, XMM, and NuSTAR joint fit of the inner nebula ( $0.96 \times 10^{22}$  cm<sup>-2</sup>). The best-fit model with  $\Gamma = 1.82 \pm 0.03$  yields a reasonable fit ( $\chi^2/d.o.f = 509/541$ ). The unabsorbed flux of the outer nebula in 2 – 10 keV is  $F_{2-10} = (4.20 \pm 0.07) \times 10^{-12}$  erg/s/cm<sup>2</sup>. The best-fit  $\Gamma$  is clearly harder than [168] ( $\Gamma = 2.10 \pm 0.12$ ), yet the flux value is comparable ( $F_{2-10} \sim 4.1 \times 10^{-12}$  erg/s/cm<sup>2</sup> for the PWN-west).

### 4.3 Fermi-LAT analysis

The gamma-ray pulsations of PSR J2021+3651 was first detected by AGILE [178] and later confirmed by Fermi-LAT [159]. The pulsar is registered in the most recent Fermi-LAT source catalog (4FGL-DR3, [179]) as 4FGL J2021.1+3651. We analyzed 13-year Fermi-LAT data (August 2008 – October 2021, MET 239557417 – 656813666) to detect the GeV emission from the Dragonfly. We selected SOURCE class and FRONT+BACK type events (`evclass=128, evtype=3`) and used the instrument response functions (IRFs) `P8R3_SOURCE_V3`. The 90° zenith angle cut and the filter expression `DATA_QUAL>0 && LAT_CONFIG==1` were applied. The region of interest (ROI) is a 10° × 10° box region centered at 4FGL J2021.1+3651.

We performed a binned likelihood analysis (spatial bin = 0.1°, energy bin = 8 bins per decade) using `Fermipy v1.0.1` [180]. The ROI model includes the 4FGL-DR2 sources (`gll_psc_v27.fit`, [181]) within a 30 × 30 box region centered on 4FGL J2021.1+3651, the Galactic diffuse emission model (`gll_iem_v07.fits`), and the isotropic emission model (`iso_P8R3_SOURCE_V3_v1.txt`)<sup>3</sup>. We used the `optimize()` and `fit()` methods in `Fermipy` to optimize the model in 100 MeV–300 GeV. For the `fit()` method, the parameters of bright nearby

<sup>2</sup><https://www.swift.ac.uk/analysis/nhtot/>

<sup>3</sup><https://fermi.gsfc.nasa.gov/ssc/data/access/lat/BackgroundModels.html>

sources (within  $5^\circ$  of 4FGL J2021.1+3651 and TS (test statistics)  $> 25$ ) were left free. After fitting, the residual map was visually inspected, and a standard normal distribution was fitted to the residual significance histogram to ensure that the residuals are statistical fluctuations.

4FGL J2021.1+3651 is modeled with `PLSuperExp-Cutoff`<sup>4</sup>. The best-fit parameters of 4FGL J2021.1+3651 agreed with those of 4FGL-DR2 within  $1\sigma$  error. Since the emission from 4FGL J2021.1+3651 cuts off in the 10–30 GeV range, we created a  $\sqrt{\text{TS}}$  map of the ROI above 30 GeV to avoid contamination by the pulsar and investigate any possible diffuse emission from the PWN. We did not find any excess in the vicinity of 4FGL J2021.1+3651 that can be attributed to the emission from the PWN. This result confirms the non-detection of the GeV PWN in the vicinity of PSR J2021+3651 from the previous studies of the off-pulse data [159].

GeV gamma rays are IC upscattered photons off the low energy electrons that emit synchrotron radiation in radio – infrared. Given the large ( $> 20'$ ) size of the radio nebula, a putative GeV nebula may be largely extended and too faint to be significantly detected over the background. The large ( $\sim 1^\circ$ ) size of the IC nebula in the VHE range (eHWC J2019+368) may also indicate a largely extended GeV nebula. [182] calculated upper limits for a GeV PWN of PSR J2021+3651 assuming a size of MGRO J2019+37. [183] used an ICS template with the best-fit diffusion coefficient for eHWC J2019+368 to place GeV upper limits of the PWN. Both works resulted in GeV upper limits similar to the flux of eHWC J2019+368.

#### 4.4 Multiwavelength SED modeling

Figure 4.5 shows the multiwavelength counterparts of the Dragonfly overlaid on the HAWC significance map. PSR J2021+3651 is located at the Eastern edge of the extended TeV source eHWC J2019+368. Its PWN, the Dragonfly, extends toward the centroid of eHWC J2019+368. We model the SED of the Dragonfly using these multiwavelength data to investigate the Dragonfly as a leptonic PeVatron.

While our NuSTAR observation allowed an in-depth study of the inner nebula, the faint emis-

---

<sup>4</sup>[https://fermi.gsfc.nasa.gov/ssc/data/analysis/scitools/source\\_models.html](https://fermi.gsfc.nasa.gov/ssc/data/analysis/scitools/source_models.html)

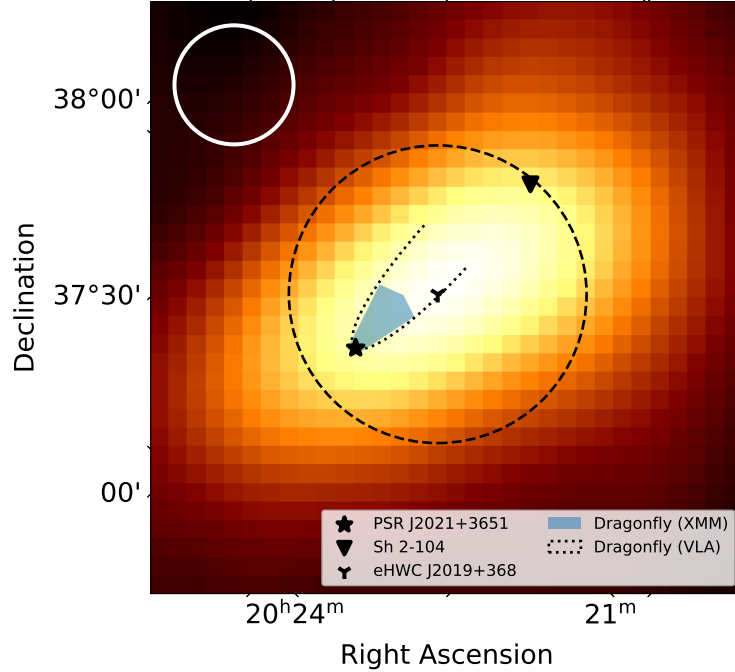


Figure 4.5: HAWC significance map ( $2^\circ \times 2^\circ$ ) centered at the centroid of eHWC J2019+368. The eHWC J2019+368 flux extraction region is marked with a dashed circle (radius  $0.5^\circ$ ). PSR J2021+3651 and Sh 2-104 are marked with a star and a triangle, respectively. The shaded region is the XMM spectrum extraction region of the outer nebula. The dotted line shows the extent of the outer nebula seen by VLA. The angular resolution of HAWC varies depending on the energy and zenith angle. The approximate size of the 68% containment region at 56 TeV (radius  $0.2^\circ$ ) is marked with a solid white circle at the top left corner. The HAWC image was obtained from the 3HWC survey public data (<https://data.hawc-observatory.org/datasets/3hwc-survey/fitmaps.php>), and the VLA nebular extent was estimated from [161].

sion from the outer nebula was not detected due to the limited sensitivity. Instead, we used our XMM analysis result of the outer nebula presented in §4.2.3. The radio spectrum and the GeV upper limits were taken from [161] and [183] (“IEM-4FGL”), respectively. In the TeV band, three independent flux measurements by VERITAS (VER J2019+368), HAWC (eHWC J2019+368), and LHAASO (LHAASO J2018+3651) are available. [147] did not provide detailed spectral information of LHAASO J2018+3651 except for its flux at 100 TeV. [163] and [145] provide the spectrum of VER J2019+368 and eHWC J2019+368, respectively, over three decades of energy. While VER J2019+368 and eHWC J2019+368 exhibit similar source size, the flux of VER J2019+368 reported in [163] was extracted from a region smaller than the source size, yielding a 2 – 3 times lower flux than that of eHWC J2019+368 in the overlapping energy range (see also [184]). Therefore, we

used the spectrum of eHWC J2019+368 from [145] for SED modeling in this work.

The distance estimates of PSR J2021+3651 vary widely depending on different distance measures. [154] used the dispersion measure (DM)  $\sim 371 \text{ pc cm}^{-3}$  to put the pulsar at  $\geq 10 \text{ kpc}$  on the outer edge of the Galaxy, although they left a possibility of a nearer distance in case of a contribution from excess gas in the Cygnus region. [158] suggested 3–4 kpc based on various arguments, such as the X-ray spectral fit to a neutron star atmosphere model and the gamma-ray efficiency of the pulsar. [159] estimated a distance  $\geq 4 \text{ kpc}$  based on the pulsar rotation measure (RM). [185] suggested  $1.8_{-1.4}^{+1.7} \text{ kpc}$  using the interstellar extinction and distance relation. The 1.8 kpc distance was adopted by [168], [186], and [184] for their multiwavelength SED modeling.

We start with preliminary modeling of the multiwavelength SED using `Naima` [187], a generic model for non-thermal radiation from relativistic particles. We do not make assumptions about the distance or evolutionary history of the PWN at this stage. Our purpose for this preliminary modeling is to provide a basic understanding of the current status of the PWN and initial estimation of the input parameters for a more sophisticated model, namely the dynamical model [188]. Then we move on to multiwavelength SED modeling using the dynamical model to acquire insight into the dynamical evolution of the Dragonfly over its lifetime while the interactions between the PWN, SNR, and ISM are accounted for.

#### 4.4.1 Naima

`Naima` allows us to characterize the current particle population using a minimal number of parameters without introducing any physical assumptions on the evolutionary history of the system.

For a leptonic particle accelerator, synchrotron (SC) emission and emission via inverse Compton (IC) scattering off the input seed photon fields (CMB and interstellar dust emission (IR)) are calculated based on a particle distribution model. We vary the model parameters of a single particle distribution so that the SC and IC spectra are consistent with the observed flux in radio, X-ray, and TeV gamma-ray bands. The minimum particle energy ( $E_{min}$ ) and the reference energy ( $E_0$ ) were fixed to 1 MeV and 1 TeV, respectively. The best-fit parameters are summarized in Table 2, and

Table 2: Best-fit SED model parameters using Naima

$\alpha$	2.4
$E_{cut}$	0.9 PeV
Magnetic field	1.6 $\mu$ G
IR temperature	26 K
IR energy density	1.0 eV/cm <sup>3</sup>
Total particle energy <sup>†</sup>	$6.1d_{3.5}^2 \times 10^{49}$ erg

<sup>†</sup>  $d_{3.5}$  is the distance to the Dragonfly scaled to the nominal distance of 3.5 kpc.

the best-fit SED model is plotted with the multiwavelength data and residuals in Figure 4.6.

The TeV spectrum exhibits a smooth cutoff after 20 TeV. This cutoff is better explained by an exponential cutoff power law distribution of particles,  $dN/dE = A(E/E_0)^{-\alpha} e^{-E/E_{cut}}$ , than a simple power law with a sharp cutoff at  $E_{max}$ . The best-fit particle index is  $\alpha = 2.4$ . Adding an IR field gives a better fit than the CMB-only model, although the IR field energy density tends to grow indefinitely to an unphysical value. Therefore, we fixed the IR field energy density to the average CR energy density (1 eV/cm<sup>3</sup>, [189]). This yields the best-fit IR field temperature  $T = 26$  K, magnetic field  $B = 1.6 \mu$ G, and cutoff energy  $E_{cut} = 0.9$  PeV. This SED model shows a good fit to the multiwavelength data as seen in the residuals plotted in Figure 4.6; however, the narrow IC peak resolved by HAWC is difficult to explain with physically reasonable model parameters. Such a narrow peak originates from the flux point in the lowest energy bin, the range in which air imaging Cherenkov telescopes (IACTs), such as VERITAS, are more sensitive. A deeper VERITAS observation and more accurate flux measurement of the region have been proposed for our future work to resolve the IC spectrum of the Dragonfly better.

The best-fit cutoff energy  $E_{cut} = 0.9$  PeV strongly suggests that the Dragonfly is likely a PeVatarn. The cutoff energy is greater than 0.3 PeV by [184] and 0.4 PeV by [186] mainly due to the difference in the X-ray spectra used in each work (see §4.4). The magnetic field inside the PWN is at the level of interstellar magnetic field ( $\sim 3 \mu$ G, [190]), as one may infer from the low X-ray to gamma-ray luminosity ratio.

The IR field temperature is higher than the IR emission from cold dust grains ( $\sim 15$  K). A pos-

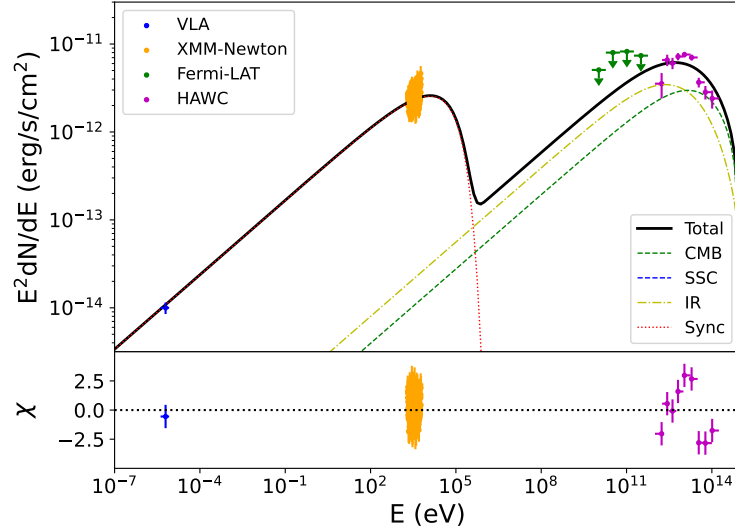


Figure 4.6: The best-fit SED model from Naima. The model parameters are given in Table 2. Synchrotron flux (Sync), inverse Compton flux from the CMB (CMB), infrared emission from the interstellar dust grains (IR), synchrotron self-Compton component (SSC), and total flux are plotted. The SSC flux level is very low and located below the lower bound of the y-axis. Radio, X-ray, and TeV flux data points, and GeV upper limits are overlaid. The residuals are plotted in terms of significance  $((\text{data} - \text{model}) / (1\sigma \text{ uncertainty of data}))$ .

sible source of this warm dust emission is an H II region Sh2-104 (marked with an inverted triangle in Figure 4.5). Located at  $4 \pm 0.5$  kpc from the Earth, Sh2-104 is visible in radio through X-ray [191], [192], [193], and [194]. Sh 2-104 hosts an ultra-compact H II (UCHII) region on the eastern periphery of its dense molecular shell. As strong candidates for active star formation [191] and [193], Sh2-104 and the UCHII region each contain a stellar cluster, MASS J20174184+3645264 and IRAS 20160+3636, respectively, ionizing the regions [191] and [195]. [192] used Herschel observations to estimate the dust temperature in Sh2-104 to be 20 – 30 K on the exterior. Our best-fit IR field temperature (26 K) lies in this temperature range. Since the lower bound of the distance to Sh2-104 [191] and the upper bound of the distance to PSR J2021+3651 [185] coincide (3.5 kpc), we adopt 3.5 kpc as a nominal distance to the Dragonfly hereafter and scale relevant parameters to this distance whenever possible.

Table 3: SED model parameters using the dynamical model

	Source distance	3.5 kpc
Input	$E_{SN}$	$1.0 \times 10^{51}$ erg
	$M_{ej}$	$7.2 M_{\odot}$
	$n_{ISM}$	$0.03 \text{ cm}^{-3}$
	Braking index $p$	2.5
	Age	16 kyr
	$\eta_B$	0.008
	$E_{max}$	1.4 PeV
	Particle index $\alpha$	2.4
	IR field temperature	9.9 K
	IR field energy density	$1.4 \text{ eV cm}^{-3}$
Output	$t_{RS}$	12 kyr
	$R_{PWN}$	9.5 pc
	Magnetic field	$2.7 \mu\text{G}$
	Total particle energy	$3.9 \times 10^{48}$ erg

#### 4.4.2 Dynamical model

Taking the result from `Naima` as a starting point, we fit the dynamical model to the multiwavelength data of the Dragonfly. The dynamical model is a time-evolutionary model for a composite system of a PWN and its host SNR. The model assumes a spherical single-zone system whose SNR is in a free-expansion or Sedov-Taylor phase. The model evolves a PWN and its SNR from their birth to the true age of the system, calculating the interaction between them and with the surrounding ISM. The model output includes a pulsar wind particle distribution, its synchrotron and inverse Compton emission spectrum, and the dynamics of a system (e.g., a radius of a PWN, a radius of an SNR forward and reverse shock, and a magnetic field inside a PWN) at each evolutionary phase.

The dynamical model evolves the particle distribution inside a PWN via three mechanisms: continuous particle injection of a fraction of the pulsar spin-down luminosity, adiabatic energy loss due to the expansion of the PWN, and radiative energy loss due to synchrotron and inverse Compton emission. The spin-down luminosity  $\dot{E}$  of a PWN at its age  $t$  is formulated as

$$\dot{E}(t) = \dot{E}_0 \left(1 + \frac{t}{\tau_{sd}}\right)^{-\frac{p+1}{p-1}}, \quad (4.1)$$

where  $\dot{E}_0$  is the initial spin-down luminosity,  $p$  is the pulsar braking index, and  $\tau_{sd}$  is the characteristic pulsar spin-down timescale.  $\tau_{sd}$  is related to a pulsar's characteristic age  $\tau$  and true age  $t_{age}$  as

$$t_{age} = \frac{2\tau}{p-1} - \tau_{sd}. \quad (4.2)$$

A fraction of the spin-down luminosity  $\eta_B \dot{E}$  is injected into the PWN as magnetic fields, while the rest of the spin-down luminosity,  $(1 - \eta_B) \dot{E}$ , is injected as particles (electrons and positrons). The particle injection spectrum is defined within the energy range between  $E_{min}$  (minimum energy of the injected particle, fixed to 0.1 GeV in this work) and  $E_{max}$  (maximum energy of the injected particle). The magnetic field is assumed to be homogeneous throughout the volume of the PWN, and thus it decreases as the PWN expands and increases as the PWN is crushed by the collision with the SNR reverse shock. The radiative loss changes accordingly – synchrotron emission is much stronger than inverse Compton emission in the early stage or post-collision era of the PWN, whereas inverse Compton flux becomes comparable with synchrotron flux as the PWN ages. Adiabatic loss is most severe when a PWN freely expands against only ram pressure from the unshocked supernova ejecta in the free-expansion phase. Once the PWN collides with the SNR reverse shock and starts encountering the pressure from shocked ejecta, the expansion of the PWN slows down until the compression starts, during which the PWN undergoes adiabatic heating.

The dynamical evolution of a system is calculated based on input parameters related to a supernova, SNR, and surroundings, such as supernova explosion energy ( $E_{SN}$ ), ejecta mass inside an SNR ( $M_{ej}$ ), and ISM density just outside an SNR forward shock ( $n_{ISM}$ ). These parameters determine the pressure just outside a PWN and at the location of a reverse shock. A PWN size changes such that the pressure from the ejecta is in balance with the pressure inside a PWN, which comprises magnetic pressure and pressure from particles as a relativistic ideal gas. When a reverse shock reaches a PWN, the pressure experienced by a PWN increases dramatically. This leads to a rapid decrease in the size of a PWN and, consequently, a sharp increase in the magnetic field inside a PWN. Synchrotron loss is extreme at this point. Once a PWN is highly compressed, and its pressure exceeds the ejecta pressure, the PWN starts re-expanding, and hence the magnetic field

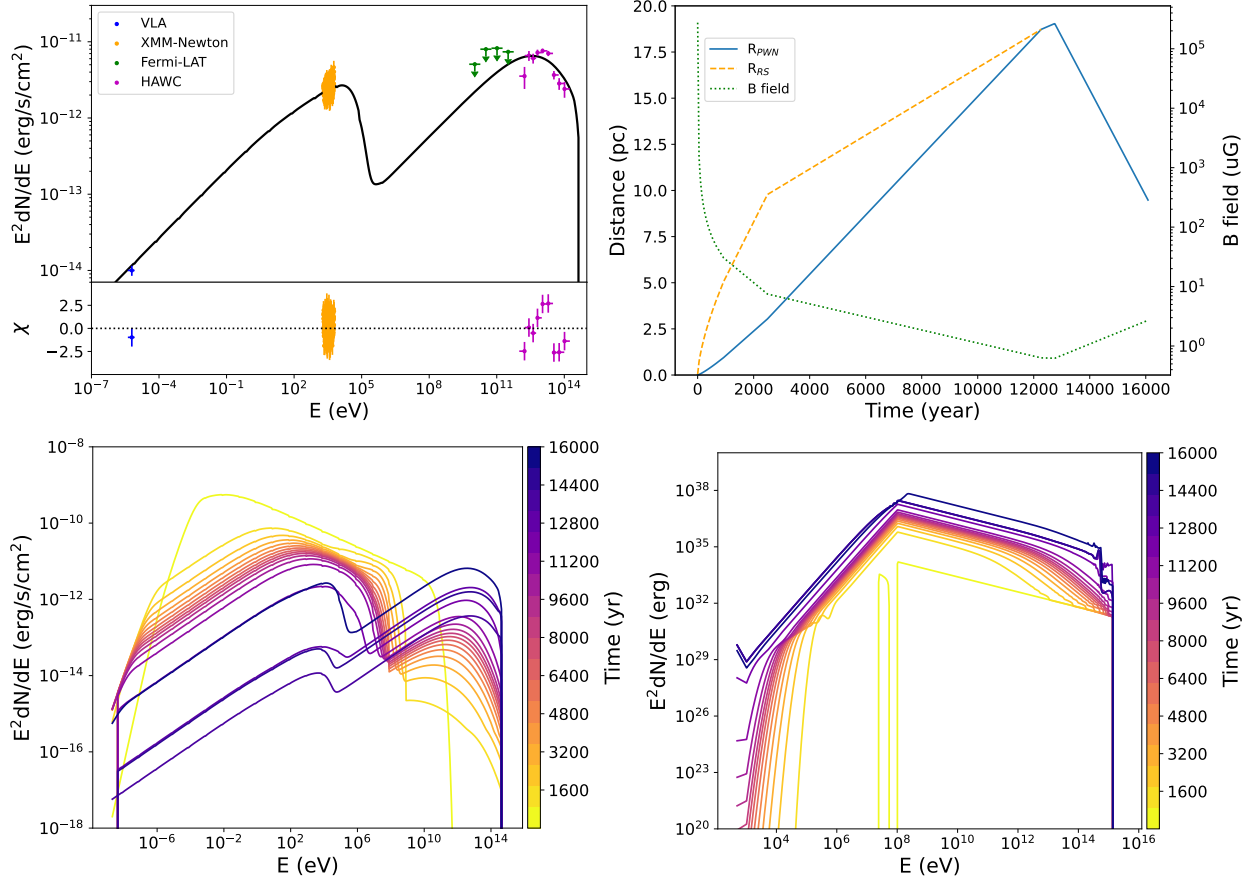


Figure 4.7: *Top left*: The SED model for the Dragonfly from the dynamical model. The model parameters are given in Table 3. Radio, X-ray, and TeV flux data points are overlaid. The residuals are plotted in terms of significance  $((\text{data}-\text{model})/(1\sigma \text{ uncertainty of data}))$ . *Top right*: Time evolution of the PWN radius ( $R_{pwn}$ , blue solid line), SNR reverse shock radius ( $R_{RS}$ , orange dashed line), and magnetic field inside the PWN (B field, green dotted line) over the true age from our model (16 kyr). The PWN collided with the SNR reverse shock at  $t_{RS} = 12$  kyr. *Bottom*: Time evolution of the radiation (*left*) and particle (*right*) spectrum of the Dragonfly.

inside the PWN starts decreasing. As a PWN ages, its size grows as large as several parsecs or more, and its magnetic field becomes as low as a few  $\mu\text{G}$ . The resulting spectrum yields a similar level of SC and IC flux, a typical spectrum observed in middle-aged PWNe.

We aimed to find a set of model parameters that reproduces not only the multiwavelength spectrum but also the observed size of the Dragonfly. The Dragonfly displays a highly asymmetric morphology, although the dynamical model assumes a spherical system. Given this limitation of the model, we focus on characterizing the evolution of the PWN properties averaged over the entire system rather than their spatial dependency. We approximated a nominal radius of the PWN to be

Table 4.4: Comparison between PeVatron pulsar wind nebulae

		G75.23+0.12 (“Dragonfly”)	G18.5-0.4 (“Eel”) <sup>a</sup>	G106.65+2.96 (“Boomerang”) <sup>b</sup>
TeV counterpart		eHWC J2019+368 LHAASO J2018+3651	HAWC J1826-128 LHAASO J1825-1326	HAWC J2227+610 LHAASO J2226+6057
Name		PSR J2021+3651	PSR J1825-1256	PSR J2220+6114
Pulsar	$\tau$ (kyr)	17	14	10
	$\dot{E}$ ( $10^{36}$ erg/s)	3.4	3.6	22
	Distance <sup>c</sup> (kpc)	0.4 – 12 (3.5)	3.5	0.8 – 7.5 (7.5)
PWN	$E_{max}$ (PeV)	1.4	4.6	3.3
	Magnetic field ( $\mu\text{G}$ )	2.7	0.6	2.2
	True age (kyr)	16	4.6	3.3
	$t_{RS}$ (kyr)	12	–	1.5

<sup>a</sup>[151] and references therein. <sup>b</sup>[196] and references therein.

<sup>c</sup>For the sources with a wide range of distance estimates, the distance used for SED modeling is given in parentheses.

10' so that its spherical volume roughly matches the physical volume of the outer nebula. The radio nebula size  $\sim 20'$  was used for this calculation – the lowest energy particles seen in the radio band would have a much longer lifetime than its synchrotron cooling time and thus best reflect the true extent of the PWN. The angular size of 10' is equivalent to  $R_{PWN} = 10$  pc at the nominal distance  $d = 3.5$  kpc.

The input and output parameters of the dynamical model are listed in Table 3. Figure 4.7 shows the SED model plotted with the multiwavelength data and residuals, the time evolution of the dynamical parameters (magnetic field, PWN radius  $R_{PWN}$ , and SNR reverse shock radius  $R_{RS}$ ), radiation and particle spectra.

The maximum particle energy  $E_{max} = 1.4$  PeV provides strong evidence that the Dragonfly is a PeVatron PWN. The true age of 16 kyr was found to be slightly younger than its characteristic age  $\tau = 17$  kyr. The true age found by our model is much older than 7 kyr found by [184]. This difference can be attributed most likely to the assumed source distance (3.5 kpc in this work, 1.8 kpc in [184]), as well as to the SED models and the X-ray spectra (see §4.4). The low magnetic field (2.7  $\mu\text{G}$ ) is consistent with that from Naima, [168], [186], and [184]. The low magnetic fraction  $\eta_B = 0.008$  contributes to this low magnetic field.

Our model predicts that the PWN expanded to  $\sim 20$  pc, collided with the supernova reverse

shock 4 kyrs ago ( $t_{RS} = 12$  kyr), and has been shrinking since then to reach the current size  $\sim 10$  pc (Figure 4.7 (b)). Relatively low ISM density  $n_{ISM} = 0.03 \text{ cm}^{-3}$  drove a slow reverse shock, allowing the PWN to grow large enough to reach the reverse shock even before it started heading back toward the PWN. Combined with the substantial ejecta mass  $M_{ej} = 7.2M_{\odot}$ , this low ISM density may indicate that the host SNR of the Dragonfly evolved into the wind-blown bubble of a massive progenitor star with an extremely low density (below  $0.001 \text{ cm}^{-3}$ ) during the first few kyrs of its lifetime [197].

The particle index  $\alpha = 2.4$  is consistent with *Naima*. The IR field temperature (9.9 K) falls below the range of the dust temperature in Sh2-104 (see §4.4.1). Using the braking index  $p = 2.5$  and  $\tau_{sd} = 6.8$  kyr of our model, the total particle energy ( $3.9 \times 10^{48}$  erg) is 50% of the total injected energy over the true age (16 kyr) of the Dragonfly.

## 4.5 Discussion

### 4.5.1 PeVatron pulsar wind nebulae

We compare three PeVatron PWNe studied in our NuSTAR observational program of energetic PWNe: G75.23+0.12 (“Dragonfly”, this work), G18.5-0.4 (“Eel”, [151]), and G106.65+2.96 (“Boomerang”, [196]). All three PWNe were modeled with the dynamical model. Key facts and the model parameters of the three PWNe are summarized in Table 4.4. The common features of the three PeVatron PWNe are the following:

1. The maximum particle energy is greater than 1 PeV.
2. The source morphology is highly asymmetric and energy-dependent. The pulsar is located on the edge of the extended radio and soft X-ray nebulae and is offset from the centroid of its TeV counterparts.
3. The magnetic field strength inside the PWNe is low  $< 3 \mu\text{G}$ .
4. Compact hard X-ray nebula was detected up to 20 keV by NuSTAR. The nebular size is

much smaller than the lower-energy nebula (radio and soft X-ray).

5. The compact hard X-ray nebular spectrum does not exhibit a spectral break or cutoff. A synchrotron burnoff is observed from the shrinkage of its size at higher energies.
6. The dynamical model predicts that the PWN collided with the reverse shock of the host SNR “recently” (the Dragonfly and Boomerang), or such a collision is about to happen (the Eel).

Features 2 and 3 are known properties of bright TeV PWNe (e.g., [198] and [64]). While asymmetric morphology bears a few different possibilities (fast pulsar velocity, asymmetric SNR reverse shock – PWN interaction, or a combination of both effects – see §4.5.2), energy dependency of morphology can be attributed to particle transport and cooling. Particles that emit synchrotron radiation in the radio band (particle energy  $E \sim 1$  GeV in the interstellar magnetic field  $\sim 3 \mu\text{G}$ ) have cooling times much longer than the age of the PWN and hence transport to large distances away from the pulsar without losing much of their energies. Particles that radiate in the hard X-ray band ( $E \sim 100$  TeV), on the other hand, have much shorter cooling times than the PWN age. Such particles can travel only to short distances before cooling down to lower energies, resulting in feature 4 (see §4.5.3). Therefore, only freshly injected highly energetic particles contribute to the compact hard X-ray nebula. Relic particles, after cooling, exhibit larger extents in lower energies.

Looking at an IC spectrum, relic particles with energies  $E \sim 10$  TeV upscatter the CMB photons to TeV energies. Such particles can be dim in the synchrotron spectrum due to a lower magnetic field farther away from the pulsar, explaining the offset of the TeV emission from the pulsar. Feature 3 is necessary for this reason and manifests as the observed low X-ray to gamma-ray luminosity ratios. GeV-emitting particles ( $E \sim 10$  GeV) are expected to form even fainter SC and IC nebulae due to their lower energies and larger distances traveled. No GeV nebulae were detected for the PeVatron PWNe except for the “tail” region of the Boomerang whose emission is attributed to its parent SNR (e.g., [199]).

Feature 6 provides a hint as to how particles are accelerated in PeVatron PWNe. [200] proposed using a Monte Carlo simulation that particles may be accelerated to 1 PeV during the compression

of a PWN by the collision with the reverse shock of its host SNR.

Some of the above properties are in contrast to those of other TeV PWNe in our NuSTAR observational campaign, such as G313.54+0.23 (“K3” or “Kookaburra”, [153]) and G313.3+0.1 (“Rabbit”, [152]). These southern sources are invisible to HAWC and LHAASO, the telescopes that operate in the highest energy regime ( $> 100$  TeV). Their NuSTAR hard X-ray nebulae are extended (radius  $\sim 3'$  at the source distance  $\sim 5.6$  kpc for both PWNe), and the nebular sizes do not change significantly with energy. Multi-zone SED modeling using the spatially resolved NuSTAR spectra along with multiwavelength flux data yielded the maximum particle energies below 1 PeV for both PWNe. The PWNe have bright GeV counterparts whose spectra connect smoothly to the spectra of their TeV counterparts. Future gamma-ray observatories in the southern hemisphere, the Southern Wide-field Gamma-ray Observatory (SWGGO) and Cherenkov Telescope Observatory (CTAO) – South, will play a crucial role in studying the true energetics of these PWNe and their relation to the multiwavelength observations.

#### 4.5.2 Distance and proper motion

The distance of the Dragonfly is relevant to not only its brightness but also its physical size, and hence the proper motion of PSR J2021+3651. Like many other TeV PWNe (e.g., [55]), the Dragonfly is offset from the center of the nebula and its TeV counterparts. Such highly asymmetric morphology is often attributed to a fast proper motion of the pulsar. [162] estimated the transverse velocity of PSR J2021+3651 to be  $840d_5t_{17}^{-1}$  km/s, where  $d_5$  is the distance of the Dragonfly scaled to 5 kpc and  $t_{17}$  is the age of PSR J2021+3651 scaled to its characteristic age of 17 kyr, in case it was born at the end of the radio nebula. [184] estimated it to be  $\sim 1,300$  km/s in case PSR J2021+3651 is located at 1.8 kpc and was born 7 kyrs ago at the location of HAWC J2019+368. [158] and [170] claimed the detection of a bow shock structure on the East side of the Dragonfly, yet noted a possibility of at most a mildly supersonic motion of PSR J2021+3651 considering the well-preserved substructures of the inner nebula.

Given the true age of 16 kyr from our model, the Dragonfly may be too young to have escaped

its host SNR and form a bow shock in the ISM (e.g., [201]). Instead, the bow shock structure with the well-defined inner nebula and the asymmetric PWN morphology could be explained by an asymmetric interaction between the PWN and the reverse shock of its host SNR due to an ambient density gradient (e.g., [202] and [172]). In this case, the orientation of the bow shock does not necessarily align with the direction of the pulsar’s proper motion [203]. There is no known dense object on the East of PSR J2021+3651, and the host SNR has not been detected. This mystery could be solved by a deep and expansive radio observation that covers a large ( $\sim 1^\circ$ ) region to search for the faint host SNR of PSR J2021+3651. Here, we focus on discussing the proper motion of PSR J2021+3651 that may have caused the asymmetric morphology of the Dragonfly.

The angular separation between PSR J2021+3651 and the centroid of eHWC J2019+368 is  $\sim 16'$ . If PSR J2021+3651 was born near the centroid of eHWC J2019+368 and traveled to the current location at a constant speed, the corresponding transverse velocity of the pulsar is  $v_{psr} = 996d_{3.5}t_{16}^{-1}$  km/s, where  $t_{16}$  is the true age scaled to 16 kyr. This is above the average pulsar velocity (540 km/s, [204]), but not exceptionally high [205]. In this case, measuring the pulsar proper motion of  $\sim 0.06''d_{3.5}t_{16}^{-1}/\text{yr}$  may not be feasible unless PSR J2021+3651 is significantly closer than 3.5 kpc or significantly younger than 16 kyr. Another Chandra observation of PSR J2021+3651, nearly 20 years after the last observation, to detect the pulsar motion could provide insight into the source distance and age; however, their degeneracy will still need to be disentangled. Our future work will combine new radio (VLA) and X-ray (Chandra) observation with an energy-dependent morphology study using VERITAS and Fermi-LAT to place tight constraints on the source distance and evolutionary history of the Dragonfly.

### 4.5.3 Magnetic field

For particles with a synchrotron lifetime shorter than the age of the system, the distance that a particle can travel is determined by its synchrotron lifetime rather than the system age. In the vicinity of the pulsar where the magnetic field is strong, and the particles are transported mainly by energy-independent advection, the PWN size in different energy bands should be proportional to

the synchrotron lifetime of the electrons (e.g., [206]). This is demonstrated by the changing nebula size in energy observed with NuSTAR. A synchrotron lifetime  $t_{sync}$  can be defined as a time scale that an electron with Lorentz factor  $\gamma$  loses all of its energy  $E$  via synchrotron radiation in magnetic field strength  $B$ . A synchrotron spectrum of a single electron is highly peaked around its critical frequency  $\nu_{crit}(E) \propto BE^2$ . A rough estimation of a synchrotron lifetime using this information yields

$$t_{sync} = \frac{E}{P_{synch}} \sim \frac{\gamma mc^2}{\gamma^2 B^2} \sim \frac{1}{\sqrt{B^3 \nu_{crit}(\gamma)}}. \quad (4.3)$$

Assuming a constant average magnetic field and advection velocity in the region, the ratio of a synchrotron lifetime between particles emitting 3 keV photons and those emitting 6 keV photons is calculated as  $\sqrt{6 \text{ keV}/3 \text{ keV}} = 1.4$ . This ratio is indeed comparable to the ratio of the nebula size in two different energy bands:  $\text{FWHM}(3\text{--}6 \text{ keV})/\text{FWHM}(6\text{--}20 \text{ keV}) = 26.5''/15.2'' = 1.3$ .

Comparing the nebula sizes in the two energy bands also allows placing an upper limit of the magnetic field inside the compact nebula. The inner nebula detected by NuSTAR is located well outside the termination shock (2–3 smaller than the torii  $\sim 10''$  [158]), where the advection velocity can be approximated to the overall PWN expansion velocity (e.g., [207]). The expansion velocity of the Dragonfly has not been measured, yet some other PWNe were estimated to expand at  $\sim 1,000$  km/s (e.g., [207], [208], and [209]). Eq. (6) in [208] gives the time it takes for an electron to lose half its energy via synchrotron radiation ( $t_{1/2}$ ). For example, an electron that was emitting 12 keV photons  $t_{1/2}$  years ago has cooled down by now to emit 3 keV photons ( $\nu_{crit} \propto E^2$ ). Assuming that this electron traveled from the edge of the hard-band nebula ( $\text{FWHM} = 15.2''$ ) to the edge of the soft-band nebula ( $\text{FWHM} = 26.5''$ ) at velocity  $v_{ad} = 1,000$  km/s, the constant average magnetic field inside the compact nebula yields  $B = 24d_{3.5}^{-3/2} \mu\text{G}$ . Compared with the  $2.7 \mu\text{G}$  in the outer nebula, the much stronger magnetic field for the outer nebula was anticipated from the compact size of the hard X-ray inner nebula. This magnetic field estimate is consistent with the inner nebula magnetic field estimated by [158] ( $\sim 20 \mu\text{G}$  assuming a dipolar field) and [170] ( $\sim 22 \mu\text{G}$  assuming equipartition between the magnetic field and particle energy).

## 4.6 Summary

As part of our NuSTAR observational campaign of energetic PWNe, we studied the X-ray properties of the Dragonfly PWN and its viability as a leptonic PeVatron. Our NuSTAR observation detected a compact ( $r = 1'$ ) inner nebula of the Dragonfly in 3 – 20 keV. The size of this nebula decreases at higher energies, indicating synchrotron burnoff in a strong ( $\sim 24 \mu\text{G}$ ) magnetic field near its pulsar PSR J2021+3651. The large diffuse outer nebula of the Dragonfly is observed in soft X-ray ( $\sim 10'$ ) and radio ( $\sim 2'$ ). We used these outer nebula spectra along with the TeV spectrum of eHWC J2019+368 to model the multiwavelength SED of the Dragonfly. The dynamical model yields the maximum particle energy of 1.4 PeV, and a low magnetic field ( $2.7 \mu\text{G}$ ) averaged over the outer nebula in contrast to the high magnetic field in the inner nebula. At a nominal distance of 3.5 kpc, this 16-kyr-old PWN was found to have collided with the SNR reverse shock 4 kyrs ago. The highly asymmetric and energy-dependent morphology of the Dragonfly implies a fast proper motion of its pulsar ( $\sim 1,000 \text{ km/s}$ ) and/or inhomogeneity in the ISM that initiated an asymmetric SNR – PWN interaction. Our future work will investigate these scenarios and provide a deeper understanding of particle transport in such an evolved system using radio, X-ray, and gamma-ray observations.

The Dragonfly shares common features with other PWNe in our NuSTAR observational campaigns with the maximum particle energies above 1 PeV – the Eel [151] and Boomerang [196]. These features include a compact hard X-ray inner nebula undergoing synchrotron burnoff, a large diffuse outer nebula in lower energy, and an absence of a GeV nebula. Opposite patterns are observed in two of our target PWNe, the K3 [153], and Rabbit [152]. These PWNe exhibit extended hard X-ray nebulae without a sign of synchrotron burnoff, energy-insensitive morphologies, and bright GeV nebulae. The best-fit multi-zone models of the two PWNe yield the maximum particle energies below 1 PeV, while the PWNe are invisible to the current UHE observatories. The next-generation UHE observatories in the southern hemisphere (SWG0 and CTAO–South) will enable us to study the true energetics of the PWNe and its relation to the multiwavelength observations.

## Chapter 5: LHAASO J0621+3755 – pulsar halo?

The contents of this chapter have been peer-reviewed and accepted for publication [210]. The result of SED modeling, performed by Silvia Manconi, is cited from [210]. The summary and key findings of this chapter are as follows.

- We observe the inverse Compton radiation (§1.3.3) of a candidate pulsar halo (§1.4.2, “Stage 3” in Figure 1.10) LHAASO J0621+3755 in the VHE band using VERITAS (§2.3). A sophisticated background estimation technique is developed to address challenges in extended source analysis.
- We observe the synchrotron radiation (§1.3.4) of LHAASO J0621+3755 in the soft X-ray band using XMM-Newton (§2.1.1).
- Neither the inverse Compton or synchrotron emission of the pulsar halo is detected. On the other hand, the spectrum and spatial profile of the inverse Compton gamma rays are measured by LHAASO (§2.4, [148]). We model this spatial profile as well as the multi-wavelength SED as synchrotron and inverse Compton emission of CR electrons accelerated by an old pulsar PSR J0622+3749. The injected CR electron spectrum and the diffusion coefficient and magnetic field within the halo are deduced.
- The CR electron spectrum cuts off at 200 TeV, indicating LHAASO J0621+3755 is not a leptonic PeVatron.
- Diffusion around the pulsar is suppressed by two orders of magnitude compared with the galactic average value, possibly due to the magnetic turbulence generated by the CR electrons (§1.1).

## 5.1 Introduction

Pulsar halos [44] are regions around middle-aged (characteristic age  $\tau > 100$  kyr) pulsars extending out to a few tens of parsecs, typically found as very-high-energy (VHE,  $E > 100$  GeV) gamma-ray sources. These halos are believed to be the last evolutionary stage of pulsar wind nebulae (PWNe), when relativistic electrons and positrons (collectively referred to as electrons hereafter) escape from the central PWN, diffuse in the interstellar medium and scatter interstellar photons up to TeV energies through inverse Compton (IC) scattering. Since the first pulsar halos around the nearby pulsars Geminga and Monogem were discovered by Milagro Gamma-Ray Observatory [211] and studied in detail by the High-Altitude Water Cherenkov (HAWC) observatory [65], more than a dozen other VHE sources have been categorized as candidate pulsar halos ([212], [148], [213], [214]). The majority of these sources are spatially coincident with middle-aged pulsars with spin-down luminosities of the order of  $10^{34}$  erg s<sup>-1</sup>. Detecting the lower-energy IC emission of these candidate pulsar halos in the Fermi Large Area Telescope (Fermi-LAT) data has been unsuccessful except for the case of Geminga [215]. While the electrons within the halos are expected to produce extended, low-surface-brightness synchrotron emission in the interstellar magnetic field, no such emission has been found from radio to X-ray energies (e.g., [216]).

Pulsar halos have been studied extensively as an ideal probe for the cosmic-ray (CR) transport mechanism near energetic CR accelerators. Numerous theoretical CR diffusion models have successfully reproduced the gamma-ray spectra and morphologies of different halos (e.g., [217, 218, 219, 220]). Such models<sup>1</sup> consistently suggest diffusion coefficients within pulsar halos 2–3 orders of magnitude lower than the Galactic average inferred from the secondary-to-primary CR ratio [20]. The origin of diffusion inhibition within pulsar halos is unknown. Among the proposed origins are the parent supernova remnant’s shocks or magnetohydrodynamic turbulence generated by the CRs themselves. Further details on the recent developments in observation and theory of pulsar halos can be found in [62, 222, 223].

---

<sup>1</sup>An exception is the ballistic diffusion model [221], which explains the observed gamma-ray emission from Geminga, Monogem, and LHAASO J0621+3755 without invoking suppressed diffusion.

LHAASO J0621+3755 is a candidate pulsar halo detected by the Large High Altitude Air Shower Observatory (LHAASO). The LHAASO Kilometer Square Array (KM2A) detected this extended (2D Gaussian  $\sigma = 0.40^\circ \pm 0.07^\circ$ ) VHE source up to 158 TeV [148]. Its counterpart in the first LHAASO catalog [6] is 1LHAASO J0622+3754, an extended source also detected by the LHAASO Water Cherenkov Detector Array (WCDA) in the 1–25 TeV energy range (2D Gaussian  $\sigma = 0.46^\circ \pm 0.03^\circ$ ). LHAASO J0621+3755 is spatially coincident with a Geminga-like (Table 5.1) pulsar PSR J0622+3749 (angular separation  $0.11^\circ \pm 0.12^\circ$ ). PSR J0622+3749 is a gamma-ray pulsar detected by Fermi-LAT (4FGL J0622.2+3749 in the latest Fermi-LAT point source catalog [77]); see Table 5.1. The pulsar is detected below 10 GeV during the on-pulse phase, while it is not detected during the off-pulse phase [224]. No multiwavelength counterparts of the pulsar or its halo have been found in the radio, infrared, and X-ray bands [225, 148, 224].

Multiwavelength observation plays a key role in understanding the physical nature of pulsar halos. VHE observation using imaging atmospheric Cherenkov telescopes (IACTs) can map the spatial distribution of a halo’s gamma-ray emission with a superior angular resolution ( $< 0.1^\circ$ ), thereby placing a tight constraint on the diffusion coefficient within the halo. X-ray observation can uniquely determine the magnetic field within a halo, which is one of the key factors characterizing CR diffusion. In this work, we present the VHE observation of LHAASO J0621+3755 with the Very Energetic Radiation Imaging Telescope Array System (VERITAS) in §5.2 and present a novel background estimation technique for observations of extended sources in §5.2.1. We present the X-ray observation of LHAASO J0621+3755 with XMM-Newton and report the first X-ray detection of PSR J0622+3749 in §5.3. We discuss the multiwavelength aspect of LHAASO J0621+3755 as a pulsar halo in §5.4.

## 5.2 VERITAS analysis

VERITAS is a ground-based gamma-ray observatory located in Amado, Arizona, consisting of an array of four imaging atmospheric Cherenkov telescopes sensitive in the 85 GeV to  $>30$  TeV energy range. Each telescope is equipped with a 12m optical reflector and 499-pixel photomulti-

Table 5.1: PSR J0622+3749, Geminga, and Monogem pulsar properties.

Name	$P$ (ms)	$\dot{P}$ ( $10^{-14}$ s s $^{-1}$ )	$\tau$ (kyr)	$\dot{E}$ ( $10^{34}$ erg s $^{-1}$ )	$B_s^\dagger$ ( $10^{12}$ G)	$d$ (kpc)
PSR J0622+3749	333.2	2.542	207.7	2.713	2.945	1.67 $^\ddagger$
Geminga	237.1	1.097	342.4	3.250	1.632	0.25 $^{+0.23}_{-0.08}$
Monogem	384.9	5.496	111.0	3.804	4.654	0.29 $\pm$ 0.03

$^\dagger$ Minimum magnetic field strength at the neutron star surface, assuming the  $\dot{E}$  is converted into magnetic dipole radiation.

$^\ddagger$ “Pseudo-distance” derived from the phenomenological correlation between pulsar gamma-ray luminosity and distance [225]. This distance was adopted for the pulsar halo modeling in this work. Distance estimate by parallax, dispersion measure, or other methods is unavailable.

References: [226] for the Geminga distance, [227] for the Monogem distance, [228] for everything else.

plier tube camera, providing a field of view (FoV) of 3.5° in diameter and angular resolution of 0.08° (68% containment radius) at 1 TeV [9].

VERITAS observed LHAASO J0621+3755 in 2022 and 2023 for 40 hours at a mean elevation of 72°. Observations were taken in a “wobble mode” [229] in which the telescopes were pointed 0.7° offset from the centroid of LHAASO J0621+3755. We used Eventdisplay v490.2 [230, 231], a standard VERITAS data analysis pipeline, for event reconstruction and gamma-hadron separation. For gamma-hadron separation, we applied a cut on the air shower image parameters (mean scaled length and mean scaled width) predetermined for a Crab-like spectrum using boosted decision trees [232]. The gamma-like events, as well as full-enclosure instrument response functions (effective area and point spread function), were written into DL3 files for analysis in Gammapy [233, 234]. The source region was set to a circular region with a radius of 1° corresponding to the 86% containment radius of 1LHAASO J0622+3754. Such a large source extent, compared with VERITAS’s FoV (radius of 1.75°), poses challenges in background estimation. We developed a code to generate a 3D acceptance map for the observations and apply the FoV technique [235] for background estimation. The FoV technique estimates the background of the entire FoV by scaling the acceptance in each energy and spatial bin by the observed count rate in the source-free region. Therefore, accurate telescope acceptance estimation is crucial. The energy and spatial dependence of the telescope acceptance are mainly determined by observing conditions such as

elevation and azimuth. The details of acceptance map generation and background estimation using Gammapy are described in §5.2.1. The analysis was cross-checked with an independent analysis using Eventdisplay v490.2 for event reconstruction and the low-rank perturbation method for background estimation [236].

Figure 5.1 *left* panel shows a significance<sup>2</sup> map around LHAASO J0621+3755 in 0.3–10 TeV. No significant gamma-ray emission was detected within the source region shown by the black solid line in the figure. The significance distributions drawn from the bins within both the entire FoV and the FoV excluding the source region are consistent with a standard normal distribution expected from statistical fluctuations. The total significance of excess counts in 0.3–10 TeV within the source region (a circle with a radius of 1°) is  $1\sigma$ . We derived the 95% flux upper limits in six logarithmic bins in 0.3–10 TeV (bin edges 0.3, 0.5, 1.0, 1.7, 3.1, 5.6 and 10 TeV) as shown in Figure 5.1 *right* panel.<sup>3</sup>

### 5.2.1 3D acceptance map and FOV technique in Gammapy

Observing nearby pulsar halos with IACTs enables high-resolution ( $< 0.1^\circ$ ) morphology studies, a unique advantage for studying CR transport mechanisms. However, such observations bear challenges in background estimation due to the IACTs’ limited FoV (diameter of  $3.5^\circ$  for VERITAS) and nearby halos’ source extensions over  $1^\circ$ . We developed a technique to accurately estimate the telescope acceptance map of the entire FoV. The acceptance map reflects the spatial and energy dependence (“3D acceptance”) of gamma-like CR background, the dominant background component for IACT observations originating from different observing conditions and CR shower properties. The acceptance map can be scaled utilizing a minimal available source-free region in the FoV to generate a background for the entire FoV. This technique is useful for any IACT data analyses of extended sources. The code was developed based on Gammapy v1.1 and is available at <https://github.com/VERITAS-Observatory/gammapy-fov.git>.

<sup>2</sup> $\sqrt{TS}$  where TS (test statistic) is the Cash statistic [237] for Poisson-distributed data and modeled background.

<sup>3</sup>To scale the LHAASO data for the VERITAS source region size, we calculated the corresponding containment fraction using the 2D Gaussian sigma of the LHAASO source and multiplied it by the LHAASO spectrum.

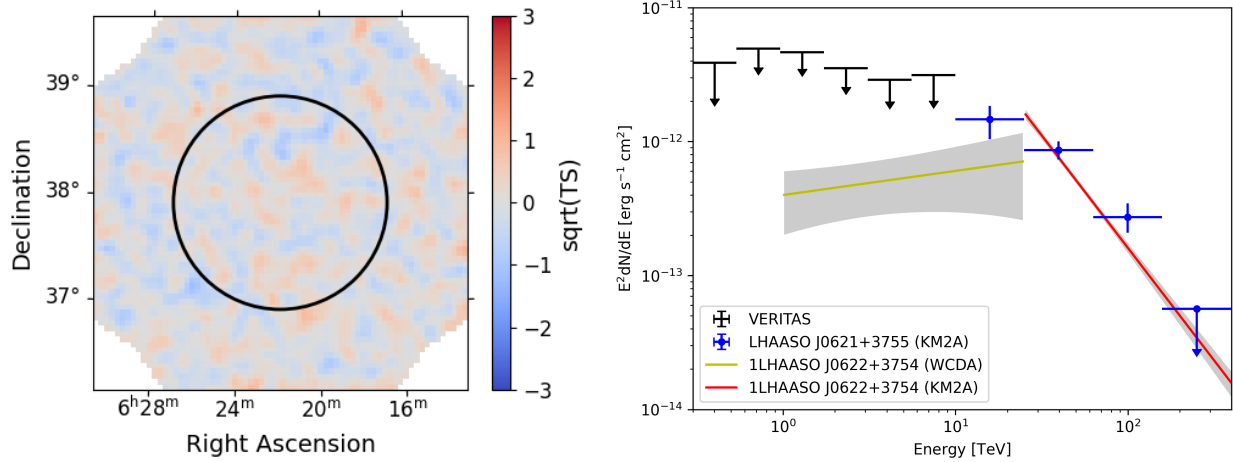


Figure 5.1: **Left:** A significance map ( $3.5^\circ \times 3.5^\circ$ ) of the region around LHAASO J0621+3755 in 0.3–10 TeV. The source region (86% containment region of 1LHAASO J0622+3754, a circular region with a radius of  $1^\circ$  centered at the centroid of LHAASO J0621+3755) is overlaid with a black solid line. The pixel size is  $0.05^\circ \times 0.05^\circ$ , and the image was smoothed using a Gaussian kernel ( $\sigma = 1$  pixel). **Right:** TeV gamma-ray SED of LHAASO J0621+3755. The 95% VERITAS flux upper limits for a circular region with a radius of  $1^\circ$  from this work (black), LHAASO KM2A flux points and 95% flux upper limit from [148] (blue), LHAASO WCDA and KM2A best-fit power-law spectral models (yellow and red solid lines, respectively) and statistical uncertainties (grey shaded area) for 1LHAASO J0622+3754 are overlaid. The LHAASO flux points, upper limits, spectral models and uncertainties were scaled to the same region size as the VERITAS source region size for comparability.

### 5.2.2 Generating a 3D acceptance map

A 3D acceptance map has two spatial axes (detector X and detector Y) and one energy axis. In this map, each spatial and energy bin ( $0.1^\circ \times 0.1^\circ$  six logarithmic bins in 0.3–10 TeV for this work) contains an acceptance value. The size of this map is  $3.5^\circ \times 3.5^\circ$ ; that is, the map covers the range of detector X coordinates  $[-1.75^\circ, 1.75^\circ]$  and detector Y coordinates  $[-1.75^\circ, 1.75^\circ]$ . A single 3D acceptance map is used for all the observing runs of LHAASO J0621+3755 (“on runs”). The steps for acceptance map generation are summarized below and elaborated upon in the following text.

1. Select “off runs,” observations with either no gamma-ray source or a point-like gamma-ray source within the FoV, taken under the observing conditions similar to those of the on runs.
2. For each off run, excise any gamma-ray sources and stars in the FoV and patch up the excised regions with reflected regions within the same FoV.
3. Create a stacked count map by adding up the count maps of the off runs.
4. Create a stacked exposure map (in units of TeV s sr) by adding up the exposure map (in units of s) of the off runs and multiplying it by the volume of each spatial and energy bin (in the unit of TeV sr).
5. Calculate the acceptance (gamma-like event rate) in each spatial and energy bin (in units of  $\text{TeV}^{-1} \text{s}^{-1} \text{sr}^{-1}$ ) by dividing the stacked counts map by the stacked exposure map.

Selecting the off runs that closely match the on runs’ observing conditions is crucial for accurate telescope acceptance estimation. We create a pool of extragalactic (galactic latitude  $b > 10^\circ$ ) observing runs with a duration of at least 10 minutes under good sky condition. The pool only includes the runs taken after August 2012, before which the hardware conditions were different from those of the LHAASO J0621+3755 observations [238, 239]. Elevation and azimuth of an observing run are among the most important factors for the spatial dependence of telescope acceptance. For each on run, we narrow down the pool to the observing runs taken at the azimuth within  $45^\circ$  of

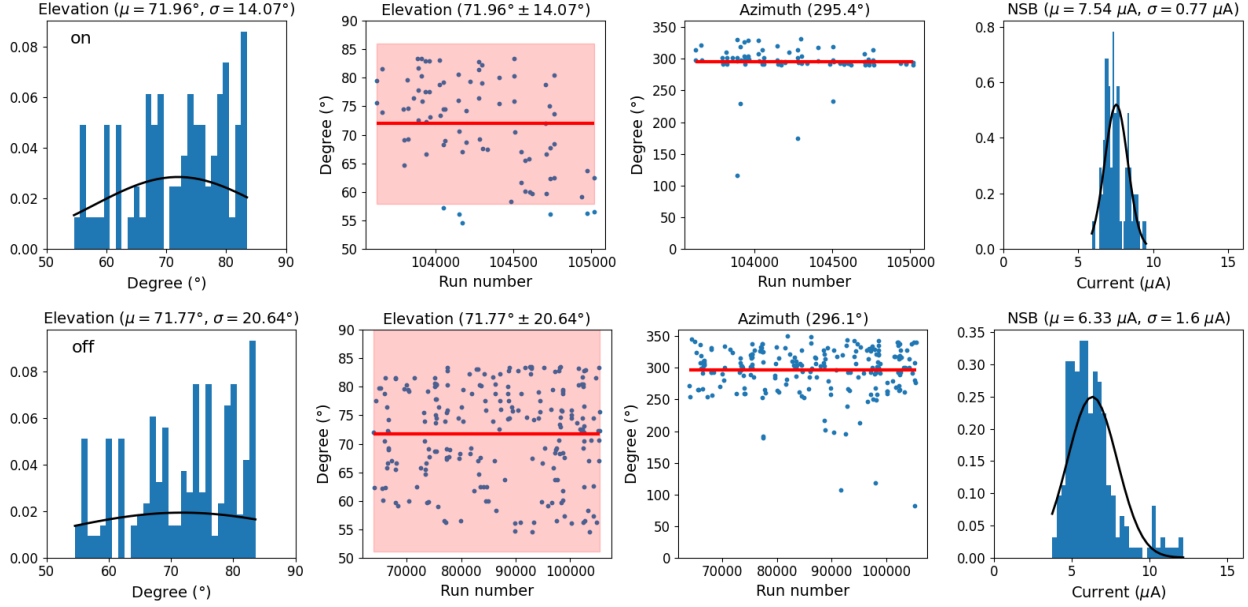


Figure 5.2: Observing conditions of the on runs (top row, labeled “on” ) and off runs for the 3D acceptance map (bottom row, labeled “off”). On each row, from the left, the **first plot** is a histogram of elevations (blue bar) and an exposure-weighted Gaussian fit to the histogram (black curve). The mean ( $\mu$ ) and standard deviation ( $\sigma$ ) of the fit are provided in the figure title. The **second plot** is a scatter plot of elevations (blue dot). The mean and ( $\text{mean} \pm 1\sigma$ ) are marked as a red line and a red-shaded region. The **third plot** is a scatter plot of azimuths (blue dot) and the exposure-weighted mean of azimuths (red line). The **last plot** is a histogram of a night sky background (NSB) averaged over a run duration (blue bar). An exposure-weighted Gaussian fit to the histogram is overlaid as a black curve, and the mean ( $\mu$ ) and the standard deviation ( $\sigma$ ) of the fit are provided in the figure title.

the on-run azimuth. Out of this reduced pool, off runs taken at the elevation closest to the on-run elevation are selected until the total duration of the off runs reaches two times the on-run duration. Selected off runs are used only once for a particular on run, and are not used again for the rest of the analysis. The observing conditions of the on runs and the off runs selected for 3D acceptance map generation are consistent with each other, as shown in Figure 5.2. The discrepancy in the current distributions likely originates from the proximity to the Galactic Plane and the presence of a bright point-like source and stars in the FoV. The off runs have much higher galactic latitudes on average ( $b > 40^\circ$ ) than LHAASO J0621+3755 ( $b = 10.95^\circ$ ), and hence the lower average current. On the other hand, the presence of bright stars in the off runs may create the high-current tail.

Point-like gamma-ray sources or stars in the FoV of the off runs are excised by a circle with  $0.4^\circ$

radius. The excised region is filled with the events from a region with the same shape, size, and offset from the center of the FoV (“reflected region”). A Gammapy class `ReflectedRegionsFinder` is used to find such a region. The coordinates of the events within the reflected region are rotated around the center of the FoV so that those events fill the excised region. The impact of this procedure in the accurate estimation of the acceptance spatial distribution is minimal as only  $\sim 10\%$  of the off runs contain a point-like gamma-ray source at one of four locations:  $0.5^\circ$  offset to the east, west, south, and north of the center of the FoV. Figure 5.3 demonstrates this procedure using an observation of Markarian 421 taken at the  $0.5^\circ$  south wobble. This procedure is currently necessary for a technical reason, but an alternative way of leaving the excised region empty could be made possible in principle.

Once the off runs are selected for all the on runs and sources are excised, the 3D acceptance map is calculated. After replacing zero acceptances with small definite values, the acceptance map is smoothed using a 2D Gaussian kernel with  $\sigma = 1 \text{ bin} = 0.1^\circ$ . Figure 5.4 shows the resulting 3D acceptance map used for the analysis of the on runs. The azimuthal asymmetry of the acceptance is the outcome of the varying atmospheric depth along the line of sight (related to the elevation) and the Earth’s magnetic field strength (related to the azimuth) throughout the FoV. The optical axis of the telescope, i.e., the center of the FoV, has the highest acceptance in the lower energies, as expected, but has the lowest acceptance in the higher energies due to the loss of more elongated, and hence truncated, shower images.

### 5.2.3 3D acceptance map validation and bias correction

The 3D acceptance map is validated by comparing five mimic datasets with their backgrounds estimated using the 3D acceptance map and the FoV technique. A mimic dataset is constructed out of the remaining pool of off runs mentioned in §5.2.2 to mimic the on runs in terms of observing conditions and duration. The off runs are selected by the same criteria as those for the off runs used for acceptance map generation. Once an off run is selected for a mimic dataset, it is removed from the pool of off runs. Figures 5.5 and 5.6 show that the observing conditions of the five mimic

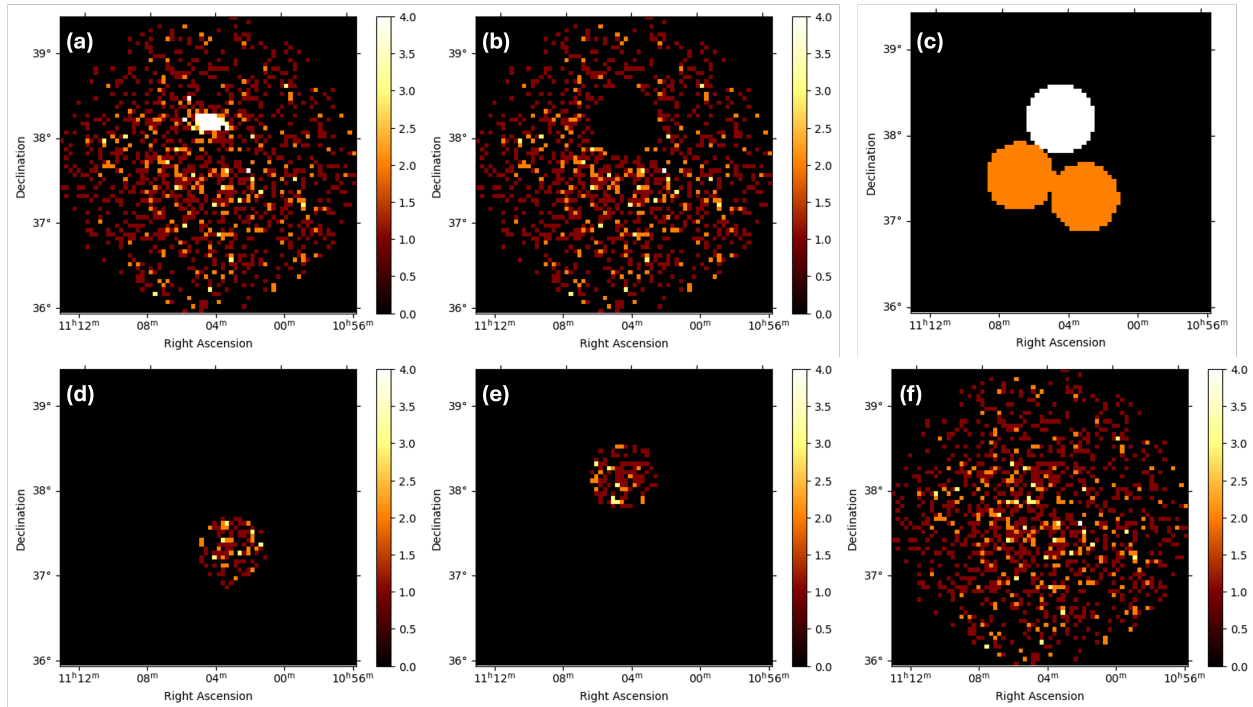


Figure 5.3: Demonstration of excising a point-like gamma-ray source and filling the excised region with the events from a reflected region. All the sky maps are  $3.5^\circ \times 3.5^\circ$ , and the bin size is  $0.05^\circ \times 0.05^\circ$ . (c) is a mask map (black is zero, white and orange are one), and all the other maps are count maps whose color bars show the number of counts in each bin. For the counts map, all the gamma-like events were plotted (lowest energy 0.1 TeV, highest energy 9.8 TeV). (a) The bright gamma-ray source in the FoV is Markarian 421. The observation was taken at the  $0.5^\circ$  south wobble. (b) Events from a circle with radius  $0.4^\circ$  centered at the position of Markarian 421 are excised. (c) The white circle is the excised region, and the orange circles are the reflected regions. All three regions are  $0.5^\circ$  offset from the center of the FoV. (d) Events from one of the reflected regions are plotted. (e) The events plotted in (d) are copied, and their coordinates are rotated around the center of the FoV such that the events are located at the excised region. (f) The events from (b) and (e) are added to create a blank sky map.

datasets are consistent with each other and with the on runs (with the off runs for the current). Figure 5.6 also shows the observing conditions of the sixth mimic dataset used for validation of bias correction in the acceptance map, as described later in this section.

Any point-like gamma-ray sources or stars in the off runs are excised. The analysis of the mimic datasets is performed exactly as the on runs would be analyzed. Figures 5.7 and 5.8 show the analysis results of the mimic datasets. The distribution of the factors by which the acceptance map was scaled to estimate the background of the off runs ("FoV norm") is centered at 1 with a

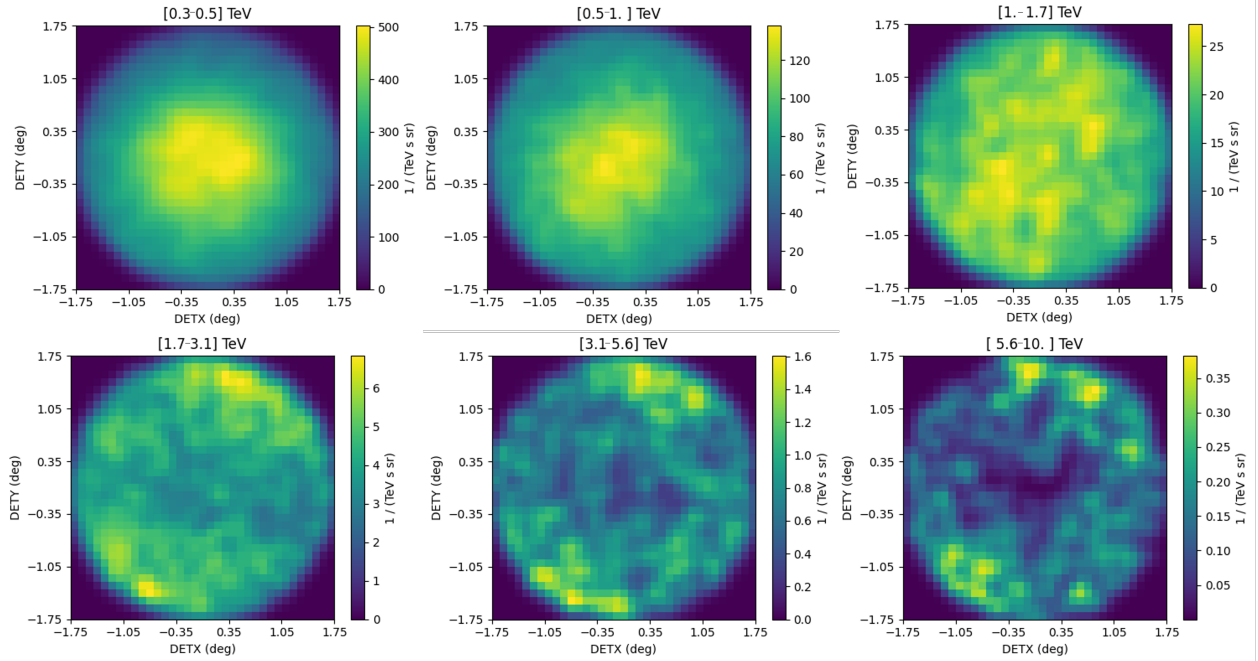


Figure 5.4: 3D acceptance map in the unit of  $\text{TeV}^{-1} \text{s}^{-1} \text{sr}^{-1}$ . Each image is a 2D (detector X and detector Y) acceptance map in each energy bin, as labeled in the figure titles.

small spread, indicating the acceptance map is already a good approximation of the off runs. The sky maps of the mimic datasets show no noticeable bias, and the distribution of significance in each bin is consistent with that of statistical fluctuations.

Nevertheless, we calculate the bias in the acceptance map as a ratio of the observed background counts (stacked off runs) to the estimated background averaged over the five mimic datasets in each spatial and energy bin. The bias map is smoothed using a 2D Gaussian kernel with  $\sigma = 1$  bin. Figure 5.9 shows the resulting 3D bias map. Biases are observed mainly along the FoV edge of each run where the exposure is small and the uncertainty on the counts is high. The bias map becomes patchy in the highest energy bins due to the low counts.

We first validate the bias map by analyzing the last mimic dataset and applying bias correction to the estimated background. This last mimic dataset is analyzed in the same way as the previous five mimic datasets. Figure 5.8 shows that the estimated background after bias correction is consistent with the observed counts of this last mimic dataset. Finally, the on runs are analyzed using the 3D acceptance map, 3D bias map, and the FoV technique as shown in Figure 5.10. The signif-

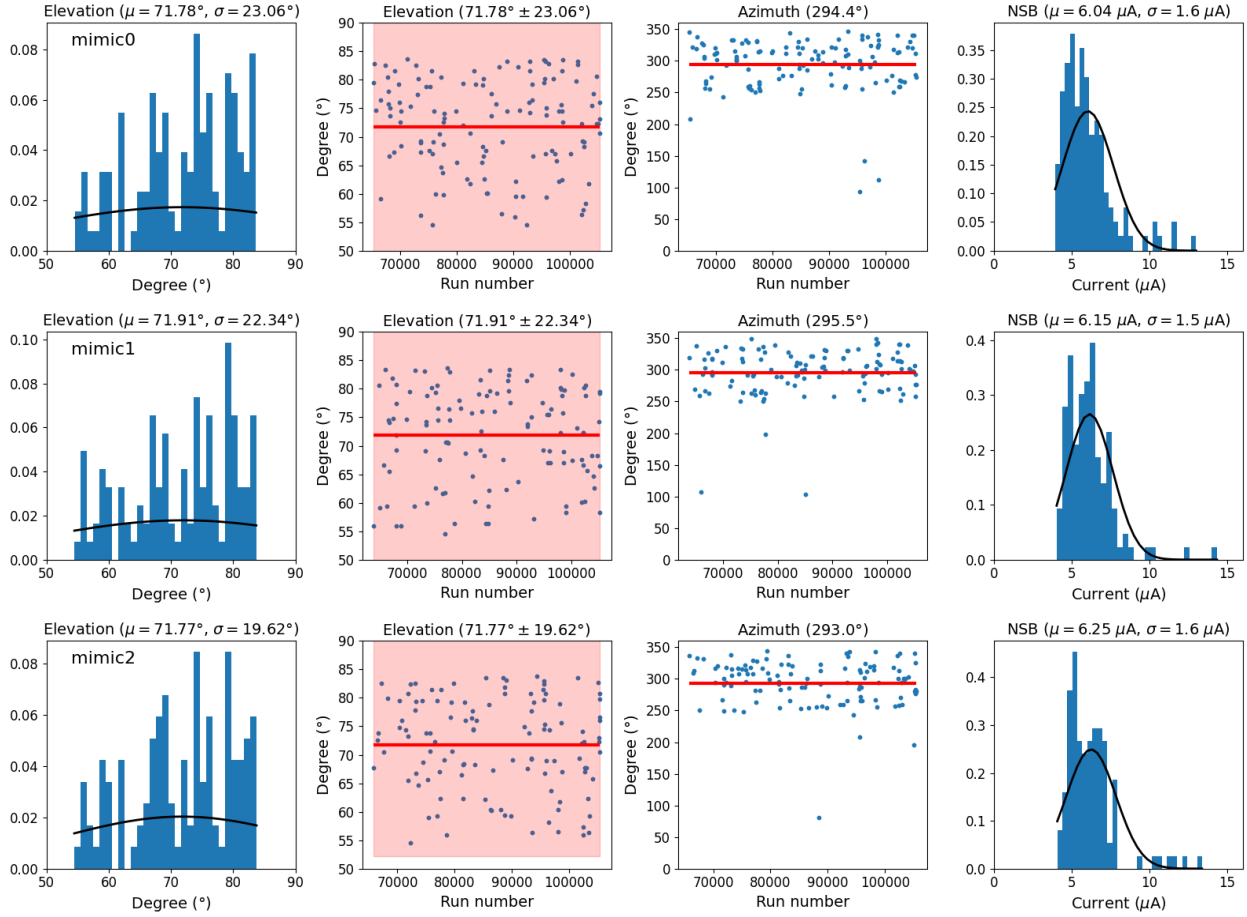


Figure 5.5: The same plots as Figure 5.2 for the off runs for three mimic datasets (“mimic0–2”).

incance distribution is consistent with the distribution of statistical fluctuations. The FoV norm is smaller than one due to the different proximity to the Galactic Plane between the on runs and the off runs used for the acceptance map generation.

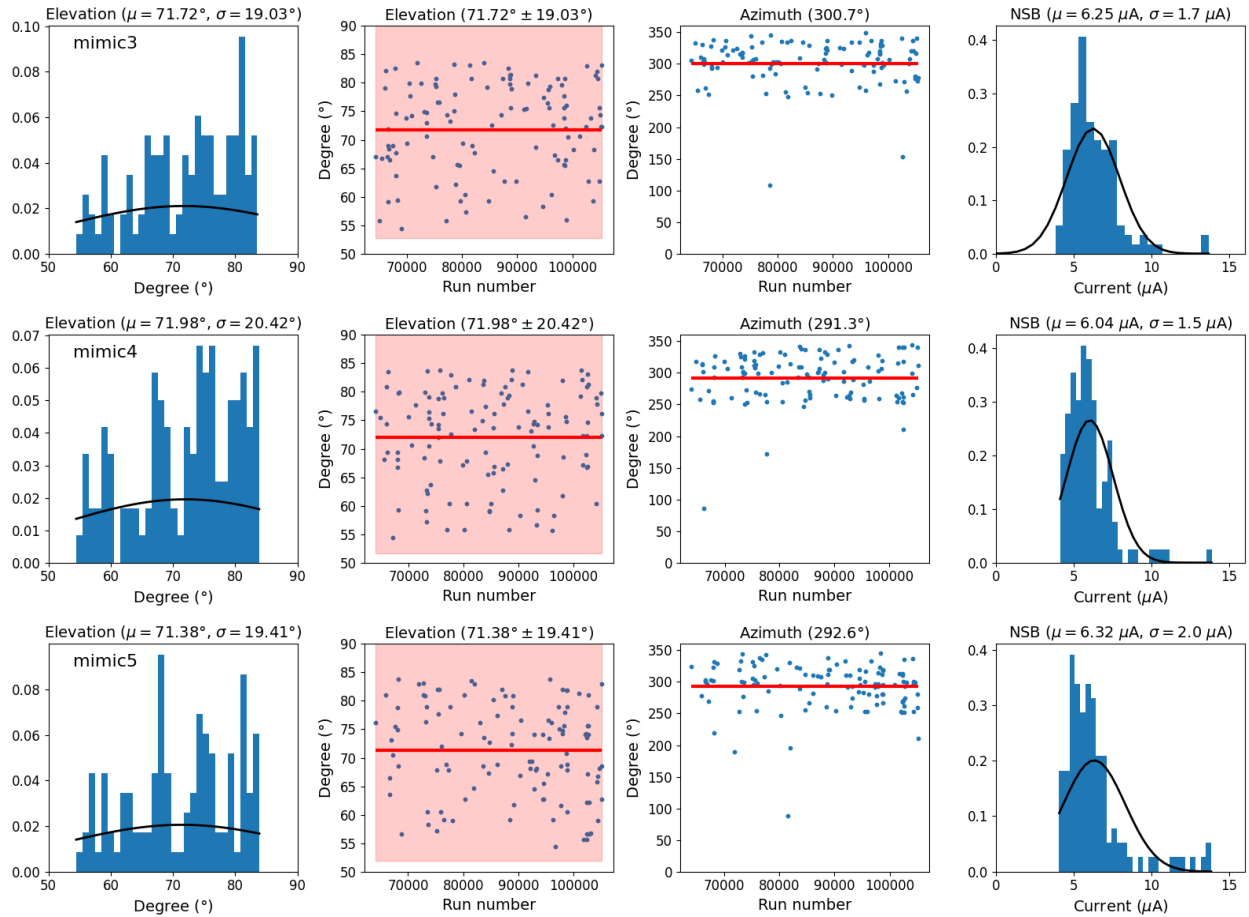


Figure 5.6: The same plots as Figure 5.2 for the off runs for three mimic datasets (“mimic3–5”).

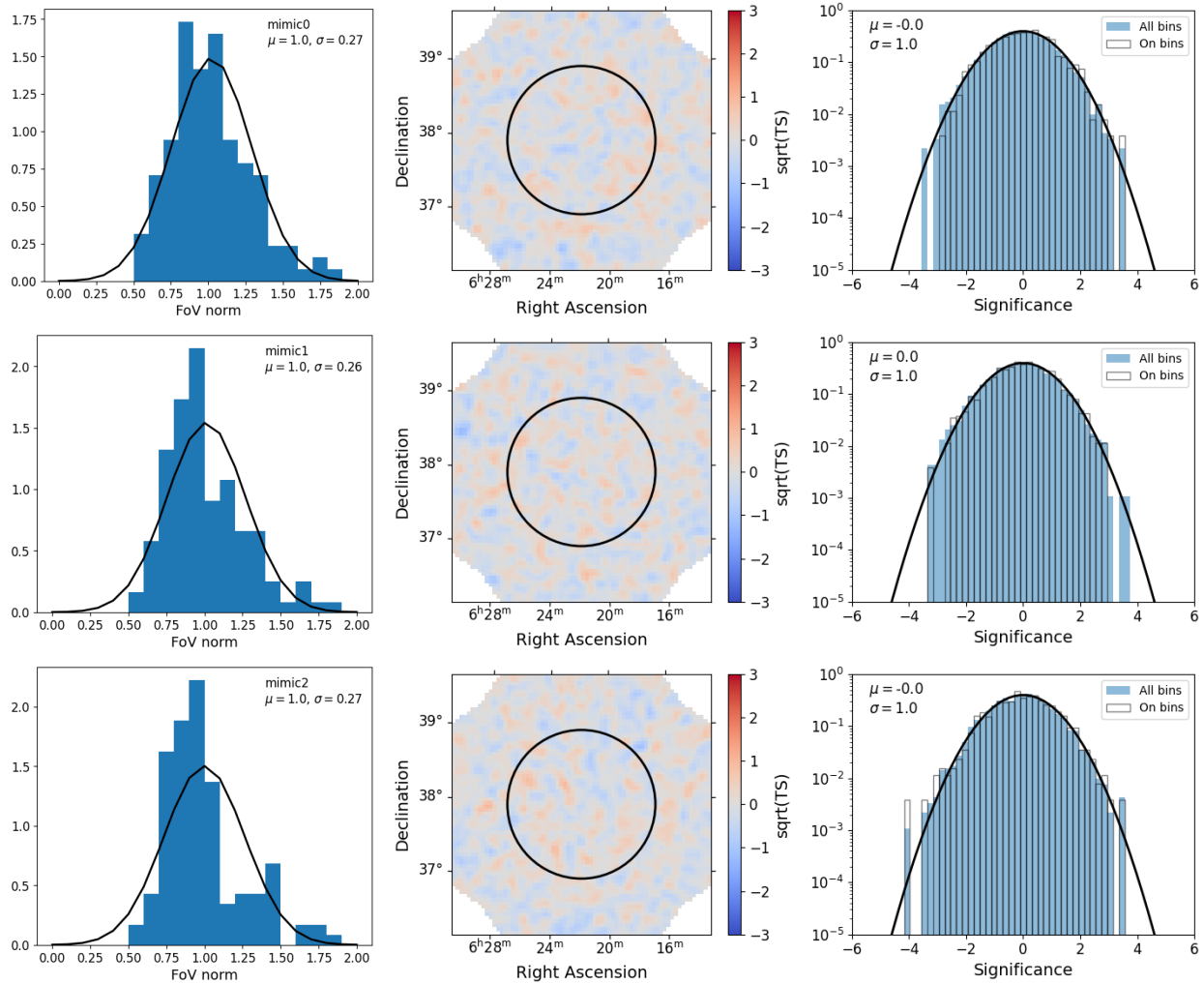


Figure 5.7: Mimic datasets 0–2 on each row: the **first plot** is the distribution of FoV norms of each off run (blue bar) and a Gaussian fit to the distribution (black curve). The numbers on the top right corner are the mean  $\pm$  standard deviation of the fit. The **second plot** is the significance map, and the **third plot** is the significance distribution from all (FoV) and on (source extraction region) regions as well as a Gaussian fit to the significances from the on region. The mean ( $\mu$ ) and standard deviation (std) of the fit are labeled on the left top corner of the plot.

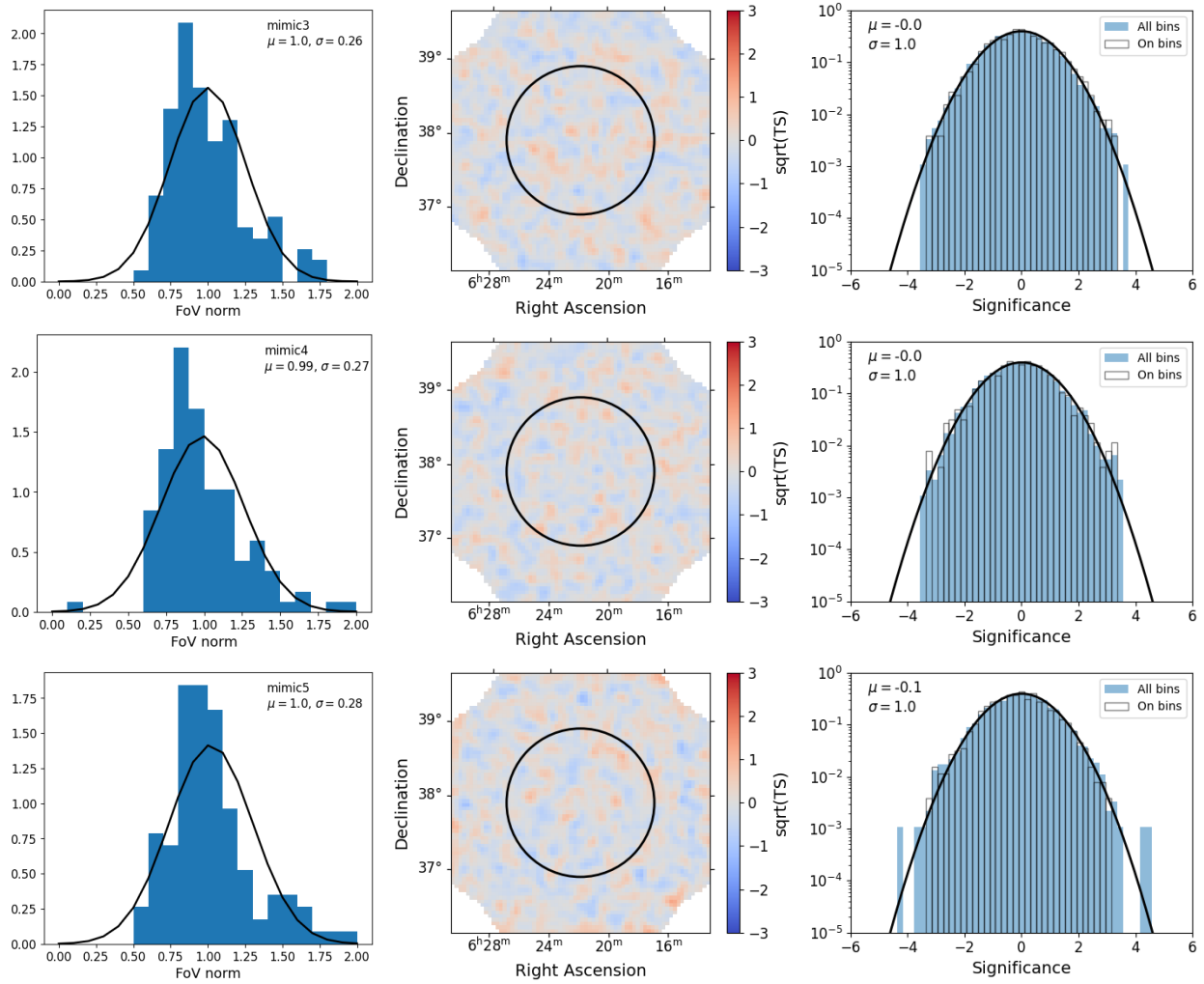


Figure 5.8: The same plots as Figure 5.7 for mimic datasets 3–5. Note that the significance map and distribution of mimic dataset 5 are after bias correction.

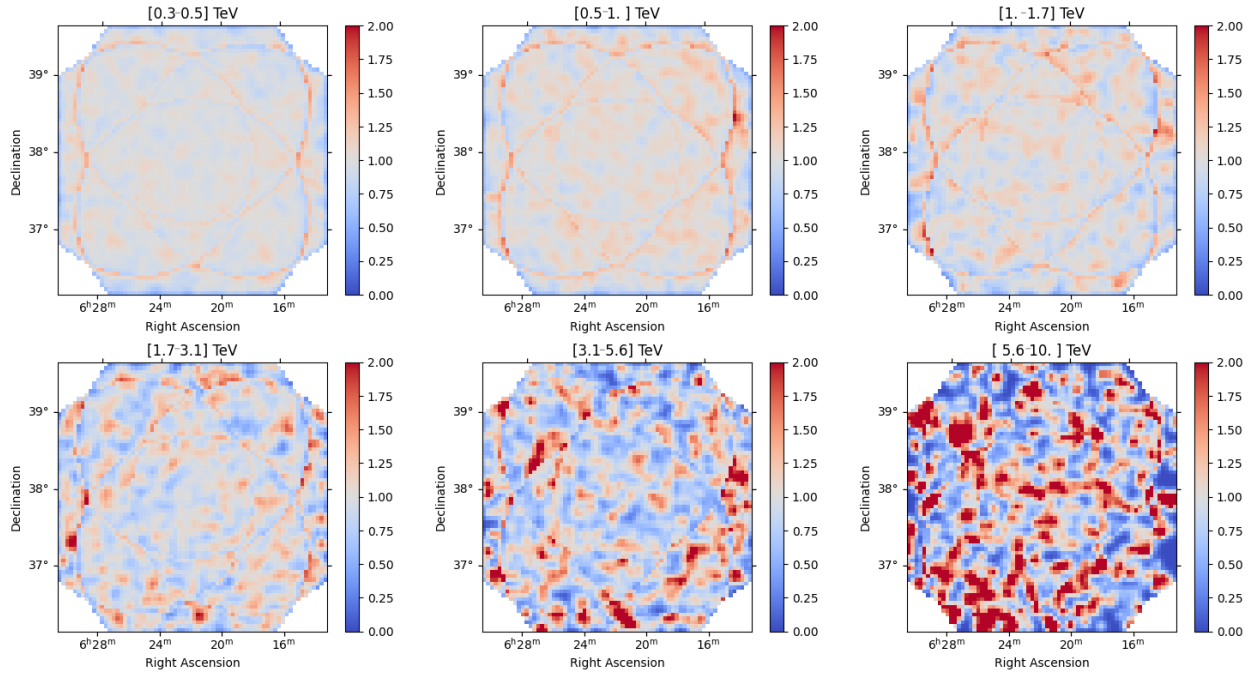


Figure 5.9: Bias maps for the six energy bins as labeled in the figure titles.

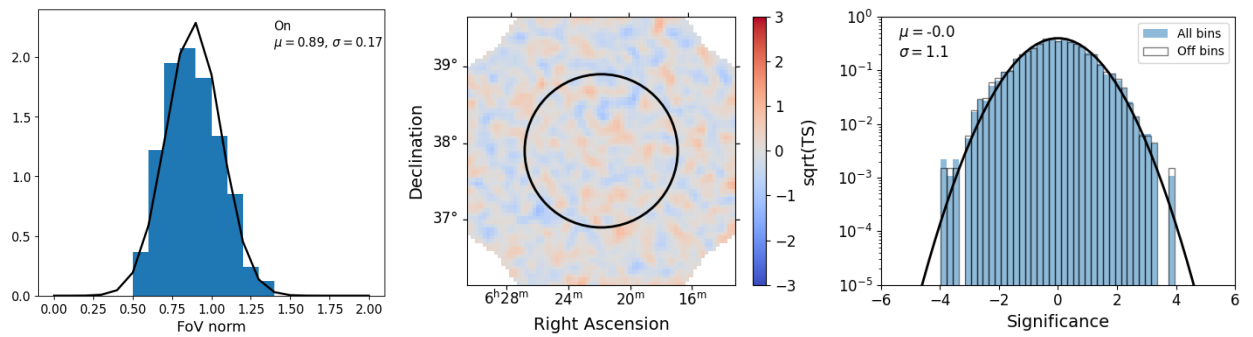


Figure 5.10: The same **first** and **second** plots as Figure 5.7 for on runs. The **third** plot is the significance distribution from all (Fov) and off (FoV minus source extraction region) regions as well as a Gaussian fit to the significances from the off region. Note that the significance map and distribution are after bias correction.

### 5.3 XMM-Newton analysis

XMM-Newton is a space-based observatory carrying three coaligned X-ray telescopes and the European Photon Imaging Camera (EPIC) sensitive in the 0.1–15 keV band. The EPIC consists of three CCD cameras (MOS1, MOS2, PN), each providing a FoV  $\sim 0.5^\circ$  in diameter with an angular resolution of  $\sim 6''$  (FWHM). We observed LHAASO J0621+3755 with XMM-Newton in March–April 2023 (observation IDs 0923400101, 0923400601, and 0923401501) with a total exposure of 74 ks. The telescope was pointed at PSR J0622+3749 for all three observations to capture the brightest part of the pulsar halo. We used the Science Analysis System (SAS)<sup>4</sup> for XMM-Newton data analysis. We produced event files using the `emchain` (for MOS) and `epchain` (for PN) tasks and filtered out the good time intervals affected by soft proton flares using the `espfilt` task. After filtering, the cleaned event files have a net exposure of 48 ks. Most of observation 0923401501 was affected by strong soft proton flares, and hence, it was not used in this work.

We used the `cheese` task on the cleaned event files to detect point sources and create Swiss-cheese masks to remove them. Among several point sources, we detected PSR J0622+3749 for the first time in the X-ray band. The analysis of this central engine of the pulsar halo is presented in [210], and the study of other point sources is left for future work. We generated images and vignetting-corrected exposure maps of the entire FoV using the `mos-spectra` and `pn-spectra` tasks. The particle background images were modeled using the filter wheel closed data and the corner chips data by the `mos_back` and `pn_back` tasks. We set the energy range of our analysis to 2–7 keV to avoid instrumental and solar charge exchange lines [240, 241]. We applied the Swiss-cheese masks to the background-subtracted FoV images, mosaiced the masked and background-subtracted images, and divided it by the mosaiced exposure map to create a flux map of the entire FoV. No hint of diffuse emission is present in the FoV as shown in Figure 5.11 *left* panel.

We extracted the source spectra using the `mos-spectra` and `pn-spectra` tasks from a

---

<sup>4</sup>Due to software errors from the extended source analysis commands, we used SAS v21 up to event cleaning and v20 afterward.

circular region with a radius of  $10'$  centered at the location of PSR J0622+3749, the largest region MOS2 and PN can cover. Since MOS1 can only cover a much smaller region due to the nonoperational CCD chips (CCD 3 and 6), we excluded MOS1 from the spectral analysis. The particle background spectra were modeled using the `mos_back` and `pn_back` tasks. The Swiss-cheese masks from the `cheese` task were applied to both the source and background spectra. Thanks to the location of LHAASO J0621+3755 off the Galactic Plane and far outside of the Galactic Bulge ( $l = 175.76^\circ$ ,  $b = 10.95^\circ$ ), we did not expect significant galactic background emission. We modeled the cosmic X-ray background (CXB) using an absorbed power-law with an index  $\Gamma = 1.41$  and normalization of  $11.6 \text{ photons cm}^{-2} \text{ s}^{-1} \text{ sr}^{-1} \text{ keV}^{-1}$  at 1 keV [177], and adopt a hydrogen column density  $N_H = 3.14 \times 10^{21} \text{ cm}^{-2}$  (Galactic column density towards PSR J0622+3749).<sup>5</sup> We used `tbabs` model in Xspec [242] for the absorption model with the `wilm` abundance table [107] for all the X-ray analyses presented in this work. The particle and CXB background components dominate the source spectra in the energy range of our analysis (2–7 keV), leaving no room for putative emission associated with LHAASO J0621+3755. We calculated a  $2\sigma$  flux upper limit in 2–7 keV of  $5.2 \times 10^{-14} \text{ erg cm}^{-2} \text{ s}^{-1}$ , assuming a fully absorbed power-law spectrum with  $\Gamma = 2$ .

#### 5.4 Discussion: LHAASO J0621+3755 as a pulsar halo

We modeled the spatial profile of LHAASO J0621+3755 measured by LHAASO [148] and the multiwavelength SED measured by XMM Newton, VERITAS (this work), Fermi-LAT and LHAASO [148] with synchrotron and inverse Compton emission of CR electrons injected, radiatively cooled, and diffusing for the lifetime of the central engine PSR J0622+3749. The details of the modeling are provided in [210]. The observed emission is reproduced by a two-zone model with suppressed diffusion ( $D = 2 \times 10^{25} \text{ cm}^2 \text{ s}^{-1}$ ) within 30 pc of the pulsar and galactic-average diffusion outside. The injected CR electron spectrum is an exponential cutoff power law ( $dN/dE_\gamma \propto E^{-\Gamma} \exp(-E/E_{cut})$ ) with a spectral index  $\gamma = 1.4$  and a cutoff energy  $E_{cut} = 200$  TeV. The magnetic field within the halo is  $B \lesssim 1 \mu\text{G}$ . The observed and modeled multiwavelength

<sup>5</sup><https://www.swift.ac.uk/analysis/nhtot/>

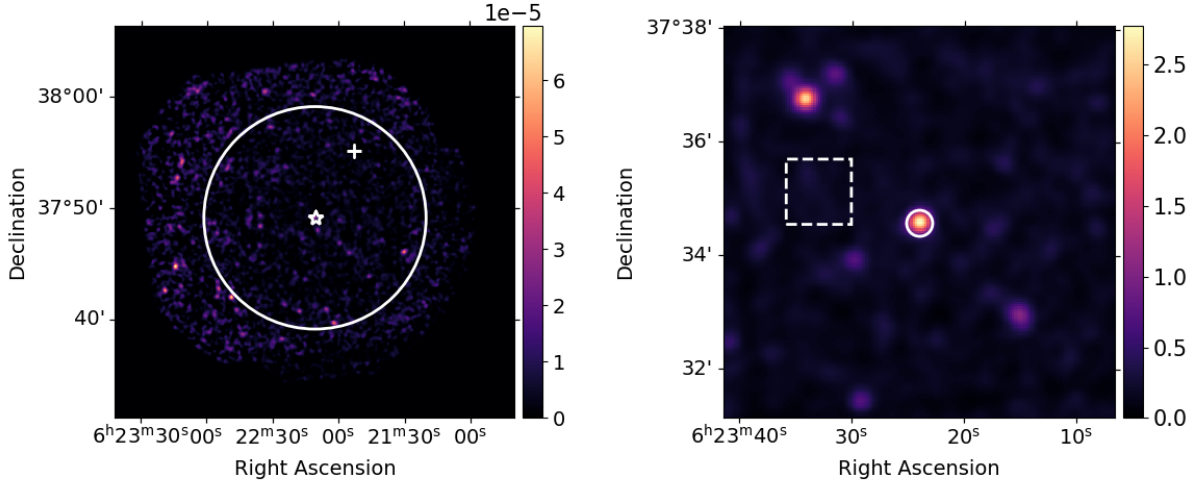


Figure 5.11: **Left:** Mosaiced, background-subtracted, and exposure-corrected image of the XMM-Newton FoV in 2–7 keV. The white circle (radius  $10'$  centered at PSR J0622+3749) marks the source region from which the flux upper limit for a putative halo was calculated. The location of PSR J0622+3749 and the centroid of LHAASO J0621+3755 are marked with a white star and a white cross, respectively. **Right:** Observation ID 923400101 MOS2 counts map in 0.2–3 keV around PSR J0622+3749 ( $0.2^\circ \times 0.2^\circ$ ). The source and background regions for the pulsar spectrum presented in [210] are marked with solid circle and dashed box, respectively.

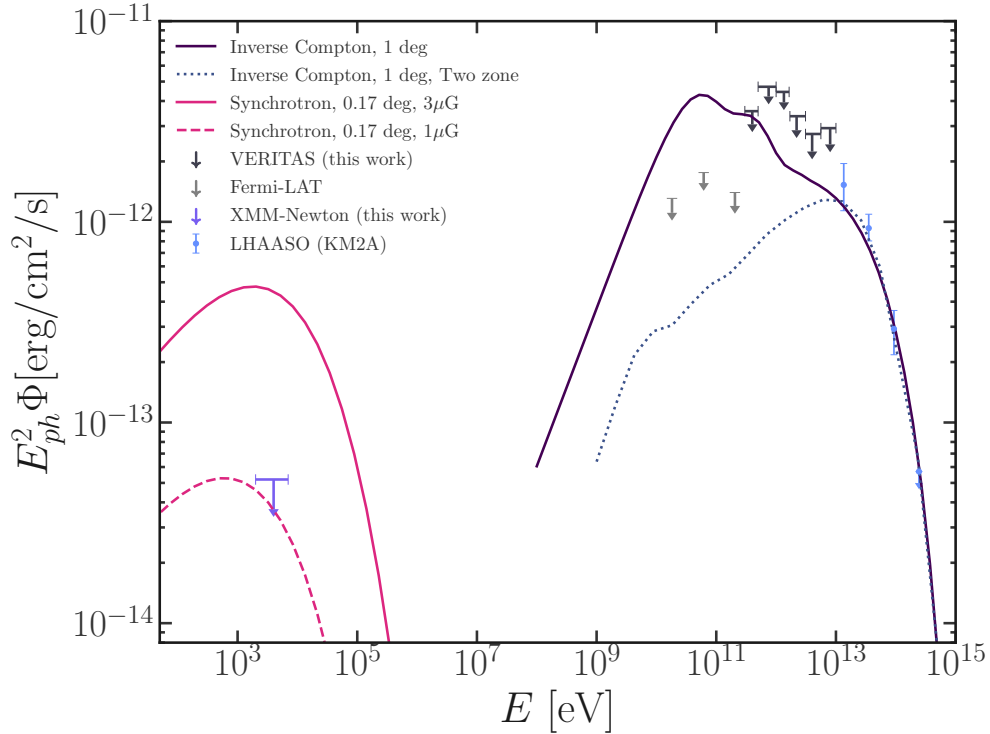


Figure 5.12: Multiwavelength SED model for LHAASO J0621+3755 as a pulsar halo [210].

SED of LHAASO J0621+3755 is shown in Figure 5.12.

PSR J0622+3749 possesses properties similar to the Geminga pulsar, as shown in Table 5.1. In addition, the diffusion coefficient and magnetic field of LHAASO J0621+3755 found by our pulsar halo modeling are consistent with those of Geminga (e.g., [65, 216]). However, the IACT and X-ray observations of LHAASO J0621+3755 significantly differ from those of Geminga. H.E.S.S. detected the Geminga halo with a radius of at least  $3^\circ$  in 0.5–40 TeV and a flux normalization of  $(2.8 \pm 0.7) \times 10^{-12} \text{ cm}^{-2} \text{ s}^{-1} \text{ TeV}^{-1}$  at 1 TeV within a radius of  $1^\circ$  around the pulsar [243]. Our VERITAS observation yielded a null detection of a halo within a radius of  $1^\circ$  around the LHAASO J0621+3755 centroid. Let us assume the physical size of the two sources are identical in all energies, and the difference in their angular sizes is due to their different distances from Earth. In this case, the ratio of the halo extensions measured by HAWC and LHAASO,  $\theta_d(\text{Geminga})/\theta_d(\text{LHAASO J0621+3755}) = 5.5^\circ/0.91^\circ = 6$  [65, 148], indicates the expected extension of LHAASO J0621+3755 in the VERITAS energy range is  $\sim 0.5^\circ$ , i.e., six times smaller than the extension of Geminga measured by H.E.S.S. Since the expected extension of  $0.5^\circ$  is well within our source region, it is unlikely that background over-subtraction causes the null detection. A more plausible explanation for the null detection is that the halo flux is below the VERITAS sensitivity limit. The 50-hr point-source sensitivity of VERITAS is comparable to the flux of LHAASO J0621+3755 measured by WCDA [244]. Given the much larger extension ( $0.5^\circ$ – $1^\circ$ ) of LHAASO J0621+3755, VERITAS may not be able to achieve detection of this source even with a few times longer exposure time. On the other hand, the spectrum measured by WCDA is inconsistent with both measurements by KM2A presented in [148] and [6] in the energy range common to the two instruments as shown in Figure 5.1. The WCDA spectrum forms an extremely sharp peak at a few tens of TeV, for which it is difficult to provide a physical explanation. The inconsistency between the WCDA and KM2A spectra and a sharp peak in the overlapping energy range between the WCDA and KM2A are seen in other LHAASO catalog sources, such as LHAASO J2108+5157. This discrepancy may arise from the generic nature of the data analysis for catalog generation in [6]. A dedicated WCDA analysis will enable more detailed spectral measurement

of LHAASO J0621+3755 in the TeV range. Our VERITAS observation provides an alternative constraint on the TeV flux of LHAASO J0621+3755 consistent with the KM2A spectrum and physically plausible.

In the X-ray band, thanks to its proximity to Earth ( $250_{-62}^{+120}$  pc, [226]), complicated sub-structures of the PWN were resolved around the Geminga pulsar. The sub-structures include a bow shock ( $\sim 8''$ ), compact central nebula ( $\sim 2'$ ), diffuse axisymmetric wings ( $\sim 3'$ ) and a tail ( $\sim 45''$ ) [245, 246, 247, 248]. These structures, if they existed in LHAASO J0621+3755, would be too small to be resolved at a distance 6 times larger than that of Geminga (i.e., 1.5 kpc). This is consistent with our XMM-Newton observation, where PSR J0622+3749 was detected as a point source. The contribution from a putative PWN to the point source emission is likely minimal as no significant nonthermal (power-law) component was found from the spectral analysis presented in [210]. No extended X-ray halo emission was detected from Geminga [216] or LHAASO J0621+3755. Even if LHAASO J0621+3755 is farther away from Earth than Geminga, the X-ray halo is likely much larger than the FoV covered by typical pointing X-ray telescopes. Still, pointing the telescope at the central pulsar will allow the most stringent estimate of flux upper limits from the brightest part of a halo. All-sky survey telescopes such as the eROSITA and Einstein Probe have the advantage of observing these extended halos. However, the sensitivity of their spectral measurement is limited by the shallow exposure (a few 100 s, [249, 250]).

Independent from the WCDA spectrum, our VERITAS flux upper limits constrain the electron injection spectral index to  $\gamma = 1.4$  as shown in Figure 5.12, a spectrum much harder than that of the Geminga halo found by [65, 215] and other works ( $\gamma \gtrsim 2$ ). The electrons emitting TeV gamma rays have energies of tens to hundreds of TeV [65] and a cooling time of only a few kyr. Considering such a short cooling time, a diffusion coefficient 100 times smaller than the Galactic average is necessary to confine such high-energy electrons within the observed source size  $\sim 30$  pc. On the other hand, electrons emitting gamma rays with energies of tens to hundreds of GeV have a cooling time comparable to the age of the pulsar  $\sim 100$  kyrs, and hence, the number of low-energy electrons around the pulsar is much greater in case of stronger suppression of diffusion.

This leads to an observed GeV flux that is much higher than what is expected from the injection spectrum, as seen from the Geminga or Monogem halo whose IC spectra are most likely peaked at or below GeV energies (e.g., [215]). This is not the case for LHAASO J0621+3755, as the Fermi-LAT upper limits tightly constrain the extent of the region in which such diffusion suppression can be present. The combined effect of a hard injection spectrum and a narrow region of suppressed diffusion creates a peak in the broadband gamma-ray spectrum at 1–10 TeV. Our findings, along with the magnetic field strength  $\lesssim 1 \mu\text{G}$  obtained from our XMM-Newton observation, provide ingredients for studying the formation of magnetohydrodynamic turbulence around a pulsar – a possible origin of suppressed diffusion.

## 5.5 Summary and conclusion

We observed a pulsar halo candidate LHAASO J0621+3755 with VERITAS in the TeV gamma-ray band and XMM-Newton in the X-ray band. To address the challenge of extended source analysis using IACTs with limited FoV, as part of this work, we developed a sophisticated technique to accurately measure the telescope acceptance and estimate the background of the entire FoV. The code implementing this technique is publicly available and can be useful for elucidating the mysterious nature of many extended Galactic PeVatrons discovered by LHAASO and HAWC.

Our VERITAS and XMM-Newton observations resulted in null detection of emission associated with LHAASO J0621+3755 within radii of  $1^\circ$  and  $10'$ , respectively. We modeled the multiwavelength SED and gamma-ray surface brightness profile of LHAASO J0621+3755 as synchrotron and IC emissions from a pulsar halo accounting for electron injection, cooling, and diffusion over the characteristic age of PSR J0622+3749 (208 kyr) at an assumed distance of 1.6 kpc. Our VERITAS flux upper limits in the 0.3–10 TeV band constrain the electron injection spectral index to  $\gamma \sim 1.4$  and the diffusion coefficient to  $2 \times 10^{25} \text{ cm}^2 \text{ s}^{-1}$ . This diffusion coefficient is similar to that of Geminga, and lower than the Galactic average by two orders of magnitude. Moreover, our VERITAS flux upper limits indicate a break in the gamma-ray spectrum at 1–10 TeV. Utilizing additional flux upper limits from the Fermi-LAT, this spectral break constrains the

diffusion suppression region to  $\sim 30$  pc around the pulsar. Our XMM-Newton flux upper limit in the 2–7 keV band ( $5.2 \times 10^{-14}$  erg cm<sup>2</sup> s<sup>-1</sup>) constrains the magnetic field strength to  $\lesssim 1$   $\mu$ G. Our findings of the electron injection spectrum, diffusion coefficient, diffusion suppression length, and magnetic field strength can be used to study the formation of magnetohydrodynamic turbulence around the pulsar as the origin of suppressed diffusion. Even though LHAASO J0621+3755 is likely at a much larger distance than Geminga, the large extent and low surface brightness of the halo are major challenges of observing this source with the current-generation IACTs and pointing X-ray telescopes. The Cherenkov Telescope Array Observatory (CTAO), the next-generation high-sensitivity and wide-field IACT, and X-ray survey telescopes with large FoV, such as the eROSITA and the Einstein Probe, are expected to play a significant role in studying pulsar halos.

## Conclusion

This work aimed to identify Galactic PeVatrons by observing three energetic galactic CR accelerators in the X-ray and gamma-ray bands. While the Dragonfly PWN was found to be a leptonic PeVatron, a young SNR Cas A does not seem to be either a leptonic or hadronic PeVatron. A pulsar halo candidate, LHAASO J0621+3755, provides insight into CR diffusion but is clearly not a PeVatron. Then where are PeV CRs, especially protons, coming from? How can this question be answered in future studies? One way is to consider new source classes. For example, microquasars have recently emerged as Galactic PeVatron candidates after UHE detection of V4641 Sgr [251]. Another way is to build more sensitive instruments. LHAASO will continue finding more galactic PeVatrons with its revolutionary sensitivity. However, the limited angular resolution (inherent to EASAs) prohibits localizing the CR acceleration sites in extended UHE sources. IACTs can contribute to this aspect, but the current-generation IACTs' sensitivity falls below the flux of many LHAASO sources. The limited FOVs of IACTs cannot capture the entirety of extended LHAASO sources. The CTAO will resolve these issues with broadband sensitivity comparable with LHAASO (Figure 5.13) and much larger FOVs than the current-generation IACTs. Its improved angular resolution will greatly improve multi-wavelength observation of galactic PeVatrons with arcsecond-resolution X-ray telescopes. The CTAO will cover both hemispheres, whereas the SWGO will open up the high-sensitivity UHE sky in the southern hemisphere.

Theoretical improvement can also help answer the question of the origin of PeV CRs. For SNRs,

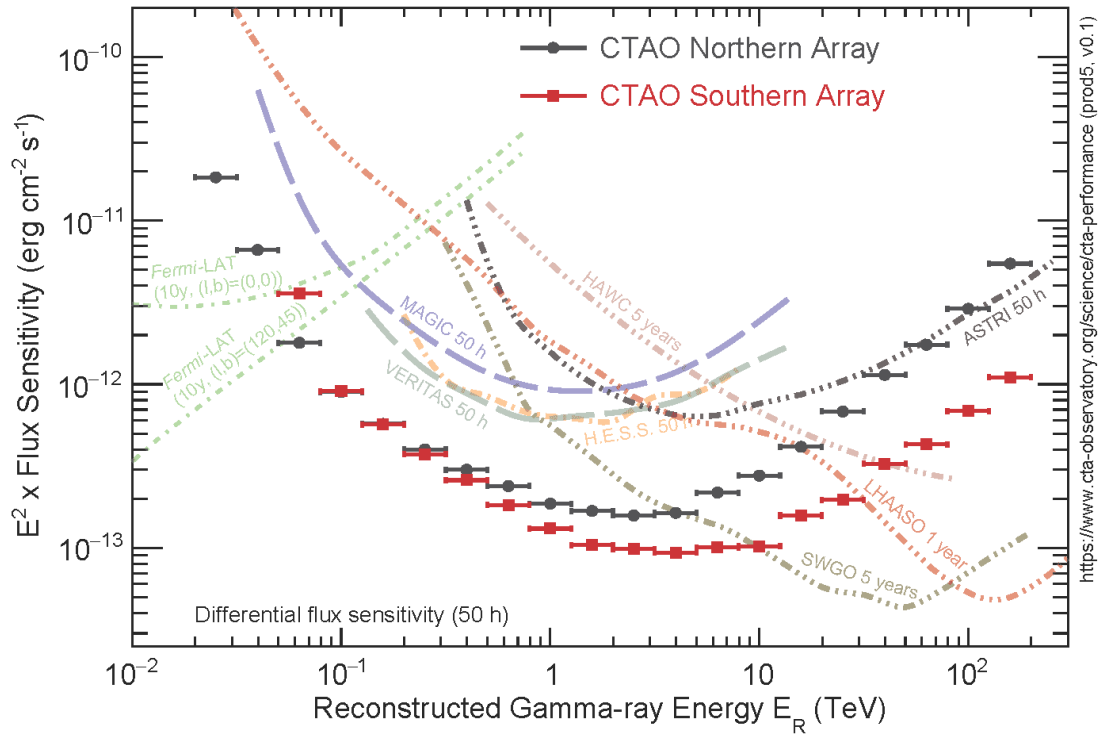


Figure 5.13: The sensitivity curves for different gamma-ray experiments ( $5\sigma$  detection of a point-like source).

a full particle-in-cell simulation will be able to investigate the shock acceleration mechanism more accurately and predict the CR electron spectra. Shock acceleration at an SNR reverse shock is an important topic that has yet to be studied with numerical simulation. For PWNe, current SED models sacrifice either the evolutionary aspect (multi-zone time-independent model; e.g., [153]) or spatial inhomogeneity (one-zone time-dependent model; e.g., [188]). Both approaches are too simplified to explain the actual physical processes in PWNe. A multi-zone time-dependent model will be able to explain the observed highly asymmetric morphology of PeVatron PWNe and their mysterious particle acceleration mechanism.

## References

- [1] V. Hess, *On the observations of the penetrating radiation during seven balloon flights*, Version Number: 2, 2018.
- [2] C. Evoli, *The cosmic-ray energy spectrum*, Publisher: Zenodo, Oct. 22, 2018.
- [3] E. N. Parker, “The passage of energetic charged particles through interplanetary space,” *Planetary and Space Science*, vol. 13, no. 1, pp. 9–49, Jan. 1965.
- [4] P. Blasi, *Charged particles in magnetic fields and cosmic ray transport*, 2023. arXiv: 2307.11640 [astro-ph.HE].
- [5] C. Evoli and U. Dupletsa, *Phenomenological models of cosmic ray transport in galaxies*, 2023. arXiv: 2309.00298 [astro-ph.HE].
- [6] Z. Cao *et al.*, “The First LHAASO Catalog of Gamma-Ray Sources,” *Astrophysical Journal Supplement Series*, vol. 271, no. 1, 25, p. 25, Mar. 2024. arXiv: 2305.17030 [astro-ph.HE].
- [7] Icecube Collaboration *et al.*, “Observation of high-energy neutrinos from the Galactic plane,” *Science*, vol. 380, no. 6652, pp. 1338–1343, Jun. 2023. arXiv: 2307.04427 [astro-ph.HE].
- [8] X.-H. Ma *et al.*, “Chapter 1 LHAASO Instruments and Detector technology,” *Chinese Physics C*, vol. 46, no. 3, 030001, p. 030 001, Mar. 2022.
- [9] J. Holder *et al.*, “The first VERITAS telescope,” *Astroparticle Physics*, vol. 25, no. 6, pp. 391–401, Jul. 2006. arXiv: astro-ph/0604119 [astro-ph].
- [10] F. A. Harrison *et al.*, “The Nuclear Spectroscopic Telescope Array (NuSTAR) High-energy X-Ray Mission,” *Astrophysical Journal*, vol. 770, no. 2, 103, p. 103, Jun. 2013. arXiv: 1301.7307 [astro-ph.IM].
- [11] S. Gabici *et al.*, “The origin of Galactic cosmic rays: Challenges to the standard paradigm,” *International Journal of Modern Physics D*, vol. 28, no. 15, 1930022-339, pp. 1 930 022–339, Jan. 2019. arXiv: 1903.11584 [astro-ph.HE].
- [12] E. Fermi, “On the origin of the cosmic radiation,” *Phys. Rev.*, vol. 75, pp. 1169–1174, 8 Apr. 1949.

- [13] M. Hoshino, “Nonthermal Particle Acceleration in Shock Front Region: “Shock Surfing Accelerations”,” *Progress of Theoretical Physics Supplement*, vol. 143, pp. 149–181, Jan. 2001.
- [14] D. Caprioli, *Particle acceleration at shocks: An introduction*, 2023. arXiv: 2307.00284 [astro-ph.HE].
- [15] G. F. Krymskii, “A regular mechanism for the acceleration of charged particles on the front of a shock wave,” *Akademiia Nauk SSSR Doklady*, vol. 234, pp. 1306–1308, Jun. 1977.
- [16] W. I. Axford, E. Leer, and G. Skadron, “The Acceleration of Cosmic Rays by Shock Waves,” in *International Cosmic Ray Conference*, ser. International Cosmic Ray Conference, vol. 11, Jan. 1977, p. 132.
- [17] R. D. Blandford and J. P. Ostriker, “Particle acceleration by astrophysical shocks.,” *Astrophysical Journal Letters*, vol. 221, pp. L29–L32, Apr. 1978.
- [18] A. R. Bell, “The acceleration of cosmic rays in shock fronts - I.,” *Monthly Notices of the Royal Astronomical Society*, vol. 182, pp. 147–156, Jan. 1978.
- [19] A. R. Bell, “The acceleration of cosmic rays in shock fronts - II.,” *Monthly Notices of the Royal Astronomical Society*, vol. 182, pp. 443–455, Feb. 1978.
- [20] Q. Yuan, S.-J. Lin, K. Fang, and X.-J. Bi, “Propagation of cosmic rays in the AMS-02 era,” *Physical Review D*, vol. 95, no. 8, 083007, p. 083 007, Apr. 2017. arXiv: 1701.06149 [astro-ph.HE].
- [21] R. Diesing and D. Caprioli, “Steep Cosmic-Ray Spectra with Revised Diffusive Shock Acceleration,” *Astrophysical Journal*, vol. 922, no. 1, 1, p. 1, Nov. 2021. arXiv: 2107.08520 [astro-ph.HE].
- [22] F. C. Jones and D. C. Ellison, “The plasma physics of shock acceleration,” *Space Science Reviews*, vol. 58, no. 1, pp. 259–346, Dec. 1991.
- [23] M. A. Malkov and L. O. Drury, “Nonlinear theory of diffusive acceleration of particles by shock waves,” *Reports on Progress in Physics*, vol. 64, no. 4, pp. 429–481, Apr. 2001.
- [24] C. C. Haggerty and D. Caprioli, “Kinetic Simulations of Cosmic-Ray-modified Shocks. I. Hydrodynamics,” *Astrophysical Journal*, vol. 905, no. 1, 1, p. 1, Dec. 2020. arXiv: 2008.12308 [astro-ph.HE].
- [25] D. Caprioli, C. C. Haggerty, and P. Blasi, “Kinetic Simulations of Cosmic-Ray-modified Shocks. II. Particle Spectra,” *Astrophysical Journal*, vol. 905, no. 1, 2, p. 2, Dec. 2020. arXiv: 2009.00007 [astro-ph.HE].

- [26] D. C. Ellison, F. C. Jones, and D. Eichler, “Monte Carlo simulation of collisionless shocks showing preferential acceleration of high  $A/Z$  particles,” *Journal of Geophysics Zeitschrift Geophysik*, vol. 50, no. 2, pp. 110–113, Jan. 1981.
- [27] M. A. Malkov, “Analytic Solution for Nonlinear Shock Acceleration in the Bohm Limit,” *Astrophysical Journal*, vol. 485, no. 2, pp. 638–654, Aug. 1997. arXiv: astro-ph/9707152 [astro-ph].
- [28] H. Kang, T. W. Jones, and U. D. J. Gieseler, “Numerical Studies of Cosmic-Ray Injection and Acceleration,” *Astrophysical Journal*, vol. 579, no. 1, pp. 337–358, Nov. 2002. arXiv: astro-ph/0207410 [astro-ph].
- [29] P. Blasi, S. Gabici, and G. Vannoni, “On the role of injection in kinetic approaches to non-linear particle acceleration at non-relativistic shock waves,” *Monthly Notices of the Royal Astronomical Society*, vol. 361, no. 3, pp. 907–918, Aug. 2005. arXiv: astro-ph/0505351 [astro-ph].
- [30] S. Navas *et al.*, “Review of particle physics,” *Phys. Rev. D*, vol. 110, p. 030001, 3 Aug. 2024.
- [31] P. D. Serpico, “Cosmic ray interactions with matter and radiation,” *arXiv e-prints*, arXiv:2308.04361, arXiv:2308.04361, Aug. 2023. arXiv: 2308.04361 [astro-ph.HE].
- [32] F. A. Aharonian, *Very high energy cosmic gamma radiation : a crucial window on the extreme Universe*. World Scientific, 2004.
- [33] J. A. Hinton and W. Hofmann, “Teraelectronvolt Astronomy,” *Annual Review of Astronomy & Astrophysics*, vol. 47, no. 1, pp. 523–565, Sep. 2009. arXiv: 1006.5210 [astro-ph.HE].
- [34] J. J. Condon and S. M. Ransom, *Essential Radio Astronomy*. Princeton University Press, 2016.
- [35] J. D. Jackson, *Classical Electrodynamics*, 3rd ed. Nashville, TN: John Wiley & Sons, Jul. 1998.
- [36] M. Ackermann *et al.*, “Detection of the Characteristic Pion-Decay Signature in Supernova Remnants,” *Science*, vol. 339, no. 6121, pp. 807–811, Feb. 2013. arXiv: 1302.3307 [astro-ph.HE].
- [37] G. Peron, F. Aharonian, S. Casanova, R. Zanin, and C. Romoli, “On the Gamma-Ray Emission of W44 and Its Surroundings,” *Astrophysical Journal Letters*, vol. 896, no. 2, L23, p. L23, Jun. 2020. arXiv: 2007.04821 [astro-ph.HE].

- [38] A. Strong, “Truths universally acknowledged? reflections on some common notions in cosmic rays,” *Nuclear and Particle Physics Proceedings*, vol. 297-299, pp. 165–170, 2018, Cosmic Ray Origin - Beyond the Standard Models.
- [39] K. Greisen, “End to the Cosmic-Ray Spectrum?” *Physical Review Letters*, vol. 16, no. 17, pp. 748–750, Apr. 1966.
- [40] G. T. Zatsepin and V. A. Kuz’min, “Upper Limit of the Spectrum of Cosmic Rays,” *Soviet Journal of Experimental and Theoretical Physics Letters*, vol. 4, p. 78, Aug. 1966.
- [41] P. Chardonnet, J. Orloff, and P. Salati, “The production of anti-matter in our galaxy,” *Physics Letters B*, vol. 409, no. 1, pp. 313–320, 1997.
- [42] F. Donato, N. Fornengo, and P. Salati, “Antideuterons as a signature of supersymmetric dark matter,” *Phys. Rev. D*, vol. 62, p. 043 003, 4 Jul. 2000.
- [43] K. Mori *et al.*, “A novel antimatter detector based on x-ray deexcitation of exotic atoms,” *The Astrophysical Journal*, vol. 566, no. 1, p. 604, Feb. 2002.
- [44] G. Giacinti, A. M. W. Mitchell, R. López-Coto, V. Joshi, R. D. Parsons, and J. A. Hinton, “Halo fraction in TeV-bright pulsar wind nebulae,” *Astronomy & Astrophysics*, vol. 636, A113, A113, Apr. 2020. arXiv: 1907.12121 [astro-ph.HE].
- [45] W. Baade and F. Zwicky, “Cosmic Rays from Super-novae,” *Proceedings of the National Academy of Science*, vol. 20, no. 5, pp. 259–263, May 1934.
- [46] A. Hewish, S. J. Bell, J. D. H. Pilkington, P. F. Scott, and R. A. Collins, “Observation of a Rapidly Pulsating Radio Source,” *Nature*, vol. 217, no. 5130, pp. 709–713, Feb. 1968.
- [47] L. I. Sedov, *Similarity and Dimensional Methods in Mechanics*. Elsevier, 1959, ISBN: 9781483200880.
- [48] R. A. Chevalier, “Self-similar solutions for the interaction of stellar ejecta with an external medium.,” *Astrophysical Journal*, vol. 258, pp. 790–797, Jul. 1982.
- [49] V. L. Ginzburg and S. I. Syrovatskii, “Cosmic Magnetobremstrahlung (synchrotron Radiation),” *Annual Review of Astronomy & Astrophysics*, vol. 3, p. 297, Jan. 1965.
- [50] J. Vink and J. M. Laming, “On the Magnetic Fields and Particle Acceleration in Cassiopeia A,” *Astrophysical Journal*, vol. 584, no. 2, pp. 758–769, Feb. 2003. arXiv: astro-ph/0210669 [astro-ph].
- [51] A. A. Abdo *et al.*, “Observation of Supernova Remnant IC 443 with the Fermi Large Area Telescope,” *Astrophysical Journal*, vol. 712, no. 1, pp. 459–468, Mar. 2010. arXiv: 1002.2198 [astro-ph.HE].

- [52] A. A. Abdo *et al.*, “Gamma-Ray Emission from the Shell of Supernova Remnant W44 Revealed by the Fermi LAT,” *Science*, vol. 327, no. 5969, p. 1103, Feb. 2010.
- [53] A. U. Abeysekara *et al.*, “Evidence for Proton Acceleration up to TeV Energies Based on VERITAS and Fermi-LAT Observations of the Cas A SNR,” *Astrophysical Journal*, vol. 894, no. 1, 51, p. 51, May 2020. arXiv: 2003.13615 [astro-ph.HE].
- [54] J. Gelfand *et al.*, “MeV Emission from Pulsar Wind Nebulae: Understanding Extreme Particle Acceleration in Highly Relativistic Outflows,” *Bulletin of the American Astronomical Society*, vol. 51, no. 3, 513, p. 513, May 2019.
- [55] H.E.S.S. Collaboration *et al.*, “The population of tev pulsar wind nebulae in the h.e.s.s. galactic plane survey,” *A&A*, vol. 612, A2, 2018.
- [56] A. G. Cameron, “Neutron Star Models.,” *Astrophysical Journal*, vol. 130, p. 884, Nov. 1959.
- [57] V. Kalogera and G. Baym, “The Maximum Mass of a Neutron Star,” *Astrophysical Journal Letters*, vol. 470, p. L61, Oct. 1996. arXiv: astro-ph/9608059 [astro-ph].
- [58] P. Goldreich and W. H. Julian, “Pulsar Electrodynamics,” *Astrophysical Journal*, vol. 157, p. 869, Aug. 1969.
- [59] M. A. Ruderman and P. G. Sutherland, “Theory of pulsars: polar gaps, sparks, and coherent microwave radiation.,” *Astrophysical Journal*, vol. 196, pp. 51–72, Feb. 1975.
- [60] A. N. Timokhin and A. K. Harding, “On the Maximum Pair Multiplicity of Pulsar Cascades,” *Astrophysical Journal*, vol. 871, no. 1, 12, p. 12, Jan. 2019. arXiv: 1803.08924 [astro-ph.HE].
- [61] L. Sironi and A. Spitkovsky, “Acceleration of Particles at the Termination Shock of a Relativistic Striped Wind,” *Astrophysical Journal*, vol. 741, no. 1, 39, p. 39, Nov. 2011. arXiv: 1107.0977 [astro-ph.HE].
- [62] E. Amato and S. Recchia, “Gamma-ray halos around pulsars: impact on pulsar wind physics and galactic cosmic ray transport,” *Nuovo Cimento Rivista Serie*, vol. 47, no. 7, pp. 399–452, Jul. 2024. arXiv: 2409.00659 [astro-ph.HE].
- [63] B.-C. Koo and C. Park, “Supernova remnant cassiopeia a,” in *Handbook of Supernovae*, A. W. Alsabti and P. Murdin, Eds. Cham: Springer International Publishing, 2017, pp. 161–178, ISBN: 978-3-319-21846-5.
- [64] D. F. Torres, Ed., *Modelling Pulsar Wind Nebulae*. Springer International Publishing, 2017.

- [65] A. U. Abeysekara *et al.*, “Extended gamma-ray sources around pulsars constrain the origin of the positron flux at Earth,” *Science*, vol. 358, no. 6365, pp. 911–914, Nov. 2017, HAWC collaboration’s announcement of the detection of extended emission around Geminga and Monogem which indicates inhibited diffusion. arXiv: 1711.06223 [astro-ph.HE].
- [66] J. E. Koglin *et al.*, “NuSTAR hard x-ray optics design and performance,” in *Optics for EUV, X-Ray, and Gamma-Ray Astronomy IV*, S. L. O’Dell and G. Pareschi, Eds., ser. Society of Photo-Optical Instrumentation Engineers (SPIE) Conference Series, vol. 7437, Aug. 2009, 74370C, p. 74370C.
- [67] T. Kitaguchi *et al.*, “Spectral calibration and modeling of the NuSTAR CdZnTe pixel detectors,” in *Society of Photo-Optical Instrumentation Engineers (SPIE) Conference Series*, ser. Society of Photo-Optical Instrumentation Engineers (SPIE) Conference Series, vol. 8145, Sep. 2011, 814507, p. 814 507. arXiv: 1109.0378 [astro-ph.IM].
- [68] K. K. Madsen *et al.*, “Observational artifacts of Nuclear Spectroscopic Telescope Array: ghost rays and stray light,” *Journal of Astronomical Telescopes, Instruments, and Systems*, vol. 3, 044003, p. 044 003, Oct. 2017.
- [69] B. W. Grefenstette, K. K. Madsen, H. Miyasaka, and A. Zoglauer, “NuSTAR non-x-ray background,” *Journal of Astronomical Telescopes, Instruments, and Systems*, vol. 8, 047001, p. 047 001, Oct. 2022.
- [70] D. R. Wik *et al.*, “NuSTAR Observations of the Bullet Cluster: Constraints on Inverse Compton Emission,” *Astrophysical Journal*, vol. 792, no. 1, 48, p. 48, Sep. 2014. arXiv: 1403.2722 [astro-ph.HE].
- [71] M. C. Weisskopf, H. D. Tananbaum, L. P. Van Speybroeck, and S. L. O’Dell, “Chandra X-ray Observatory (CXO): overview,” in *X-Ray Optics, Instruments, and Missions III*, J. E. Truemper and B. Aschenbach, Eds., ser. Society of Photo-Optical Instrumentation Engineers (SPIE) Conference Series, vol. 4012, Jul. 2000, pp. 2–16. arXiv: astro-ph/0004127 [astro-ph].
- [72] F. Jansen *et al.*, “XMM-Newton observatory. I. The spacecraft and operations,” *Astronomy & Astrophysics*, vol. 365, pp. L1–L6, Jan. 2001.
- [73] W. B. Atwood *et al.*, “The Large Area Telescope on the Fermi Gamma-Ray Space Telescope Mission,” *Astrophysical Journal*, vol. 697, no. 2, pp. 1071–1102, Jun. 2009. arXiv: 0902.1089 [astro-ph.IM].
- [74] M. Ackermann *et al.*, “The Fermi Large Area Telescope on Orbit: Event Classification, Instrument Response Functions, and Calibration,” *Astrophysical Journal Supplement Series*, vol. 203, no. 1, 4, p. 4, Nov. 2012. arXiv: 1206.1896 [astro-ph.IM].

- [75] F. Acero *et al.*, “Development of the Model of Galactic Interstellar Emission for Standard Point-source Analysis of Fermi Large Area Telescope Data,” *Astrophysical Journal Supplement Series*, vol. 223, no. 2, 26, p. 26, Apr. 2016. arXiv: 1602.07246 [astro-ph.HE].
- [76] S. Abdollahi *et al.*, “Incremental Fermi Large Area Telescope Fourth Source Catalog,” *Astrophysical Journal Supplement Series*, vol. 260, no. 2, 53, p. 53, Jun. 2022. arXiv: 2201.11184 [astro-ph.HE].
- [77] J. Ballet, P. Bruel, T. H. Burnett, B. Lott, and The Fermi-LAT collaboration, “Fermi Large Area Telescope Fourth Source Catalog Data Release 4 (4FGL-DR4),” *arXiv e-prints*, arXiv:2307.12546, arXiv:2307.12546, Jul. 2023. arXiv: 2307.12546 [astro-ph.HE].
- [78] Weekes, “Radiation and absorption processes,” in *Very High Energy Gamma-Ray Astronomy*, Taylor & Francis, Apr. 2003.
- [79] F. Aharonian, J. Buckley, T. Kifune, and G. Sinnis, “High energy astrophysics with ground-based gamma ray detectors,” *Reports on Progress in Physics*, vol. 71, no. 9, 096901, p. 096 901, Sep. 2008.
- [80] D. N. Burrows, *The WSPC Handbook of Astronomical Instrumentation, Volume 5: Gamma-Ray and Multimessenger Astronomical Instrumentation*. World Scientific, 2021.
- [81] D. Ferenc and MAGIC Collaboration, “The MAGIC gamma-ray observatory,” *Nuclear Instruments and Methods in Physics Research A*, vol. 553, no. 1-2, pp. 274–281, Nov. 2005.
- [82] C. van Eldik *et al.*, “Observations of the Crab Nebula with H.E.S.S. phase II,” in *34th International Cosmic Ray Conference (ICRC2015)*, ser. International Cosmic Ray Conference, vol. 34, Jul. 2015, 847, p. 847.
- [83] G. Di Sciascio, “Ground-based Gamma-Ray Astronomy: an Introduction,” in *Journal of Physics Conference Series*, ser. Journal of Physics Conference Series, vol. 1263, IOP, Jun. 2019, 012003, p. 012 003. arXiv: 1904.06218 [astro-ph.IM].
- [84] R. W. Springer and HAWC Collaboration, “The High Altitude water Cherenkov (HAWC) Observatory,” *Nuclear and Particle Physics Proceedings*, vol. 279-281, pp. 87–94, Oct. 2016.
- [85] M. Amenomori *et al.*, “Multi-TeV Gamma-Ray Observation from the Crab Nebula Using the Tibet-III Air Shower Array Finely Tuned by the Cosmic Ray Moon’s Shadow,” *Astrophysical Journal*, vol. 692, no. 1, pp. 61–72, Feb. 2009. arXiv: 0810.3757 [astro-ph].
- [86] D. Cyranoski, “Chinese mountain observatory to probe cosmic-ray origins,” *Nature*, vol. 543, no. 7645, pp. 300–301, Mar. 2017.

- [87] J. Woo *et al.*, “Spectrum and location of ongoing extreme particle acceleration in cassiopeia a,” *The Astrophysical Journal*, vol. 979, no. 1, p. 72, Jan. 2025.
- [88] Y. Uchiyama, F. A. Aharonian, T. Tanaka, T. Takahashi, and Y. Maeda, “Extremely fast acceleration of cosmic rays in a supernova remnant,” *Nature*, vol. 449, no. 7162, pp. 576–578, Oct. 2007.
- [89] Y. Uchiyama and F. A. Aharonian, “Fast Variability of Nonthermal X-Ray Emission in Cassiopeia A: Probing Electron Acceleration in Reverse-Shocked Ejecta,” *The Astrophysical Journal Letters*, vol. 677, no. 2, p. L105, Apr. 2008. arXiv: 0803.3410 [astro-ph].
- [90] T. Okuno *et al.*, “Time Variability of Nonthermal X-Ray Stripes in Tycho’s Supernova Remnant with Chandra,” *Astrophysical Journal*, vol. 894, no. 1, 50, p. 50, May 2020. arXiv: 2003.10035 [astro-ph.HE].
- [91] R. A. Fesen *et al.*, “The Expansion Asymmetry and Age of the Cassiopeia A Supernova Remnant,” *Astrophysical Journal*, vol. 645, no. 1, pp. 283–292, Jul. 2006. arXiv: astro-ph/0603371 [astro-ph].
- [92] J. E. Reed, J. J. Hester, A. C. Fabian, and P. F. Winkler, “The Three-dimensional Structure of the Cassiopeia A Supernova Remnant. I. The Spherical Shell,” *Astrophysical Journal*, vol. 440, p. 706, Feb. 1995.
- [93] B. W. Grefenstette *et al.*, “Locating the Most Energetic Electrons in Cassiopeia A,” *Astrophysical Journal*, vol. 802, no. 1, 15, p. 15, Mar. 2015. arXiv: 1502.03024 [astro-ph.HE].
- [94] D. J. Patnaude and R. A. Fesen, “Proper Motions and Brightness Variations of Nonthermal X-ray Filaments in the Cassiopeia A Supernova Remnant,” *Astrophysical Journal*, vol. 697, no. 1, pp. 535–543, May 2009. arXiv: 0808.0692 [astro-ph].
- [95] T. Sato *et al.*, “X-Ray Measurements of the Particle Acceleration Properties at Inward Shocks in Cassiopeia A,” *Astrophysical Journal*, vol. 853, no. 1, 46, p. 46, Jan. 2018. arXiv: 1710.06992 [astro-ph.HE].
- [96] S. H. Pravdo and B. W. Smith, “X-ray evidence for electron-ion equilibrium and ionization nonequilibrium in Young supernova remnants,” *Astrophysical Journal*, vol. 234, pp. L195–L198, Dec. 1979.
- [97] L.-S. The, M. D. Leising, D. H. Hartmann, J. D. Kurfess, P. Blanco, and D. Bhattacharya, “Hard x-ray emission from cassiopeia a snr,” in *AIP Conference Proceedings*, AIP, 1997.
- [98] G. E. Allen *et al.*, “Evidence of X-Ray Synchrotron Emission from Electrons Accelerated to 40 TeV in the Supernova Remnant Cassiopeia A,” *Astrophysical Journal*, vol. 487, no. 1, pp. L97–L100, Sep. 1997. arXiv: astro-ph/9707110 [astro-ph].

- [99] F. Favata *et al.*, “The broad-band X-ray spectrum of the CAS A supernova remnant as seen by the BeppoSAX observatory,” *Astronomy and Astrophysics*, vol. 324, pp. L49–L52, Aug. 1997. arXiv: astro-ph/9707052 [astro-ph].
- [100] Y. Maeda *et al.*, “Suzaku X-Ray Imaging and Spectroscopy of Cassiopeia A,” *Publications of the Astronomical Society of Japan*, vol. 61, p. 1217, Dec. 2009. arXiv: 0912.5020 [astro-ph.HE].
- [101] U. Hwang and J. M. Laming, “A Chandra X-Ray Survey of Ejecta in the Cassiopeia A Supernova Remnant,” *Astrophysical Journal*, vol. 746, no. 2, p. 130, Feb. 2012. arXiv: 1111.7316 [astro-ph.HE].
- [102] J. A. M. Bleeker *et al.*, “Cassiopeia A: On the origin of the hard X-ray continuum and the implication of the observed O VIII Ly-alpha /Ly-beta distribution,” *Astronomy and Astrophysics*, vol. 365, pp. L225–L230, Jan. 2001. arXiv: astro-ph/0010606 [astro-ph].
- [103] Y. Maeda *et al.*, “Suzaku X-Ray Imaging and Spectroscopy of Cassiopeia A,” *Publications of the Astronomical Society of Japan*, vol. 61, p. 1217, Dec. 2009. arXiv: 0912.5020 [astro-ph.HE].
- [104] F. Favata *et al.*, “The broad-band X-ray spectrum of the CAS A supernova remnant as seen by the BeppoSAX observatory,” *Astronomy and Astrophysics*, vol. 324, pp. L49–L52, Aug. 1997. arXiv: astro-ph/9707052 [astro-ph].
- [105] G. E. Allen *et al.*, “Evidence of X-Ray Synchrotron Emission from Electrons Accelerated to 40 TeV in the Supernova Remnant Cassiopeia A,” *The Astrophysical Journal Letters*, vol. 487, no. 1, pp. L97–L100, Sep. 1997. arXiv: astro-ph/9707110 [astro-ph].
- [106] B. Posselt and G. G. Pavlov, “The Cooling of the Central Compact Object in Cas A from 2006 to 2020,” *Astrophysical Journal*, vol. 932, no. 2, p. 83, Jun. 2022. arXiv: 2205.06552 [astro-ph.HE].
- [107] J. Wilms, A. Allen, and R. McCray, “On the Absorption of X-Rays in the Interstellar Medium,” *Astrophysical Journal*, vol. 542, no. 2, pp. 914–924, Oct. 2000. arXiv: astro-ph/0008425 [astro-ph].
- [108] W. H. Richardson, “Bayesian-Based Iterative Method of Image Restoration,” *Journal of the Optical Society of America (1917-1983)*, vol. 62, no. 1, p. 55, Jan. 1972.
- [109] L. B. Lucy, “An iterative technique for the rectification of observed distributions,” *Astronomical Journal*, vol. 79, p. 745, Jun. 1974.
- [110] V. Domček, J. Vink, J. V. Hernández Santisteban, T. DeLaney, and P. Zhou, “Mapping the spectral index of Cassiopeia A: evidence for flattening from radio to infrared,” *Monthly*

- Notices of the Royal Astronomical Society*, vol. 502, no. 1, pp. 1026–1040, Mar. 2021. arXiv: 2005.12677 [astro-ph.HE].
- [111] M. Wright, J. Dickel, B. Koralesky, and L. Rudnick, “The Supernova Remnant Cassiopeia A at Millimeter Wavelengths,” *Astrophysical Journal*, vol. 518, no. 1, pp. 284–297, Jun. 1999.
- [112] A. M. Atoyan, F. A. Aharonian, R. J. Tuffs, and H. J. Völk, “On the gamma-ray fluxes expected from Cassiopeia A,” *Astronomy and Astrophysics*, vol. 355, pp. 211–220, Mar. 2000. arXiv: astro-ph/0001186 [astro-ph].
- [113] E. G. Berezhko, G. Pühlhofer, and H. J. Völk, “Gamma-ray emission from Cassiopeia A produced by accelerated cosmic rays,” *Astronomy and Astrophysics*, vol. 400, pp. 971–980, Mar. 2003. arXiv: astro-ph/0301205 [astro-ph].
- [114] A. Bamba, R. Yamazaki, T. Yoshida, T. Terasawa, and K. Koyama, “A Spatial and Spectral Study of Nonthermal Filaments in Historical Supernova Remnants: Observational Results with Chandra,” *Astrophysical Journal*, vol. 621, no. 2, pp. 793–802, Mar. 2005. arXiv: astro-ph/0411326 [astro-ph].
- [115] S. P. Reynolds, K. J. Borkowski, and P. H. Gwynne, “Expansion and Brightness Changes in the Pulsar-wind Nebula in the Composite Supernova Remnant Kes 75,” *Astrophysical Journal*, vol. 856, no. 2, p. 133, Apr. 2018. arXiv: 1803.09128 [astro-ph.HE].
- [116] A. S. Trotter *et al.*, “The fading of Cassiopeia A, and improved models for the absolute spectrum of primary radio calibration sources,” *Monthly Notices of the Royal Astronomical Society*, vol. 469, no. 2, pp. 1299–1313, Aug. 2017. arXiv: 1704.00002 [astro-ph.HE].
- [117] E. Derishev and F. Aharonian, “Exact Analytical Expression for the Synchrotron Radiation Spectrum in the Gaussian Turbulent Magnetic Field,” *Astrophysical Journal*, vol. 887, no. 2, p. 181, Dec. 2019. arXiv: 1907.11663 [astro-ph.HE].
- [118] J. Vink *et al.*, “X-Ray Polarization Detection of Cassiopeia A with IXPE,” *Astrophysical Journal*, vol. 938, no. 1, p. 40, Oct. 2022. arXiv: 2206.06713 [astro-ph.HE].
- [119] A. M. Bykov, Y. A. Uvarov, and D. C. Ellison, “Dots, Clumps, and Filaments: The Intermittent Images of Synchrotron Emission in Random Magnetic Fields of Young Supernova Remnants,” *The Astrophysical Journal Letters*, vol. 689, no. 2, p. L133, Dec. 2008. arXiv: 0811.2498 [astro-ph].
- [120] V. N. Zirakashvili and F. Aharonian, “Analytical solutions for energy spectra of electrons accelerated by nonrelativistic shock-waves in shell type supernova remnants,” *Astronomy and Astrophysics*, vol. 465, no. 3, pp. 695–702, Apr. 2007. arXiv: astro-ph/0612717 [astro-ph].

- [121] J. Vink, D. J. Patnaude, and D. Castro, “The Forward and Reverse Shock Dynamics of Cassiopeia A,” *Astrophysical Journal*, vol. 929, no. 1, 57, p. 57, Apr. 2022. arXiv: 2201.08911 [astro-ph.HE].
- [122] D. Khangulyan, F. A. Aharonian, and S. R. Kelner, “Simple Analytical Approximations for Treatment of Inverse Compton Scattering of Relativistic Electrons in the Blackbody Radiation Field,” *Astrophysical Journal*, vol. 783, no. 2, 100, p. 100, Mar. 2014. arXiv: 1310.7971 [astro-ph.HE].
- [123] P. G. Mezger, R. J. Tuffs, R. Chini, E. Kreysa, and H. P. Gemuend, “Maps of Cassiopeia A and the Crab nebula at lambda 1.2 mm.,” *Astronomy and Astrophysics*, vol. 167, pp. 145–150, Oct. 1986.
- [124] M. L. Ahnen *et al.*, “A cut-off in the TeV gamma-ray spectrum of the SNR Cassiopeia A,” *Monthly Notices of the Royal Astronomical Society*, vol. 472, no. 3, pp. 2956–2962, Dec. 2017. arXiv: 1707.01583 [astro-ph.HE].
- [125] J. W. M. Baars, R. Genzel, I. I. K. Pauliny-Toth, and A. Witzel, “The absolute spectrum of Cas A: an accurate flux density scale and a set of secondary calibrators.,” *Astronomy and Astrophysics*, vol. 61, pp. 99–106, Oct. 1977.
- [126] E. N. Vinyaikin, “Frequency dependence of the evolution of the radio emission of the supernova remnant Cas A,” *Astronomy Reports*, vol. 58, no. 9, pp. 626–639, Sep. 2014.
- [127] A. Gorbynov, A. Sukharev, M. Ryabov, V. Bezrukovs, and A. Orbidans, “Features of Secular Changes in the Flux Density of the Cas a Supernova Remnant, from Centimeter to Decameter Wavelengths,” *Galaxies*, vol. 9, no. 2, 30, p. 30, May 2021.
- [128] J. Rho, S. P. Reynolds, W. T. Reach, T. H. Jarrett, G. E. Allen, and J. C. Wilson, “Near-Infrared Synchrotron Emission from Cassiopeia A,” *Astrophysical Journal*, vol. 592, no. 1, pp. 299–310, Jul. 2003. arXiv: astro-ph/0303215 [astro-ph].
- [129] T. J. Jones, L. Rudnick, T. DeLaney, and J. Bowden, “The Identification of Infrared Synchrotron Radiation from Cassiopeia A,” *Astrophysical Journal*, vol. 587, no. 1, pp. 227–234, Apr. 2003. arXiv: astro-ph/0212544 [astro-ph].
- [130] V. N. Zirakashvili, F. A. Aharonian, R. Yang, E. Oña-Wilhelmi, and R. J. Tuffs, “Non-thermal Radiation of Young Supernova Remnants: The Case of CAS A,” *Astrophysical Journal*, vol. 785, no. 2, 130, p. 130, Apr. 2014. arXiv: 1308.3742 [astro-ph.HE].
- [131] S. Zhan, W. Wang, G. Mou, and Z. Li, “An asymmetrical model for high-energy radiation of Cassiopeia A,” *Monthly Notices of the Royal Astronomical Society*, vol. 513, no. 2, pp. 2471–2477, Jun. 2022. arXiv: 2204.02664 [astro-ph.HE].

- [132] I. N. Toptygin and G. D. Fleishman, “A Role of Cosmic-Rays in Generation of Radio and Optical Radiation by Plasma Mechanisms,” *Astrophysics and Space Science*, vol. 132, no. 2, pp. 213–248, Apr. 1987.
- [133] M. V. Medvedev, “Theory of “Jitter” Radiation from Small-Scale Random Magnetic Fields and Prompt Emission from Gamma-Ray Burst Shocks,” *Astrophysical Journal*, vol. 540, no. 2, pp. 704–714, Sep. 2000. arXiv: astro-ph/0001314 [astro-ph].
- [134] S. R. Kelner, F. A. Aharonian, and D. Khangulyan, “On the Jitter Radiation,” *Astrophysical Journal*, vol. 774, no. 1, 61, p. 61, Sep. 2013. arXiv: 1304.0493 [astro-ph.HE].
- [135] E. Greco, J. Vink, A. Ellien, and C. Ferrigno, “Jitter Radiation as an Alternative Mechanism for the Nonthermal X-Ray Emission of Cassiopeia A,” *Astrophysical Journal*, vol. 956, no. 2, 116, p. 116, Oct. 2023. arXiv: 2308.15956 [astro-ph.HE].
- [136] Z. Cao *et al.*, “Does or Did the Supernova Remnant Cassiopeia A Operate as a PeVatron?” *The Astrophysical Journal Letters*, vol. 961, no. 2, L43, p. L43, Feb. 2024. arXiv: 2310.17082 [astro-ph.HE].
- [137] L. O. Drury and J. H. Voelk, “Hydromagnetic shock structure in the presence of cosmic rays,” *Astrophysical Journal*, vol. 248, pp. 344–351, Aug. 1981.
- [138] L. O. Drury, “REVIEW ARTICLE: An introduction to the theory of diffusive shock acceleration of energetic particles in tenuous plasmas,” *Reports on Progress in Physics*, vol. 46, no. 8, pp. 973–1027, Aug. 1983.
- [139] R. Giuffrida *et al.*, “The supernova remnant SN 1006 as a Galactic particle accelerator,” *Nature Communications*, vol. 13, 5098, p. 5098, Aug. 2022. arXiv: 2208.14491 [astro-ph.HE].
- [140] J.-J. Lee, S. Park, J. P. Hughes, and P. O. Slane, “X-Ray Observation of the Shocked Red Supergiant Wind of Cassiopeia A,” *Astrophysical Journal*, vol. 789, no. 1, 7, p. 7, Jul. 2014. arXiv: 1304.3973 [astro-ph.HE].
- [141] C. D. Kilpatrick, J. H. Bieging, and G. H. Rieke, “Interaction between Cassiopeia A and Nearby Molecular Clouds,” *Astrophysical Journal*, vol. 796, no. 2, 144, p. 144, Dec. 2014. arXiv: 1411.4308 [astro-ph.SR].
- [142] F. Fraschetti, S. Katsuda, T. Sato, J. R. Jokipii, and J. Giacalone, “Vortical Amplification of the Magnetic Field at an Inward Shock of Supernova Remnant Cassiopeia A,” *Physical Review Letters*, vol. 120, no. 25, 251101, p. 251 101, Jun. 2018. arXiv: 1805.05951 [astro-ph.HE].

- [143] S. Orlando *et al.*, “Evidence for past interaction with an asymmetric circumstellar shell in the young SNR Cassiopeia A,” *Astronomy and Astrophysics*, vol. 666, A2, A2, Oct. 2022. arXiv: 2202.01643 [astro-ph.HE].
- [144] J. Woo *et al.*, “Hard x-ray observation and multiwavelength study of the pevatron candidate pulsar wind nebula “dragonfly”,” *The Astrophysical Journal*, vol. 954, no. 1, p. 9, Aug. 2023.
- [145] A. U. Abeysekara *et al.*, “Multiple galactic sources with emission above 56 tev detected by hawc,” *Phys. Rev. Lett.*, vol. 124, p. 021 102, 2 Jan. 2020.
- [146] T. Sudoh, T. Linden, and D. Hooper, “The highest energy hawc sources are likely leptonic and powered by pulsars,” *Journal of Cosmology and Astroparticle Physics*, vol. 2021, no. 08, p. 010, Aug. 2021.
- [147] Z. Cao *et al.*, “Ultrahigh-energy photons up to 1.4 petaelectronvolts from 12 gamma-ray galactic sources,” *Nature*, vol. 594, no. 7861, pp. 33–36, Jun. 2021a.
- [148] F. Aharonian *et al.*, “Extended very-high-energy gamma-ray emission surrounding psr j0622+3749 observed by lhaaso-km2a,” *Phys. Rev. Lett.*, vol. 126, p. 241 103, 24 Jun. 2021c.
- [149] Z. Cao *et al.*, “Discovery of a New Gamma-Ray Source, LHAASO J0341+5258, with Emission up to 200 TeV,” *Astrophysical Journal Letters*, vol. 917, no. 1, L4, p. L4, Aug. 2021b. arXiv: 2107.02020 [astro-ph.HE].
- [150] K. Mori *et al.*, “NuSTAR broad-band X-ray observational campaign of energetic pulsar wind nebulae in synergy with VERITAS, HAWC and Fermi gamma-ray telescopes,” in *37th International Cosmic Ray Conference*, Mar. 2022, 963, p. 963. arXiv: 2108.00557 [astro-ph.HE].
- [151] D. A. Burgess *et al.*, “The eel pulsar wind nebula: A pevatron-candidate origin for hawc j1826-128 and hess j1826-130,” *Astrophysical Journal*, vol. 930, no. 2, p. 148, May 2022.
- [152] J. Park *et al.*, “A broadband x-ray study of the rabbit pulsar wind nebula powered by psr j1418-6058,” *Astrophysical Journal*, vol. 945, no. 1, p. 66, Mar. 2023.
- [153] J. Park *et al.*, “X-ray studies of the pulsar psr j1420–6048 and its tev pulsar wind nebula in the kookaburra region,” *Astrophysical Journal*, vol. 945, no. 1, p. 33, Mar. 2023.
- [154] M. S. E. Roberts *et al.*, “PSR J2021+3651: A Young Radio Pulsar Coincident with an Unidentified EGRET Gamma-Ray Source,” *Astrophysical Journal Letters*, vol. 577, no. 1, pp. L19–L22, Sep. 2002. arXiv: astro-ph/0206443 [astro-ph].

- [155] M. S. E. Roberts, R. W. Romani, and N. Kawai, “The asca catalog of potential x-ray counterparts of gev sources,” *The Astrophysical Journal Supplement Series*, vol. 133, no. 2, p. 451, Apr. 2001.
- [156] R. C. Hartman *et al.*, “The Third EGRET Catalog of High-Energy Gamma-Ray Sources,” *Astrophysical Journal Supplement Series*, vol. 123, no. 1, pp. 79–202, Jul. 1999.
- [157] J. W. T. Hessels *et al.*, “Observations of PSR J2021+3651 and its X-Ray Pulsar Wind Nebula G75.2+0.1,” *Astrophysical Journal*, vol. 612, no. 1, pp. 389–397, Sep. 2004. arXiv: astro-ph/0403632 [astro-ph].
- [158] A. Van Etten, R. W. Romani, and C. Y. Ng, “Rings and Jets around PSR J2021+3651: The “Dragonfly Nebula”,” *Astrophysical Journal*, vol. 680, no. 2, pp. 1417–1425, Jun. 2008. arXiv: 0802.3707 [astro-ph].
- [159] A. A. Abdo *et al.*, “PULSED GAMMA-RAYS FROM PSR j2021+3651 WITH THE FERMI LARGE AREA TELESCOPE,” *Astrophysical Journal*, vol. 700, no. 2, pp. 1059–1066, Jul. 2009.
- [160] A. A. Abdo *et al.*, “Discovery of TeV Gamma-Ray Emission from the Cygnus Region of the Galaxy,” *Astrophysical Journal Letters*, vol. 658, no. 1, pp. L33–L36, Mar. 2007. arXiv: astro-ph/0611691 [astro-ph].
- [161] M. S. E. Roberts *et al.*, “The Full Spectrum Galactic Terrarium: MHz to TeV Observations of Various Critters,” in *American Institute of Physics Conference Series*, F. A. Aharonian, W. Hofmann, and F. Rieger, Eds., ser. American Institute of Physics Conference Series, vol. 1085, Dec. 2008, pp. 328–331. arXiv: 0811.0570 [astro-ph].
- [162] E. Aliu *et al.*, “Spatially Resolving the Very High Energy Emission from MGRO J2019+37 with VERITAS,” *Astrophysical Journal*, vol. 788, no. 1, 78, p. 78, Jun. 2014. arXiv: 1404.1841 [astro-ph.HE].
- [163] A. U. Abeysekara *et al.*, “A very high energy gamma-ray survey toward the cygnus region of the galaxy,” *Astrophysical Journal*, vol. 861, no. 2, p. 134, Jul. 2018.
- [164] A. Fruscione *et al.*, “CIAO: Chandra’s data analysis system,” in *Observatory Operations: Strategies, Processes, and Systems*, D. R. Silva and R. E. Doxsey, Eds., ser. Society of Photo-Optical Instrumentation Engineers (SPIE) Conference Series, vol. 6270, Jun. 2006, 62701V, p. 62701V.
- [165] M. Bachetti, *HENDRICS: High ENergy Data Reduction Interface from the Command Shell*, Astrophysics Source Code Library, record ascl:1805.019, May 2018. ascl: 1805.019.

- [166] D. Huppenkothen *et al.*, “Stingray: A Modern Python Library for Spectral Timing,” *Astrophysical Journal*, vol. 881, no. 1, p. 39, Aug. 2019. arXiv: 1901.07681 [astro-ph.IM].
- [167] V. Zabalza, J. M. Paredes, J. Martí, J. R. Sánchez-Sutil, and A. J. Muñoz-Arjonilla, “XMM-Newton Observations of the Inner Region of MGRO J2019+37,” in *High Energy Phenomena in Massive Stars*, J. Martí, P. L. Luque-Escamilla, and J. A. Combi, Eds., ser. Astronomical Society of the Pacific Conference Series, vol. 422, May 2010, p. 186.
- [168] T. Mizuno, N. Tanaka, H. Takahashi, J. Katsuta, K. Hayashi, and R. Yamazaki, “X-ray studies of the extended TeV gamma-ray source VER j2019+368,” *Astrophysical Journal*, vol. 841, no. 2, p. 104, May 2017.
- [169] P. Freeman, S. Doe, and A. Siemiginowska, “Sherpa: a mission-independent data analysis application,” in *Astronomical Data Analysis*, J.-L. Starck and F. D. Murtagh, Eds., ser. Society of Photo-Optical Instrumentation Engineers (SPIE) Conference Series, vol. 4477, Nov. 2001, pp. 76–87. arXiv: astro-ph/0108426 [astro-ph].
- [170] R. Jin, C.-Y. Ng, M. S. E. Roberts, and K.-L. Li, “High-resolution radio study of the dragonfly pulsar wind nebula powered by psr j2021+3651,” *Astrophysical Journal*, vol. 942, no. 2, p. 100, Jan. 2023.
- [171] M. V. Barkov, M. Lyutikov, N. Klingler, and P. Bordas, “Kinetic ‘jets’ from fast-moving pulsars,” *Monthly Notices of the Royal Astronomical Society*, vol. 485, no. 2, pp. 2041–2053, May 2019. arXiv: 1804.07341 [astro-ph.HE].
- [172] T. Temim, P. Slane, P. P. Plucinsky, J. Gelfand, D. Castro, and C. Kolb, “Proper motion of the high-velocity pulsar in snr msh 15-56,” *Astrophysical Journal*, vol. 851, no. 2, p. 128, Dec. 2017.
- [173] R. Weaver, R. McCray, J. Castor, P. Shapiro, and R. Moore, “Interstellar bubbles. II. Structure and evolution,” *Astrophysical Journal*, vol. 218, pp. 377–395, Dec. 1977.
- [174] J. A. Toalá *et al.*, “X-ray emission from the wolf–rayet bubble s 308\*,” *Astrophysical Journal*, vol. 755, no. 1, p. 77, Jul. 2012.
- [175] G. Collaboration, A. Vallenari, A. Brown, and T. P. et al., “Gaia data release 3. summary of the content and survey properties,” *Astronomy & Astrophysics*, Jun. 2022.
- [176] D. R. Law, K. DeGioia-Eastwood, and K. L. Moore, “Empirical Bounds for the Ionizing Fluxes of Wolf-Rayet Stars,” *Astrophysical Journal*, vol. 565, no. 2, pp. 1239–1250, Feb. 2002.
- [177] De Luca, A. and Molendi, S., “The 2-8 keV cosmic x-ray background spectrum as observed with xmm-newton \*\*\*,” *A&A*, vol. 419, no. 3, pp. 837–848, 2004.

- [178] J. P. Halpern *et al.*, “Discovery of high-energy gamma-ray pulsations from PSR j2021+3651 with AGILE,” *Astrophysical Journal*, vol. 688, no. 1, pp. L33–L36, Oct. 2008.
- [179] Fermi-LAT collaboration *et al.*, “Incremental Fermi Large Area Telescope Fourth Source Catalog,” *arXiv e-prints*, arXiv:2201.11184, arXiv:2201.11184, Jan. 2022. arXiv: 2201.11184 [astro-ph.HE].
- [180] M. Wood *et al.*, “Fermipy: An open-source Python package for analysis of Fermi-LAT Data,” in *35th International Cosmic Ray Conference (ICRC2017)*, ser. International Cosmic Ray Conference, vol. 301, Jan. 2017, 824, p. 824. arXiv: 1707.09551 [astro-ph.IM].
- [181] J. Ballet, T. H. Burnett, S. W. Digel, and B. Lott, *Fermi large area telescope fourth source catalog data release 2*, 2020.
- [182] F. Acero *et al.*, “Constraints on the Galactic Population of TeV Pulsar Wind Nebulae Using Fermi Large Area Telescope Observations,” *Astrophysical Journal*, vol. 773, no. 1, 77, p. 77, Aug. 2013. arXiv: 1306.5735 [astro-ph.HE].
- [183] M. Di Mauro, S. Manconi, M. Negro, and F. Donato, “Investigating gamma-ray halos around three hawc bright sources in fermi-lat data,” *Phys. Rev. D*, vol. 104, p. 103 002, 10 Nov. 2021.
- [184] A. Albert *et al.*, “Spectrum and Morphology of the Very-high-energy Source HAWC J2019+368,” *Astrophysical Journal*, vol. 911, no. 2, 143, p. 143, Apr. 2021.
- [185] A. Kirichenko *et al.*, “OPTICAL OBSERVATIONS OF PSR j2021+3651 IN THE DRAGONFLY NEBULA WITH THE GTC,” *Astrophysical Journal*, vol. 802, no. 1, p. 17, Mar. 2015.
- [186] J. Fang, L. Wen, H. Yu, and S. Chen, “Investigating the multiband non-thermal emission of the 100 TeV source eHWC J2019+368 with a pulsar wind nebula scenario,” *Monthly Notices of the Royal Astronomical Society*, vol. 498, no. 4, pp. 4901–4905, Nov. 2020. arXiv: 2007.13943 [astro-ph.HE].
- [187] V. Zabalza, “Naima: A python package for inference of relativistic particle energy distributions from observed nonthermal spectra,” *Proc. of International Cosmic Ray Conference 2015*, p. 922, 2015. eprint: 1509.03319.
- [188] J. D. Gelfand, P. O. Slane, and W. Zhang, “A DYNAMICAL MODEL FOR THE EVOLUTION OF a PULSAR WIND NEBULA INSIDE a NONRADIATIVE SUPERNOVA REMNANT,” *Astrophysical Journal*, vol. 703, no. 2, pp. 2051–2067, Sep. 2009.
- [189] A. C. Cummings *et al.*, “Galactic cosmic rays in the local interstellar medium: Voyager 1 observations and model results,” *Astrophysical Journal*, vol. 831, no. 1, p. 18, Oct. 2016.

- [190] R. Jansson and G. R. Farrar, “A New Model of the Galactic Magnetic Field,” *Astrophysical Journal*, vol. 757, no. 1, 14, p. 14, Sep. 2012. arXiv: 1204.3662 [astro-ph.GA].
- [191] Deharveng, L. *et al.*, “Triggered massive-star formation at the border of the hii region sh 104,” *A&A*, vol. 408, no. 3, pp. L25–L28, 2003.
- [192] J. A. Rodón *et al.*, “Physical properties of the Sh2-104 H II region as seen by Herschel,” *Astronomy & Astrophysics*, vol. 518, L80, p. L80, Jul. 2010. arXiv: 1005.3070 [astro-ph.GA].
- [193] J.-L. Xu *et al.*, “Two-dimensional molecular gas and ongoing star formation around h ii region sh2-104,” *Astrophysical Journal*, vol. 849, no. 2, p. 140, Nov. 2017.
- [194] E. V. Gotthelf *et al.*, “HARD x-RAY EMISSION FROM SH 2-104: A nustar search FOR GAMMA-RAY COUNTERPARTS,” *Astrophysical Journal*, vol. 826, no. 1, p. 25, Jul. 2016.
- [195] J. M. Paredes *et al.*, “Radio continuum and near-infrared study of the <ASTROBJ>MGRO J2019+37</ASTROBJ> region,” *Astronomy & Astrophysics*, vol. 507, no. 1, pp. 241–250, Nov. 2009. arXiv: 0909.0406 [astro-ph.HE].
- [196] I. Pope *et al.*, “A Multiwavelength Investigation of PSR J2229+6114 and its Pulsar Wind Nebula in the Radio, X-Ray, and Gamma-Ray Bands,” *Astrophysical Journal*, vol. 960, no. 1, 75, p. 75, Jan. 2024. arXiv: 2310.04512 [astro-ph.HE].
- [197] V. V. Dwarkadas, “The evolution of supernovae in circumstellar wind-blown bubbles. i. introduction and one-dimensional calculations,” *Astrophysical Journal*, vol. 630, no. 2, p. 892, Sep. 2005.
- [198] O. Kargaltsev, B. Rangelov, and G. G. Pavlov, *Gamma-ray and x-ray properties of pulsar wind nebulae and unidentified galactic tev sources*, 2013. arXiv: 1305.2552 [astro-ph.HE].
- [199] K. Fang, M. Kerr, R. Blandford, H. Fleischhack, and E. Charles, “Evidence for pev proton acceleration from fermi-lat observations of snr g106.3+2.7,” *Phys. Rev. Lett.*, vol. 129, p. 071 101, 7 Aug. 2022.
- [200] Y. Ohira, S. Kisaka, and R. Yamazaki, “Pulsar Wind Nebulae inside Supernova Remnants as Cosmic-Ray PeVatrons,” *Monthly Notices of the Royal Astronomical Society*, vol. 478, no. 1, pp. 926–931, May 2018. eprint: <https://academic.oup.com/mnras/article-pdf/478/1/926/25012963/sty1159.pdf>.
- [201] B. M. Gaensler and P. O. Slane, “The evolution and structure of pulsar wind nebulae,” *Annual Review of Astronomy and Astrophysics*, vol. 44, no. 1, pp. 17–47, 2006. eprint: <https://doi.org/10.1146/annurev.astro.44.051905.092528>.

- [202] T. Temim, P. Slane, C. Kolb, J. Blondin, J. P. Hughes, and N. Bucciantini, “Late-Time Evolution of Composite Supernova Remnants: Deep Chandra Observations and Hydrodynamical Modeling of a Crushed Pulsar Wind Nebula in SNR G327.1-1.1,” *Astrophysical Journal*, vol. 808, no. 1, p. 100, Jul. 2015. arXiv: 1506.03069 [astro-ph.HE].
- [203] C. Kolb, J. Blondin, P. Slane, and T. Temim, “Evolution of a Pulsar Wind Nebula within a Composite Supernova Remnant,” *Astrophysical Journal*, vol. 844, no. 1, p. 1, Jul. 2017. arXiv: 1707.06352 [astro-ph.HE].
- [204] F. Verbunt, A. Igoshev, and E. Cator, “The observed velocity distribution of young pulsars,” *Astronomy & Astrophysics*, vol. 608, A57, A57, Dec. 2017. arXiv: 1708.08281 [astro-ph.HE].
- [205] O. Kargaltsev, G. G. Pavlov, N. Klingler, and B. Rangelov, “Pulsar wind nebulae created by fast-moving pulsars,” *Journal of Plasma Physics*, vol. 83, no. 5, 635830501, p. 635 830 501, Oct. 2017. arXiv: 1708.00456 [astro-ph.HE].
- [206] X. Tang and R. A. Chevalier, “Particle transport in young pulsar wind nebulae,” *Astrophysical Journal*, vol. 752, no. 2, p. 83, May 2012.
- [207] O. Porth, M. J. Vorster, M. Lyutikov, and N. E. Engelbrecht, “Diffusion in pulsar wind nebulae: an investigation using magnetohydrodynamic and particle transport models,” *Monthly Notices of the Royal Astronomical Society*, vol. 460, no. 4, pp. 4135–4149, May 2016. eprint: <https://academic.oup.com/mnras/article-pdf/460/4/4135/8116708/stw1152.pdf>.
- [208] S. P. Reynolds, K. J. Borkowski, and P. H. Gwynne, “Expansion and Brightness Changes in the Pulsar-wind Nebula in the Composite Supernova Remnant Kes 75,” *Astrophysical Journal*, vol. 856, no. 2, 133, p. 133, Apr. 2018. arXiv: 1803.09128 [astro-ph.HE].
- [209] M. J. Vorster, O. Tibolla, S. E. S. Ferreira, and S. Kaufmann, “Time-dependent modeling of pulsar wind nebulae,” *Astrophysical Journal*, vol. 773, no. 2, p. 139, Aug. 2013.
- [210] C. B. Adams *et al.*, “Multiwavelength observation of a candidate pulsar halo Ihaaso j0621+3755 and the first x-ray detection of psr j0622+3749,” *The Astrophysical Journal (in press)*, 2025.
- [211] A. A. Abdo *et al.*, “Milagro Observations of Multi-TeV Emission from Galactic Sources in the Fermi Bright Source List,” *Astrophysical Journal Letters*, vol. 700, no. 2, pp. L127–L131, Aug. 2009, First detection of Geminga at TeV energies(?) and some evidence of extension. arXiv: 0904.1018 [astro-ph.HE].
- [212] A. Albert *et al.*, “3HWC: The Third HAWC Catalog of Very-high-energy Gamma-Ray Sources,” *Astrophysical Journal*, vol. 905, no. 1, 76, p. 76, Dec. 2020. arXiv: 2007.08582 [astro-ph.HE].

- [213] A. Albert *et al.*, “HAWC Detection of a TeV Halo Candidate Surrounding a Radio-quiet Pulsar,” *Astrophysical Journal Letters*, vol. 944, no. 2, L29, p. L29, Feb. 2023. arXiv: 2301.04646 [astro-ph.HE].
- [214] Z. Cao *et al.*, “LHAASO detection of very-high-energy gamma-ray emission surrounding PSR J0248+6021,” *arXiv e-prints*, arXiv:2410.04425, arXiv:2410.04425, Oct. 2024. arXiv: 2410.04425 [astro-ph.HE].
- [215] M. Di Mauro, S. Manconi, and F. Donato, “Detection of a gamma-ray halo around Geminga with the Fermi -LAT data and implications for the positron flux,” *Phys. Rev. D*, vol. 100, no. 12, p. 123 015, 2019, [Erratum: Phys.Rev.D 104, 089903 (2021)]. arXiv: 1903 . 05647 [astro-ph.HE].
- [216] S. Manconi *et al.*, “Geminga’s pulsar halo: An X-ray view,” *Astron. Astrophys.*, vol. 689, A326, 2024. arXiv: 2403.10902 [astro-ph.HE].
- [217] B. Schroer, C. Evoli, and P. Blasi, “TeV halos and the role of pulsar wind nebulae as sources of cosmic-ray positrons,” *Physical Review D*, vol. 107, no. 12, 123020, p. 123 020, Jun. 2023. arXiv: 2305.08019 [astro-ph.HE].
- [218] K. Fang, S.-Q. Xi, and X.-J. Bi, “Self-consistent interpretations of the multiwavelength gamma-ray spectrum of LHAASO J0621+3755,” *Phys. Rev. D*, vol. 104, no. 10, p. 103 024, 2021. arXiv: 2107.02140 [astro-ph.HE].
- [219] L.-Z. Bao, K. Fang, X.-J. Bi, and S.-H. Wang, “Slow Diffusion is Necessary to Explain the Gamma-Ray Pulsar Halos,” *Astrophys. J.*, vol. 936, no. 2, p. 183, 2022. arXiv: 2107 . 07395 [astro-ph.HE].
- [220] M. Di Mauro, S. Manconi, and F. Donato, “Evidences of low-diffusion bubbles around Galactic pulsars,” *Phys. Rev. D*, vol. 101, no. 10, p. 103 035, 2020. arXiv: 1908 . 03216 [astro-ph.HE].
- [221] S. Recchia *et al.*, “Do the Geminga, Monogem and PSR J0622+3749 gamma-ray halos imply slow diffusion around pulsars?” *Phys. Rev. D*, vol. 104, no. 12, p. 123 017, 2021. arXiv: 2106.02275 [astro-ph.HE].
- [222] K. Fang, “Gamma-ray pulsar halos in the Galaxy,” *Front. Astron. Space Sci.*, vol. 9, p. 1 022 100, 2022. arXiv: 2209.13294 [astro-ph.HE].
- [223] R.-Y. Liu, “The physics of pulsar halos: Research progress and prospect,” *Int. J. Mod. Phys. A*, vol. 37, no. 22, p. 2 230 011, 2022. arXiv: 2207.04011 [astro-ph.HE].
- [224] D. Zheng and Z. Wang, “Finding Candidate TeV Halos among Very-high-energy Sources,” *Astrophysical Journal*, vol. 968, no. 2, 117, p. 117, Jun. 2024. arXiv: 2403 . 16074 [astro-ph.HE].

- [225] H. J. Pletsch *et al.*, “Discovery of Nine Gamma-Ray Pulsars in Fermi Large Area Telescope Data Using a New Blind Search Method,” *Astrophysical Journal*, vol. 744, no. 2, 105, p. 105, Jan. 2012. arXiv: 1111.0523 [astro-ph.HE].
- [226] J. P. W. Verbiest, J. M. Weisberg, A. A. Chael, K. J. Lee, and D. R. Lorimer, “On Pulsar Distance Measurements and Their Uncertainties,” *Astrophysical Journal*, vol. 755, no. 1, 39, p. 39, Aug. 2012. arXiv: 1206.0428 [astro-ph.GA].
- [227] W. F. Brisken, S. E. Thorsett, A. Golden, and W. M. Goss, “The Distance and Radius of the Neutron Star PSR B0656+14,” *Astrophysical Journal Letters*, vol. 593, no. 2, pp. L89–L92, Aug. 2003. arXiv: astro-ph/0306232 [astro-ph].
- [228] D. A. Smith *et al.*, “The Third Fermi Large Area Telescope Catalog of Gamma-Ray Pulsars,” *Astrophysical Journal*, vol. 958, no. 2, 191, p. 191, Dec. 2023. arXiv: 2307.11132 [astro-ph.HE].
- [229] V. P. Fomin, A. A. Stepanian, R. C. Lamb, D. A. Lewis, M. Punch, and T. C. Weekes, “New methods of atmospheric Cherenkov imaging for gamma-ray astronomy. I. The false source method,” *Astroparticle Physics*, vol. 2, no. 2, pp. 137–150, May 1994.
- [230] G. Maier and J. Holder, “Eventdisplay: An Analysis and Reconstruction Package for Ground-based Gamma-ray Astronomy,” in *35th International Cosmic Ray Conference (ICRC2017)*, ser. International Cosmic Ray Conference, vol. 301, Jul. 2017, 747, p. 747. arXiv: 1708.04048 [astro-ph.IM].
- [231] G. Maier *et al.*, *Eventdisplay: An analysis and reconstruction package for veritas*, version v490.2, Jul. 2023.
- [232] M. Krause, E. Pueschel, and G. Maier, “Improved gamma-hadron separation for the detection of faint gamma-ray sources using boosted decision trees,” *Astroparticle Physics*, vol. 89, pp. 1–9, Mar. 2017. arXiv: 1701.06928 [astro-ph.IM].
- [233] A. Donath *et al.*, “Gammapy: A python package for gamma-ray astronomy,” *Astronomy and Astrophysics*, vol. 678, A157, 2023.
- [234] A. Aguasca-Cabot *et al.*, *Gammapy: Python toolbox for gamma-ray astronomy*, version v1.1, Jun. 2023.
- [235] D. Berge, S. Funk, and J. Hinton, “Background modelling in very-high-energy gamma-ray astronomy,” *Astronomy & Astrophysics*, vol. 466, no. 3, pp. 1219–1229, May 2007. arXiv: astro-ph/0610959 [astro-ph].
- [236] A. Acharyya *et al.*, “Multiwavelength Investigation of Gamma-Ray Source MGRO J1908+06 Emission Using Fermi-LAT, VERITAS and HAWC,” *Astrophysical Journal*, vol. 974, no. 1, 61, p. 61, Oct. 2024. arXiv: 2408.01625 [astro-ph.HE].

- [237] W. Cash, “Parameter estimation in astronomy through application of the likelihood ratio.,” *Astrophysical Journal*, vol. 228, pp. 939–947, Mar. 1979.
- [238] D. Kieda, “Status of the VERITAS Upgrade,” in *International Cosmic Ray Conference*, ser. International Cosmic Ray Conference, vol. 9, Jan. 2011, p. 14. arXiv: 1110.4360 [astro-ph.IM].
- [239] A. Nepomuk Otte, “The Upgrade of VERITAS with High Efficiency Photomultipliers,” *arXiv e-prints*, arXiv:1110.4702, arXiv:1110.4702, Oct. 2011. arXiv: 1110.4702 [astro-ph.IM].
- [240] S. L. Snowden, M. R. Collier, and K. D. Kuntz, “XMM-Newton Observation of Solar Wind Charge Exchange Emission,” *Astrophysical Journal*, vol. 610, no. 2, pp. 1182–1190, Aug. 2004. arXiv: astro-ph/0404354 [astro-ph].
- [241] K. D. Kuntz and S. L. Snowden, “The EPIC-MOS particle-induced background spectra,” *Astronomy & Astrophysics*, vol. 478, no. 2, pp. 575–596, Feb. 2008.
- [242] K. A. Arnaud, “XSPEC: The First Ten Years,” in *Astronomical Data Analysis Software and Systems V*, G. H. Jacoby and J. Barnes, Eds., ser. Astronomical Society of the Pacific Conference Series, vol. 101, Jan. 1996, p. 17.
- [243] H. E. S. S. Collaboration *et al.*, “Detection of extended Gamma-ray emission around the Geminga pulsar with H.E.S.S.,” *Astronomy & Astrophysics*, vol. 673, A148, A148, May 2023. arXiv: 2304.02631 [astro-ph.HE].
- [244] C. B. Adams *et al.*, “The throughput calibration of the VERITAS telescopes,” *Astronomy & Astrophysics*, vol. 658, A83, A83, Feb. 2022. arXiv: 2111.04676 [astro-ph.IM].
- [245] G. G. Pavlov, S. Bhattacharyya, and V. E. Zavlin, “New X-ray Observations of the Geminga Pulsar Wind Nebula,” *Astrophysical Journal*, vol. 715, no. 1, pp. 66–77, May 2010. arXiv: 1002.1109 [astro-ph.HE].
- [246] B. Posselt *et al.*, “Geminga’s Puzzling Pulsar Wind Nebula,” *Astrophysical Journal*, vol. 835, no. 1, p. 66, Jan. 2017. arXiv: 1611.03496 [astro-ph.HE].
- [247] P. A. Caraveo *et al.*, “Geminga’s Tails: A Pulsar Bow Shock Probing the Interstellar Medium,” *Science*, vol. 301, no. 5638, pp. 1345–1348, Sep. 2003.
- [248] K. Mori *et al.*, “A Broadband X-Ray Study of the Geminga Pulsar with NuSTAR and XMM-Newton,” *Astrophysical Journal*, vol. 793, no. 2, p. 88, Oct. 2014. arXiv: 1408.1644 [astro-ph.HE].
- [249] A. Khokhriakova, W. Becker, G. Ponti, M. Sasaki, B. Li, and R. Y. Liu, “Searching for X-ray counterparts of degree-wide TeV halos around middle-aged pulsars with SRG/eROSITA,”

*Astronomy & Astrophysics*, vol. 683, A180, A180, Mar. 2024. arXiv: 2310 . 10454 [astro-ph.HE].

- [250] Q.-Z. Wu, C.-M. Li, X.-H. Liang, C. Ge, and R.-Y. Liu, “Diagnosing the Particle Transport Mechanism in the Pulsar Halo via X-Ray Observations,” *Astrophysical Journal*, vol. 969, no. 1, 9, p. 9, Jul. 2024. arXiv: 2401.17982 [astro-ph.HE].
- [251] R. Alfaro *et al.*, “Ultra-high-energy gamma-ray bubble around microquasar V4641 Sgr,” *Nature*, vol. 634, no. 8034, pp. 557–560, Oct. 2024. arXiv: 2410.16117 [astro-ph.HE].